Analytical, Numerical, and Experimental Investigation of Air- and Liquid-Based Synthetic Jet Devices for Next-Generation Solid-State Cooling in Data Centers and High-Flux Electronics

by

Mohammad Azarifar

A dissertation submitted to the Graduate Faculty of
Auburn University
in partial fulfillment of the
requirements for the Degree of
Doctor of Philosophy

Auburn, Alabama
August 9, 2025

Keywords: Heat Transfer, Synthetic Jet, Liquid Cooling, Forced Convection

Approved by

Dr. Mehmet Arik, Chair, Associate Professor of Mechanical Engineering
Dr. Daniel Harris, Co-chair, Associate Professor of Mechanical Engineering
Dr. Mark A. Hoffman, Associate Professor of Mechanical Engineering
Dr. Michel Smith, Professor of Mathematics and Statistics
University Reader: Dr. Hossein Jahromi, Assistant Professor of Biosystems Engineering

Abstract

Modern high-power electronic systems, specifically high-power computer chips, demand transformative liquid cooling solutions as traditional air cooling struggles to meet ever-increasing heat fluxes. In data centers, rising microprocessor thermal design powers—escalating from air cooling limits of 280 W to beyond 700 W—necessitate a shift toward liquid cooling. Thus, this dissertation begins with a literature survey on the necessity of liquid cooling in data centers. One key observation from this review establishes that while single-phase immersion cooling offers potential, it requires localized enhancement to overcome inherent inefficiencies. Recognizing the promise of synthetic jet devices for targeted heat removal, this work pioneers the development of mesoscale Liquid Synthetic Jet Devices, a class previously explored mostly in air. To bridge this gap, dual air and water, analytical, numerical, and experimental studies were performed.

Regarding air-based synthetic jet cooling, a new fabrication approach based on additive manufacturing was presented. This method enabled the production of ultra-thin devices—as thin as 4 mm—without mechanical fasteners and with complete freedom in device cavity design. Hotwire anemometry tests revealed air jet exit velocities exceeding 106 m/s using a single piezoelectric diaphragm, among the highest reported in the literature. Diaphragm deflection measurements were performed using a laser displacement sensor. Next, lumped element modeling, tuned solely on diaphragm deflection behavior, accurately predicted device performance and was validated using hotwire anemometry. By fabricating and testing multiple synthetic jet devices with different geometries, it was demonstrated that the impulse generation rate—which accounts for both jet velocity and flow rate—better correlates with enhanced heat transfer capabilities than jet velocity alone. Thermal tests showed that, compared to natural convection, the manufactured devices achieved over 13 times greater heat removal rates, with an average heat transfer coefficient exceeding 120 W/(m^2·K) over a 30 mm $\times$ 30 mm heated surface.

Next, the fabrication extended to liquid synthetic jet device design and manufacturing. The devices were waterproofed and operated at higher voltages than air-based devices. Due

to reduced operating frequencies, they achieved operational jet generation with minimal power consumption as low as 50 mW. In an immersion cooling test setup designed to evaluate liquid-based synthetic jet devices in deionized water, liquid synthetic jet impingement showed a heat transfer coefficient of up to 1.52 W/(cm^2·K). Compared to existing methods, superior heat removal per unit of consumed power was achieved. This work demonstrates an advancement in sustainable thermal management, showing that such a small and inexpensive device can improve the coefficient of performance of single-phase immersion cooling by up to 12 times. Furthermore, the first lumped element model for liquid synthetic jet devices was proposed.

Lastly, the analytical model was further studied in conjunction with numerical computational fluid dynamics simulations and additional thermal tests in harsher environments. Fabrication improvements increased the device's operational frequency from 155 Hz to 210 Hz. Results demonstrated heat transfer enhancement, with the liquid synthetic jet device achieving a peak heat transfer coefficient of 1.7 W/(cm^2·K), an 8.7-fold improvement over mixed convection cooling, while maintaining low power consumption (0.22 W). The device cooled a 144 W heated surface from 72 °C to 31.5 °C under a crossflow rate of 2 GPM at 20 °C. Particle Image Velocimetry experiments and high-speed videography helped determine diaphragm deflection values based on a parametric study using computational fluid dynamics simulations. Later, lumped element models tuned with computational fluid dynamics results were used to understand liquid synthetic jet operation in an expanded frequency domain. This enabled the first report on the jet formation criterion for water-based liquid synthetic jet devices, with a value of +6 for circular orifices.

Collectively, this dissertation charts a roadmap that unites immersion liquid cooling strategies with liquid synthetic jet technology, offering scalable, energy-efficient, and solid state and sustainable thermal management solution for next-generation data centers and high-power electronics. Future work will explore multi-jet array configurations, enhanced surface integrations, optimized voltage amplification, and long-term reliability—particularly in two-phase immersion cooling environments—to further refine and commercialize this approach.

Acknowledgments

As I reflect upon the journey that has culminated in the completion of this PhD dissertation, I am filled with awe at the collective experience that has carried me to this moment. While reading the book *Why We Believe: Evolution and the Human Way of Being* by Agustin Fuentes, I came to realize that my path is not solely my own—it is the product of innumerable contributions spanning generations. From the very origins of life, through the evolution of Homo sapiens and the legacy of my ancestors, to every individual and every society I have ever encountered, a vast network of lives and experiences has converged to make this accomplishment possible. In many ways, each of these contributions can be seen as an essential "boundary condition," setting the stage for my journey to Auburn University and for the writing of this dissertation.

I would like to express my profound gratitude to everyone who has played a role in this process. At the heart of my appreciation lies the unwavering support of those closest to me: my family—my mother, my father, and my sister. My parents sacrificed their own dreams and comforts to ensure that I could pursue my goals. Their abundant love and belief in me have been the solid foundation upon which I have built my aspirations, and I cannot thank them enough. My gratitude also extends to Esthefany, my love and now my family, whose steady hand and compassionate support transformed my time at Auburn into an experience of both personal and academic growth. Meeting her during this PhD period is one of the most unexpected and cherished blessings of my life.

I am deeply indebted to my advisor, Dr. Arik, whose guidance and mentorship opened the door to Auburn and illuminated the path forward when the journey grew challenging.

I would also like to extend my thanks to the many individuals and institutions that enriched my academic environment: Auburn University, Makerspace, Dr. Roberts, Dr. Harris, Dr. Abdel Hadi, Dr. Antic, Dr. Ayasoufi, Dr. Hoffman, Dr. Khodadai, Dr. Smith, Dr. Suhling, and all the staff—Elizabeth, Merideth, Karen, Kimberly, Kayla, and Jason; my lab mates Faisal and Shafiq; and my friends Faramarz, Ehsan, and Mehrab. Each of you has contributed in a unique and meaningful way to the realization of this work.

I must also acknowledge Kash, our delightfully eccentric dog, whose constant presence provided both comfort and levity throughout the arduous days of research and writing.

Finally, I extend my sincere appreciation to the United States for placing its trust in me and affording me the opportunity to study in this beautiful country. I am particularly moved by the words of Albert Einstein:

> "The sense of equality and human dignity is particularly strong in this country. This is what makes it possible for me, a human being from abroad, who was received here as a guest, to speak to you today. In these days of hate and fear, this country, by its tradition and by its devotion to the freedom of the individual, still stands as a beacon of hope."

Coming from a country that has faced its share of challenges, these words resonate deeply with me. I remain profoundly grateful for the shelter, the opportunities, and the freedom that have allowed me to pursue my dreams and further my work. I hope to one day give back to this nation and to the broader community that has so generously supported me on my journey.

Mohammad Azarifar, February of 2025.

Table of Contents

List of Tables

List of Figures

List of Abbreviations

β	coefficient of thermal expansion (1/K)
$\dot{I}$	hydrodynamic impulse rate per unit width (kg·m/s^2)
γ	ratios of specific heat
$\hat{U}$	maximum area averaged jet exit velocity (m/s)
μ	dynamic viscosity (Pa.s)
ν	kinematic viscosity (m^2/s)
ν_∞	kinematic viscosity in the ambient (m^2/s)
ω_n	natural frequency (Hz)
ω	angular frequency (rad/s)
ω_h	Helmholtz frequency (Hz)
$\overline{U}$	time and area averaged velocity magnitude (m/s)
ρ	density (kg/m^3)
ρ_∞	unperturbed fluid density (kg/m^3)
τ	period (s)
ζ	damping ratio
A	orifice area (m^2)

A_w surface area of the oscillating wall (m^2)

A_{HS} heat spreader surface area (m^2)

c damping coefficient

C_c contraction coefficient

C_d viscous loss coefficient

c_f acoustic radiation damping factor (N·s/m)

C_l inertia coefficient

c_v specific heat in constant volume (J/(kg·K)

c_w structural damping of the oscillating wall (N·s/m)

c_p specific heat (kJ/(kg.K))

D diameter (m)

D_w diameter of the oscillating wall (m)

fr frequency (Hz)

fr_H Helmholtz resonance (Hz)

fr_w wall resonance frequency (Hz)

FRP flexural rigidity of plate (N·m)

H_1 Struve function of the first kind

h_{eff} effective heat transfer coefficient (W/(m^2· K)

h_{fg} latent heat of vaporization (J/kg)

I impulse generation (kg·m/s)

J_1 Bessel function of the first kind

K bulk modulus (Pa)

k thermal conductivity (W/(m.K)) / stiffness (N/m)

K^* jet formation constant

L^* stroke length (m)

L_e effective length of the air jet/slug at the orifice (m)

L_o length of the orifice (m)

L_{es} equivalent length of an ejected slug (m)

m_f acoustic mass of fluid (kg)

m_w mass of wall/diaphragm (kg)

N Poisson's ratio

P_∞ initial cavity pressure or pressure outside the cavity (Pa)

p_i gauge pressure (Pa)

p_{pump} pumping power (W)

q heat transfer rate (W)

T_f film temperature (K)

T_s surface temperature (K)

T_b boiling temperature (K)

T_i inlet temperature (K)

T_w wall temperature (K)

U area averaged velocity magnitude (m/s)

U_{sound} speed of sound (m/s)

v	voltage (V)
3D	Three Dimensional
ASJD	Air Synthetic Jet Device
BC	Boundary Condition
CFD	Computational Fluid Dynamics
CJ	Continuous Jet
CPI	Cooling Performance Index
AI	Artificial Intelligence
CDU	Cooling Distribution Unit
COP	Coefficient of Performance
CRAC	Computer Room Air Conditioner
CRAC	Computer Room Air Handler
DECS	Datacom Equipment Cooling System
FWS	Facility Water System
GWP	Global Warming Potential
HDD	Hard Disk Drive
HFC	Hydrofluorocarbons
HFO	Hydrofluoroolefin
IoT	Internet of Things
IT	Information Technology
PUE	Power Usage Effectiveness

SMR Small Modular Reactor

SSD Solid State Drive

TCS Technology Cooling System

TDP Thermal Design Power

TE Thermoelectric

DI Dielectric

FOM Figure of Merit

FPGA Field Programmable Gate Array

JFC Jet Formation Criteria

LEM Lumped Element Model

LSJ Liquid Synthetic Jet

LSJD Liquid Synthetic Jet Device

Nu Nusselt Number

ODE Ordinary Differential Equation

P_{in} power consumption (W)

PCM Phase Change Materical

PFAS Per- and Polyfluoroalkyl Substances

PIV Particle Image Velocimetry

PIV Particle Image Velocimetry

Pr Prandtl number

RDHx Rear Door Heat Exchanger

Re	Reynolds Number
Ri	Richardson number
SJ	Synthetic Jet
SJD	Synthetic Jet Device
St	Strouhal number
Stk	Stokes number
TC	thermocouple
TEC	Thermoelectric Cooler
TIM	Thermal Interface Material
ZNMF	Zero Net Mass Flux

Chapter 1

An Insight into the Shift from Air to Liquid Cooling in Electronics Cooling: a Survey on Component-Level Data Center Cooling

The increasing heat flux in electronic components has driven a notable shift from air cooling to liquid cooling solutions. To explore this transition, this chapter delves into the move towards liquid cooling in data center applications, as presented in our recently published review article [1].The evolving data-generation landscape requires faster and more efficient microprocessors, prompting innovative manufacturing methods for smaller and faster transistors. Transistor congestion and increasing demand for parallel processing push the thermal design power of microprocessors well beyond 280 W, a limit for air cooling, and are expected to surpass 700 W by 2025. Consequently, transitioning towards liquid cooling is necessary. This chapter is intended to serve as a comprehensive road map for understanding this shift. It covers four major liquid cooling techniques: indirect water cooling with rear door heat exchangers, direct liquid cooling using water blocks or evaporators, single-phase, and two-phase immersion cooling. Indirect water cooling with rear door heat exchangers is a simple water cooling adaptation for reducing the power consumption of existing air-cooled data centers, but it faces the same limitations as air cooling for high-power servers. With enhancements such as reduced hot air leakage, active rear door heat exchangers, and deployment in locations conducive to free cooling, this approach could provide highly efficient data centers for the foreseeable future. Direct liquid cooling is well suited to meet the increasing demands for thermal design power with the highest heat transfer coefficient report of 25 W/(m^2·K), using the microjet impingement of a water-based manifold in the die. Emerging technologies are new thermosyphon systems, on-die/on-lid refrigeration/impingement, two phase impingement, and on/in die microchannel cooling. Air

cooling is still required for peripheral equipment in this method, adding to the complexity and power consumption. Immersion cooling has the potential of reducing infrastructure size by one-third of air-cooled data centers. Single-phase immersion cooling, while the most simple to implement, is limited by the low thermophysical properties of the dielectric liquids and lack of flow control mechanism. In contrast, two-phase immersion cooling faces significant challenges related to the use of engineered fluids with global warming potential, health hazards, and long-term reliability.

1.1 Introduction

Microprocessors, the workhorses of today's data centers, are shouldering a constantly escalating computational burden. In 2018, the data center industry was estimated to consume 205 Terawatt-hours, approximately 1% of global energy consumption [2]. Data centers in the United States consume about 2% of national electricity [3]. Back in 2007, even when the global data sphere was nascent, measuring merely in the zettabytes, the information and communication technology sector was already responsible for 2% of global anthropogenic CO_2 emissions [4, 5]. Fast forward to today, the data landscape has ballooned over one hundred times with forecasts indicating 175 zettabytes by 2025 [5]. Hyperscale companies invested $ 37 billion in data centers in just the third quarter of 2020 alone [6]. Global spending is expected to exceed $ 222 billion in 2023, up from $ 212 billion in 2022 [7]. The industry is in the midst of what can only be described as a "snowball effect" in data generation, propelled by the ever-increasing power of data and data processing [8]. This amplification loop is fueled by an insatiable demand for higher power processors, internet of things internet of things (IoT), artificial intelligence (AI), streaming, edge deployment, and 5G+ mobile networks. To address these growing demands, advanced small modular reactors (SMRs) are being considered to power data centers [9]. A notable example of this approach is the construction of power plants based on 24 SMRs in Ohio and Pennsylvania with a total capacity of 1.8 GW for nearby data centers [10].

Data centers are grappling with cooling systems that pose logistical and environmental challenges. But the thermal challenges do not stop at mere power usage; they are intricately tied

to the ongoing evolution of semiconductor technologies. High-numerical-aperture extreme-ultraviolet lithography seems to still keep "Moore's law on track" [11, 12]. As we navigate the transition from 7 nm to 5 nm technology nodes, and potentially to 1 nm within a decade[13], the impact on thermal management becomes increasingly significant. It merits attention that 3 nm complementary metal-oxide semiconductor platform technology [14] has already achieved commercial penetration, finding applications in personal smartphones and computing devices. Although smaller transistors are more efficient, resulting in reduced heat dissipation on a per-transistor basis, the increasing density of these transistors offsets these gains. For example, 5 nm technology will host 171.3 million transistors per square millimeter, which is 1.8 times more than the current 7 nm technology [15]. Yet, the industry estimates suggest only a 10-15% reduction in power usage for this transition [16]. Consequently, the net effect is an increase in thermal design power (TDP), projected to exceed 700 W by 2025 for even the most thermally efficient CPUs [17]. Various manufacturers already showcase this trend, with NVIDIA's Hopper [18] having a TDP of 700 W for AI applications, and NVIDIA Ada Lovelace [19] anticipated to have a TDP of 616 W. Similarly, Intel's Sapphire Rapids-SP [20] and AMD's Genoa [21] CPUs, based on 10 nm and 7 nm technologies, respectively, exhibit TDPs of 350 W and 400 W. TDP values are expected to rise further as the demand for AI-accelerated tasks, parallel processing, and neural network training grows.

As high-performance computing continues to ascend, they are compelling a fundamental redesign of data center infrastructure — most critically, their thermal management systems. Operating with cooling systems that consume up to 40% of total energy in a data center is no longer tenable [22]. The urgent need for more energy-efficient cooling solutions is not merely a matter of operational efficiency; it's a key strategy for lessening the environmental impact of the data industry as a whole [23]. Traditional air cooling, long the stalwart in data center thermal management, is facing an unprecedented challenge: it can no longer efficiently mitigate the escalating heat produced by the ever-increasing power densities of modern processors. Air, as a conventional cooling medium, has to be replaced by liquids, as it has reached a tipping point where its thermophysical nature has become inadequate for the task. The heat removal capacity of air is only around 37% of water in data centers [24]. As succinctly pointed out by Huang et

al. [25], the choice to transition to liquid cooling is backed by a compelling logic; Whatever liquid cooling technology is chosen, it will always be more efficient than air since the amount of energy required for forced convection with air will always be several times greater than that to move a liquid for the same amount of cooling.

1.1.1 A Broad Look at Data Center Cooling and Previous Review Studies

Cooling systems in data centers currently face a bifurcated mandate: they must simultaneously augment their operational efficiency while accommodating the exigencies of escalating power densities [26]. While the shift towards liquid cooling appears to address these dual objectives, liquid cooling is still a new topic.

From an industrial perspective, it is not obvious when the complete global transition from air cooling will happen. First, information technology (IT) equipment manufacturers will need to adjust their designs to accommodate liquid cooling. They may also require a form factor change, perhaps changing some configurations to allow boards to be mounted and packaged differently with respect to the motherboard and other components. Other modifications that cannot be foreseen now, may also be required [27]. It needs to be mentioned that with most liquid cooling applications, there is still a need for a small air-side system to carry the minor heat load from convective and radiative heat dissipation through the sides and tops of the racks, as well as lighting systems and any shell loads. A humidity control system must also be provided since liquid-cooled racks cannot provide dehumidification at the rack level [28].

For those interested in a comprehensive understanding of thermal management technologies within data centers, established resources such as ASHRAE (American Society of Heating, Refrigerating and Air-Conditioning Engineers) Datacom Series [29] and the Data Center Handbook [30] offer expansive overviews. While these publications do engage with a variety of cooling methods, it is notable that a significant portion of their content is dedicated to traditional air-cooling. Additionally, both the European Commission and the US Department of Energy's Federal Energy Management Program have issued detailed guides on best practices and emerging technologies for data centers. The European Commission's "Best Practice Guidelines for the EU Code of Conduct on Data Centre Energy Efficiency" [31] and the US

Department of Energy's "Best Practices Guide for Energy-Efficient Data Center Design" [32] cover various topics including liquid cooling techniques, ranging from liquid immersion cooling to adjustments in server inlet temperature and humidity, as well as rack-level direct liquid cooling.

The later sections of this study are organized in a way that begins with air cooling and progressively advances towards various types of liquid cooling. It is important to note that each subcategory is a vast area of research. In each subsection, recent related reviews and concluding remarks from them will be provided. Here, two general overview articles need to be mentioned; Souza et al. [33] examine the complexities of modern data centers, with a focus on cooling subsystems that are vital for both reliability and cost management. The paper identifies a research gap, stating that no existing studies have addressed cooling systems in terms of reliability and environmental sustainability. The paper identifies a research gap, stating that no existing studies have addressed cooling systems in terms of reliability and environmental sustainability. The financial consequences of data center failures are also highlighted, showing a 61% increase in the cost of unplanned downtimes from 2010 to 2016. The study advocates for "green data centers" and calls for an integrated approach in designing cooling systems that balances reliability, cost, and sustainability. In another broad review, Liu et al. [34] predicts that data centers will account for 4.5% of the world's energy usage by 2025. To forecast future energy consumption and carbon emissions of data centers, the paper introduces a new predictive method. This method relies on Cisco's research for predicting global data center traffic and uses the Romonet simulation model to ascertain power usage effectiveness (PUE) in both global average terms and for high-latitude areas. Two scenarios for data center location, centralized and decentralized, are examined through polynomial fitting methods. The study concludes that a centralized data center scenario in the Pan-Arctic region could significantly reduce global energy consumption and carbon emissions by 2030 — specifically, by about 301 billion kWh and 720 million tons of CO_2, respectively.

Several key terms must be introduced. PUE is a metric used to measure data center energy efficiency, calculated as the ratio of the total amount of energy used by the data center to the energy used by the IT equipment with the smallest value of 1.0 (average global PUE in 2019

was 1.67 [35] which has improved to 1.55 in 2022 [36]). The term ”direct” is next, which can be perplexing because its interpretation varies depending on context and is used in literature with various meanings. In general, direct cooling involves directing liquid into the rack to remove heat from IT equipment. Thus, using water blocks is considered direct liquid cooling, despite the fact that there is a barrier between the water block and the lid. (This term is used in many other forms, e.g., in rack-level, it refers to the use of liquid-to-liquid heat exchangers in cooling distribution units, or it could also mean directly guiding facility water system to water blocks.).

Liquid circulation loops should also be addressed. The technology cooling system (TCS)is the first primary liquid cooling loop. The TCS creates a thermal transport loop between the server and the cooling distribution unit (CDU), removing heat from IT equipment. This heat is then transferred to either the air or the CDU's secondary liquid loop, also known as the facility water system (FWS). TCS and FWS are separated and exchange heat through a heat exchanger. The FWS is a loop that integrates the CDU and chiller. The chiller then links to a condenser, dry cooler, or cooling tower. It is important to note that when the TCS uses a coolant other than water, ASHRAE assigns another term within the TCS as the datacom equipment cooling system (DECS).

1.2 A Glimpse into Air Cooled Data Centers

In computing, a server — whether manifested as specialized hardware or software —provides an array of services and resources to other devices, termed ”clients,” within a network framework. Servers are typically bolstered by an assortment of IT equipment such as processors, storage drives, and network interface cards, which are usually mounted on server-, blade-, or tower-racks. Over 99% of the electrical energy consumed by these servers is transformed into heat [37]. For safe operation of IT equipment, air cooling has traditionally been the method of choice since not only does it act as cooling mechanism, but also controls the humidity and air quality of the room [38]. Thermodynamic state of the room should be under control to avoid condensation on the equipment surfaces for high humidity cases (2 °C above dew point), and to avoid electrostatic discharges in low humidity cases. ASHRAE [39] provide frequently

updated standards for room conditions. To achieve these conditions, data centers utilize specialized air-conditioning units, often described as precision cooling systems. These units range from floor-mounted computer room air conditioners (CRAC) and computer room air handlers (CRAH)(CRAC) (small floor-mounted up to 100 kW, and large floor-mounted up to 1 MW) to ceiling-mounted (up to 10 kW), and portable air conditioning systems (up to 5 kW). There are 13 fundamental cooling schemes used in air cooled data centers. Graphical abstract of these 13 methods is presented in Figure 1.1, which is inspired from detailed white papers published by Schneider Electric's data center science center [40].

In air-cooled data centers, air-conditioning units send chilled air into the under-floor plenum, which is then blown into the room through the perforated floor tiles (in less common configuration overhead vents can be used). Fans circulate air over electronic components (with added heat sink for high-power electronic components), intaking cooling air from "cold aisle" and expelling it into a "hot aisle" through the rear of the server chassis. Hot air returns to air-conditioning unit and cycling continues [41]. Heat will eventually be transferred to outdoor air via condenser, dry cooler, or cooling tower, or simply through air ducts to direct/indirect evaporative coolers or roof top units. It is easier for a data center manager to maintain the suitable operating temperature and guarantee the safety of servers by monitoring the air temperature rather than monitoring the IT equipment temperature [42]. Therefore, maintaining the air temperature within a reasonable range is generally sufficient to ensure the safety of servers. Most servers are designed to operate at ambient temperatures no higher than 45 °C, according to the allowable operating temperature of class A4 specified by ASHRAE. However, the recommended temperature range for data centers is typically between 18 and 27 °C. Contemporary research on air cooled data centers focuses on optimizing air flow distribution, exploring elevated temperature rooms, and challenges of new standards for refrigerants.

1.2.1 Rising Importance of Airflow Distribution

In a recent review article, Zhao et al. [42] shift the conversation from air conditioning to airflow distribution in air-cooled data centers. They identify "local hotspots" as areas where

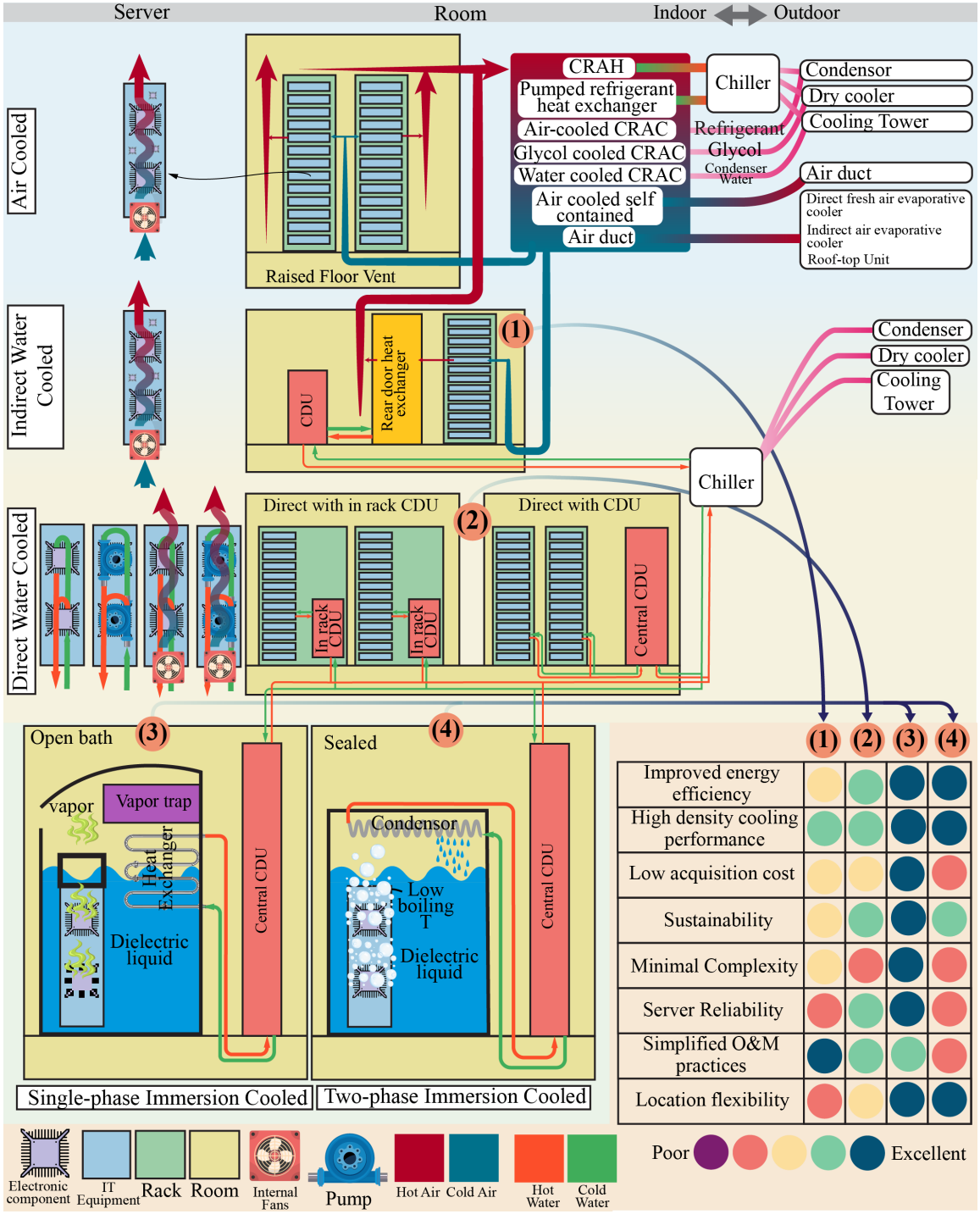

Figure 1.1: Overview of the data center cooling scheme, featuring air cooling at the top and four primary types of liquid cooling techniques in below.

servers overheat, mainly due to inefficient airflow rather than high server load. The paper advocates for two approaches to solve this: (a) regulating air flow and (b) shortening the cold air path. While various metrics are considered for identifying hotspots, local room temperature is flagged as the most reliable. The authors also highlight a research gap, emphasizing the need for localized cooling solutions and better use of existing wall and column sensors, which are important to CRAC/CRAH operators. Overall, the review serves as a comprehensive guide for data center operators seeking to understand, identify, and mitigate hotspot issues. In this vein, Han et al. [43] propose a unique demand-based air-conditioning system that blends a heat pipe-based cooling system with a vapor compression cooling cycle, utilizing evaporative condenser side of heat pipe for enhanced natural cooling. The paper establishes that manipulating the outdoor unit's airflow and the evaporator inlet temperature could lead to reduced energy consumption in both the system's compressor and pump. The coefficient of performance (COP) is highlighted as a pivotal metric, displaying optimal performance under specific air flow rates and evaporator inlet temperatures for varying cooling capacities. While promising in terms of energy efficiency, the study concludes that further research is needed to improve operational reliability and cost-effectiveness.

1.2.2 Shift Towards High Temperature Rooms, and Limit Imposed by HDDs

Recent efforts to increase the efficiency of air-cooled data centers are to move to high temperature data centers, with the ultimate goal of more hours of "free cooling". It has been reported that increasing the room temperature in data centers by 1 °C results in the saving of the total power consumption by 4–5% [44]. We are seeing an increase in the allowable sink temperatures in the thermal resistance network of new microprocessors. However, it is important to note that this increase in cold side temperature does not necessarily imply an increase in the allowable junction temperature (T_j) for semiconductor packages. The maximum T_j for typical flipped-chip packages has remained relatively consistent across generations, with a limit of around 110 °C. This limit is primarily influenced by the inherent properties of packaging materials, such as the glass transition temperature of underfill [45]. Several factors have made it possible to

unlock higher sink side temperatures. Due to advances in semiconductor technology, the thermal resistance of microprocessors has decreased over time. Third-generation semiconductors with a wider bandgap (such as GaN/SiC) are not only more energy efficient [34], but also allow for higher voltage and faster switching frequency [46]. They also have improved thermal interfaces and thermal conductivity, which leads to lower package thermal resistance. Zhang et al. [22] provide a comprehensive review of high-temperature data centers, focusing on their potential for energy savings through ”free cooling” and the challenges they face in terms of technical bottlenecks, reliability, and performance of servers and IT components like CPUs and hard disk drives. Concerning the bottlenecks and limitations, the most replaced component in servers is the hard disk drive (HDD) and interestingly authors concluded that the HDD is a key limitation for high-temperature operation.

In contemporary data centers, conversion from HDDs to solid state drives (SSDs) are occurring incrementally due to various economic and performance factors. Despite SSDs costing eight times more per unit of storage [47], their falling prices and lower energy consumption—initially averaging 6.0 W per drive compared to HDDs' 8.1 W—are rendering them increasingly attractive [48]. SSDs have a 9.5% annual increase compared to a 2.9% annual decrease for HDDs. Meanwhile, market intelligence reveals that more than 90% exabytes (260 bytes) stored in cloud data centers are still in HDDs, largely because they offer a better total cost of ownership for the majority of workloads [49]. However, the challenging thermal conditions of high-temperature data centers—where SSDs can operate at up to 70 °C compared to HDDs' 55 °C—pose an additional impetus for the ongoing transition to SSDs. Overall, the complete transition is expected to unfold gradually as SSD costs continue to decline and their capacities increase.

1.2.3 New Standards for Refrigerants

The operational principle underpinning data center air-cooling systems relies on the refrigeration cycle, a technology that has been in use for over a century [50]. This cycle involves the evaporation, pressure alteration, condensation, and flow regulation of a refrigerant. Currently, the predominant choices are Hydrofluorocarbons (HFCs); R410A is commonly used in smaller

data centers requiring up to 300 – 400 kW of cooling per unit, while R134a is more typical in larger installations [51], favored for their non-toxic and non-flammable qualities [52]. This selection has been shaped by regulations that prohibited older refrigerants like R-22 and R142b starting in 2010 [53]. However, a shift is underway due to the high global warming potential (GWP) of current HFCs [54]. For instance, R-134a has a GWP of 1430, R410A stands in 2088, and R407C in 1774. With environmental regulations tightening, Canada plans to cut HFC usage by 85% by 2036 [55], and the US will ban HFCs such as R134a, R410A, and R407C in new chillers starting January 1, 2024 [56]. The industry is now exploring alternative refrigerants with lower GWP. Hydrofluoroolefins (HFOs) like HFO-1234ze(E) offer a GWP as low as 6 [57]. Zeotropic mixtures, with their distinctive temperature glide and composition shift driven by volatility differences among their constituents, observed to boost the efficiency and performance of vapor compression systems while offering lower GWP over single-constituent refrigerants [58, 59]. Natural refrigerants like ammonia and CO_2 are also under consideration, although each comes with its own set of challenges; ammonia is toxic and flammable, while CO_2 is less efficient as a refrigerant compared to traditional HFCs. Refrigerant transition poses several challenges and opportunities. While new refrigerants can be more expensive and potentially less efficient, they are more environmentally friendly. Academic discourse on this transition remains limited, with the most existing information found in commercial white papers.

1.3 Towards Liquid Cooling

Up to this point, challenges facing modern data centers, particularly concerning air-cooling limitations, are discussed. Based on previous discussion, the necessity to transition to liquid cooling has been emphasized. Specifically, when the TDP ranges exceed 250 and 280 W, and the heat generation at the rack level surpasses 100 kW [17], traditional air-cooling methods fail (or basically are not efficient enough) to maintain microprocessor temperatures within recommended limits. In response, the academia has seen a surge of innovation in this area (specifically in chip level), with alternative techniques ranging from thermoelectric (TE) assisted air-cooling [60] to phase change material (PCM)-based thermal management systems

[61]. General challenges of these technologies have limited their widespread adoption are complexity and expense, the high-level coordination required between electrical circuit and thermal engineers, new manufacturing processes, reliability risks, yield reduction, restricted re-workability, and supply-chain risks [62]. Given the extensive variety of these emergent technologies, it's almost implausible for a single review to capture the full breadth of all solutions. This paper only covers an overview of four major types of liquid cooling techniques, as shown Figure 1.1.

It's noteworthy that liquid cooling is a highly explored concept. As early as the 1960s, IBM began implementing water cooling in their System 360 computers [63]. Cooling microelectronic components with liquids began to attract serious attention in the mid-1980s, as IBM, Honeywell, Sperry-Univac, Control Data, and Hitachi all introduced indirectly water-cooled mainframe computers [64]. Since then, liquid cooling has been ubiquitously employed in large computer systems, and evolved into four main categories:

- Indirect water-cooled data centers (a bridge between air cooling and liquid cooling),
- Direct water/liquid-cooled data centers,
- Open bath immersion cooling of data centers with dielectric liquids, and
- Sealed immersion cooling of data centers with engineered dielectric liquids.

Liquid cooling for data centers is still an emerging discipline. Comprehensive thermodynamic analysis, such as Ref. [65, 66], that encompasses all pertinent factors across various scales—from chip and server to rack, room, and facility—is scarce for liquid cooled data centers. Much of this gap exists because existing thermodynamic studies primarily derive their empirical data from air-cooled configurations, thereby potentially limiting their relevance to current challenges [67]. However, industry specialists (Green Revolution Cooling and Intel) presented a graphical comparison which is provided in Figure 1.1 regarding, cost, reliability, sustainability, complexity and location flexibility between these four liquid cooling methods in their recent white paper [68].

1.3.1 Indirect Water-cooled Data Centers

One of the most straightforward transitions to water-cooling for existing data centers involves retrofitting them with rear door heat exchangers (RDHx). In 2005, IBM released the first water cooled RDHx (sometimes referred as a side car) product [69], demonstrating substantial energy savings. The general configuration is illustrated in Figure 1.2, (passive, active, and future direction towards row-level contained RDHx). Typical water-cooled RDHx systems function like radiators affixed to the back of server racks, equipped with coils to facilitate heat exchange with the circulating water. These are commonly known as passive RDHx. To counteract pressure loss in RDHx, some systems incorporate suction fans, making them active RDHx. These systems require chilled water, conditioned to above dew point by CDUs, to cool the warm air emanating from IT equipment.

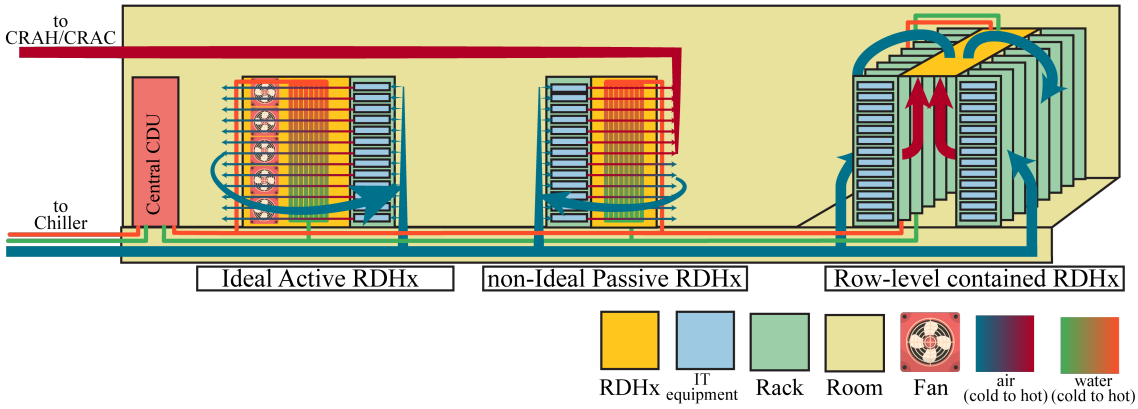

Figure 1.2: Side by side comparison for general configuration of passive, active, and row-level contained RDHx.

One of the primary advantages of adopting this technology is that, in an ideal scenario, there's no need for hot aisle containment or a return plenum. However, in practice, a portion of the rack-level heat is absorbed by the water coolant, thus reducing the thermal load on the primary refrigeration cycle [70]. RDHx systems also offer a proven solution to issues like hot aisle recirculation or cold air bypass, as they quickly absorb heat, minimizing the chance of air being redirected toward other outlets. Furthermore, RDHx systems reduce the mixing of warm ejected air with ambient air, potentially leading to lower inlet temperatures. Lastly, RDHx technology provides the opportunity for waste heat recovery. Simon et al. [71]

investigated the feasibility of using RDHx in high-capacity data centers. They employed a baseline computational fluid dynamics (CFD) model featuring a generic data center layout with peripheral CRAH/CRAC units and RDHx systems. The study was conducted using the commercial CFD tool 6SigmaRoom. Both active and passive RDHx modes were compared. In all rack-level analyses, a consistent air temperature difference of 12°C was maintained. The team examined four cases with different rack power levels between 7 kW and 11 kW. In each study, fan power was adjusted to maintain a 12°C air temperature difference at the front and back of the server. A fourth case featured an 11 kW rack with an active RDHx. Passive RDHx systems showed air flow leakage, an issue mitigated by using active RDHx. Despite the extra 500W power consumed by the fan in active RDHx, overall power savings were achieved through reduced cooling load on CRAC/CRAH units.

A hyper-scale data center layout with over 500 racks was also analyzed. It showed that RDHx systems could negate the need for mechanical cooling units, still requiring a chiller but potentially reducing its usage depending on the location's ambient conditions. Spatial temperature variation was not considered risky, as the average server inlet air temperature was around 29.7°C. Finally, the study examined airflow patterns post-RDHx. The air was directed upwards, circulating back into the cold aisle within 1.22 m from the top of the rack. This suggests potential for lowering the data center's height. The study also indicated room for optimization in aisle widths, which could further reduce the data center's size without negatively affecting RDHx performance Wakefield Thermal and Infosys partnered to demonstrate that a PUE of less than 1.1 was attainable using direct evaporative cooling in conjunction with RDHxs. The study was conducted at a Tier 3, 300 kW data center in Bangalore, India, and its findings have been published in [72]. An impressive PUE of 1.06 was initially achieved; however, the PUE increased due to excessive air leaks around the RDHx, stated to be caused by movement and modifications in the rack-mounted components. These leaks necessitated the use of a chilled water loop to maintain the desired water temperature through the RDHx. Despite these challenges, the data center successfully maintained a server room temperature of 27ºC. The RDHx system utilized tubes and aluminum fins to transfer heat from air to water. Out of the 26 active racks, 18 were equipped with RDHx, and chilled water was supplied to each RDHx unit via

a centralized CDU. The cooling system accounted for 12 to 21% of the facility's total energy load, with the lowest consumption occurring in the winter due to the use of free cooling and chiller off-modes. The chiller was switched off for the first 46 days and the last 46 days of the year, during which the cooling tower assumed the cooling responsibilities. The data center operated with a PUE above 1.4 for 209 days (approximately 63% of the year), resulting in an annualized PUE of 1.38. Thermal analysis revealed that the precision air conditioning units (PAC) accounted for one-third of the total cooling load, in comparison to the chiller. Figure 1.3 shows the cooling load shared by the PAC and RDHx units during the year 2017.

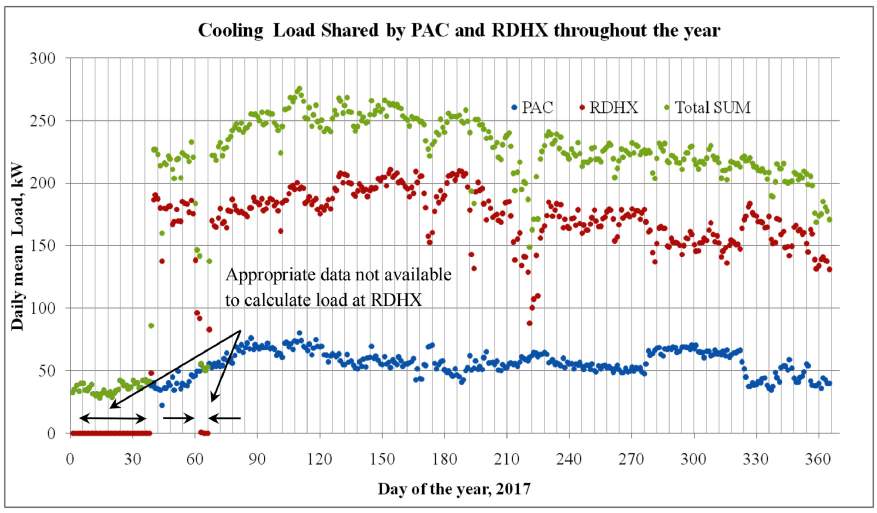

Figure 1.3: Distribution of the cooling load between PAC and RDHX based on one-year data collected from a data center in Bangalore, India [72].

Gao et al. [68] conducted an in-depth analysis focusing on both the steady-state and transient impacts of RDHx on data center cooling. Employing a three-dimensional (3D) room-level model, the study considered variables such as airflow, the height of the underfloor plenum, and potential failures of CRAC units. The results indicated that incorporating RDHx significantly improved dynamic performance, particularly during fluctuations in IT equipment load or instances of CRAC failure. The study revealed that the integration of RDHx could negate the temperature fluctuations commonly observed with standalone air-cooling systems. This hybrid approach also stabilized airflow patterns, preventing intense fluctuations in response to sudden changes in power, both temporally and spatially. Additionally, the hybrid cooling system expedited the time required to reach a steady-state following localized CRAC failures or sudden

power shifts. Thus, the employment of RDHx enhances the safety and predictability of data center operations, particularly when the data center experiences substantial and abrupt changes in rack power and airflow rates. The overhead row-based cooling solution [73] positions air handlers above the hot aisle, often in conjunction with a hot aisle containment system. Hot air, exhausted by the server racks, ascends and is then drawn into these overhead air handlers. These handlers not only extract heat proximal to the server racks but also create a pool of cold air, supplying chilled air directly to the racks. Current literature suggests that row-based cooling solutions hold the most promise for future air-cooled data center thermal management [74]. Generally, these solutions are more efficient than traditional room-based cooling systems. Although the initial capital expenditure for row-based cooling systems may be higher due to the dispersed nature of the cooling equipment [75], this setup allows for lower cooling capacities per unit. This, in turn, reduces the costs associated with implementing redundant cooling mechanisms. Furthermore, the row-based architecture simplifies the task of enhancing both the redundancy of cooling equipment and the overall reliability of IT equipment. RDHxs on the other hand, are designed primarily as rack-level solutions that can be affixed to standard 19-inch or 23-inch server racks. To the best of our knowledge, row based RDHx are not practiced yet. While not inherently "row-based," RDHx can be seamlessly integrated into row-based cooling frameworks. This integration significantly diminishes the load on the overhead air handlers. Such an amalgamation complements the benefits already associated with row-based systems, including cost reduction, simplified layout, minimized chiller pressure drop, and the utilization of larger, more efficient fans. By emphasizing the harmonization between RDHx and row-based cooling strategies, this approach offers a multifaceted solution to data center cooling, balancing both efficiency and simplicity. Instead of releasing heat into the atmosphere, a potential solution for addressing a major barrier in data center cooling could be to eject heat into the ocean. Microsoft plans to utilize cold seawater instead of traditional refrigeration cycles in their undersea data centers [76]. In 2018, they unveiled the "Northern Isles Data-center," innovative self-sufficient underwater data centers submerged in a 40 ft long capsule placed 100 ft beneath the North Sea's surface near the UK's Orkney islands. The system runs entirely on renewable energy using undersea cable, filled with dry nitrogen air, and includes 12 racks,

totaling 864 servers. Cooling is achieved through a combination of fans and a heat exchange plumbing system that circulates seawater via sealed tubes. Absence of Oxygen, less human interaction, and improved cooling results in 87.5% reduction in failure rate in comparison to equivalent land data center. Design concept for the third generation of the project can be seen in Figure 1.4 [77].

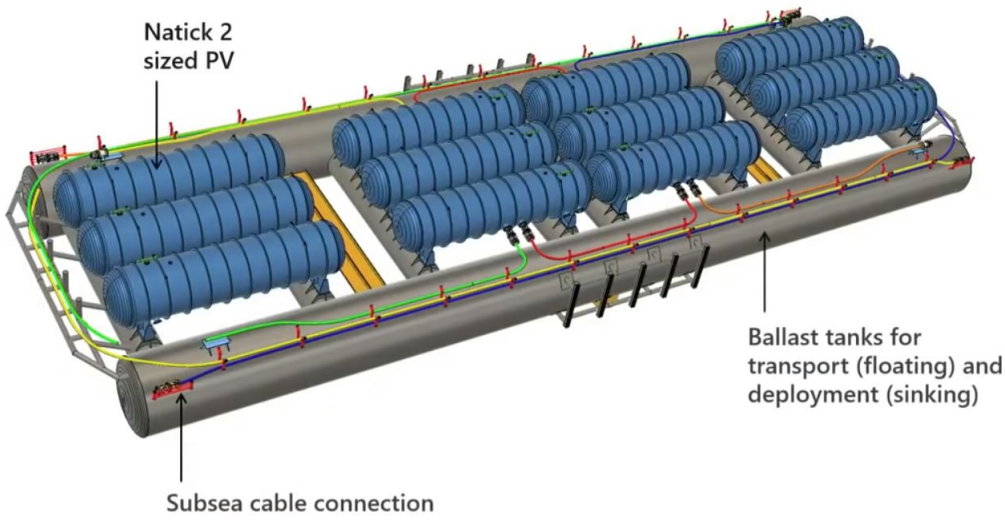

Figure 1.4: Microsoft Azure 3rd generation underwater data center scheme [77].

1.3.2 Direct Liquid-Cooled Data Centers

What if we were to remove the air barrier that separates RDHx from the IT components, enabling direct heat exchange from the IT equipment itself? This concept is known as a direct liquid-cooled data center. Although some literature may refer to this methodology as indirect liquid cooling, ASHRAE officially designates it as direct liquid cooling—a term we adhere to for uniformity.

Figure 51.5(a) aims to depict a simplified direct liquid cooling arrangement involving a cold plate mounted over a processor; A ”flip-chipped” die is soldered onto a substrate to establish an external circuit connection. The solder joints are encapsulated by underfill epoxy, which serves to absorb thermal stresses. This design strategy exposes the rear side of the die to facilitate heat transfer. Maintaining the flatness of the mounting surface is crucial for optimal thermal contacts. This is achieved by regulating both the amount of pressure exerted on the

die and its uniform distribution, while also accounting for thermal cycling effects (such considerations inherently restrict the maximum size of the microprocessors) [78, 79]. To enhance heat dissipation and offer protection, the die is covered by a lid. Thermal interface materials (TIMs) are applied to both its inner and outer surfaces [80] and cold plate sits on top. This integration introduces low conductivity interfaces between the exposed side of the cold plate to TCS (T_w) and the thermal junction of the die (the location of the T_j, which is typically at the center of the die, near the interface between the die and underfill). As shown in Figure 1.5(b), other components in the server, such as memory modules and voltage regulators, can also be liquid cooled by wrap around special cold plates [81], however, a chip-specific liquid cooling with peripheral air cooling approach is generally preferred.

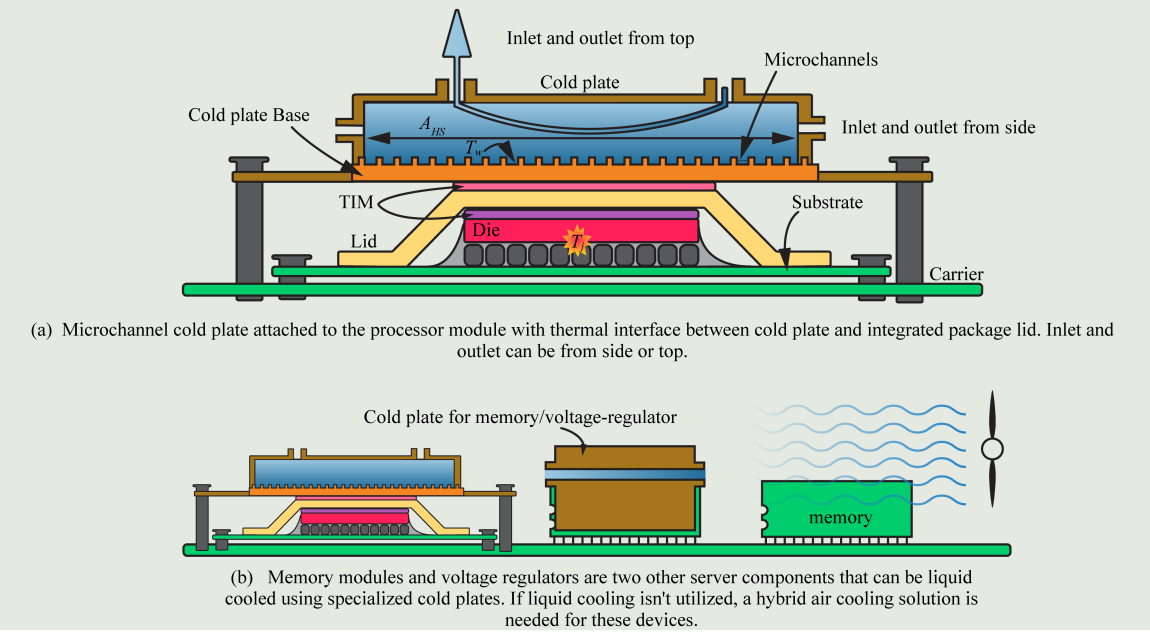

Figure 1.5: (a) A simplified thermo-physical arrangement involving a cold plate mounted over a processor, (b) On chip-specific water cooling with memory being cooled by peripheral air cooling or wrap around special cold plates.

Direct liquid cooling creates a complex heat exchanging loop composed of pump, piping and manifolds, fluid couplings, and terminators, where the CDU acts as its brain and facilitates heat exchange between TCS and FWS. CDUs can either be localized within an individual rack—thus providing TCS coolant solely to that rack—or act as floor-standing entities that distribute coolant across multiple racks. A less conventional approach, which is not covered herein, involves the absence of a CDU altogether. In such instances, FWS is guided directly

into rack, and manifolds distribute FWS into cold plates, thereby cooling components without the intermediation of a separate internal loops. The focus in this section is narrowly tailored to the TCS loop, whose prescribed constraints and conditions serve as the defining boundary conditions (BCs) for heat exchange within the cold plate apparatus. The rest of this overview section is an effort to quantify these BCs based on the ASHRAE Technical Committee 9.9's seminal 2019 white paper [27].

- **Circulating TCS Coolant.** One of the primary roles of the CDU is to circulate coolant in TCS within the internal rack/chassis. To adapt to fluctuations in temperature of FWS temperatures, and IT equipment heat loads, CDU employs sophisticated mechanisms such as bypass loops, proportional control valves, and variable speed pumps. TCS is governed by defined temperature bounds, with an upper and a lower limit. The upper bound represents the maximal allowable TCS supply temperature at a specific flow rate to ensure adequate cooling for the connected IT equipment; exceeding this temperature may necessitate an increased flow rate and could result in overheating. Conversely, the lower bound often correlates with the dew point inside and around the rack. CDU is responsible for monitoring this to adjust the TCS temperature to at least 2°C above the room dew point, thereby averting condensation issues. Similar to air-cooled equipment, ASHRAE provides a framework for categorizing liquid-cooled IT equipment based on FWS temperatures, as W1 (17°C), W2 (27°C), W3 (32°C), W4 (45°C), and W5 (>45°C). Apart from temperature limits, TCS has pressure limitation. In compliance with the ASME codes, TCS should be designed with safety margin of 1.5x. Both the TCS and FWS within the CDU include pressure relief valves and adhering to a relatively low 1.5x safety factor for pressure, enables a broader and more cost-effective designs. For water-cooled systems, the typical flowrate may range from 0.38 to 31.85 L/min, with an operating pressure range up to 827.4 kPa. Cold plates are typically equipped with microchannels. Reducing hydraulic diameter within the cold plate results in taking full advantage of the caloric density of TCS. While reducing hydraulic diameter generally improves heat transfer performance, it often comes at the expense of increased static pressure drop from the inlet to the exit ports as shown in Figure 1.6.

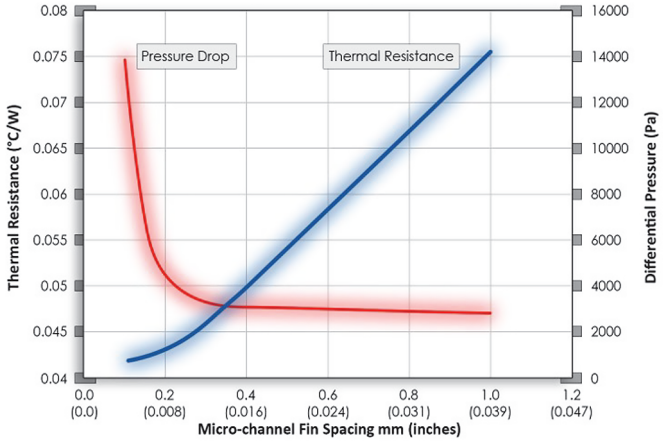

Figure 1.6: Effect of fin spacing on thermal resistance on pressure drop in microchannel cold plate [27].

Therefore, optimizing the trade-off between enhanced thermal performance and pressure drop becomes a critical design and safety aspect. Based on the microchannel size, effective filtration of TCS will be required. Strategic distribution of coolant among various cold plates is another important factor, which is recently studied by Heydari et al. [82]. Authors conducted experiments on in-row liquid-to-air CDUs. Three distinct cooling loops; X, Y, and Z (depicted in Figure 1.7) were considered. Designed thermal test vehicle comprised 8 large heaters (Type A, up to 1000 W) and 6 small heaters (Type B, up to 200 W). The investigation highlighted the significance of organizing flow distribution from each manifold outlet to the cold plates. Among studied loops, cooling loop Y exhibited superior thermal and hydraulic efficiency, boasting a thermal resistance of 0.0198 K/W at pressure drop of 45.1 kPa. In this configuration, for small cold plates attached to Type B heaters, the fluid follows a sequential path through cold plates 1, 2, and 3 before exiting the cooling loop (a mirrored sequence for cold plates 6 to 5, and 4). For large cold plates, the even-numbered ones received coolant first, followed by traversal through odd-numbered cold plates before exiting the cooling loop.

- **Facilitating Heat Transfer from the TCS to the FWS.** CDU exchanges heat between TCS and FWS, or TCS to air (radiator based). TCS to FWS is examined here. Inside the CDU, the liquid-to-liquid heat exchanger often features a flat plate construction, with

plate spacing typically varying from 2 to 8 mm. Due to these dimensions, varying degrees of filtration are necessary upstream of the CDU and also within the FWS loop to ensure optimal performance. CDU serves to segregate the FWS from the TCS, allowing for the use of alternative coolants and specially engineered fluids within the TCS loop. It's crucial, then, that the internal loop of the CDU and cold plates are chemically compatible for their wetted material list with whichever coolant is being utilized. This points to yet another essential function of the CDU; maintaining the quality and chemistry of the coolant throughout the operational cycle, which is indispensable for the long-term reliability and efficiency of the cooling system.

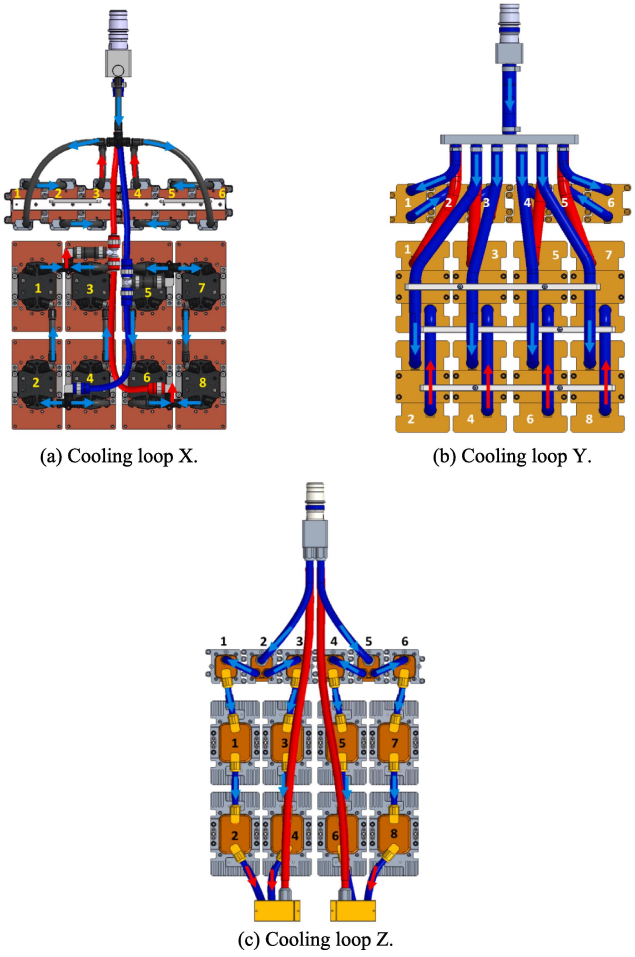

(a) Cooling loop X.

(b) Cooling loop Y.

(c) Cooling loop Z.

Figure 1.7: Three different types of cooling loops, (a) X, (b) Y, and (c) Z studied by Heydari et al. [82].

A similar conclusion can be drawn for cold plates from study of Kini et al. [83], as authors strongly recommend continuous monitoring of fluid chemical properties and periodic replenishment of fresh coolant to mitigate the potential adverse effects of corrosion on microchannel cold plates during long-term operation. In their research, corrosion behavior of microchannel cold plates was examined during continuous loop operation for over 600 hours. The study monitored both the thermal performance of the cold plates and the fluid's chemical properties, specifically pH and electrical conductivity, during long-term corrosion testing with a water-based coolant. The dominant observed failure mechanism was galvanic corrosion. The experimental data revealed that, under temperature-accelerated test conditions, no thermal degradation occurred within the given time frame. However, significant changes in fluid chemical properties indicated an ongoing progression of corrosion. Part two of the study [84] concludes that corrosion reliability can be assessed using the kinetic model, which incorporates temperature and external voltage as acceleration factors in the corrosion rate.

- **Constraints of Fluid Coupling.** TCS is only possible with fluid coupling architectures, each with distinct characteristics that dictate the volume flow rate and pressure within the TCS. These characteristics are broadly cataloged in Table 1.1. Couplings with shut-off mechanism (dry-break connectors) are being used to avoid fluid spillage. Liquid spillage within the server should not exceed 1 cc. When utilizing flexible hoses, additional clamps or ties are required for management and reduce pressure drop. Flexible hoses offer cost-efficiency, ease of maintenance, and design streamlining, particularly in scenarios involving multiple cold plates. In contrast, when employing rigid tubing or directly mating the connector to a manifold or port, threaded terminations are generally the method of choice. For tapered pipe threads, the application of supplemental sealing paste during installation is often mandated to guarantee a sealed interface. In this context, straight-thread terminations complemented with elastomeric O-ring seals are the preferred dry-break configuration. Lastly, when situating fluid connections in proximity

to IT equipment, attention must be paid to the vibrational factors that may impact long-term reliability. Appropriate installation torque should be rigorously adhered to during installation to counteract any potential loosening over extended operational periods. For instance, the connection force standard inside the server is below 50 N.

Parameter	Unit	CDU to Cabinet/Chassis	Cabinet/Chassis to Drawers	Drawer to Server/Blade and to cold plate
Size	in.	$2-4$	$0.5-2$	≤ 0.5
Flow rate	L/min	$<$ 1000 (cabinet), $<$ 100 (chassis)	100	≤ 5
Operating maximum P	bar	10	10	5
Maximum T	°C	200	200	150

Table 1.1: A concise overview sourced from ASHRAE Technical Committee 9.9 showcasing typical fluid couplings characteristics [27].

Cold plate designs promoting jet impingement cooling are gaining popularity. This can be inferred by comparing heat transfer performance of different cooling methods. Kheirabadi and Groulx [85] uses heat spreader heat flux to facilitate this comparison. While conventional metrics like wall heat flux and heat transfer coefficient offer valuable insights, they fall short in enabling direct comparisons across different cooling methodologies. Based on heat spreader heat flux, authors evaluated effective heat transfer coefficient (h_{eff}) from various published articles. Formulation is shown in Equation 1.1, which is based on heat transfer rate q, heat spreader surface area A_{HS}, surface temperature of the heat spreader T_w, and inlet temperature T_i:

$$h_{eff} = \frac{q}{A_{HS}\left(T_w - T_i\right)} \tag{1.1}$$

Ranges of h_{eff} can be seen in Figure 1.8, where jet impingement, spray cooling, and two phase cooling offer values above 8 W/(cm^2·K). Among these methods, spray cooling has received the least attention due to implementation challenges (and low CPI as shown later in Figure 1.9(b)). However, jet impingement and two-phase cooling have gained popularity and are now demonstrating practical applications in data centers. In order to compare these methods based on their energy efficiency, Sarkar et al. [86] compares the cooling performance index (CPI) - the rate of

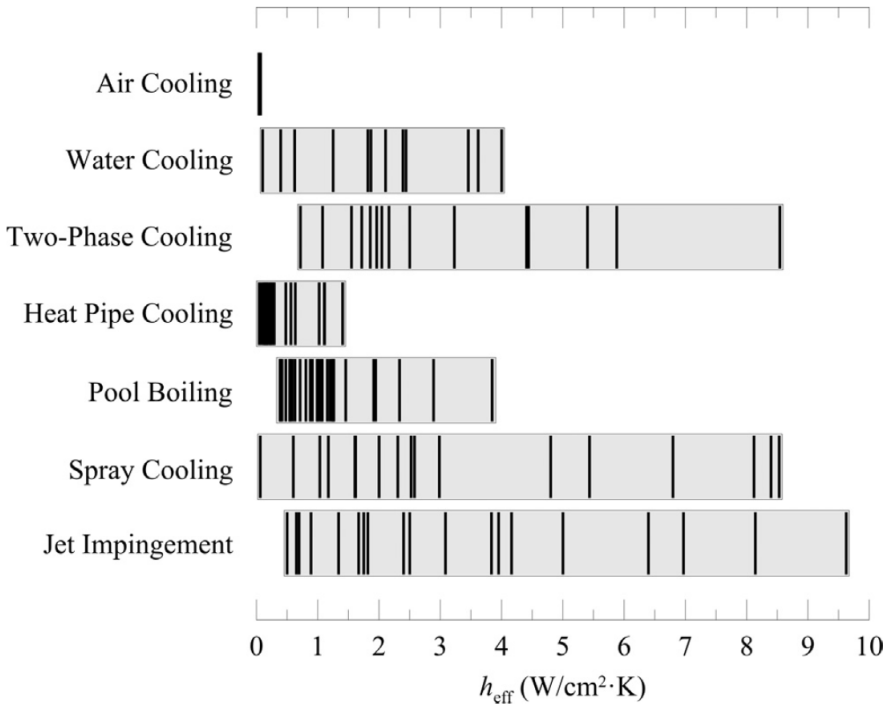

Figure 1.8: Ranges of effective heat transfer coefficients (h_{eff}) for microprocessor cooling in data centers [85] (In this figure, water cooling refers to microchannel cooling with water).

heat transfer (q) per unit of pumping power (p_{pump}) consumed - of different cooling methods which can be seen in Figure 1.9 (b). We have also included heat transfer coefficient attainable from different cooling methods in Figure. 1.9 (a) which is derived from Ref. [87, 88]. In Figure. 1.9(b), it can be seen that 4.7 times higher CPI is offered by impinging jets. Furthermore, authors show that in comparison to active cooling methods of spray and microchannel cooling, and passive methods of pool boiling and heat pipes, jet impingement presents highest Carnot COP (based on supply temperature and the heat source temperature). The low CPI of jet impingement, coupled with its high heat transfer coefficient, is attracting attention in the water block industry. However, the challenge here is how to integrate jet impingement successfully into cold plates? The earlier approach from industry was to choose inlet to cold plate usually from top to promote impingement on the surface. This jet is impinged on a low resistive heat spreader with microchannels in rectangular, fractal, serpentine, wavy, spiral, zigzag, pin fin, etc. patterns [89]. The jet is usually unorganized and has low velocity resulting in non-uniform cooling. The better answer was in array of impingement with the introduction of a manifold

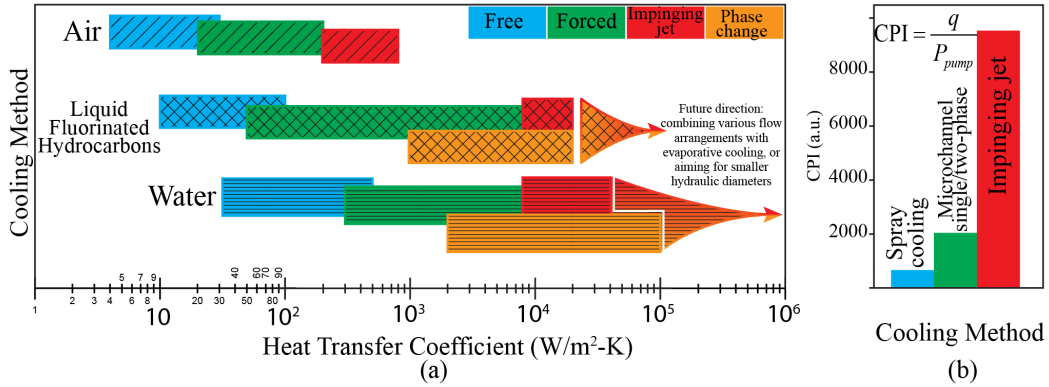

Figure 1.9: (a) Range of heat transfer coefficient of different cooling methods, and (b) experimentally evaluated cooling performance index (CPI) of different active cooling methods.

section. Industry refers to this as a "water block with a mid-plate," effectively emulating traditional manifold heat sinks within existing water blocks. With having manifold, there is no necessity for top flow inlet as the manifold section of cold plate intakes coolant from side and distributes coolant into arranged multitude array of nozzles for submerged jet or confined-jet impingement on the spreader.

Introduction of manifold to the design of heat sinks is proven effective way to utilize high heat transfer coefficient of jet impingement flows with reduce pressure drop [90]. Simply put, manifold heat sinks work by taking in coolant through the manifold section and distributing it evenly to arranged nozzles (see Figure 1.10(c)). At the bottom of these nozzles, there are interconnected microchannel networks. From these nozzles, coolant impinges on to the heat spreader, and travel a short distance parallel to the heat spreader inside microchannels (pin fins with improved performance can be used instead of microchannels [91]). Finally, the liquid gets collected by the outlet manifold and exits the cold plate. This design reduces pressure drop in the cold plate by having liquid travel a shorter distance in microchannels. A traditional microchannel heat sink with channel size of 50 µm wide and 300 µm deep at a pressure drop of 214 kPa [92] achieved the same heat transfer coefficient of 11.1 W/(cm^2·K) to manifold microchannel heatsink with similar channel characteristics and a pressure drop of 22 kPa [93]. Manifold heatsinks also provide uniform cooling on the spreader in comparison to conventional microchannel heat sinks. Walsh et al. [94] utilized an array of 19 silicon microjets, each with a diameter of 116 µm, to direct water microjets at a velocity of 16.93 m/s at temperature of 20°C

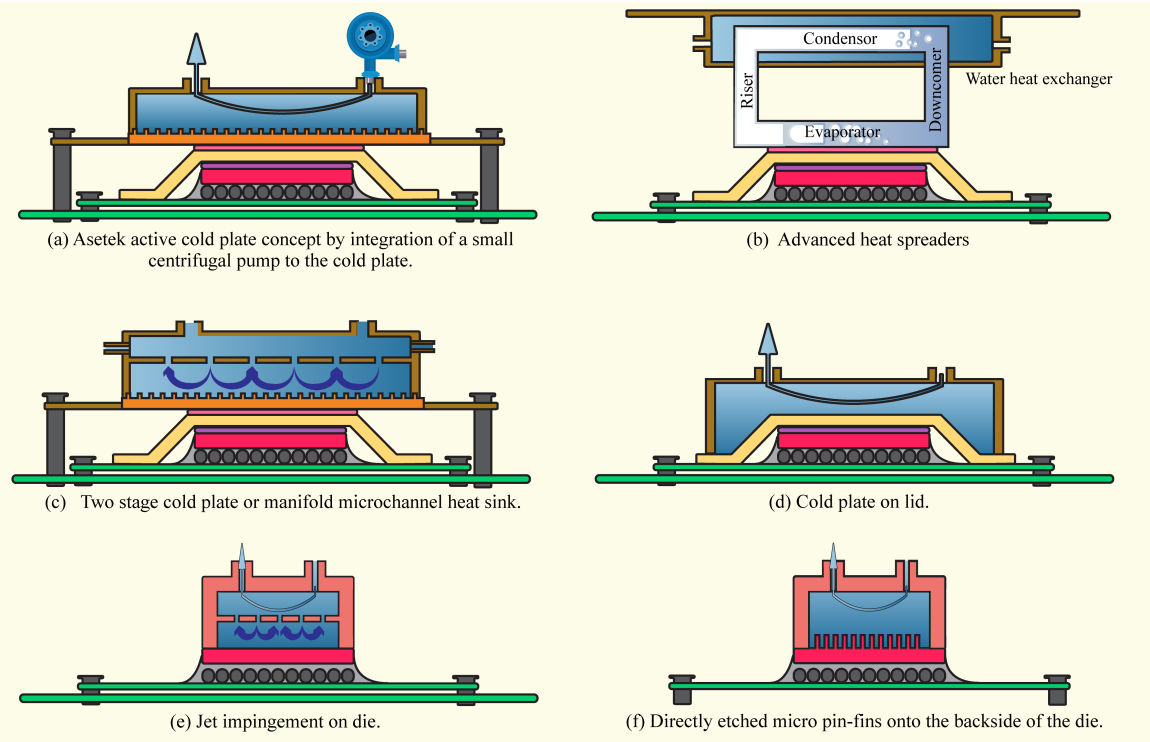

(a) Asetek active cold plate concept by integration of a small centrifugal pump to the cold plate.

(b) Advanced heat spreaders

(c) Two stage cold plate or manifold microchannel heat sink.

(d) Cold plate on lid.

(e) Jet impingement on die.

(f) Directly etched micro pin-fins onto the backside of the die.

Figure 1.10: An illustrative simplified thermo-physical demonstration of different direct liquid cooling methods including: (a) Asetek active cold plate concept, (b) thermosyphon cooling at chip level, (c) manifold cold plate, (d) on lid cold plate, (e) on die impingement, and (f) cold plate on die with directly etched micro pin-fins onto the backside of the die.

onto a resistive heater substrate designed to emulate an integrated circuit. The experiment was conducted with an overall flow rate of 204 mL/min and an available pressure of 209.6 kPa. They achieved heat transfer coefficients exceeding 25 W/(cm^2·K), with a device heat flux of 5500 W/(cm^2) and a temperature rise of 46 ± 2°C. Building on their research, JETCOOL is founded [95] and developed a similar commercial solution for data center cooling called SmartLid [96]. This technology is depicted in Figure 1.10(e) where there is no thermal barrier between the coolant and die. To the best of our knowledge, this is the highest heat transfer coefficient ever attained in the field, approaching the limits for single phase water cooling. In a similar vein, IMEC [97] employed jet impingement cooling using a manifold shared by 41 jets. These jets have a larger diameter of 300 µm and apparatus is made of polymers fabricated using high-resolution stereolithography 3D printing.

In the field of on-die cooling, it is worth mentioning the work of Rajan et al. [98] as an exemplary thermal management solution for 2.5D and 3D heterogeneous integrated circuits. Figure 1.10(f) provides an illustrative depiction of their methodology. The researchers used a 2.5D Stratix 10 GX field programmable gate arrays (FPGA) package featuring five discrete dies to evaluate two distinct cooling configurations. The first uses an attached silicon micro cold plate with micro pin-fin heat sinks etched on a separate silicon substrate. The second approach utilizes a monolithic design where micro pin-fins are directly etched onto the back-side of the dies. Both configurations incorporate low-profile, 3D-printed polymer-based fluid delivery manifolds and utilize deionized water as a coolant while running a resource-intensive benchmark on the FPGA. The study yielded remarkably low junction-to-inlet thermal resistance values: 0.094 °C/W for the attached silicon cooler and 0.074 °C/W for the monolithic heat sink. Both configurations were effective in dissipating more than 110 W of heat generation from the FPGA core die.

Turning our attention to established industry standards for cold plates, we find that the integration of water cooling at the chip level is still an emerging practice. The pressure drop requirements for such methods are often too high and hot swapping and warranty void of equipment is still a problem. Scaling this type of liquid cooling to industrial data centers introduces

challenging complexity [99]. An intermediate technology that bridges the gap between into-chip and cold-plate-on-lid, involves exposing the lid itself to the coolant [100]. This technique is illustrated in Figure 1.10(d) and is gaining popularity. In this regard, Chang et al. [101] introduced microchannels into the lid, effectively transforming the lid into an integrated cold plate and eliminating the TIM interface between cold plate and lid. With cooling capability exceeding 1,000 W, the result indicated a 30% increase in capability over a standard cold plate. Thermal resistance of 0.05 °C/W is obtained at flow rates of 1.0 l/min. In this survey, this is the lowest reported thermal resistance between different methods.

The question of what happens to the energy efficiency of the data center when water blocks are used needs to be addressed. Interesting performance comparison between air cooled data center after equipping with cold plates can be seen in retrofitting the Lawrence Livermore National Laboratory's high-performance computing cluster, "Cabernet," with Asetek cooling systems. The cooling solution is again based on chip-specific water cooling with peripheral air cooling. The study [102, 103] assessed the energy savings of this new system using both top-down statistical models and bottom-up engineering models. Because both the "before" and "after" scenarios utilized the same chilled water system, energy savings were solely attributed to reductions in CRAH fan power. The top-down analysis indicated a 4% overall energy savings for the cluster, with a PUE reduction from 1.60 to 1.53. The bottom-up model showed a slightly lower overall energy savings of 3%. The research suggests that even greater energy savings (15-20%) could be achieved if the free cooling was used for rejecting the heat from the liquid cooling system. About 37% of the heat from the Cabernet system was rejected into the cooling water, which is lower compared to other installations. It can be seen that direct water cooling still offers elevated PUE values, owing to the necessity for peripheral air cooling. This PUE can be reduced by considering waste heat recovery in various forms, such as heat exchange with hot water system of nearby facilities [104]. At the Energy Systems Integration Facility (ESIF) at the US Department of Energy's National Renewable Energy Laboratory (NREL), a PUE of 1.06 is achieved by utilizing waste heat from the data center to heat the building's water system [105]. ESIF also employed Asetek's in-rack CDU and cold plates in conjunction with low power air cooling.

A few novel approaches from industry deserve to be noted here: active cold plates, and leak detection in cold plates. In order to alleviate pressure of the cooling loop inside racks, Asetek introduces an interesting solution. As shown in Figure 1.10(a) cold plates can be equipped with centrifugal pumps into a single package names as active cold plate, this reduces connections and improves reliability by reducing pressure in manifold section of rack. This design is patented by Asetek and cold plate is compact enough that can be used in 1U chassis [106]. Another important aspect of directing water inside the server is leak detection in which CoolIT Systems showcased a leak detectors sensor for cold plate implementation in servers [107] and their cold plate practical design can be seen in GIGABYTE's AMD EPYC H262 Series [108].

Heat pipes provide high thermal conductivity and can efficiently distribute heat from small sources to larger areas in the condenser. As a result, they are an indispensable method for cooling in devices like laptop computers. Similar techniques of employing heat pipes in data centers exist, although they are typically used outside of racks. Ling et al. [109] provides a state-of-the-art review of application of heat pipes in data centers and categories heat pipes into three types based on driving force including (a) thermosyphon, (b) separate heat pipe, and (c) heat pipe system coupled with a liquid pump, gas pump, or air conditioner. In facility level, heat pipe systems are being used as a mediator for heat exchange between air-air or air-liquid and in most cases proven reliable and showed improvement. For instance, in ESIF's HPC data center [105] (which we discussed earlier), hybrid heat rejection system thermosyphon cooler located upstream and in series with an open cooling tower saved 1.16 million gallons of water in its first year of operation, and 2.10 million gallons during a two-year period, cutting water usage in the data center in half while continuing to operate at optimal energy efficiency [110].

- **Heat pipes.** In rack level, heat pipes showed improvement in air cooled data centers. Zheng et al. [111] retrofitted heat pipe systems in 14 air-cooled cabinets of a data center in Shanxi province. The evaporator was positioned inside the cabinet (in contact with air), while the condenser was linked to an outdoor chilled water system at the back of the cabinets, akin to RDHx systems. This retrofitting brought the air temperature within

the required operational safety limits. Subsequently the retrofitting resulted in an 18% reduction in the summer energy consumption of CRACs.

- **Thermosyphons.** Heat pipe based systems can also be used for direct chip cooling. Ding et al. [112] review the loop thermosyphon and its application in room- and rack-level cooling of data centers. The majority of applications are designed for air-cooled data centers. However, there is an innovative way of using thermosyphon at the chip level, as shown in Figure 1.10(b). In a vertical configuration, thermosyphons are gravity-assisted, wickless heat pipes. They utilize gravitational force to transport the working fluid from the condenser section via the riser to the evaporator and then bring it back via the downcomer, either through gravity or external energy. In this context, Chauhan and Kandlikar [113] studied and tested a dual taper-configured evaporator in a thermosyphon system working with HFE-7000. They showed that the loop can dissipate 280 W without reaching the critical flux point, and it has a heat transfer coefficient of 2.6 W/(cm^2·K). Amalfi et al. [114] later introduced a thermosyphon-based technology that extends risers and downcomers to rack levels, removing heat using R1234ze and directing it to a compact overhead water-cooled condenser. The profile of the evaporator was 7 cm, suitable for 2-U servers, and it was experimentally tested at Nokia Bell Labs. A thermal resistance of 0.113 K/W at a power level of 120 W was achieved. The mean T_j of 43 °C with FWS of 15°C was obtained and is reported to be below the values achieved with traditional air-cooling technologies. Lamaison et al. [115] studied concerns about the feasibility of such a system by investigating microprocessors cooled in parallel evaporators with different levels of heat flux. They demonstrated that the system's dynamic operation should be controlled by adjusting the pump's operation during heat load disturbances to avoid reaching critical heat flux conditions.

- **Two phase Impingement.**Fan and Duan [116] state that pool boiling, being the simplest submerged boiling configuration, offers relatively poor heat transfer performance when compared to submerged and confined jet impingement boiling. This observation

is supported by Figure 1.9(a), which shows that the heat transfer coefficient can be increased further by combining jet impingement and phase change. However, if one aims to harness the advantages of phase change within a cold plate, a low boiling point liquid must be used in the TCS. As shown in Figure 1.9(a) heat transfer coefficients up to 10 W/(cm^2·K) can be reached with fluorinated hydrocarbons. Ramakrishnan et al. [117] investigated a liquid-cooled manifold cold plate that facilitates two-phase jet impingement on a microchannel base. The dielectric fluid HFE-7000 was employed, and variables such as inlet pressure, subcooling, flow rates, and heat flux were considered. At a heat flux of 63.6 W/(cm^2), corresponding to a chip power of 410 W, the base temperature remained below 75 °C, and the pressure drop did not surpass 21 kPa. The cold plate is being commercialized by Ebullient [118].

- **Refrigeration on chip.** Schmidt and Notohardjono [119] outline the history of infusing refrigeration cooling for server electronics, resulting into the IBM S/390® G4 CMOS system, which was first supplied in 1997 and was the first high-end server to employ refrigeration. In recent attempts, a miniature vapor compression refrigeration system using R134a with an evaporator equipped with micro-channels has been tested for chip cooling [120]. The highest COP achieved is 9.069 to remove 200 W from heated surface at 73.3 °C. In another study, a water block is placed over a thermoelectric cooler (TEC), which is attached to a CPU. Dynamic performance comparisons of three configurations, including TEC with and without temperature control as well as passive water cooling, are investigated under variable operating conditions in a severe environment. A COP of above 0.65 for the cooling system is obtained [121]. In another innovative research, a thin TEC is fabricated from a nanostructured Bi_2Te_3-based superlattice and attached to the bottom of the lid. The temperature of the localized heater region was 124.5°C without the TEC and decreased to 116.9°C when the cooler was attached to the lid. After powering the TEC with a current of 3 A, a total localized cooling led to temperature reduction of 14.9°C with a heat flux of 1,300 W/(cm^2) [122].

Achieving futuristic high performance direct liquid cooling apparatus needs the incorporation of jet impingement, and phase change mechanisms directly on lid or die, or microchannel cooling inside die. Manifold microchannel heat sinks are an excellent example of such integration where an array of liquid jets impinge on microchannel structures of heat spreader inside a cold plate, or directly on lid/die. From such designs comes the highest reported heat transfer coefficient of 25 W/(cm$^2\cdot$ K) [94], reaching the limits of direct water based cooling. Two-phase cooling could enhance such systems even further, with theoretical heat transfer coefficients of up to 100 W/(cm$^2\cdot$ K) possible. Further exploration of two-phase cold plate systems is required to pave the way for the convergence of two phase micro jet impingement or refrigeration on lid/die. However, it should be emphasized that multiphase cold plate systems are vulnerable to changes in heat loads, posing problems to their functioning stability and efficiency. Thus, such futuristic solutions require a coolant with appropriate flow rate and cooling capacity to safely operate in different thermal loads.

1.4 Immersion Cooling

Direct liquid cooling in data centers has been recognized for its high heat removal capacity provided by attached cold plates and evaporators on microprocessors. However, it poses challenges such as leakage, micromanagement, maintenance, and the need for CDUs that demand pumping and flow distribution via manifolds. Furthermore, air cooling remains necessary for peripheral equipment and condensation prevention, resulting in elevated PUE for these methods. Immersion cooling builds upon this by submerging the entire server in a bath of dielectric liquid. In this setup, all components are in direct contact with heat transfer liquid [123]. Research into immersion cooling extends to other high-density electronics like solar photovoltaics [124], batteries [125], and power transformers [126]. Notably, the first concept of a dielectric-cooled computer was patented by IBM in 1966 [127], and they subsequently introduced the concept of immersion cooling in 1968 [128]. A recent review by Pambudi et al. [129] highlights immersion cooling as a method that offers numerous benefits: energy savings,

cost-effectiveness, a 1/3 reduction in infrastructure size compared to air cooling, ease of installation and maintenance, and environmental advantages due to reduced noise and greenhouse gas emissions.

Moreover, immersion cooling involving phase change provides consistent temperature cooling solution [123], ensuring no performance drop, hotspot, or energy consumption spikes. This cooling method is projected to grow from $243 million to $700 million in 2026 [130]. As shown in Table 1.2, common dielectric liquids used for immersion cooling have significantly lower thermophysical properties than water. However, the dielectric quality of these liquids allows for no resistive network to obstruct the heat transfer path, though in most cases, the lid remains on the microprocessor to improve surface contact. When comparing the average specific heat and thermal conductivity of popular dielectric liquids to water, with similar density, they are found to be 66% lower in terms of specific heat and 86% lower in terms of thermal conductivity (it is important to note that in TCS, a mixture of 30 to 50% Propylene Glycol and water, often with corrosion inhibitors, is used instead of only water. Mixture serves several functions, including freeze protection during shipping and handling and the prevention of corrosion, foaming, pH change, bio-growth, and other issues. When glycols are added to water, thermal conductivity and specific heat decrease while density, viscosity, and Pr increase).

1.4.1 Single Phase Immersion Cooling

In single-phase immersion cooling, the boiling temperature of coolant is generally engineered to be high enough to prevent phase change. Referring to Figure 1.1, these cooling solutions, which are exposed to atmospheric pressure, usually allow for low-maintenance and easier hot swapping. However, additional maintenance procedures are necessary to prevent fluid losses and to degas systems of infiltrating air and humidity [142]. The presence of impurities, gases, or other substances can influence thermophysical properties. Thus, any immersed IT equipment should be stripped of all stickers or coloring that can contaminate the liquid. Cooling fluid is more cost-effective in comparison to two phase immersion systems. Furthermore, liquid loss exists and the facility requires coolant and gas filtering due to diffusive evaporation [99]. The fluid's circulation is powered either by a pump or through natural convection [143]. In pumpless

Name	Type	T_b [°C]	c_p [kJ/(kg.K)]	h_{fg} [kJ/kg]	ρ [kg/m^3]	k [W/(m.K)]	$\mu \times 10^6$ [Pa.s]	Pr	$\beta \times 10^6$ [K^{-1}]	GWP
Water[131]	Inorganic Compound	100	4.17	2438	997	0.6	855	5.9	276	- 0.001 to 0.0005
Novec 72DE [132]	Hydrofluoroether	43	1.10	235	1280	0.06	450	8.2	1300	42
Novec 7300 [132]	Hydrofluoroether	98	1.14	92	1645	0.06	1000	18.8	1300	200
Novec 774 [99]	Fluorinated Ketone	74	1.13	90	1670	0.06	520	9.8	1500	1
FC-72 [133]	Fluorinert	56	1.10	84.5	1620	0.052	454	9.6	1560	5000
Crystal Plus 70T [134, 135]	Mineral oil	218-800	2.22	-	825	0.13-0.15	12320	195.3	764	2.1
Dow Corning DC-550 [136]	Silicone oil	>300	1.50	-	934	0.13	125	1.4	10^5	6.31 [137]
Shell Thermal Transfer Fluid [138]	Synthetic oil - Polyalphaolefin (PAO)	355	1.88	-	865	0.134	65503	919	600	1
Novec 7100 [139, 140, 141]	Methoxy-nonafluorobutane	61	1.18	112	1520	0.07	380	6.4	1800	297
Average for above dielectric liquids	-	-	1.41	-	1295	0.08	-	-	-	-

Table 1.2: Type, GWP, and thermophysical properties of common dielectric liquids being used for immersion cooling, including boiling temperature (T_b), specific heat (c_p), latent heat of vaporization (h_{fg}), density (ρ), thermal conductivity (k), dynamic viscosity (μ), Prandtl number (Pr), and coefficient of thermal expansion (β). Water is included in the table for comparison.

tanks, Rayleigh–Bénard convection occurs, utilizing a hot vertical wall of a hot server and another vertical wall for heat exchange, connected to an external FWS. Figure 1.9(a) shows that free convection in dielectric liquids is limited to low heat transfer coefficients. Optimization study by Luiten [144] shows that buoyancy driven Hydrocarbon based immersion cooling with copper heat sink with 80 vertically oriented fins at height of 20 mm and heat spreader size of 200 mm by 200 mm can maintain 500 W IC at 85 deg C, showing effective thermal resistance of 0.091 K/W.]. In buoyancy driven systems, higher density, higher expansion coefficient, and lower viscosity are the preferred liquid choices. This issue is examined at Ref. [145]. Authors determined the figure of merit (FOM) by examining the Nusselt number (Nu) correlation of a heatsink with a vertically oriented plate. The FOM, where higher being better, was given as:

$$\text{FOM} = k \left(\frac{\rho^2 c_p}{\mu k} \right)^{0.2813} \tag{1.2}$$

To adapt the system for high power servers, forced convection must be used. Typically, a pump promotes forced convection by propelling liquid from the CDU through an inlet on the bottom of the tank (assisting flow). In this case, based on the Nu correlations for developing laminar flow through pipes, the FOM is defined as [145]:

$$\text{FOM} = k \left(\frac{\rho c_p}{k} \right)^{0.333} \tag{1.3}$$

Huang et al. [146] use numerical models to compare pump-driven and buoyancy-driven immersion cooling in a tank containing two CPUs, each with a TDP of 270 W, for a total server power of 1331.9 W. The Nu for the pump-driven case was evaluated as 261.2, while for the buoyancy-driven case was 105.4. The study shows that the pump-driven immersion cooling system reduces processor temperature by up to 55.5% while also lowering PUE by 11.6%, highlighting its efficiency and effectiveness in improving cooling performance. Aligning with our insights, synthetic oils are the preferred choice in the industry for single phase immersion cooling. Probably, apart from environmental concerns, many uncertainties persist regarding the effects of mineral oil immersion cooling on the reliability of the IT equipment both at the

component and chassis level [147]. Moreover, silicone oils tend to be more expensive and cannot compete with proven track records of synthetic oil usage in data center industry. Further information regarding other coolants such as nanofluids can be found in [148]. Referring back to the table in Figure 1.1, this method is superiors regarding, cost, reliability, sustainability, complexity and location flexibility between different liquid cooling methods [68]. Thus, it presents opportunities for successful commercialization. Asperitas utilizes pumpless server enclosures employing single-phase immersion cooling, employing the low-viscosity Shell immersion cooling fluid S5 X [149]. These servers are thermally insulated for waste heat recovery. Each enclosure can house 48 servers or 288 GPUs while occupying a footprint of 60 cm × 120 cm [143]. Alibaba, likewise, utilizing Shell immersion cooling fluid S5 X [150], opts for pump-driven single-phase immersion cooling tanks, resulting in a 36% reduction in power consumption and an achieved PUE of 1.07 [143]. On the other hand, Submer [151] has developed its own coolant named SmartCoolant for single-phase immersion cooling. This coolant is a low-viscosity, dielectric synthetic fluid crafted from a diverse array of components, including hydrocarbons, esters, and various additives. The company offers cabinet-sized enclosures known as microPods and setups within shipping containers, referred to as megaPods. These systems are engineered for waste heat recovery, contributing to the provision of hot water for nearby buildings. Riot Blockchain's Massena data center utilizes Shell immersion cooling fluid in a pump-driven single-phase immersion cooling setup, accommodating a 40,000 servers. However, the PUE remains undisclosed [152]. In addition to traditional approaches aimed at enhancing heat transfer in single phase immersion cooling systems, the utilization of acoustic flow presents an intriguing alternative. Acoustic flows involve convective currents induced in a fluid exposed to an ultrasonic field [153, 154]. A recent investigation by Ozer et al. [155] delves into the impact of ultrasonic sound waves on the cooling efficacy of single-phase immersion cooling systems utilizing fully-fluorinated PF-5060 dielectric liquid (even though the boiling point of this liquid is 56 °C, the experiments were done in liquid phase with maximum 14 °C temperature rise in relatively low 30 W power levels). The study explores ultrasonic sound waves at frequencies of 9.6 kHz, 14.4 kHz, 19.2 kHz, and 24 kHz, comparing them to silent natural convection. The experimental setup involves two discretely heated regions positioned

on a vertical plate, simulating servers within immersion cooling tanks. The findings reveal an increase in the heat transfer coefficient, with the highest reported value reaching 1.7 W/(m^2· K) due to cavitation induced in the liquid by the sound waves and the resultant flow fluctuations of the acoustic flow phenomenon. Further in-depth analysis is required to understand the energy performance of such systems, and their long-term impact on the quality of the immersion cooling liquid.

1.4.2 Two Phase Immersion Cooling

Two-phase immersion offers improved heat transfer coefficient and minimize temperature gradients across the heated surface [123]. These enhancements are attributed to the isothermal nucleation processes present in two-phase flow and the associated latent heat of vaporization [156]. The primary concerns with this approach relate to flow instabilities, which induce pressure and temperature fluctuations, flow reversal, and other behaviors that may ultimately lead to superheating and burnout of heated surfaces [157]. Boiling takes place on copper boilers attached to the lid or directly on the lid. Then, as depicted in Figure 1.1, vapor naturally rises to the top of the tank after, where a cold coil (or surface) condenses it back into liquid. Typically copper boilers are mounted on the lid, and for heat flux greater than 10 W/cm^2, a common strategy is to use a commercial boiling enhancement coating on boilers [158].

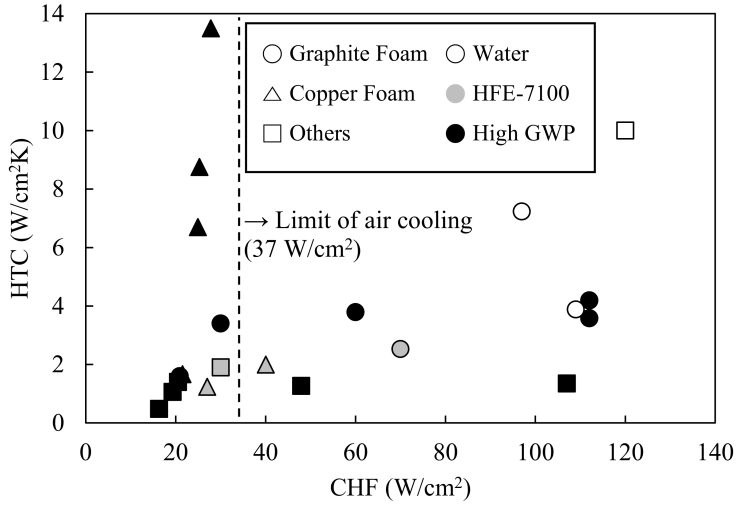

Figure 1.11: Comparison of heat transfer coefficient (HTC) and critical heat flux (CHF) of recent pool boiling enhancement with surface modifications [35]

The improvement of the surface or coating for enhancing pool boiling is an active area of research. Larimi et al. [159] conducted pool boiling experiments using Nove 649 with different surface characteristics, including bare copper, a commercial boiling enhancement coating, and their developed multi-scale electroplated porous (MuSEP) coating. The MuSEP coating enhanced the boiling heat transfer coefficient by 108% compared to the bare copper surface and by 38% compared to the commercial coating at 250 W, with an average heat flux through the boiling surface of 11.3 W/cm^2. Furthermore, the reliability of the MuSEP coating was studied after undergoing more than 22000 integrated hours of tests for a functioning CPU in a two-phase thermosyphon cooling prototype and more than 5500 integrated hours in a total immersion cooling application. Recent advancements in two-phase immersion cooling involving surface modifications have been comprehensively reviewed in [35]. The attempts to enhance pool boiling heat flux are categorized into surface treatment and forming structures on the surface, with authors noting that structure-level research demonstrates higher performance than surface-level research, but an economic feasibility study is necessary. Figure 1.11 summarizes some of the recent experimental results in this field for pool boiling. It's important to mention that, to the best of our knowledge, there is insufficient information regarding potential cavitation damage to IT equipment during boiling. Additionally, further studies are needed to emphasize the long-term reliability of two-phase immersion systems. Recent industry insights reveal that fluid-borne contaminants originating from various IT hardware, such as solder flux residue and plasticizers from elastomer components, have been observed to interact with the working fluid. These interactions can result in unforeseen issues, ultimately leading to thermal performance degradation of the boiler plate or electronic failures.

Even with an increase in the heat transfer coefficient by two-phase immersion cooling, the heat removal is typically constrained by the small surface area. Introducing an advanced heat spreader instead of conventional boilers can further enhance performance of two-phase immersion cooling. In this context, Zhou et al. [160] utilized vapor chamber as a heat spreader in two-phase immersion cooling. They initially developed gradient capillary wicking structures with varying effective pore sizes and integrated them into the vapor chamber to effectively reduce flow resistance, facilitating improved circulation of the working fluid and enhancing

the heat spreading performance of the vapor chamber. Furthermore, to boost the pool boiling heat transfer performance, they integrated a sintered porous copper wire mesh with the outer condenser surface of the vapor chamber. Experiments were conducted at various input heating powers and test orientations in an HFE-7100 bath. The set up managed a heat load of up to 900 W without dry-out, achieving a vapor chamber thermal resistance of 0.046 °C/W.

It is worth noting that in 2016, Kheirabadi and Groulx [85] highlighted that two-phase immersion cooling was scarce in the industry. However, we are now witnessing significant interest and investigation by hyper-scale corporations into two-phase immersion cooling. Microsoft Azure, for example, is actively developing general-purpose hardware for two-phase immersion cooling, utilizing both small immersion tanks with Novec HFE-7000 and large immersion tanks with FC-3284 [161]. Figure 1.12 illustrates three perspectives of this prototype: (a) overview; (b) a removed server; and (c) servers inside the pool. Standard air-cooled servers were modified for immersion through various adjustments, including fan removal, replacement of CPU heatsinks with copper boilers, power supply unit removal, depth reduction, and firmware modifications. The tank is equipped with power, cooling, and networking interfaces connected to the data center. Engineered fluids for two phase immersion cooling can have higher GWP, health hazards [35] and generally are more expensive in comparison to single phase immersion cooling liquids. Another challenge associated with utilizing engineered dielectric liquids is the issue of proper disposal and concerns related to recycling [162]. Hot swapping is not efficient to be performed regularly and devices are maintained in yearly cycles [99]. Among these liquid, several fluorinated coolants, categorized as per- and polyfluoroalkyl substances (PFAS), which are classified as ”forever chemicals” [163]. Both the EU and the US are taking steps to limit the production of PFAS. It is important to note that major manufacturing companies in the field are phasing out the production of PFAS by the end of 2025. This poses a challenge for two-phase immersion cooling regarding the production of engineered fluids, given that all current two-phase immersion cooling systems have utilized PFAS chemicals [164]. As a result, efforts are intensifying to shift towards no-PFAS chemicals such as HFO alternatives which have zero ozone depletion potential and low GWP. This issue opens up avenues for research

Figure 1.12: (a) overview of two-phase immersion cooling tank with (b) a removed server; and (c) servers inside the pool [161].

and development into new materials and cooling methods that could redefine thermal management in data centers. Birbarah et al. [132] proposes an innovative approach that can mitigate the use of dielectric liquids. They offer immersion cooling directly in water. 1 µm of Parylene C coatings is applied on servers to insulate it from water and tested for voltages up to 200 V. Then heat flux and convection heat transfer coefficient obtained in Novec 72DE and 7300 dielectric fluids, water, and a 50/50 in volume mixture of water and ethylene glycol as a function of hot-spot-to-fluid temperature difference in both natural convection and nucleate pool boiling regimes. Heat fluxes up to 562 W/cm^2 are measured in water. As a proof of concept, water immersion cooling is tested successfully on a 2 kW power converter operating at 97.2% efficiency in deionized water.

Immersion cooling systems represent a more straightforward and denser solution for future data centers. Nonetheless, adapting to the high power requirements of microprocessors, single-phase immersion cooling necessitates a novel flow arrangement to enhance heat transfer coefficient. Currently, the flow is parallel to specialized heat sinks attached to the lid, a technique that lacks precise flow control, preventing this method from fully utilizing the cooling

potential of the available liquid. Novel methods, such as ultrasonic vibration, have been shown to boost heat transfer coefficient. Two-phase immersion cooling is at risk due to supply chain issues in the market for engineering fluids. This challenge, however, opens the door for innovative approaches. For instance, making servers and electronics waterproof and water immersion cooling could significantly push forward immersion cooling. Such an approach has demonstrated the potential for achieving heat transfer coefficient of up to 0.92 W/($cm^2 \cdot$ K) by natural convection, and up to 4.92 W/($cm^2 \cdot$ K) in nucleate pool boiling [132].

1.5 Summary and Conclusions

This chapter is aimed to underscore the imperative need for transitioning to liquid cooling in data centers. Discussions are made about the growing demand for next-generation data centers, driven by the advent of high-density transistor microprocessors and evolving environmental standards. Additionally, we addressed the hurdles faced by existing air-cooled data centers and explored four well-established liquid cooling methods. Our pivotal findings lead us to these conclusions:

- Air cooling technologies are unlikely to completely vanish from the data center industry. Moreover, with increasing incomes in densely populated countries [165], the use of air conditioning is expected to surge globally. In light of this, there's a growing need for greener refrigeration cycles that are not only eco-friendly and efficient, but also exhibit zero ozone depletion potential and lower GWP. For instance, new HFOs, Zeotropic mixtures, or natural refrigerants like ammonia and CO_2 are being considered. The transition to these alternative refrigerants presents both challenges and opportunities. New refrigerants will compete for cost and COP, while adhering to new environmental standards. It's worth noting that the academic discourse on this transition is somewhat limited, with most information currently available in commercial white papers.

- Within air-cooled data centers, extensive research is underway to enhance control over airflow distribution. This includes the exploration of smart aisle containment, increased

system responsiveness through heat pipes, and the optimization with sensor and control systems.

- As packaging architecture of microprocessors advances, it allows for the use of high-temperature coolants. Consequently, this leads to the broader adoption of free cooling solutions at the opposite end of thermal network of data centers. However, not all IT equipment in servers is designed to withstand high temperatures. As discussed in this paper, the shift from HDDs to SSDs will undoubtedly accelerate the current transition towards high-temperature data centers.

- Ultimately, the heat rejection destination for any thermodynamic cycle is natural sinks. Centralizing data centers in cold-climate regions, such as the Pan-Arctic areas, offers the potential to enhance system efficiency, especially in case of shifting towards high temperature data centers. However, this move poses crucial questions that need answers from logistical and security standpoints. Unconventional efforts to alter heat rejection sink, such as submerging data centers within tanks in the ocean, appear promising. Yet, continuous heat rejection into the ocean raises environmental concerns, potentially impacting marine ecosystems through thermal pollution. Additionally, it's essential to consider factors like the initial carbon footprint, costs, and the long-term expenses associated with maintenance and servicing.

- Up to this point, the hybrid approach of indirect water-cooled data centers, utilizing RDHx, stands out as one of successful solutions, especially in large-scale data centers, where it manages to achieve low PUEs without considering waste heat recovery (sometimes, extremely low PUE values are reported when considering waste heat recovery in various forms, such as heat exchange with hot water system of nearby facilities. However, it's essential to take a realistic approach and determine the PUE of implemented cooling method without considering waste heat recovery.) Utilization of active RDHx showed successful mitigation of pressure drop within the racks. However, a persisting issue is the problem of hot air leakage. Nonetheless, it's important to acknowledge that this

method still grapples with the limitation of relying on air cooling, which may eventually fall short in meeting the ever-increasing TDP demands of modern microprocessors.

- In the approach of direct liquid-cooled data centers, there is a noticeable shift towards manifold water blocks and evaporators, attached directly on lid or applied on die. Microchannel cooling inside die shows the least thermal resistance of 0.074 °C/W as the coolant is at the nearest proximity of the heat source. Additionally, two-phase jet impingement and interconnected thermosyphons show promising heat removal capabilities. Direct liquid cooling ins hyperscale appears challenging due to micromanagement requirements. Still, this method has found success in smaller-scale applications, such as mainframe or academic computer setups. Lastly, this method still offers elevated PUE values, owing to the necessity for peripheral air cooling.

- Immersion cooling offers benefits like high-density data centers. However, single-phase immersion cooling faces challenges with upcoming high heat flux devices due to the inferior thermophysical nature of dielectric liquids, and no local control on flow field that necessities lower inlet temperatures and increased pumping power. Transitioning to two-phase cooling appears to be a more promising approach. However, the cost for initial set up and maintenance is higher. Furthermore, effective heat removal requires enhanced boilers that need reliability studies for long-term usage. In this vein structurally enhanced boilers or boilers equipped with vapor chambers can mitigate the reliability issues. However, the industry faces another challenge related to engineered liquid itself. There are concerns about their long-term reliability, recycling, health, and environmental impact. As a result, researchers are actively seeking novel engineering fluids with no PFASs, zero ozone depletion potential and lower GWP. Furthermore, extensive research is needed to address long term compatibility of IT equipment itself where materials that may release particles during boiling can degrade exposed surfaces and thermal performance of liquid. Furthermore, the long-term health effects on individuals working with constantly boiling engineered liquids should be investigated. An innovative approach highlighted in this study involves waterproofing servers and harnessing the benefits of immersion

cooling with water. Research in this particular area is relatively limited and needs further attention.

Finally, a comprehensive thermodynamic analysis that considers all relevant factors at different scales, from the chip and server level to the rack, room, and facility level, is necessary to compare different liquid cooling schemes for data centers. In addition, long term environmental impacts need to be addressed. These impacts can range from thermal pollution to the disposal of dielectric liquids to wellbeing of employees. Addressing these challenges is crucial as high power data center demand continues to grow.

Chapter 2

Analytical and Experimental Study of Air Synthetic Jets Based on New Manufacturing

This chapter presents an approach to the design and fabrication of synthetic jet devices (SJDs) using rapid prototyping via additive manufacturing, marking the first study to employ this method for such devices. This manufacturing technique empowers researchers with complete design freedom, enabling the production of ultra-thin SJDs—as thin as 4 mm—without mechanical fasteners and facilitating the rapid fabrication of multiple devices with varying geometries. To showcase the potential of this method, synthetic jets with conical and cylindrical cavities and orifices ranging from 1.6 mm to 7 mm were designed, fabricated, and tested. These devices achieved air jet exit velocities exceeding 106 m/s using a single piezoelectric diaphragm—among the highest reported in the literature—validating the effectiveness of this manufacturing approach. This high jet velocity is significant for practical applications requiring efficient thermal management, such as cooling high-power-density electronics, where compact and energy-efficient solutions are essential. Beyond achieving high velocities, it was revealed that maximizing jet velocity alone is not always optimal for heat removal. The hydrodynamic impulse generation rate was introduced as a more significant factor influencing heat transfer performance. By fabricating and testing multiple SJDs with different geometries, it was demonstrated that the impulse generation rate, which accounts for both jet velocity and flow rate, better correlates with enhanced heat transfer capabilities than jet velocity alone. This insight addresses an often-overlooked parameter in SJD design and has substantial implications for optimizing heat removal performance. Lumped element modeling, tuned solely on diaphragm deflection behavior, accurately predicted device performance and was validated using a hotwire anemometer. This model effectively characterizes center-axis orifice devices

and confirms its applicability to thin-cavity designs, providing a valuable tool for future SJD development. Despite moderate volume flow rates (0.2 to 0.8 m^3/h), the fabricated SJDs delivered significant improvements in heat transfer. Compared to natural convection, these devices achieved over 13 times greater heat removal rates, with an average heat transfer coefficient exceeding 120 W/(m^2·K) over a 30 mm × 30 mm heated surface. These findings demonstrate the practicality and effectiveness of vortex-enhanced synthetic jet impingement for targeted and efficient cooling of localized hot spots. This approach offers multiple advantages over traditional rotary cooling systems like fans, including increased reliability, and lower profile, while consuming power less than 100 mW. The ability to rapidly prototype and optimize SJDs using additive manufacturing accelerates research and development in this field, paving the way for advanced thermal management solutions in real-world applications. This chapter has recently been published in [166].

2.1 Introduction

Jet impingement is an attractive solution for hot spot cooling, especially in electronics [167]. Kwon et al. [168] show a heat transfer coefficient up to 17.0 kW/(m^2· K) at a heat flux of 58.4 W/cm^2 from continuous air jet at a Reynolds (Re) number of 8.77×10^4. Such high-velocity jets require a high-pressure source. As a result, the design is not portable and will need three major components: a compressor/pump, storage, and piping/coupling/nozzle(s). Fans, air pumps, piezoelectric fans, and SJDs can be used to avoid such arrangements while producing jet or jet-like flows in a small and portable package.

Fans are the most common method of cooling electronics, and they use a small electric motor rotating a shaft with attached blades. The generated angular momentum is transferred to air. Modern fan designs are slim and almost silent. However, they have a number of limitations. In smaller scales, the blade-to-shaft ratio decreases, resulting in less air movement per rotation and lower overall efficiency. Smaller motors are also less efficient due to thermal and magnetic losses. Moreover, in fans airflow disperses; Axial fans move air parallel to the shaft, with airflow spreading after exit. Centrifugal fans, which move air perpendicular to the shaft, are better suited for controlled airflow. Hofer et al. [169] analyzed the velocity and structure of a

miniature centrifugal fan ($65.3 \times 64.5 \times 23.5$) mm^3 using particle image velocimetry (PIV) and hot wire anemometry. An average outlet velocity of 9.4 m/s has been measured for a maximum flow rate of 13.54 m^3/h. They showed two counter-rotating vortices at the fan outlet, resulting in a distinctive elliptical, rotating jet that deviates from perpendicular propagation relative to the outlet plane. Yen and Liu [170] compared two centrifugal fans with the same geometric design ($60 \times 60 \times 11$ mm^3) but operating at different rotational speeds under identical voltage conditions. They used PIV to observe the flow field immediately at the fan exits. The lowest flow speed is observed directly at the fan exit, increasing to a peak at 3 cm before decreasing with distance. A maximum local velocity of 7 m/s was observed.

As it can be seen, fans cannot effectively simulate jet impingement, and achieving a thinner profile is limited. Unlike fans that rotate a shaft, piezoelectric cooling devices can transfer momentum to fluids using oscillatory actuation in thin and scalable designs. This can be seen in new commercialized piezoelectric-based air pump systems that offers jet velocities of 52 m/s and are less than 3 mm thick [171]. Piezoelectric-based SJDs are another method of producing jet flows that demonstrate the capability of producing SJs of up to 250 m/s [172]. In recent years, SJs have found applications in active flow control, particularly in aerospace. These mechanisms are used in manipulating flow, altering boundary layer structure to induce favorable changes in aerodynamic forces on airfoils or vectoring jets [173, 174, 175]. Other applications are mixing enhancement [176, 177], heat transfer from compact surfaces [178, 179], spray vectoring [180, 181], micro propulsion [182, 183], active control for miniature aerial vehicles [184].

Piezoelectric-based SJDs are structurally simple, lightweight, low-power, and dependable. When compared to natural convection, SJs improved local heat transfer by at least a 3X, and in some cases exceeded 8X for small surfaces [185]. Further studies showed that SJ enhances the local heat transfer by up to 15 times compared to natural air convection [186]. Furthermore, the heat transfer characteristics of SJ with continuous jets (CJs) at same boundary conditions showed better performance of SJs. It was argued that the radial variation of time-averaged heat transfer for SJ was found to be 35% better than for CJ [187]. A similar observation has been made by other researchers as well [188, 189]. Arik et al. [190] reported 40% higher heat

dissipation for SJ as compared to the CJ for similar boundary conditions. Later studies claim that at the same range of Re number, SJs achieved further than twice the cooling effect of a CJ [191]. SJs also shows better penetration into crossflow. A comparison study between SJ's and CJ's cooling performance with the same net mass flow rate and identical jet outlet temperatures showed that without cross flow, CJ, and with cross flow, SJ outperformed in terms of heat removal [192]. Most probable reason for better thermal performance of SJs is continuous formation of vortical structures and their sweeping effect upon impingement. Meanwhile at low Re number CJs, vortex formation is not significant; hence, cooling is aligned with the streamlines forming on the surface.

Multiple comprehensive reviews are published about thermo-fluid behavior of SJs. Efforts have been made to describe the effects of orifice to plate distance, stroke length, frequency, orifice shape, jet vectoring, orifice plate thickness, cavity shape, and acoustics, on the flow, and thermal characteristics of SJ based cooling [191, 193, 194, 195, 196]. Most of these articles call for additional research in this area. Manufacturing and prototyping of SJDs is likely to be one of the most significant challenges to conducting research in this field. This study presents an innovative approach to developing high-velocity SJDs based on composite additive manufacturing, which is shown to be an appropriate rapid prototyping method. Manufactured SJDs are tested for deflection performance, and their acoustic and structural performance is documented and analyzed. To predict SJD output level, fluid dynamic-based lumped element models are tuned using deflection behavior only. Based on these models, the operation frequency of each SJD was calculated. Thermal tests were performed on devices at varying distances from the heated surface to assess their heat transfer capabilities. The jet output performance is then assessed using hot wire anemometry.

In the following sections of this chapter, a brief fundamental of SJDs, specifically piezoelectric SJDs, is discussed. The importance of impulse generation is highlighted in order to demonstrate that higher jet velocity cannot always be used to assess the performance of SJDs. Furthermore, coupled mechanical-Helmholtz resonator system of piezoelectric-based SJDs, phase lag between diaphragm and jet, and recent concerns about the accuracy of lumped element models (LEMs) for thin profile SJDs are addressed. Methods for manufacturing

piezoelectric-based SJDs and boundary conditions for actuators are discussed. A novel manufacturing method is developed that can accelerate SJD research by facilitating rapid prototyping of SJDs using additive manufacturing. The analytical and experimental analysis are then presented.

2.2 Fundamentals of Synthetic Jets

A typical SJD is depicted in Figure 2.1(a). The process of SJ generation and formation involves a fast periodic transfer of momentum to air inside a cavity, leading to an instantaneous increase in cavity pressure leading to the ejection of fluid. When air is expelled as seen in Figure 2.1(b), it forms a jet right in front of the orifice, surrounded by a vortex ring. Jet is forced through the center of the vortex ring, which on average, acts as a convergent-divergent nozzle, causing the strong acceleration of jet (in addition to vena contracta effect) through the vortex and then followed by deceleration [197]. This behavior shapes the head of the ejected fluid which looks like a jellyfish. The vortex rings are the result of fluid rolling on itself at the walls of the orifice as the ejection velocity of the fluid in the orifice varies during the diaphragm deformation cycle. The vortex ring detaches from the orifice walls because of its gained velocity and accompanies the ejected slug of fluid with a thin trailing tail. Immediately as the inflow phase starts, reduced pressure in the cavity pulls air from outside into the cavity. Here, if the previously ejected SJ obtained enough velocity to move far enough from the cavity, inflow cycle sucks the air from the ambient, not effecting the previously ejected SJ. Thus, a SJ is formed, and the ejected jet flow and vortex ring remains fairly stable and travels downstream. The released vortices are preserved, contributing to the formation of a steady SJ. In other words, each vortex ring carries a certain amount of angular and linear momentum and travelling downstream side by side by the jet flow, it interacts with jet flow, and also surrounding ambient fluid. This entrainment process effectively transfers some momentum from the vortex rings to maintain jet velocity and coherence making them more effective in terms of reach and impact [198]. Vortex rings formed from round orifices are coherent and can travel substantial distances while keeping their integrity. On the other hand, vortical structures from slot orifice, break down faster as they are highly unstable and try to attain a stable shape. Axis-switching can also occur in these

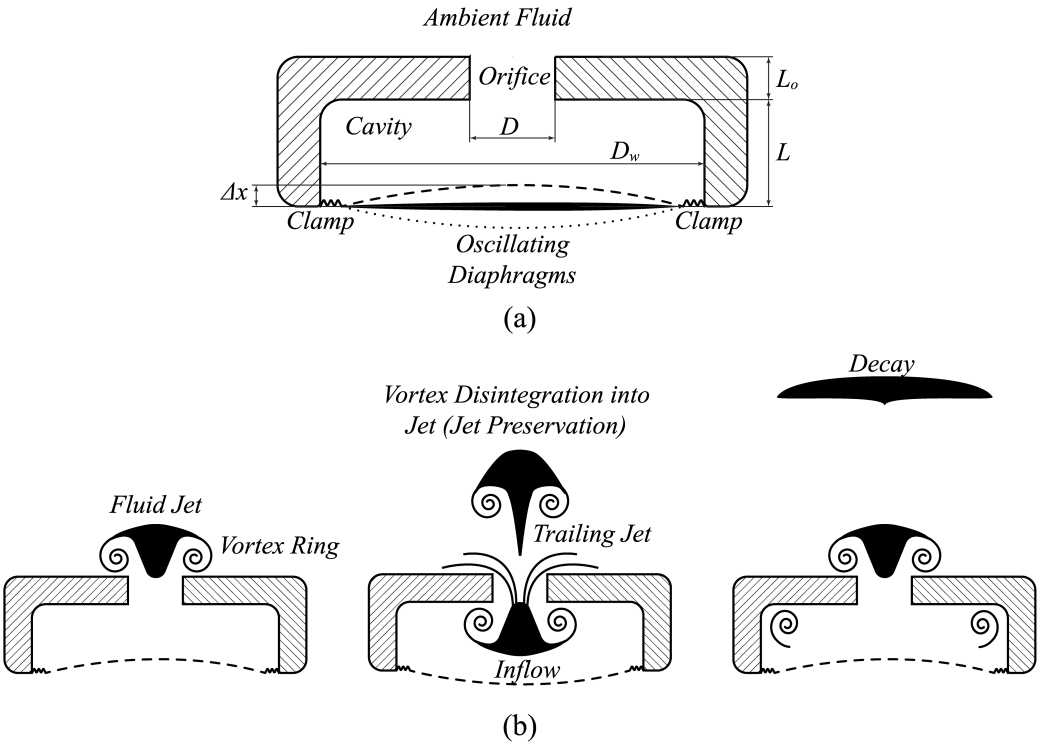

Figure 2.1: (a) Overview of a SJD, and (b) process of SJ generation.

vortical structures. When vortex spreads swiftly along the shorter side of the slot, and after a sequence of contortions, the vortex structure regains its original shape except its axis gets swapped undergo changeover of its axis [196]. It is also shown that imperfect orifice condition can result in spanwise instabilities that enhance rapid breakup of the vortical structures. This shown to lead to increased jet spreading rate and the jet decay rate [199].

It is evident that targeted heat transfer can be achieved more efficiently with round orifice SJs. These jets keep coherent vortical structures which direct more momentum and mass flux towards specific heated points. When these vortex rings impinge on a surface, they create a strong, localized impingement zone. This localized action results in higher convective heat transfer coefficients, due to intense turbulence and mixing at the point of impingement. Conversely, slot orifices are better suited for applications requiring moderate cooling over larger surface areas or for specific aerodynamic applications where the purpose of the SJ extends beyond impingement. Given these distinctions, this research will focus on the round orifice configuration.

2.2.1 SJ Formation, Impulse Generation, Impingement Characteristics, and SJD Behavior

To design a SJD for hotspot cooling three key issues need to be considered. First of all, a SJ needs to be formed (Strouhal/Stokes number criteria). Next, SJ should have high velocity and at the same time have high mass flow rate (balance between Re number, orifice diameter, and acoustic damping). Finally, SJD should be placed at an appropriate distance from the heated surface (Orifice to plate distance adjustment).

Figure 2.2 provides an illustration of SJ formation. Considering the orifice as a cylinder with diameter of D, and length of L_o, a cylindrical volume of fluid moves out of the orifice with varying radially averaged velocity $U(t)$ in each state of ejection cycle (i.e., from $t = 0$ to $\tau/2$, while assuming jet is reaching its maximum velocity at $\tau/4$ where t is time and τ is the period for diaphragm deflection). It needs to be noted that there can be phase difference between oscillation of diaphragm and velocity profile in the orifice, e.g., they can operate in opposite phase, as when there is a contraction in cavity volume, the fluid can be sucked in and when cavity is expanding SJ can be ejected from the orifice.

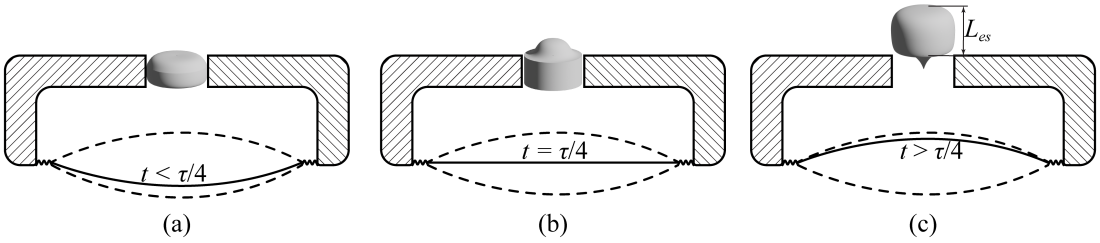

Figure 2.2: The formation process of a SJ at (a) beginning of ejection cycle, (b) at maximum velocity of the diaphragm, and (c) end of the ejection cycle.

The time (over ejection cycle) and area averaged velocity of ejected puff or slug ($\overline{U}$) (see Figure 2.3(b)) can be evaluated as [200]:

$$\overline{U} = \frac{2}{\tau}\int_0^{\tau/2} U(t)dt = 2fr\int_0^{1/(2f)} U(t)dt \tag{2.1}$$

Where fr is the frequency of diaphragm deflection. Equivalent length of the ejected slug (L_{es} - see Figure 2.2(c)) can be defined as:

$$L_{es} = \overline{U}\tau/2 = \overline{U}/(2fr) \tag{2.2}$$

Now two dimensionless parameters for the SJ in formation stage can be obtained as stroke length (L^*) and Re number [198]. Non-dimensional stroke length is:

$$L^* = L_{es}/D \tag{2.3}$$

One can build a relationship to Strouhal number (St) as:

$$\text{St} = \frac{fD}{\overline{U}} = \frac{1}{2(\overline{U}/(2fr))/D} = \frac{1}{2L^*} \tag{2.4}$$

Holman et al. [201] introduces Stokes number (Stk) as:

$$\text{Stk} = \sqrt{2\pi f D^2/\nu_\infty} \tag{2.5}$$

Where ν_∞ is the kinematic viscosity in the ambient. Re number can be defined as:

$$\text{Re} = \overline{U}D/\nu_\infty \tag{2.6}$$

One can see that:

$$\frac{\text{Re}}{\text{Stk}^2} = \frac{\overline{U}D/\nu_\infty}{2\pi f D^2/\nu_\infty} = \frac{\overline{U}}{2\pi f D} = \frac{L^*}{\pi} \tag{2.7}$$

Utturkar et al. [202] and Holman et al. [201] showed that by empirical relationship SJ formation criterion, JFC, is:

$$\text{JFC} = \frac{1}{\text{St}} = \frac{\text{Re}}{\text{Stk}^2} = \frac{L^*}{\pi}K^* \tag{2.8}$$

Where K^* is jet formation constant depending on the geometry of the orifice shape, radius of curvature, and aspect ratio of the slot. K^* is 1 for slot orifice and 0.16 for circular orifices.

From a heat transfer perspective, it is well established that Nu number is a function of Re number, which is also true in SJ impingement. In SJ impingement cooling, Nu number is correlated to Re^n with exponent n ranging from 0.492 [203] to 0.841 [204]. In CJ generation, one can achieve high Re numbers by reducing the nozzle diameter while compensating for required pressure in the reservoir tank. This is not the case in low-inertia-diaphragm actuated SJDs, where the introduced damping in the orifice section can greatly influence the behavior of the low-inertia-diaphragm (usually a voice coil or a piezoelectric diaphragm). Since the design of such devices typically centers around the actuation mechanism, Re number cannot simply be increased by tightening the orifice.

Thus, reducing the orifice diameter cannot always lead to higher Re numbers, as it can significantly damp the actuator. Conversely, significantly widening the orifice can reduce the Re number, potentially failing the device to meet the JFC criteria in Equation 2.8. As a result, the design should achieve a balance. When designing SJDs for heat transfer applications, as shown later in results, it is necessary to consider both the Re number and impulse generation (I), as well as their effects on diaphragm behavior. The hydrodynamic impulse per unit width per cycle can be defined as (see Figure 2.3(c)):

$$I = \int_0^{\tau/2} (\rho_\infty A U(t)) U(t) dt = \rho_\infty A \int_0^{\tau/2} U^2(t) dt \tag{2.9}$$

In some articles [193, 205] one can see that right hand side of the Equation 2.9 is being integrated as $I = \rho A \overline{U}^2 \tau/2$ which can be considered oversimplification since $U(t)$ is function of time. In this article we introduce a new term to assess behavior of SJDs as hydrodynamic impulse rate per unit width, $\dot{I}$. It can be defined as (see Figure 2.3(d)):

$$\dot{I} = I \cdot fr \tag{2.10}$$

This is an important parameter that contains valuable data for SJD performance evaluation. For example, if a SJD generates high velocities but has a small orifice area, $\dot{I}$ will be low. If the orifice area is large, the velocity can decrease, resulting in a reduction of I and $\dot{I}$. Additionally,

the frequency determines the rate of momentum ejection into the system. Thus, an SJD is superior if it can deliver high velocity jet through a larger orifice at a higher frequency. Because most low-inertia-diaphragm-actuated SJDs meet JFC criteria at their resonance modes, they should be manufactured in such a way that a balance between A, U, and at these resonance frequencies exists.

Figure 2.3 provides a visual aid in understanding $U(r,t)$, $U(t)$, U, $\overline{U}$, I , and $\dot{I}$. $U(t)$ is the radially averaged jet exit velocity of $U(r,t)$. U is maximum achievable $U(t)$, and $\overline{U}$ is over ejection cycles averaged $U(t)$. By considering constant density, I can be conceptualized as proportional to the area under $U^2(t)$ curve in every ejection cycle, and $\dot{I}$ can be conceptualized as proportional to the area under $U^2(t)$ curve in every ejection cycle that can happen in one second.

SJ impingement is similar to jet impingement, with two major distinctions. First, a continuous impingement of generated vortical structures occurs on the heated plate. Second, the temperature of the SJ can be affected and fluctuate depending on the distance between the orifice and the heated plate due to strong mixing, and direction of gravity driven convection on heated plate [192]. After impingement vortical structures advect in the radial direction and induces counter-rotating secondary vortices in the wall jet region [206, 207]. However, it is shown that in high spacing and also very low spacing to the heated plate secondary vorticities can be diminished [208].

It was also demonstrated that small stroke length caused vortex rings to take longer to reach the wall, resulting in a decrease in vortex strength. Weak impingement resulted in the formation of large-scale spiral vortices in the wall-jet region, whereas vortex rings with long stroke lengths were found to be strong enough to generate strong secondary vortex rings in the wall-jet region. The findings predict that smaller stroke lengths are advantageous for heat transfer due to the formation of large-scale spiral vortex rings close to the wall [209]. In contrast, in another study it was observed that the heat transfer performance increased linearly with the increase in stroke length [210]. There are multiple other disparities when trying to quantify Nu number of SJ impingement or provide correlations [194]. The main reason can be attributed to this fact that SJ impingement is more complex in comparison to CJ impingement. Numerous factors

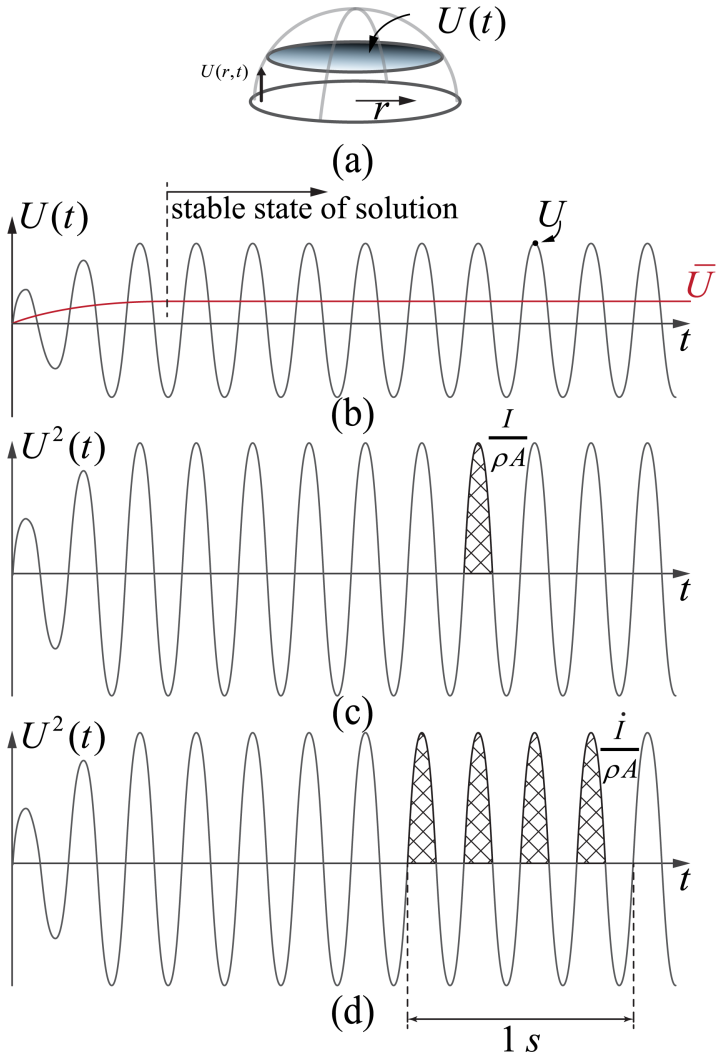

Figure 2.3: (a) Visual description of $U(t)$ as the radially averaged jet exit velocity $U(r,t)$, (b) behavior of $U(t)$ and visualization of its over ejection cycle average $\overline{U}$ and its maximum value U, (c) visualization of impulse generation per unit mass per unit area per cycle $I/(\rho A)$, and (d) its rate $\dot{I}/(\rho A)$.

influence Nu, such as Re, Stk, placement, shape and strength of vortical structure, characteristic of heated surface, shape and number of orifices, geometrical and material selection of SJDs, confinement of impingement by SJD, boundary conditions, natural convection, and the self-heating effect of SJD. All of these parameters raise the uncertainty of Nu number prediction and generalization of SJ impingement heat transfer. Probably, leveraging the Sherwood number would be more beneficial. Techniques such as naphthalene sublimation study [211] allows for more manageable experimental set ups.

In summary, the distance to the heated plate is what all studies agree on. Most studies have found an increasing and decreasing trend in the orifice-to-surface distance [189, 212, 213]. Thus, it can be stated that for any SJD impingement set up there is an optimal impingement distance where heat transfer rates are maximum.

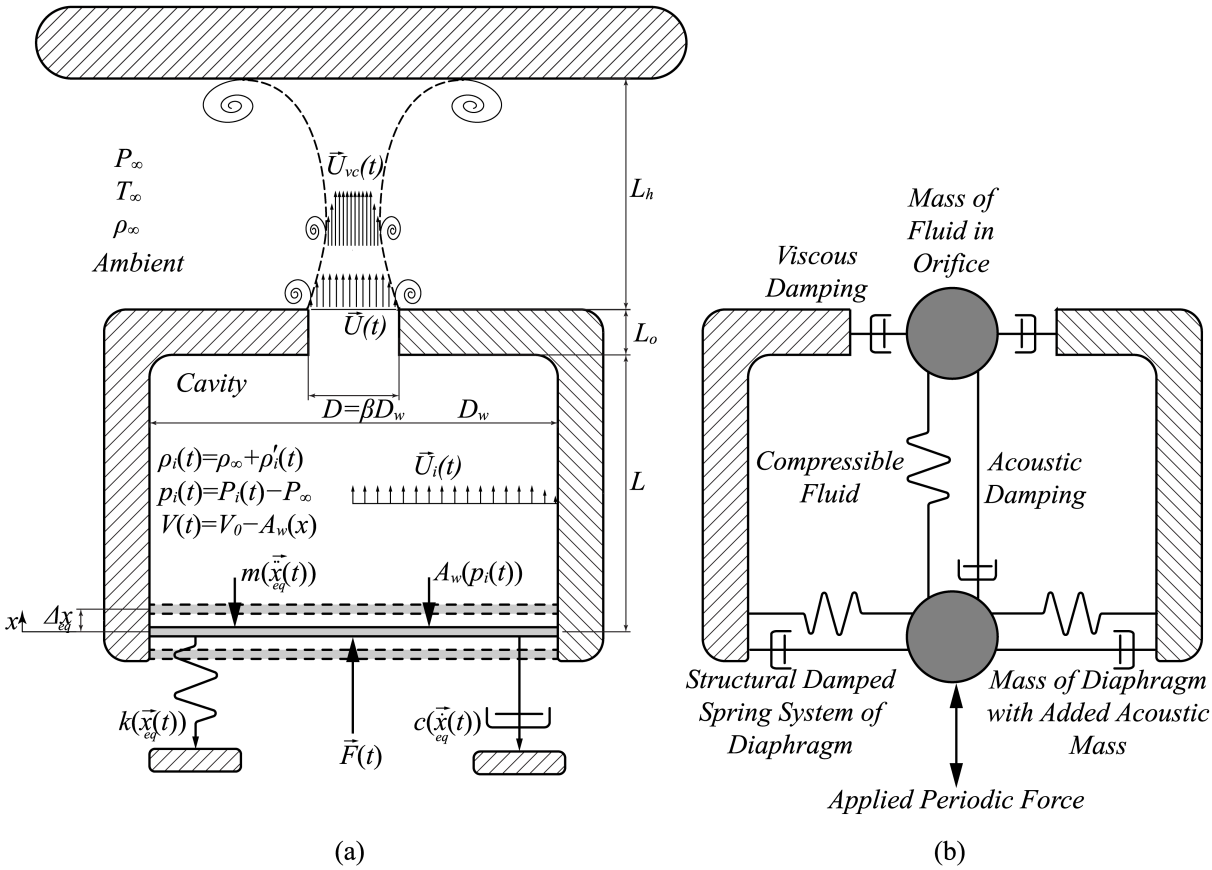

Figure 2.4: (a) Schematics of the studied SJD with body diagram, and (b) conceptualization of the SJ actuator as a coupled mechanical-Helmholtz resonator system with two degrees of freedom.

Figure 2.4 depicts a typical simplified body diagram for a piezoelectric-based SJD and its conceptualization using the LEM. LEMs can provide a swift understanding of SJD's dynamic response [214]. Sharma [215] introduces a fluid dynamics based model which is summarized herein. More details are provided in Appendix A. Driving force $F(t) = f(v(t), structure)$ can be conceptualized as a function of input voltage $v(t)$ and $structure$ of the piezoelectric actuating mechanism. As shown in Figure 2.4(a), after containing this actuator inside a cavity with on orifice, apart from mass and stiffness of the actuator itself, acoustic mass and stiffness also is added to it [216, 217]. Thus the actuator will have a total mass $m = m_w + m_f$ which includes mass of the oscillating wall m_w (mass of shim, piezoelectric ceramic, and solders) and added acoustic mass of fluid inside the cavity (m_f) [218]. The damping coefficient (c) also consists of two components: the structural damping of the oscillating wall (c_w) and the acoustic radiation damping factor (c_f). The latter results from the energy loss carried away by sound waves generated during vibration. In the context of a circular piston vibrating within an infinite baffle at a radian frequency of $\omega = 2\pi fr$ the added acoustic mass and damping terms are [215]:

$$m_f = \frac{2\rho_x A_v U_{sound} H_1(y)}{y\omega} = \frac{4\rho_x A_v U_{sound}}{\pi\omega} y \left(\frac{1}{3} - \frac{y^2}{3^2 \cdot 5} + \frac{y^4}{3^2 \cdot 5^2 \cdot 7} - ... \right) \tag{2.11a}$$

$$c_f = \rho_x A_v U_{sound} \left(1 - \frac{2J_1(y)}{y} \right) = \rho_x A_v U_{sound} y^2 \left(\frac{1}{2 \cdot 4} - \frac{y^2}{2 \cdot 4^2 \cdot 6} + \frac{y^4}{2 \cdot 4^2 \cdot 6^2 \cdot 8} - ... \right) \tag{2.11b}$$

$$y = \frac{\omega D}{U_{sound}} \tag{2.11c}$$

Where ρ_∞, A_w, U_{sound}, H_1, J_1, and D_w are unperturbed fluid density (initial density, or density outside the cavity), the surface area of the oscillating wall, speed of sound, Struve function of the first kind, Bessel function of the first kind, and diameter of the oscillating wall (herein we assume its equal to the diameter of the cavity), respectively. Moreover, speed of sound is:

$$U_{sound} = \sqrt{\gamma \frac{P_\infty}{\rho_\infty}}, \quad \gamma = c_p / c_v \tag{2.12}$$

where γ, c_p, c_v, and P_∞ are ratios of specific heat ($\approx$1.4 for air), specific heat in constant pressure, and constant volume, and initial cavity pressure (or pressure outside the cavity), respectively.

During actuation, the gauge pressure inside the cavity, $p_i(t)$, undergoes fluctuations around a zero-mean value as the fluid experiences compression and expansion. It is crucial to highlight that these pressure fluctuations are negligible compared to the overall pressure inside the cavity, allowing LEMs to assume that the cavity pressure at any given moment is approximately equal to the pressure outside the cavity($P_i(t) \approx P_\infty$). Referring to Figure 2.4(a), an equation governing the dynamics of the flexible membrane can be derived as:

$$m\ddot{x}_{eq}(t) + c\dot{x}_{eq}(t) + kx_{eq}(t) = F(t) - p_i(t)A_w \tag{2.13}$$

in which $A_w = \pi D_w^2/4$. It should be noted that in LEM, diaphragm deflection is simplified to piston cylinder motion as defined by x_{eq}. Later, it will be discussed how the piston cylinder motion relates to the actual deformation of the piezoelectric disc diaphragm x. x is the displacement in the center of deflecting disc. Equation ref Chapter2Equation13 governs the characteristics of actuation of the wall. It needs to be noted that when the force is applied in period with angular frequency of ω $F(t) = F_{max}\sin(\omega t)$, the deflection is no longer constant and varies with the frequency of the applied force. Considering simple damped spring mass system with damping ratio of ζ and undamped natural frequency of ω_n one can write [219] [54]:

$$\Delta x_\omega = \frac{\Delta x_{static}}{\sqrt{\left(1 - \frac{\omega^2}{\omega_n^2}\right)^2 + \left(2\zeta\frac{\omega}{\omega_n}\right)^2}} \tag{2.14}$$

To estimate the deflection in angular frequency of ω, Δx_ω, multiply static deflection by the dynamic amplification factor. This is a simplified analysis that shows the difference in deflection behavior between static and dynamic loads. Furthermore, it should be noted that a damped spring mass system will typically provide three distinctive frequencies: undamped natural frequency, damped natural frequency, and frequency of maximum force amplitude. Damping ratio for the wall can be defined as $\zeta = \frac{c}{2\sqrt{mk}}$. Because the damping ratios for thin

metal plates are low (≤ 0.03), these three frequencies are very close and can be considered the same. Thus, one can use single wall resonance of $\omega_w = \sqrt{\frac{k}{m}}$. ζ and ω_w are structural characteristics of the diaphragm.

By assuming $\zeta \approx 0.02-0.03$ one can determine the resonance frequency of the diaphragm by measuring its displacement in different frequencies. Knowing value of $m \approx m_w$ one can experimentally determine k as $k = \omega_w^2 m$. Next F_{max} can be evaluated. By driving actuator in very low frequency such that $\Delta x_\omega \approx \Delta x_{static}$ (Refer to Equation 2.14) one can estimate $F_{max} = k(\Delta x_\omega)$. In summary, the diaphragm's stiffness is determined by its resonance frequency, and the applied force is obtained by driving the device at a low frequency of 25 Hz.

When the diaphragm undergoes oscillation, the fluid inside the cavity experiences alternating compression and expansion. Simultaneously, there is an oscillatory flow through the orifice. Sharma [215] shows the second resonance of the system contributes to flow behavior through following equation:

$$\ddot{U} + \frac{1-\beta^4}{L_e C_d^4}|U|\dot{U} + \omega_h^2 U = \frac{A_w}{A}\omega_h^2 \chi \tag{2.15}$$

Where $\beta = \frac{D}{D_w}$, $C_d = f(\beta, Re) \approx 0.6$ is viscous loss coefficient, and $L_e = L_o + C_l\sqrt{A}$ is the effective length of the air jet/slug at the orifice , and $\omega_h = \sqrt{k_h/m_h} = \sqrt{\frac{(\gamma A^2 P_\infty)/(V_0)}{\rho_\infty A L_e}} = U_{sound}\sqrt{\frac{A}{V_0 L_e}}$ represents the Helmholtz frequency. L_o is length of the orifice and C_l is inertia coefficient which needs to be tuned for each LEM model.

Equation **??** show that SJD can be conceptualized as a coupled mechanical-Helmholtz resonator system with two degrees of freedom. This implies that the actuation mechanism has two resonance modes, and maximized output can be achieved in near resonance frequencies. Figure 2.5 depicts behavior of SJD provided in equations discussed in this section. This illustrations are based on studying LEM of Sharma [215] in different geometrical inputs. Figure 2.5(a) provides the deflection behavior vs. driven frequency of the diaphragm in constant voltage level applied to the piezoelectric bender. Deflection gradually reduces by increasing frequency until a significant deflection can be seen in the first principal wall resonance frequency (fr_w). Adding such diaphragm to a cavity in form of a SJD results in two major changes. (1) First,

added acoustic mass to the diaphragm can reduce (fr_w) to a lower level in comparison to vibration without cavity (blue curve), while added stiffness can increase (fr_w) (red curve). (2) Peak deflection in (fr_w) also reduces due to acoustic damping, which damps the vibration of the diaphragm. After adding the cavity, a slight increase in deflection at Helmholtz resonance (fr_H) can be seen. The closer the Helmholtz and first principal resonance frequencies are together, or the lower the L value (thinner the cavity), the greater the deflection in Helmholtz resonance. Ultimately, by optimizing the SJD, either by changing the size of the cavity or orifice, or by modifying the mass of the diaphragm or its stiffness, the Helmholtz and wall resonance frequencies can be brought closer to the same value, resulting in a significant increase in the system output. This can be conceptualized as mode coupling, where SJD will produce its highest jet output velocity.

Figure 2.5(b) provides the deflection behavior and instantaneous area averaged jet exit velocity ($U(t)$) vs. driven frequency of the diaphragm in constant voltage level applied to the piezoelectric bender. It can be seen that by modifying characteristics of orifice, fr_H can occur in higher or lower frequencies that of diaphragm resonance. Depending on this, phase lag existing between diaphragm and orifice the maximum jet exit velocity will occur at a slightly lower or higher frequency than the wall resonance frequency.

The velocity at which the diaphragm moves (diaphragm velocity) and the velocity of the air exiting the orifice (jet exit velocity) are inherently linked but can be out of phase. As illustrated in Figure 2.6, the phase lag between the driving diaphragm and the air movement is influenced by the resonance frequencies. The phase lag at both resonances approaches 90 degrees. This is because the resonant system's response is maximally out of phase with the driving displacement at resonance. Off-resonance, the phase lag can be less or more, which its behavior is shown in Figure 2.6 for SJD with different characteristics.

In some cases, as the cavity of SJD becomes thinner and deviates from an ideal Helmholtz resonator, Helmholtz resonance theory stated to be deviating from experimental measurements by more than 130% [220]. It is suggested that in thin cavities, quarter-wave resonance model be used which aligned much closer to the observed data, with discrepancies around 15% [220]. However, it should be noted that these conclusions were drawn using a different type of SJD

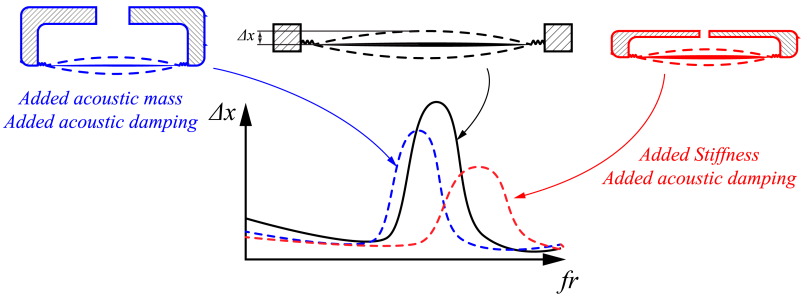

(a) *Effect of Cavity on Diaphragm Behavior*

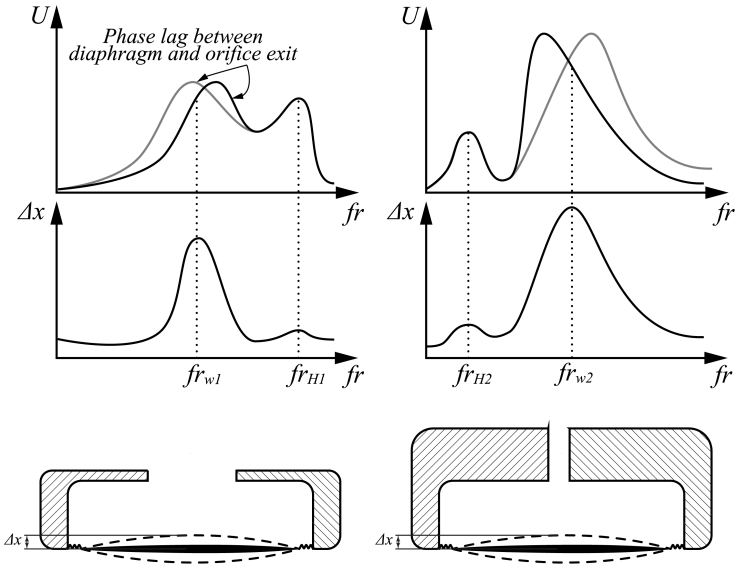

(b) *Illustration of Coupled Mechanical-Helmholtz Resonator System*

Figure 2.5: (a) Diaphragm deflection behavior before and after adding cavity. (b) Diaphragm deflection and SJ output behavior of SJD showcasing higher Helmholtz resonance in left, and lower Helmholtz resonance on the right.

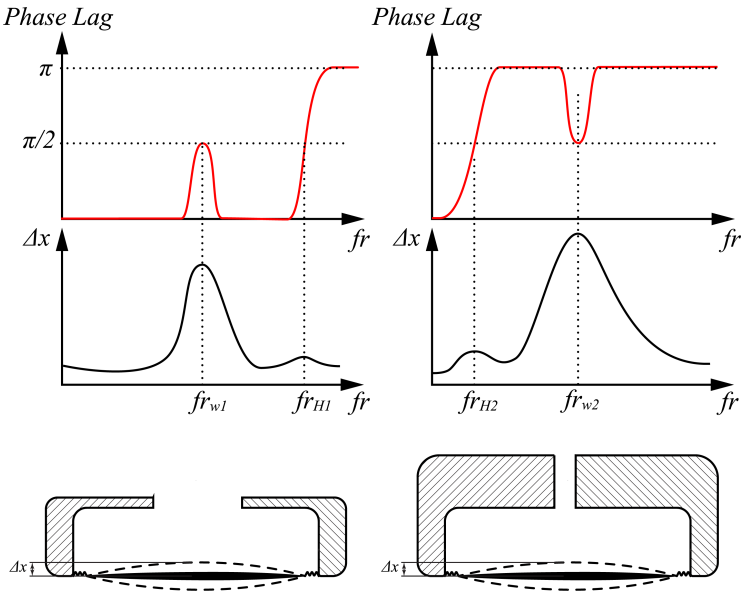

Figure 2.6: (a) Diaphragm deflection behavior before and after adding cavity. (b) Diaphragm deflection and SJ output behavior of SJD showcasing higher Helmholtz resonance in left, and lower Helmholtz resonance on the right.

that lacks axial symmetry and is not the same as the type of SJD used to derive LEMs. In other words, this type of conclusion is derived from SJD type b, as illustrated in Figure 2.7. Our experiments on type a SJD showed good accuracy of LEM model. However, more experiments would be useful for a generalizing solutions.

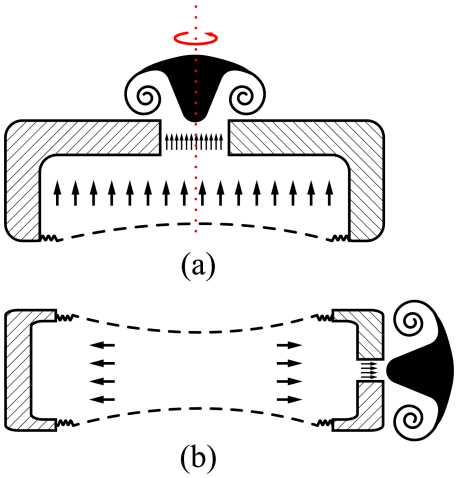

Figure 2.7: (a) Type a SJD where a sort of axial symmetry exists and LEM models are based on, and (b) type b SJD in which an orifice is introduced from side.

A recent study [221] suggest that characteristic resonance frequency of the SJD should be evaluated first based on pressure acoustic FEM model and to replace ω_h in equation **??**. The combination of replacing the Helmholtz frequency with a more accurate characteristic

frequency and using computed loss coefficients resulted in more accurate LEM performance predictions for low-profile SJDs (Type b in Figure 2.7(b)). However, this consideration undermines the first major assumption used in LEM models, so it begs the question of whether the model is still accurate if the acoustic resonance mode is changed. This assumption, which serves as the foundation for LEM models, states that the internal pressure in the cavity is uniform at any given time (except near the orifice). This is because it was considered that the wavelength of the pressure oscillations is significantly larger than a typical dimension L of the actuator cavity. This condition ensures that the frequency of the most significant standing wave of quarter-wavelength is well beyond the operating frequency range of the actuator. This can be shown by analyzing wave equation describing a standing wave field in one dimension (x) with a simple order of magnitude simplification [218]:

$$\frac{\partial^2 p}{\partial x^2} = \frac{1}{U_{sound}^2}\left(\frac{\partial^2 p}{\partial t^2}\right) \xrightarrow[\text{simplification}]{\text{order of magnitude}} \frac{\Delta p}{L^2} = \frac{1}{U_{sound}^2}\left(\frac{p}{1/f^2}\right) \rightarrow \Delta p = \frac{L^2}{\lambda^2} p \tag{2.16}$$

This consideration seems to be true in type a SJD as shown in Figure 2.7(a) since the orifice is considered to be in front of the diaphragm. However, when the orifice is located in the side of the diaphragm L in Equation **??** needs to be replaced by D_w. in this case it is obvious that the pressure inside the cavity will not be uniform (see Figure 2.7(b)) and LEM models can be inaccurate.

2.3 SJD Concept and Manufacturing

2.3.1 Actuation Mechanism

One important aspect of manufacturing an SJD is to generate an adequate oscillatory actuation. This section attempts to cover a variety of methods suitable to generate linear actuation for SJDs. SJD with high inertia piston/cylinder actuators can be built using motors [222] or solenoids [223]. Because of the high inertia of the moving armature, this approach is limited to low frequencies ($\leq$ 200 Hz). This inertia distinguishes such SJDs from other methods discussed later because the actuation is unaffected by fluid inside the cavity and the diaphragm's

displacement is primarily determined by the actuator. This allows generation of SJ at all operating frequencies, where sometimes shockwaves can also be generated with sufficient compression in cavity. In contrast, high frequency actuation is possible with low inertia motion with a voice-coil driver or a piezoelectric actuator; however, cavity pressure may affect actuation and displacement (see Figure 2.5).

Moving coil actuators use a magnetic assembly that contains either permanent soft magnets or electrodynamic magnets. In addition, a solenoidal coil is used in conjunction with a composite flexible diaphragm, or a flexible paper or metallic cone. The coil, which is typically attached to the diaphragm or cone, moves with almost no friction in response to the magnetic field generated by the assembly [218]. To build a SJD, such an electrodynamic system can be custom-made for a compact design [224], or a loud speaker can be used [225]. Moving coil transducers can produce noticeable deflections under low stress conditions. Furthermore, they can operate at frequencies of up to 50 kHz [226]. Moving coil transducer based SJD was commercialized by Nuventix for variety of applications including server processor cooling augmentation [227] and LED modules cooling [228]. Due to their bulky design, these devices were not commercially successful and were eventually discontinued.

Piezoelectric actuation is a promising way to create SJDs. Unlike any other method mentioned, actuation can be accomplished using a single piezoelectric-based bender. The piezoelectric composite diaphragms used in SJDs are typically circular metallic shim discs, often made of brass/steel, with a piezoceramic patch attached to one or both sides. A thin silver layer is coated on the surface of these patches to help them receive an electrical signal. Thin wires can then be soldered to the silver layer, forming one node of the electrical signal. The other node for the electronic signal is created by soldering another wire to the metallic shim that contacts the opposite side of the piezoelectric ceramic. These benders have a thickness of around 300 μm. Piezoelectric disc benders are available in diameters ranging from approximately 10 to 50 mm, with shim thicknesses of about 0.1 to $\approx$ 0.2 mm and piezoceramic thicknesses of 0.05 to 0.23 mm. Resonance frequencies can vary from a few hertz to ultrasonic frequencies ($>$ 20 kHz).

Chen et al. [229] provide a detailed roadmap for manufacturing such benders. However, due to the high cost of manufacturing, the piezoelectric diaphragms in most research cases are sourced from commercially available units, also known as piezoelectric disc benders, which have industrial applications in horns, tweeters, and sirens. The piezoelectric ceramic is typically made of conventional zirconate-titanate PZT-5A/5H. The electromechanical coupling ratio of conventional polycrystalline piezoceramics is low. Recent research [230] has shown that more electromechanically efficient piezoceramics, such as single-crystal lead magnesium niobate-lead titanate (PMN-PT), can achieve superior performance metrics. The PMN-PT-based SJD achieved a peak exit jet velocity of 99.5 m/s at a peak supply voltage of 40 V, with a power conversion efficiency of 72% at the SJD's Helmholtz frequency.

Manufacturing a cavity and orifice is straightforward. It can be done through the machining process or additive manufacturing. The main question is how to add piezoelectric based actuator to it. A structure is required to hold diaphragm in a sealed manner to the cavity, while giving it an ability to deform. Depending on it, diaphragm will behave as of being clamped [231], pinned [229], as shown in Fig. 8, or in between of the two. Pinning allows for

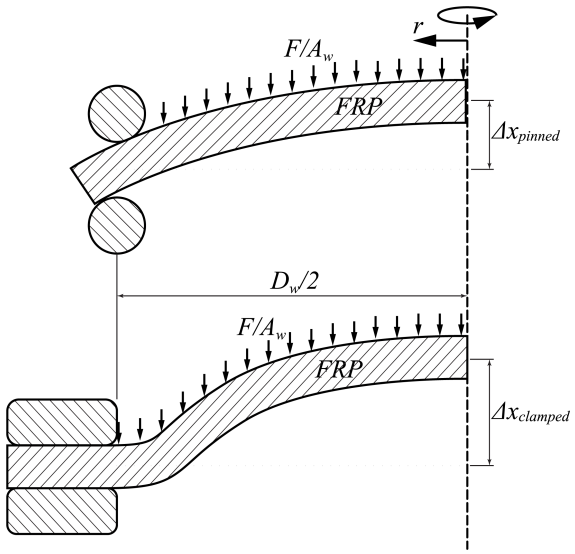

Figure 2.8: Pinned (up) and clamped (down) boundary conditions for disc with known flexural rigidity of FRP with diameter Dw and surface area Aw, with central deformation Δx under constant force (F).

more deflection, whereas clamping reduces deflection while providing a stiffer structure with a higher resonance frequency. Timoshenko [232] demonstrates that for circular plates with

known flexural rigidity of FRP, Poisson's ratio of , and uniform applied force of F/A_w, the static deflection ratio from pinned to clamped is equal to $(5 + N)/(1 + N)$. For $= 0.3$, the deflection in the center from the pinned case is approximately four times the clamped case. Thus, the pinned case can be considered the best method for piezoelectric-based actuation in SJDs. Figure 2.9 shows various types of piezoelectric-based SJD designs. Figure 2.9(a) and 2.9(c) show examples of clamped and pinned boundary conditions applied to a cavity, as previously discussed. An alternative piezoelectric assembly method for producing SJDs, suggested

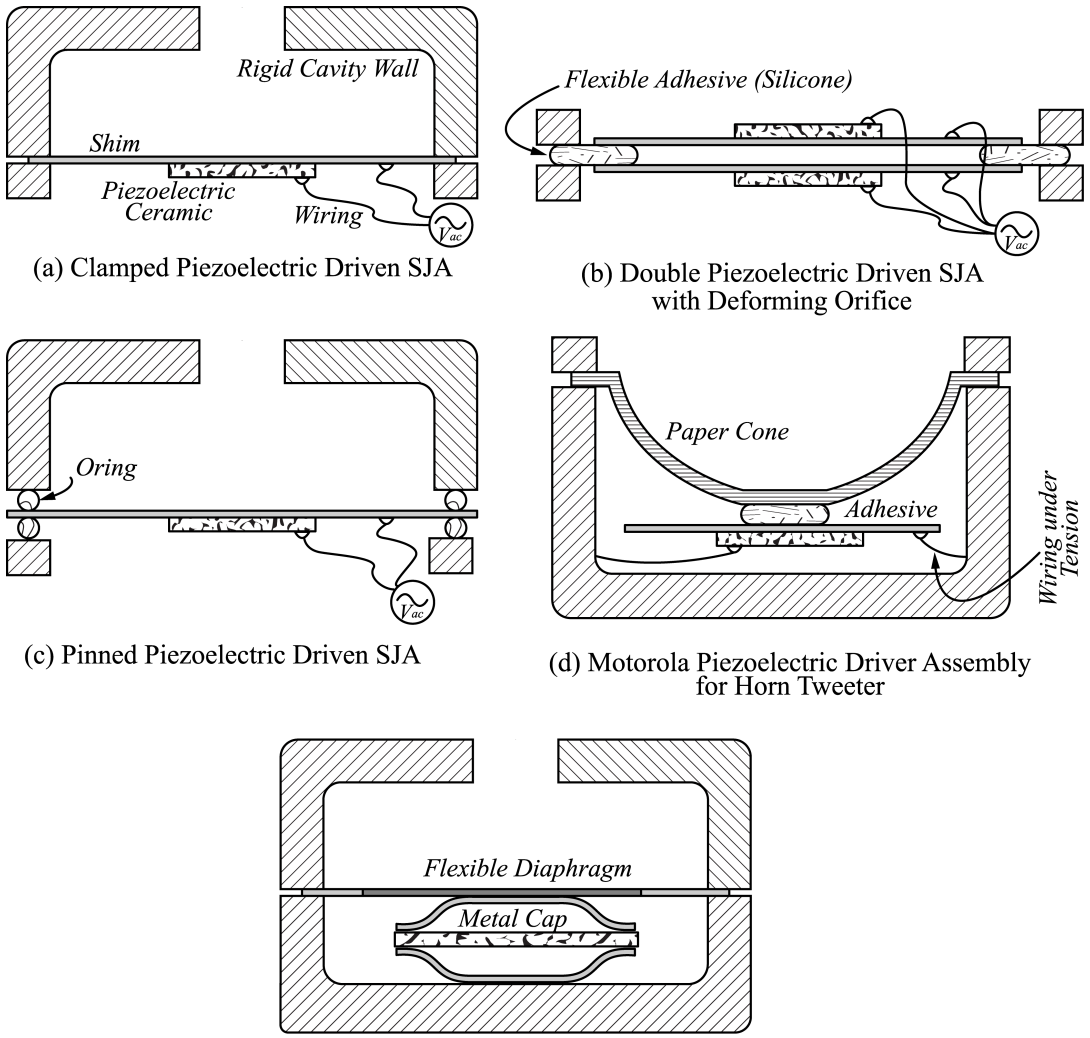

(a) Clamped Piezoelectric Driven SJA

(b) Double Piezoelectric Driven SJA with Deforming Orifice

(c) Pinned Piezoelectric Driven SJA

(d) Motorola Piezoelectric Driver Assembly for Horn Tweeter

(e) Cymbal Transducer Based Piezoelectric Driven SJA

Figure 2.9: Various deforming diaphragm mounting configurations for small scale SJDs. (a) Clamped piezoelectric bender on edges, e.g., Chiatto et al. [231], (b) clamped together piezoelectric benders by flexible adhesives and also suspended by the same flexible adhesive, e.g., De Bock et al. [233] (c) pinned piezoelectric bender, e.g., Chen et al. [229], (d) suspended piezoelectric bender, e.g., Bost [234], and (e) Piezoelectric cymbal transducer based SJD, e.g., Ayaskanta et al. [235]

by Garg et al. [236], involves using two piezoelectric bimorph disks separated by a flexible wall material with an orifice, named as advanced piezoelectric dual cooling jet (DCJ). In such configurations, piezoelectric benders are attached at the edges with flexible adhesive (typically silicone). Boundary condition of the piezoelectric disc falls in between clamped and pinned conditions [218]. The silicone adhesive could absorb and dissipate vibrational energy, reducing vibration amplitude. This was recently demonstrated in a comparison of clamped boundary condition to flexible boundary condition using neoprene rubber washers, where neoprene rubber washers reduced deflection amplitude [237]. Research on such SJDs can also be found in [189, 238, 239, 240]. The commercialization of these devices began with research of Garg et al. [186], which studied DCJs operating at resonance frequencies between 3000 and 4500 Hz. These were able to achieve jet exit velocities above 90 m/s with 110 V (peak to peak) applied to circular piezoelectric benders, and a heat transfer coefficient of approximately 239 W/(m^2·K) was reported. Subsequently, to reduce noise levels for consumer cooling applications, thinner and larger square-shaped piezoelectric discs were used to lower the resonance frequency to 150-175 Hz, with a total active device thickness of 1 mm [233]. As a result, velocities dropped to less than 4 m/s, with an effective heat transfer coefficient as high as 33 W/(m^2·K). It needs to be noted that using flexible structure, or part of the piezoelectric disc bender itself to form orifice will result in deformation of the orifice in different stages of diaphragm deformation. Phase-locked visualization of the oscillating nozzle lips for such configuration can be seen in Fig. 10. It was shown that such nozzle behavior can offer improved velocity and jet momentum output. However the studied frequencies were below 100 Hz [239]. Using two piezoelectric diaphragms, similar to the configuration shown in Figure 2.8(b), demonstrated improved performance if the piezo disc was clamped by rigid structures and had a solid orifice shape. Such designs are known as pancake SJDs, and Van Buren et al. [241] have extensively studied them. The dual disc configuration resulted in a 40% increase in jet velocity compared to the single disc configuration. The SJ reached a peak velocity of 211 m/s from a 12×1 mm^2 rectangular orifice at 700 Hz, indicating significant momentum transfer compared to other designs in the literature.

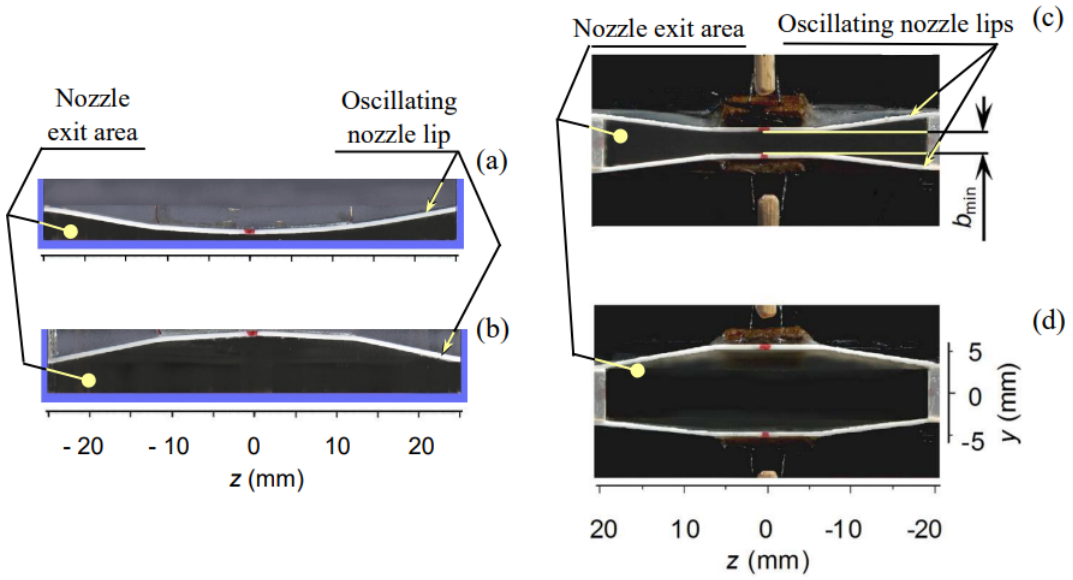

Figure 2.10: Phase-locked pictures of a temporally variable nozzle exit of SJD from [239].

An alternative approach to utilizing piezoelectric disc benders is depicted in Figure refChapter2Fig9(d), showcasing a suspended type of piezoelectric diaphragm configuration. This method was first introduced by Motorola in 1975 for their tweeter horns [234]. This design bears a resemblance to speakers, wherein the piezoelectric disc bender is suspended by being centrally glued to a paper cone. Additionally, two flexible wires are soldered to the disc, aiding in keeping the piezoelectric disc suspended alongside the paper cone. It should be noted that this particular design can be used for SJD and is tested in our laboratory.

The cymbal transducers are novel actuators that reduce stress concentration on piezoceramic disks while increasing displacement. This transducer configuration has a piezoelectric ceramic disk sandwiched between two metal end caps. A vertical load applied to these end caps causes radial stress in the piezoceramic. Because of the high cost, the use of this configuration is scarce. Ayaskanta et al. [235] used a method similar to Fig. 7(a) to produce SJ with peak velocities around 35m/s from a 0.9×0.9 mm^2 orifices at a resonance frequency between 700–750 Hz.

It needs to be mentioned about ultrasonic actuators that can generate jet flow. Using Langevin transducer SJ is created by the actuator at a high frequency of 19.7 kHz and the jet velocity jet velocity reaches 150 m/s from circular orifice diameter at 1.0 mm diameter

[242]. Piezoelectric-based actuation has demonstrated the ability to generate air jets at ultrasonic frequencies. The newly patented Frore system air pumps have been shown to produce back pressure of 1750 P and jet velocities of 52 m/s [171].

Finally, it is necessary to discuss the voltage applied to the piezoelectric-based diaphragm. Typically, an amplified sinusoidal voltage is used to provide diaphragm deflection. A recent study demonstrated that the sinusoidal waveform was superior to the square waveform. At a diaphragm resonance frequency of 150 Hz, the sine wave exhibited a 73.7% higher mass flow rate than the square wave pattern [243]. In a more recent numerical study of momentum transfer to the ambient, the best performance is achieved with triangular, sinusoidal, trapezoidal, and square wave [244]. In our experience, the sine waveform performed better than the other waveforms.

2.3.2 SJD Manufacturing with Polymer 3D Printing

To conduct this study, SJDs based on the concepts shown in Figure 2.9(a), (b), (c), and (d) are manufactured and tested. Design resulted in bulky designs, complex manufacturing, or a lack of control and manipulation over cavity and orifice characteristics. As a result, a new method is based on the power of 3D printing. Next subsections explain the novel manufacturing process.

Table 2.2 shows the diaphragm's characteristics. The diaphragm is initially powered at a peak-to-peak voltage of 140 V. However, it was realized that in continuous operation with Δx at center of disc exceeding 400 μm, ceramic fails. Thus, experiments are performed at 100 V.

Plate material	Plate diameter	Capacitance	Brass thickness	Ceramic thickness	Ceramic Dia	Mass	Nominal Resonance	Manufacturer
Brass	44 (mm)	70 (nF)	0.1 (mm)	0.13 (mm)	25 (mm)	5.1 (g)	600 (Hz)	CUI Devices/CEB-44D06 [245]

Table 2.1: Piezoelectric Diaphragm Properties

To achieve a boundary condition similar to the pinned installation of the piezoelectric disc (see Figure 2.8, and 2.9(c)), a new method was developed following extensive prototyping and trial and error to determine appropriate materials. This method was developed to ensure that the piezoelectric disc can be held with the least amount of weight and smallest structural footprint while maintaining maximum deflection and reliability in resonance actuation. The manufacturing process is illustrated in Fig. 11. The Markforged X7 industrial carbon fiber 3D printer with 50 μm resolution is used to print the body of the SJD, including the orifice, cavity shape, and supporting structures. The piezoelectric bender disc is then placed on a 45° edge designed to match its diameter and secured with a temporary clamp (Figure 2.11). The disc is then attached to the 3D printed structure with acrylic adhesive. Used acrylic adhesive has a shear strength of 20.7 to 26.2 MPa, a tensile strength of 20.7 to 27.6 MPa, and a tensile elongation of 5-15%. These properties provided a strong bond between the shim and the cavity, temperature resistance, and flexibility for fatigue resistance. Not only did fatigue not reach during our extended duration studies, but also very high amplitudes of deflection were obtained.

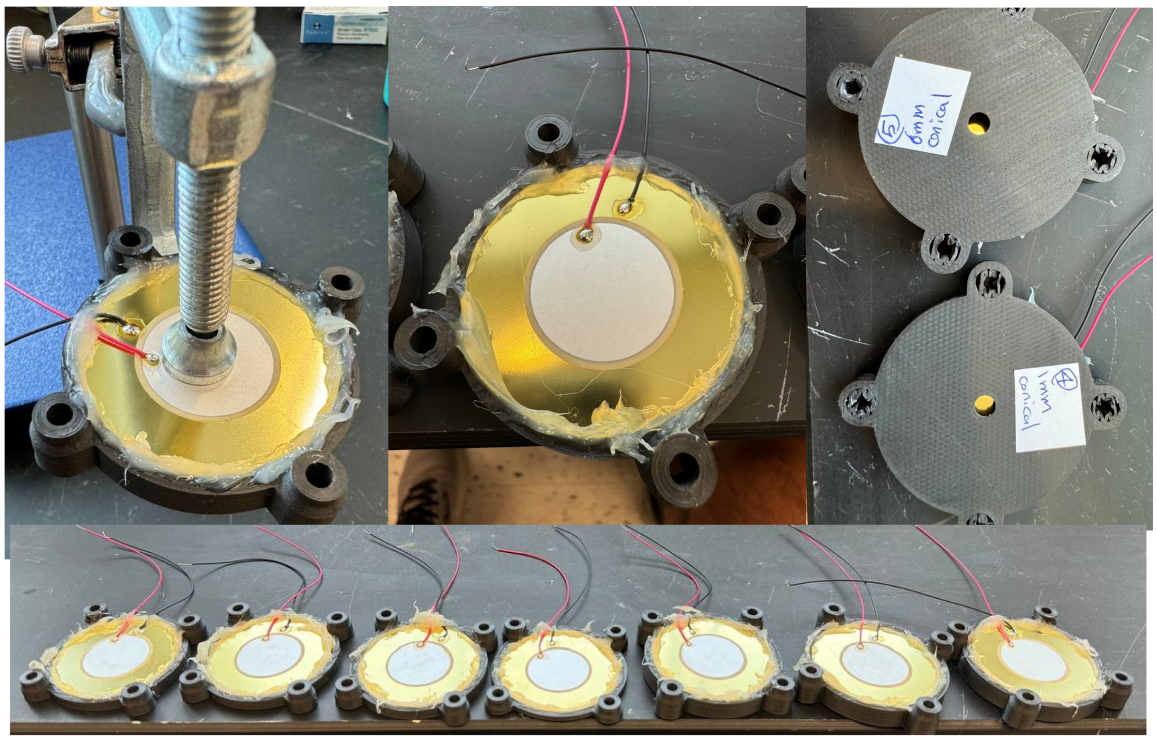

Figure 2.11: Placing piezoelectric bender disc designed edge of the SJD body with a temporary clamp and applying adhesive.

As it can be seen in Figure 2.12, two types of cavity are considered (a) conical, and (b) cylindrical. Total of seven SJD body are manufactured for first set of studies (Figure 2.12(c)). SJD-1 has conical cavity $D_o = 4.75$ mm, $L_o = 0.5$ mm, and $L = 3$ mm (see Figure 2.4(a)). SJD-2 is similar to SJD-1, but has cylindrical cavity. SJD-3 is similar to SJD-1 but has wider orifice $D_o = 6.75$ mm. SJD-4 is similar to SJD-1, but has thinner cavity $L = 3$ mm. SJD-5 is similar to SJD-1 but has larger cavity $L = 6$ mm. SJD-6 is similar to SJD-1, but has larger cavity $L = 6$ mm, and has longer orifice $L_o = 1$ mm. SJD-7 is similar to SJD-5 but has cylindrical cavity. Cavity and orifice parameters are shown in Figure 2.4(a). However, to define the body of the SJD, additional parameters are introduced in Figure 2.12(a) and (b). L_t is the perpendicular length of the 45-degree edge on which the piezoelectric disc rests. L_T is the total length of the SJD. D_t is the required thickness for the SJD's sides so it can provide enough space for applying adhesive. The SJD body's total radius is defined as $D_T + D/2$. Details of all seven SJD can be seen in Table 2.2. It can be seen that volume ratio to SJD-1 is also provided. This shows the using conical cavity instead of cylindrical cavity can help reduce the cavity volume by almost two times. This allows one to change the Helmholtz resonance, reduce the acoustic mass in the cavity, and direct the flow towards the orifice. As shown in

SJD #	Cavity	D (mm)	D_w (mm)	D_t (mm)	L (mm)	L_o (mm)	L_t (mm)	L_T (mm)	V_0 (mm^3)	Volume ratio to SJD 1
1	con	4.75	44	22.6	3	0.5	0.5	4	2307	1.00
2	cyl	5	44	22.6	3	0.5	1	4.5	4562	1.98
3	con	7	44	21.6	3	0.5	1	4	2339	1.01
4	con	7	44	22.6	1	0.5	1	3	770	0.33
5	con	5	44	22.6	6	0.5	0.5	7.5	4620	2.00
6	con	5	44	22.6	6	0.5	1	7.5	4620	2.00
7	cyl	5	44	22.6	6	1	1	7.5	9123	3.95

Table 2.2: Details of 7 manufactured SJDs (con stands for conical, and cyl stands for cylindrical).

Figure 2.5(b), there is a gap between Helmholtz resonance and wall structural resonance when SJD is not optimized to match these two resonances. By changing the structural design of the cavity and orifice so that these two resonances match, one can see a significant change in jet exit output. By using parametric study with tuned LEM $D = 1.65$ mm and $L_o = 2.3$ mm are

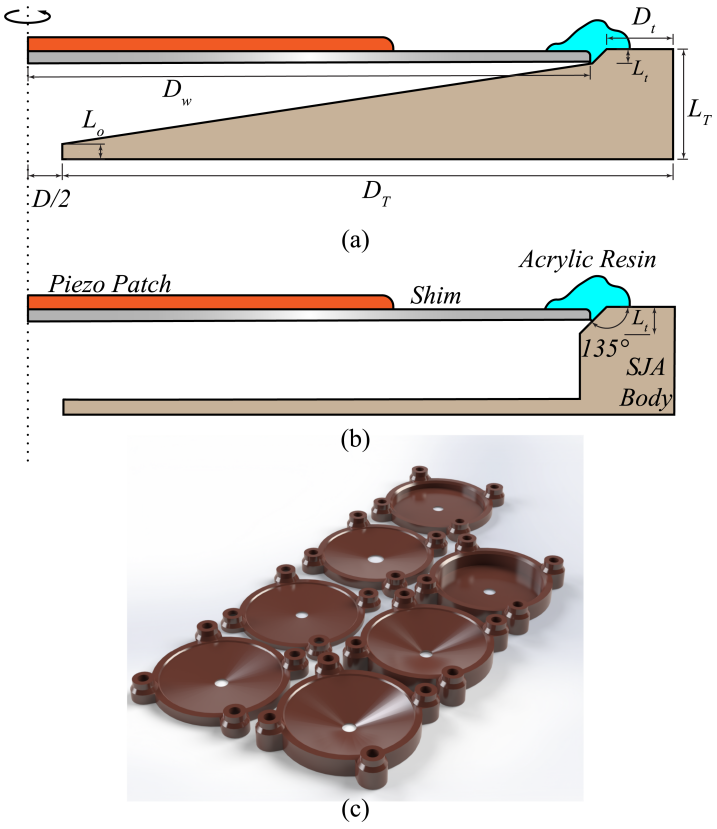

Figure 2.12: Axisymmetric cut plane view of manufactured SJDs with (a) conical cavity, and (b) cylindrical cavity show casing placement of piezoelectric disc on 45° edge and maintaining the structure using acrylic resin to provide pinned boundary condition.

set. Two SJDs are designed and manufactured and are named SJD 8-con and SJD 8-cyl. Details of optimized SJDs can be seen in Table 2.3.

SJD #	Cavity	D (mm)	D_w (mm)	D_t (mm)	L (mm)	L_o (mm)	L_t (mm)	L_T (mm)	V_0 (mm^3)	Volume ratio to SJD 1
8	cyl	1.65	44	22.6	3	2.3	1	6.3	4562	1.00
8	con	1.65	44	22.6	3	2.3	0.5	5.8	2284	0.99

Table 2.3: Details of optimized manufactured SJDs (con stands for conical, and cyl stands for cylinder).

2.4 Experimental Study

The experimental procedure of this research is illustrated in Figure 2.13. Initially, a suitable piezoelectric-based diaphragm was selected. Displacement measurements were performed using laser displacement sensors at a voltage of 140 V. However, during prolonged operation at this voltage, the high displacement of the diaphragm caused the piezoceramics to crack, with SJDs 1, 2, and 7 failing. Results of the 140 V test are presented in Appendix C. The primary reason for failure was not voltage breakdown but excessive displacement, which the ceramics could not withstand. Other aspects of the design, such as adhesive joints and the body of the SJDs, endured long-term operation. Subsequently, the voltage was reduced to 100 V, at which level the SJDs operated safely.

Experimental displacement data were then extracted and used to tune LEMs for each SJD. Force (F) and stiffness (k) were evaluated based on low frequency operation data (see Equation **??**), and C_l was tuned to match displacement curves achieved from displacement data to LEM data. By matching displacement data from with the LEM predictions, we could confidently predict the velocity behavior and identify the frequency at which the SJDs would produce the highest jet exit velocity. The LEMs were subsequently used for a parametric study to match two resonance modes ($fr_H = fr_w$) based on parametric optimization of orifice characteristics. Furthermore, the LEM provided tools to evaluate integration in Equation 2.9 and Equation 2.10.

An experimental setup was designed and constructed, with details provided in the Appendix B. The SJDs were tested at their evaluated frequencies, where they provided the highest

jet exit velocity across various orifice-to-impingement plate distance ratios. Lastly, hotwire anemometry tests were performed to verify the accuracy of the tuned LEMs in predicting SJD behavior based on their geometry and diaphragm characteristics. This validation can help future research confidently optimize devices without the need for expensive and fragile hotwire test setups, as displacement measurement techniques are significantly more cost-effective.

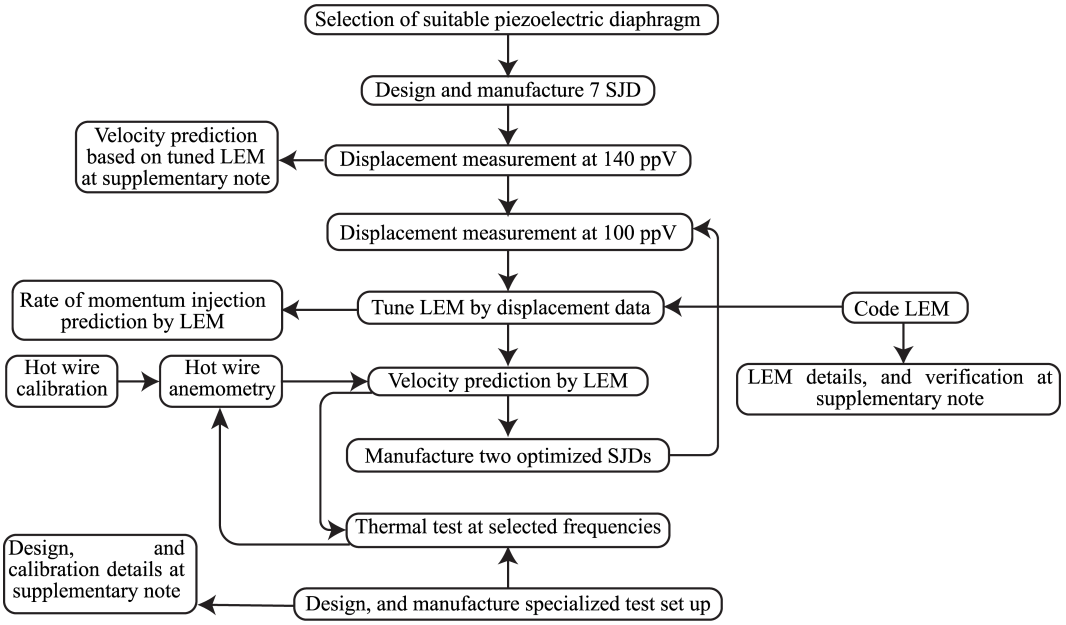

Figure 2.13: Research organization flowchart.

2.4.1 Deflection Measurement and LEM Tuning

The deflection test is performed using Acuity AR100 laser triangulation sensor that measures distance by projecting a beam of laser light that creates a spot on a target surface. Diffuse reflected light from the surface is viewed from an angle by a CMOS detector array inside the AR100 sensor. The target's distance is calculated from the image pixel data using the sensor's microprocessor. The distance is transmitted through serial communications. The range of the measurement with the current unit is 10 mm (focal point at 5mm), with resolution, of 0.01% giving the nominal accuracy of 1 μm. The laser operates at 660 nm. The data acquisition frequency is 9400 Hz. Real world accuracy of the measurements was determined to be 3 – 5 microns, due to other vibrations, the orientation of the surface with the laser beam, and centering the beam. As seen in Figure 2.14, a test bed is prepared to secure each SJD underneath

the laser displacement sensor. SJDs are secured using four bolts to the test bed. The center of the disc is marked with a black marker, this will also help reduce the specular reflectivity of the silver coating on the disc. SJDs are being controlled using a custom LabView program. The Siglent SDG 2042X function generator generates sine signals with an output amplitude of 0.7 V, which are amplified by a Trek PZD700 High Voltage Amplifier with a gain range of 200 to 140 V. Later, after a few devices (SJD 1, 2, and 7) failed at this voltage, the voltage was reduced to 100 V. Details of measurements in 140 V voltage are provided in Appendix C. Displacement measurements were carried out on two separate days. Starting at 25 Hz, the SJDs were operated for 10 seconds at each frequency increment of 25 Hz up to 800 Hz to capture the actuator's resonance. After being disconnected from the test bed, the SJDs were reinstalled and tested the next day, beginning at 2100 Hz and decreasing in 100 Hz increments. This procedure aimed to investigate the Helmholtz resonance and correlate it with the previous day's results. It was discovered that each measurement targeted slightly different points on the disc, and that the system's stiffness varied slightly with each installation due to the use of polymer body. Despite these variations, these testing methods were successful in detecting consistent behavior in SJDs. The resonance of the wall allows for an estimate of the structure's

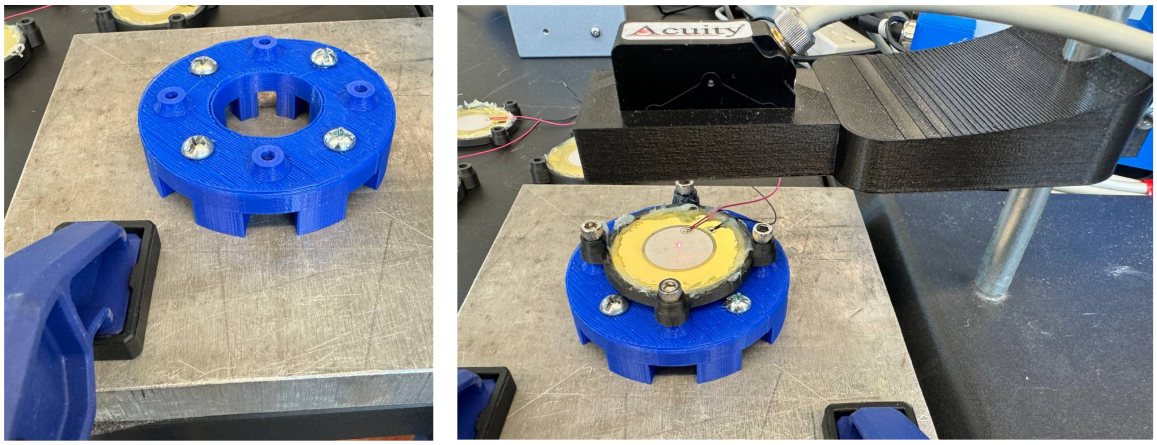

(a) (b)

Figure 2.14: (a) Test best for securing SJD and (b) showcasing installation of SJD on test bed and measurement of displacement using laser triangulation sensor.

spring constant, but this is only an approximation. This is due to the resonance being observed in a coupled system involving both acoustic mass and stiffness. Assuming that the deflection at the lowest measured frequency (25 Hz) corresponds to the static deflection, the force exerted

by the piezoelectric ceramic patch on the diaphragm can be estimated. To match the deflection behavior observed in the SJDs, ill-defined parameters in the LEM code is adjusted, the C_l. It

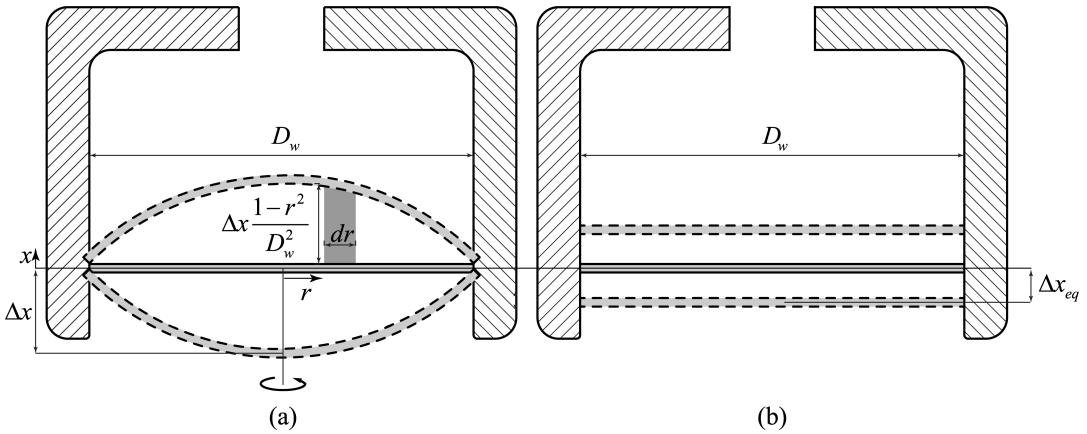

Figure 2.15: Deflection behavior of the diaphragm.

needs to be noted that the deflection behavior of the diaphragm can be approximated as shown in Figure 2.15. This is while in LEM the model assumes one dimensional (piston-in-cylinder) movement of the piezoelectric disc bender. In order to match the behavior of the experiment to LEM model, one method is to evaluate equivalent value of Δx for the LEM model Δx_{eq}. As a result, we adjust the volume change in the cavity to match the volume change of cylindrical motion from the LEM model. The behavior of diaphragm bending can be modeled as the static deflection of a circular membrane clamped on the edge under a uniform load. The deflection profile can be estimated using [232]:

$$\Delta x(r) = \Delta x(1 - 4(r/D_w)^2 + 8C(r/D_w)^2 \ln(2r/D_w)) \tag{2.17}$$

Where C is 1.0 for clamped and 0 for pinned case. Most of the time even when the piezoelectric disc is being clamped deflection behavior is towards pinned condition as seen in [241]. In our case, because the disc is held in place with flexible adhesive, we assume that deflection is completely pinned (adhesive undergoes strain in the edge, keeping disc bending behavior not effected at boundaries). This is further supported by measurement data showed disc's low resonance frequency and high deflection.

Volume change in the experiment can be considered as:

$$\Delta V_0 = \int_0^{D_w/2} \Delta x \left(1 - 4\left(\frac{r}{D_w}\right)^2\right)(2\pi r)dr = \Delta x \left[\pi r^2 - \frac{2\pi}{D_w^2} r^4\right]_0^{D_w/2} = \frac{\pi}{8}\Delta x D_w^2 \quad (2.18)$$

While in case of LEM one can write:

$$\Delta V_0 = \frac{\pi}{4}\Delta x_{eq} D_w^2 \quad (2.19)$$

where:

$$\Delta x_{eq} = 0.5\Delta x \quad (2.20)$$

2.4.2 Synthetic Jet Impingement Experiments

In order to study the impingement cooling performance of designed SJDs, a specialized heater and measurement unit is manufactured. This unit is designed to provide a surface heat flux on a 30 mm × 30 mm area on the top surface of a 30 × 30 × 2.25 mm^3 aluminum block. An array of eleven T type beaded thermocouples (TCs) from Omega (5TC-TT-T-30-36-ROHS) was inserted into the center of the block, just below 0.5 mm from its top surface. Ambient temperature is also measured using T type thermocouple. To provide a heat source to the aluminum block, a self-adhesive polyimide flexible surface heater (model KHLVA-101(1) from Omega) is installed on the bottom of the aluminum block. Power to the heater is supplied by Agilent E3633A DC power supply. Furthermore, the voltage across the heater is monitored by Hewlett 34401A multimeter. Heater control and data acquisition are performed using a custom LabView program. For a robust design, the heater, thermocouples, and the aluminum block were integrated using insulating Polyurethane foam [233]. The thermal resistance of the heater unit is determined using a comprehensive calibration process described in the Appendix B. Figure 2.16 presents an overview of the test setup. The designed heater system is located in the center of a motorized 3D axis's Z-axis. SJDs are mounted on a motorized X-Y axis with the ability to change the angle of impingement. Next, SJDs are aligned with the center of the heater unit and tested at various Lh/D values. Heater power is set to 1.42 W and generates

1578 W/m^2 resulting in an average surface temperature of 74 °C at natural convection at lab temperature of 22 - 23°C. The heater elements and heated block are similar in size, preventing heat spreading, thus all eleven thermocouples showed the same temperature with a difference of ± 0.2 K. The heat loss of the heated unit is determined to calculate an accurate heat transfer coefficient from the top surface of the heated block. Thermophysical properties of air are calculated at film temperature using a fourth-order polynomial with temperature dependent properties in atmospheric pressure. After reaching the steady state in natural convection (Nu = 2.3 -2.7), SJDs are activated and operated until no temperature variation or steady state in each condition is achieved. SJDs are first investigated at the furthest distance to the heater, from L_h/D of 9 to 3. Larger values were not possible due to the size limitations of the 3D axis.

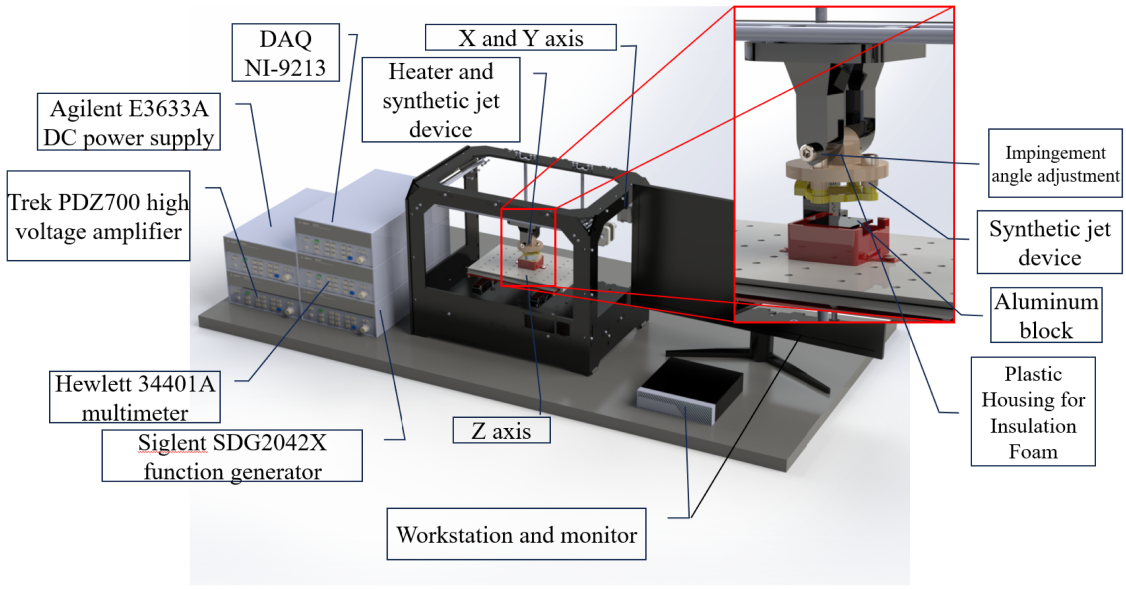

Figure 2.16: Test set up preview of SJ impingement heat transfer study.

2.4.3 Jet Exit velocity Measurements with a Hot Wire Anemometer

Maximum jet exit velocity measurements (U) were conducted using a DANTEC MiniCTA System equipped with a miniature hot wire probe, a two-point hot-wire calibrator, and StreamWare software. The probe was connected to the MiniCTA module, following the manufacturer's specifications for setup and configuration. Calibration was performed in a controlled environment using the two-point calibrator provided by DANTEC. The probe was exposed to two

precisely known velocities, and the corresponding voltage outputs were recorded to extract a 4th degree polynomial calibration function [246]. During experiments, the hotwire probe was positioned at orifice exit using Velmex precision motion-control 2D axis ensuring alignment perpendicular to the flow direction to minimize directional bias (see Figure **??**). The MiniCTA system was set to sample at kHz levels depending on operation frequency, and data was collected over a 10-second duration for each frequency (starting at 100 Hz by 100 Hz increment). StreamWare software facilitated real-time data acquisition and monitoring. To assess the reliability of the manufacturing process, hotwire measurements were repeated after a 4-month period to evaluate the performance and stability of both the device and the adhesive used in its assembly.

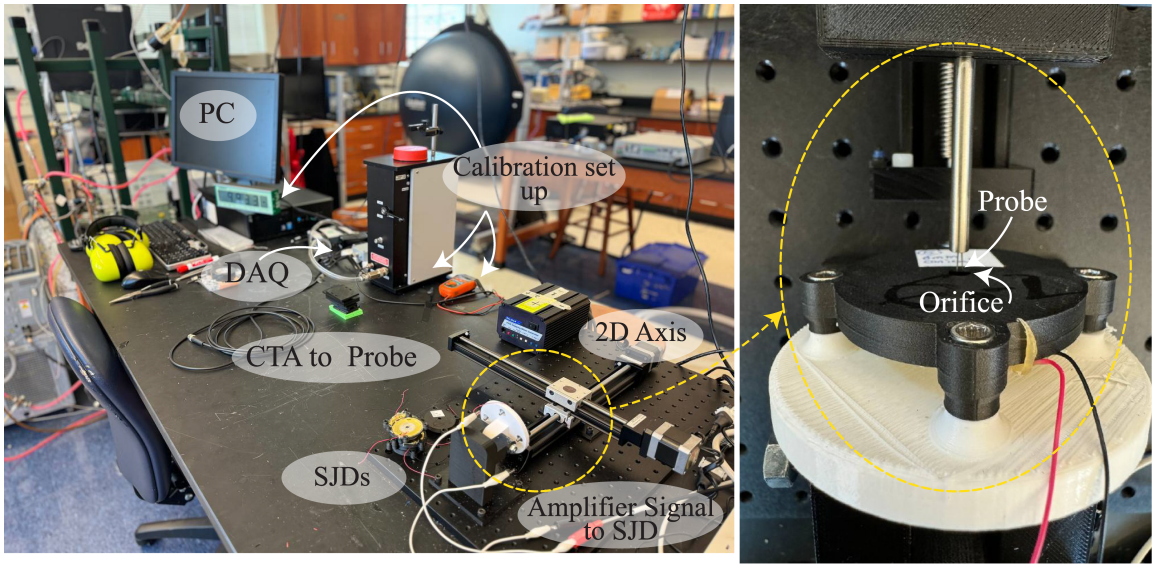

Figure 2.17: Hotwire anemometry set up overview.

2.4.4 Power Consumption Measurement

The applied voltage and current consumption of devices during operation were measured by connecting the Trek PZD700 analog input to the digital voltage converter NI–9205. Measurements were done at 4kHz for 250 ms during experiments. 1/200 voltage monitor and 0.1 V/mA voltage output were used to evaluate the current and voltage characteristics of SJDs. The power consumption rate calculation was done by integrating the absolute value of the product of voltage and current over a second of operation in MATLAB.

2.5 Results and Discussions

2.5.1 Deflection Measurement, LEM Tuning, and Hotwire Results at 100 V

Table 4 presents a summary of the deflection measurement results and LEM parameter tunning at 100 V. It needs to be stated that results are presented for SJD-3, 4, 5, and 6 only. Results for all devices in 140 V are presented in Appendix C. Based on the deflections at 25 Hz one can estimate the force being applied to the diaphragm by the piezoceramic. The applied force is estimated by tuning the LEM with equivalent deflection (Δx_q) behavior from experiments. It can be seen that the maximum force at 100 V is in the range of 1.8 -2.5 N. At 25 Hz, SJD-4 exhibits the maximum deflection, demonstrating the greatest compliance among other SJDs. The observed differences in compliance and deflection are attributed to several factors: added stiffness from the air inside the cavity, variations in diaphragm properties including location and amount of solder, and inconsistencies in adhesive application. It can also be seen that these factors lead to varying wall resonance measurements for each SJD. Specifically, SJD-4, which has the smallest cavity volume, exhibits the lowest resonance frequency, while SJD-6, with the larger cavity volume, shows resonance at 675 Hz. This issue can be explained by looking at Figure 2.5(a). In SJD-4, the deflection of the diaphragm is reduced by applying cavity due to added acoustic mass to the system, on the other hand in SJD-5 and 6 wall resonance increase increases from the nominal natural frequency of the diaphragm due to added acoustic stiffness to the system. The largest deflection at resonance, 289.3 μm, is observed in SJD-3, which has the largest orifice among other SJDs suggesting that tightening the orifice can reduce deflection. Furthermore, it can be seen that C_l is related to the length of the SJDs, with longer SJDs resulting in lower C_l values. It is important to note that C_d, the nozzle discharge coefficient, is kept constant at 0.6, which is an accurate assumption. According to a classic study by [235], C_d in small β values is almost constant in the variety of Re ranges, thus it can be kept constant throughout all stages of SJ generation. However, future research can focus on C_l's temporal behavior, which will improve the accuracy of LEM in predicting SJ behavior. Apart from wall resonance, the Helmholtz resonance of the SJDs can be estimated by observing the slight increases in deflection at specific frequencies, with resonances occurring between 1500 and

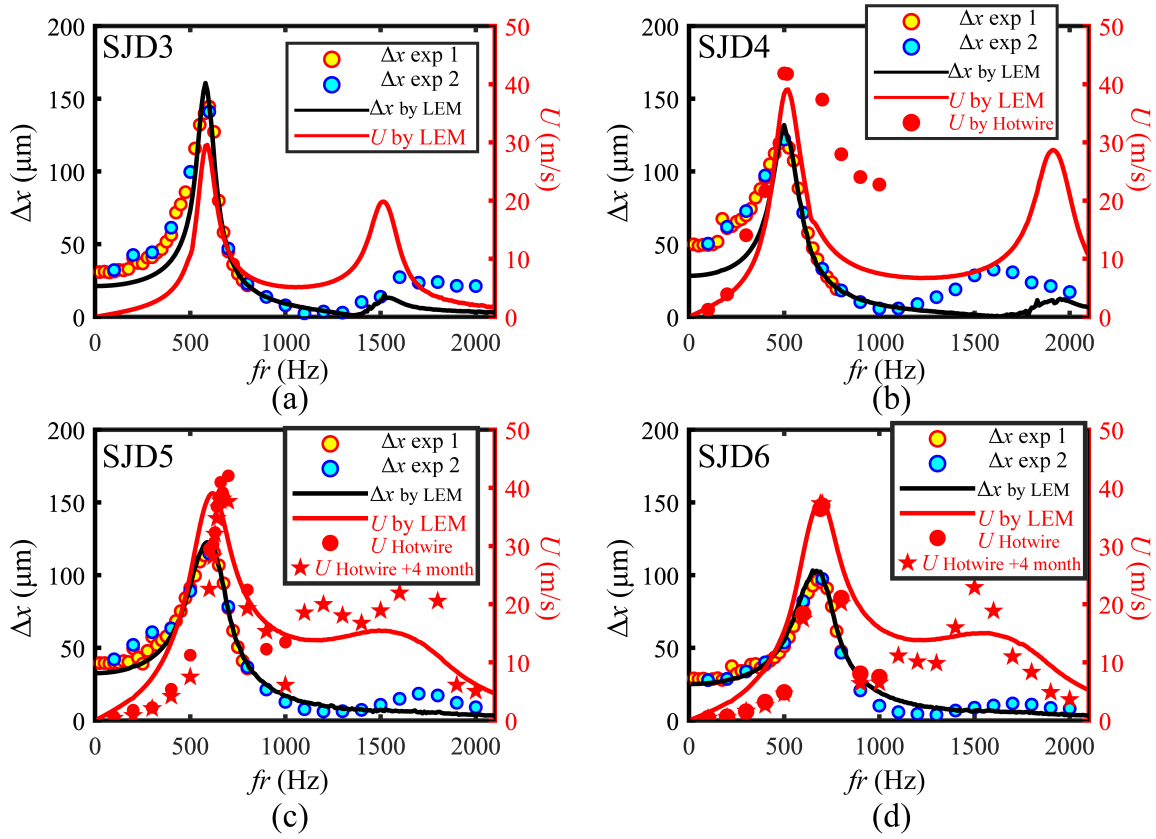

Figure 2.18: Displacement behavior of the SJD (a)3, (b)4, (c)5, and (d)6 in two different measurements vs the deflection behavior provided by tuned LEMs. Maximum area averaged velocity performance of the SJDs based on LEM and hotwire is also provided on the right axis.

		Deflection Experiment						LEM				
SJD	Cavity	fr_{min} (Hz)	Δx μm	fr_w (Hz)	Δx (μm)	fr_H(Hz)	Δx (μm)	k x 10^4(N/m)	F_{max}(N)	C_l	C_d	fr_H(Hz)
3	con	25	62	600	289.3	1600-2000	54	8.49	1.8	2	0.6	1370
4	con	25	100	500	245	1500-1800	61	7.49	2.11	2.75	0.6	1618
5	con	25	79	625	231	1600-1900	37	7.65	2.49	0.45	0.6	1556
6	con	25	58	675	193	1500-1900	23	9.58	2.41	0.3	0.6	1600

Table 2.4: Results of deflection test and LEM tuning.

1800 Hz. Notably, increasing the size of orifice lowers the Helmholtz resonance frequency (see Equation **??**). An intriguing pattern is observed with respect to cavity thickness: thinner cavities (smaller L - see Figure 2.4(a)) exhibit more pronounced effects on wall deflection in Helmholtz resonance. For instance, in a cavity with a length of 1 mm, the largest deflection in Helmholtz resonance measured is 91 microns. When the diaphragm is closer to the orifice, oscillating air in and near the cavity can be reinforced by the diaphragm's oscillation, resulting in oscillation of the wall and vice versa. As shown in SJD 5 and 6, increasing L reduces this effect.

Figure 2.18 presents the frequency-dependent displacement measurements, with "exp 1" in legend corresponding to day 1's measurements starting at 25 Hz and increasing in increments of 25 Hz up to 800 Hz, and "exp 2" representing day 2's measurements beginning at 2100 Hz and decreasing in 100 Hz increments down to 100 Hz. The results from the tuned LEMs are depicted with solid lines for each scenario. A good behavior matching between trends of x by LEM and measurements can be seen. However, for SJD-3 and 4, which have a shorter cavity length (L), intensification of wall deflection near the Helmholtz effect is not captured well enough with the LEM model. The main reason for this could be due to the fact that these SJDs have conical cavity shapes, and this phenomenon is ignored in LEM models for these SJDs (the cavity considered cylindrical in LEM). However, for SJD-3 and 4, the model predicted the results well without requiring a change in the L value. Nonetheless, the LEM model considers one-dimensional velocity and needs specific tuning to capture real-time device behavior. Table 4 also includes the evaluated Helmholtz resonances by LEM models.

The peak instantaneous area averaged jet exit velocity (U) predicted by LEM model for each SJD is also provide on Figure 2.18, shown by red line with axis at the right side the graphs. It can be seen that maximum U occurs with slight offset from resonance frequency due to phase lag (see Figure 2.5(b)). For SJD 3 maximum U is evaluated at 585 HZ with value of 29.6 m/s. For SJ 4 to 6 these values are 515 Hz with 39.1 m/s, 620 Hz with 39.1 m/s, 690 Hz with 37.8 m/s. These values are summarized in Table 5. It can be seen that SJD 3, and 4 show high jet exit velocity at Helmholtz resonance, in contrast to SJD 5, and 6. This indicates the positive effect of having a thinner cavity, as devices with thinner cavities can perform better in Helmholtz resonances. The benefit of this is that the diaphragm will perform with less input power and deflection, allowing the SJD to perform more efficiently and reliably.

Measured U values by hotwire probe are also shown in Figure 2.18, represented by red circles with an axis on the right side of the graphs (SJD3 failed due to accidental overload). Hotwire measurements are evaluated using a 100 Hz increment to determine U near wall resonance. For SJD 4, the maximum U is measured at 600 HZ and is 50.5 m/s. For SJ 5 and 6, the values are 700 Hz with 42.1 m/s and 700 Hz with 36.9 m/s. It is clear that LEM has a slight underestimation of the frequency where the maximum U is achieved, as well as the value of U itself. Probable causes can be stiffness change of the system after each installation of SJDs in the measurement stage, simplification of deflection profile shown in Figure 2.15, and intrinsic simplification of flow behavior by LEM itself. Tuned LEM shows overall acceptable agreement in predicting U and its frequency response, while only deflection measurements are used to tune it. In Figure 2.18(b) for SJD 4 with the thinnest cavity profile, at above wall resonance frequencies, sharp drop in U values predicted by LEM cannot be seen in experimental data. This suggests that displacement after wall resonance is more pronounced in thinner profiles, and any SJDs designed to operate at Helmholtz resonance (rather than wall resonance) can benefit from shorter cavity lengths. Thus, SJDs with thinner cavities perform better in Helmholtz resonances. The benefit of this is that the diaphragm will require less input power and deflection, allowing the SJD to operate more efficiently and reliably. Table 2.5 provides a summary of maximum U prediction by LEM and compares them by hotwire measurements.

Hotwire tests were conducted on SJA 5 and 6 after a 4-month period to evaluate the reliability and stability of the manufacturing process. These tests were performed at frequencies up to 2000 Hz. The results demonstrate a close match with the initial measurements, indicating that the SJAs maintained their performance after 4 months in a lab environment. However, the LEM model, tuned based on deflection data, underestimates the velocity in the Helmholtz resonance range. Despite this, the model accurately predicts the Helmholtz resonance frequency, as shown by the alignment of the second velocity peak. Additionally, the model accurately predicts the velocity drop beyond the Helmholtz resonance range, particularly near 2000 Hz.

SJD #	fr (Hz)	U (m/s)	U_{hw} (m/s)
3	585	29.6	-
4	515	39.1	41.8
5	620	39.1	30.42
6	690	37.8	36.4

Table 2.5: Predicted maximum area averaged jet exit velocity.

2.5.2 Deflection Measurement, LEM Tuning, and Hotwire Results at 100 V for High-velocity SJDs

Table 2.6 summarizes the deflection measurement results at 100 V for optimized SJDs. The results indicate that with smaller orifice smaller systems become stiffer and shifts wall resonance to higher frequencies (see Figure 2.5(a)). Conversely, increasing the length of the orifice (L_o) and reducing its size seems to successfully align Helmholtz resonance with wall resonance.

With the same geometrical characteristics, it can be seen that wall resonance of conical cavity is higher than cylindrical cavity. Thus, as it can be seen in Table 2.6, conical system's k is nearly twice that of the cylindrical cavity. Compared to previous SJDs, it is important to note that acoustic effects become more pronounced as the orifice becomes smaller. Therefore, in the LEM for SJD8-con, the length of the cavity is multiplied by a factor of 0.58 to match experimental results. Regarding diaphragm deflection, good matching can be observed with LEM and experimental results. It can be seen that since both resonance modes are overlapping each other maximum velocity output and maximum deflection output are occurring in same

		Deflection Experiment					LEM				
SJD	Cavity	fr_{min} (Hz)	Δx μm	fr_w (Hz)	Δx (μm)	fr_H(Hz)	Δx (μm)	k x 10^4(N/m)	F_{max}(N)	C_l	C_d	fr_H(Hz)
8	cyl	25	94	850	265	-	-	6.52	2.58	1.5	0.6	-
8	con	25	77.2	1175	265	-	-	12.2	3.05	1.5	0.6	-

Table 2.6: Results of deflection test and LEM tuning for optimized SJD-8.

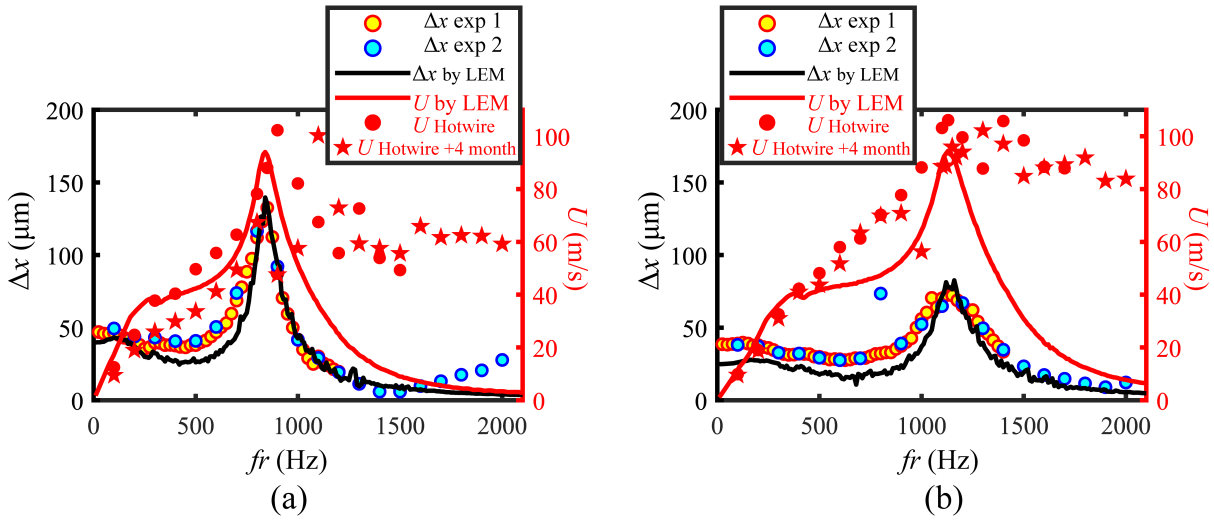

Figure 2.19: Displacement behavior of SJD (a)8-cyl, and (b)8-con in two different measurements vs the deflection behavior provided by tuned LEMs. Maximum area averaged velocity performance of the SJDs based on LEM is also provided on the right axis.

resonance modes where maximum velocity at 840 Hz of 94 m/s is theoretically evaluated for SJD8-cyl and 94.48 m/s at 1130 Hz for SJD8-con. These values are summarized in Table 2.7. Similar to previous cases, LEM underestimates the actual jet exit behavior velocity. The maximum velocities recorded by hotwire measurements were 102.3 m/s at 900 Hz for SJD8-cyl and 106.1 m/s at 1130 Hz for SJD8-con. It should be noted that experimental data show a second peak in U for SJD8-cyl at 1300 Hz with 72.6 m/s and for at 1400 Hz with 105.7 m/s. This is more highlighted in second hotwire data. This might suggest that LEM's optimization (or matching of Helmholtz and wall resonance) was unsuccessful. However, when we examined wall deflection behavior, we could not detect a rise in deflection behavior at these frequencies. This increase in jet exit behavior might is due to higher order acoustic effects in SJDs at these frequencies. The results also show that the manufacturing process is capable of achieving the

highest reposted SJ velocities using a single piezoelectric diaphragm at actuation frequencies below 1 kHz.

SJD #	fr (Hz)	U (m/s)	U_{hw} (m/s)
8-cyl	840	94.00	87.2
8-con	1130	94.5	106.1

Table 2.7: Predicted maximum U for optimized SJDs.

2.5.3 Heat Transfer Test Results

Figure 2.20 provides the enhancement of natural convection ($\mathrm{Nu}/\mathrm{Nu}_{nc}$) with the presence of SJDs at different distances between the orifice and the heater, L_h/D. Furthermore, it shows the achieved heat transfer coefficient at room temperature. Due to the larger size of orifice in SJD 3, L_h/D of 2 to 6 in considered for this device, while rest of the SJDs are tested in L_h/D of 3 to 9. Devices are tested in frequencies shown in Table 5 and 7

The mutual behavior of SJDs is that the heat transfer coefficient increases with increasing distance. As the SJD approached the surface, air began to mix in large vortical structures trapped between the heated wall and the SJD body, increasing film temperature and reducing SJ's cooling capacity. SJD 3, 5, and 6 exhibited similar heat removal behavior. SJD 4 exhibited similar behavior, but it had a slightly lower heat transfer coefficient at L_h/D of 7 and 8. It is clear that optimized devices, despite having higher jet exit velocities, did not provide as much heat transfer capability as SJDs with larger orifice sizes. This emphasizes the importance of Equations 2.9 and 2.10 in SJD behavior analysis. Despite having a 2 to 3 times higher jet exit velocity, SJs generate by SJD 8-cyl and 8-con are thermally inferior due to their lower impulse injection rate ($\dot{I}$).

To understand this, the rate of injected momentum towards the heater $\dot{I}$ (see Equation 2.10) is evaluated based on the LEM model and is provided in Figure 21(a). There is a clear correlation between $\dot{I}$ in Figure 2.21(a), with the achieved thermal performance shown in Fig. 20. In other words, by following the peaks of $\dot{I}$, it can be observed that the higher the generated momentum rate, the better the device performs, even though the jet can have lower jet velocity. This correlation is particularly significant considering that the surface temperature of

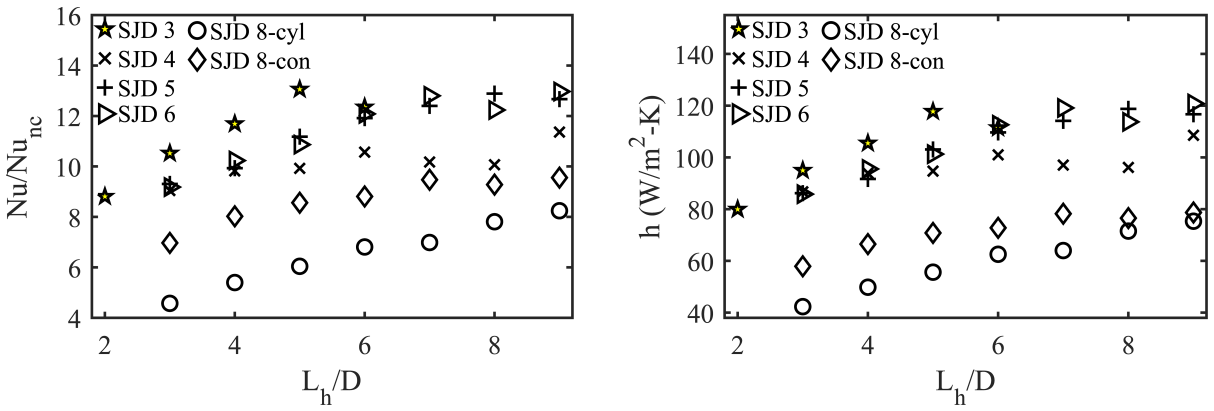

Figure 2.20: Factor of Nu number enhancement in comparison to steady state natural convection case (left), and heat transfer coefficient (right) in different orifice to heat place distance ratios.

the heater in this experiment can be considered uniform due to the nature of its design. Thus, SJDs with small orifices can produce high heat transfer coefficients from a local perspective, but their overall (useful) heat removal behavior can be related to $\dot{I}$. This aspect is occasionally overlooked when tuning SJDs for specific tasks. In other words, optimizing piezoelectric based SJDs solely to achieve higher jet exit velocity may be misleading, and optimization should also consider $\dot{I}$. Figure 21(b) shows the flow rate ejected towards the heated surface, with an interesting contrast between $\dot{I}$ and flow rate trends. Furthermore, it is interesting to see that SJs, by fraction of flowrate in comparison to fan systems, are capable of similar cooling performance, highlighting their superior impingement characteristics in comparison to dispersed air impingement. For example, the maximum average heat transfer coefficient observed here (120 W/(m^2·K) is comparable to the local heat transfer coefficient achieved by a 59 mm diameter axial fan at 2000 rpm [247], which generally consumes about 1.5 W of power at this speed. Similarly, the average heat transfer coefficient (120 W/(m^2·K)) achieved by high-speed axial fans operating at 9000 rpm [248], with a typical power consumption rating of 3–5 W at this rpm, is matched by our SJDs. Power consumption figures for SJD 5 at 670 Hz were evaluated at 0.66 W, for SJD 7 at 700 Hz at 0.49 W, for SJD 8-cyl at 1100 Hz at 1.12 W, and for SJD 8-con at 1.20 W.

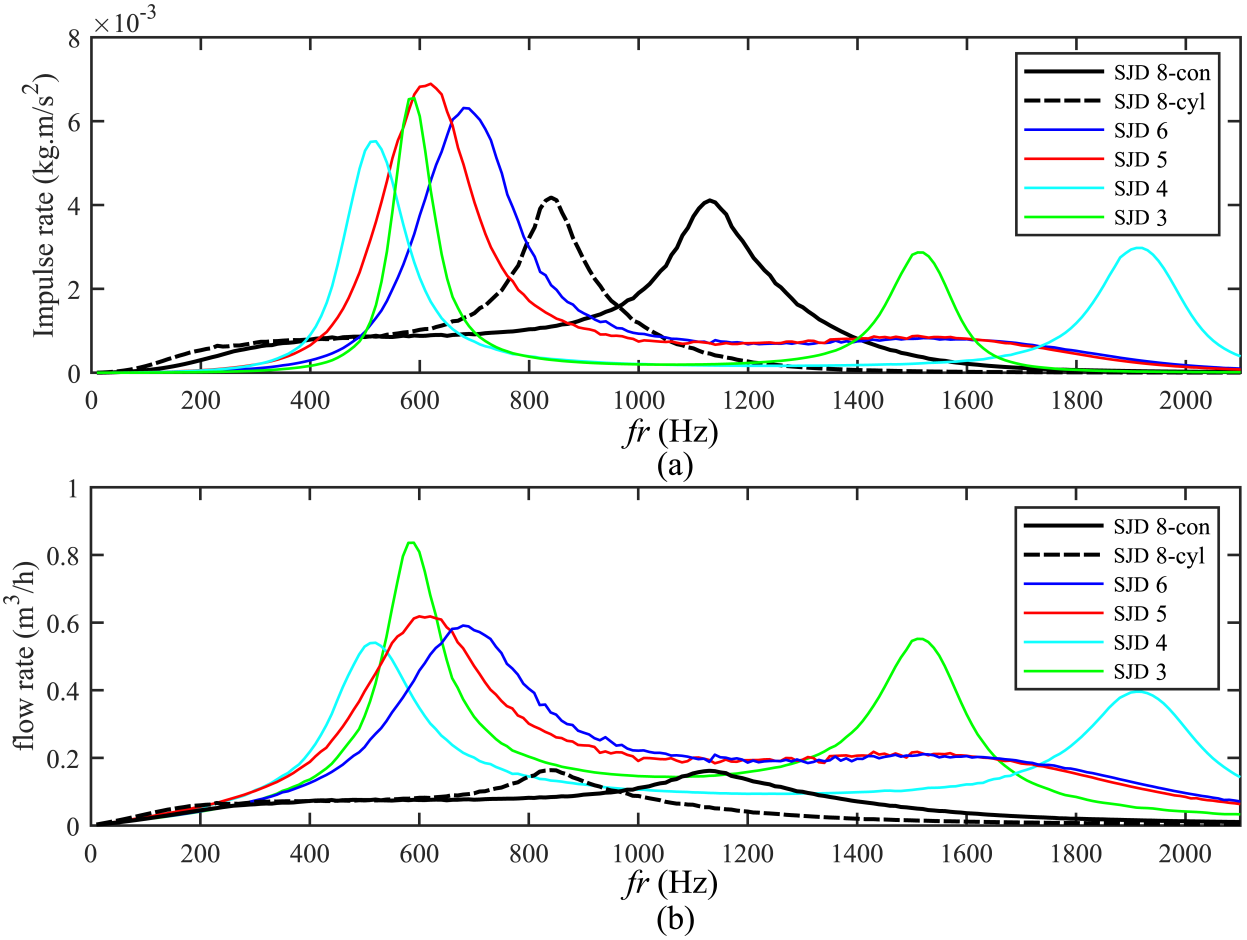

Figure 2.21: (a) Rate of injected momentum ($\dot{I}$), and (b) rate of injected flow in different operation frequency evaluated by LEM.

Table 2.8 provides a summary of performed thermal tests. It can be observed that even when operated at different frequencies, SJDs with similar $\dot{I}$ performance show similar Nu number values. Therefore, from an average heat removal capability perspective, we can conclude that the performance of SJDs is more correlated to the distance of impingement and their capability of momentum generation rate Nu $\approx$ Nu$(L_h/D, \dot{I})$.

SJD	Voltage (V)	fr (Hz)	Nu_{nc}	Nu							
				$L_h/D = 9$	$L_h/D = 8$	$L_h/D = 7$	$L_h/D = 6$	$L_h/D = 5$	$L_h/D = 4$	$L_h/D = 3$	$L_h/D = 2$
3	100	585	2.6	-	-	-	31.5	33.3	29.8	26.8	22.4
4	100	515	2.7	30.6	27.1	27.4	28.5	26.8	26.5	24.4	-
5	100	620	2.6	33.0	33.6	32.3	31.0	29.1	25.9	24.2	-
6	100	690	2.6	34.1	32.2	33.7	31.8	28.6	26.9	24.1	-
8-cyl	100	840	2.6	21.2	20.1	18.0	17.5	15.5	13.9	11.8	-
8-con	100	1130	2.3	22.1	21.5	21.9	20.4	19.8	18.6	16.1	-

Table 2.8: Summary of thermal test results.

2.6 Conclusions

This chapter presents a novel 3D printing method for fabricating SJDs that offers significant advantages for researchers. This method enables rapid prototyping, complete design freedom, and the creation of ultra-thin devices (down to 4 mm) without requiring mechanical fasteners. The fabricated SJDs achieved high jet exit velocities of up to 106 m/s using a single piezoelectric diaphragm, which is among the highest reported values. The deflection profile of the diaphragm in these devices closely resembles a pinned disc boundary condition, which enables high deflection rate. 3D-printed SJDs demonstrated reliable operation even at high voltage levels over several months of testing under various heated and installation conditions. The primary failure mode observed was cracking of the piezoceramic patch in piezoelectric diaphragms when the central deflection exceeded 400 micrometers (in 44 mm shim diameter).

LEM proved to be a reliable approach for characterizing SJDs with orifices located on the axis of rotation. This study demonstrates that tuning the LEM based solely on diaphragm deflection behavior is sufficient to predict the fluidic behavior of manufactured SJDs with reasonable accuracy. However, a slight underestimation of jet exit velocity was observed at Helmholtz resonance frequencies, likely due to the model or measurements not fully capturing wall behavior at these frequencies or neglecting other acoustic/vibration effects. Despite this limitation, LEM with deflection-based tuning remains a valuable tool for researchers designing SJDs, particularly when hotwire anemometry measurements are not feasible.

This research also highlights the importance of hydrodynamic impulse over jet exit velocity alone when optimizing SJDs for heat removal applications. Devices with lower jet exit velocities but higher impulse achieved superior heat transfer through synthetic jet impingement. This finding suggests that a focus on impulse generation, which incorporates both velocity and mass flow rate, provides a more comprehensive parameter for optimizing SJD heat transfer performance.

Finally, the study confirms previous observations regarding the existence of an optimal spacing between the SJD and the target surface for maximizing heat transfer. Orifice distance to heated plated ratio to orifice diameter of 8 or above is recommended. In this distance and above SJDs achieved a significant (over 13 times) enhancement in heat transfer compared to natural convection, using only a fraction of the mass flow rate typically required by conventional cooling methods (less than 1.0 m^3/hr). Additionally, the average heat transfer coefficients achieved by these devices rival those of high-speed axial and centrifugal fans.

Chapter 3

Proof of Concept Liquid Synthetic Jet Impingement for High Flux Electronics Cooling

This chapter presents an approach to high-efficiency, low-energy liquid cooling using liquid synthetic jet devices. These devices generate dynamic pressure exactly where needed, addressing the inefficiencies of conventional liquid cooling systems. Powered by piezoelectric actuators, localized, high-velocity jet impingement is achieved with minimal power consumption as low as 50 mW. With working fluid as deionized water, liquid synthetic jet impingement showed a heat transfer coefficient of up to 1.52 W/(cm^2·K). Compared to existing methods, superior heat removal per unit of consumed power is achieved. This work presents an advancement in sustainable thermal management, with broad potential applications, including immersion cooling in data centers. Results of this chapter have been published in [249].

3.1 Introduction

About six years ago, the article "How to Stop Data Centres from Gobbling Up the World's Electricity" was published [23]. Initial projections predicted a dramatic increase in data center energy consumption. While energy consumption has increased, it has not increased at the rate expected due to the widespread adoption of hyperscale centers with efficient cooling technologies. Still, energy problems in data centers remain dynamic, with a sharp turn towards liquid cooling adaptation. Although transistor miniaturization results in more efficient and faster logic switches, increased congestion, and an AI-driven necessity for parallel computing lead to higher heat flux cooling that renders traditional air cooling impractical. This necessitates a shift to liquid cooling solutions, a critical turning point in the data center landscape as discussed more in details in first Chapter.

From a heat transfer perspective, future data centers can be seen as rooms filled with racks containing hundreds of high-flux heat generation zones, with total heat loads reaching ¿ 100 kW per rack. To circulate coolant into this thermal maze, CDUs use pumps, which significantly impact the PUE of data centers. Rotary pumps, which account for about 20% of energy consumption in motor-driven devices [250], have power efficiencies ranging from 42% to 83% for large pumps, and often less than 30% for smaller ones [250]. This efficiency is further reduced by frictional losses in complex networks of couplings, piping, manifolds, cold plates or nozzles, and heat exchangers in the CDU. In other words, dynamic pressure is generated upstream and directed with frictional losses toward target surfaces. Here, we introduce liquid synthetic jet devices (LSJDs) that generate dynamic pressure precisely where and when it is needed.

As discussed in the second Chapter, an SJ is a rapid and periodic discharge of pressurized fluid from a cavity through an orifice. Pressure variation is provided via an oscillating diaphragm. The generated jet is accompanied by a vortex ring formed during discharge. To meet the criterion for SJ formation, a specific ejection velocity is required. Thus, sufficient diaphragm displacement and displacement frequency are necessary, for which a piezoelectric-based actuator is a popular choice. Moreover, SJD should be placed at an appropriate distance from the heated surface, ideally in an impinging configuration, to agitate the thermal boundary layer to augment heat transfer.

In 2002, one of the earliest attempts to utilize LSJDs focused on enhancing natural convection and pool boiling heat transfer within an FC-72 enclosure [251]. For the device to produce SJ, the cavity was open to atmospheric pressure through a pipe. Limited details were provided on the actuator's properties. Such a piping system would potentially reduce cavity pressure and enable easier operation of the diaphragm in liquid; thus resonance was achieved at 275-300 Hz. Produced submerged SJs toward a flat foil heater, improved convection by four times compared to unassisted natural convection. Subsequent efforts on LSJDs primarily shifted toward underwater steering and propulsion for small-scale underwater vehicles [252, 253]. These designs focused on generating sufficient momentum for maneuvering, relying on relatively large, piston-cylinder motion powered by motors [222] or solenoids [223]. Due to the inertia of these

actuators, their operation was limited to lower frequencies while the armature's movement had enough strength to overcome fluidic oscillation within the cavity, allowing for larger displacement, jet strokes, and liquid synthetic jet (LSJ) generation across various operating frequencies.

To achieve a thinner design, low-inertia actuators based on voice-coil-driven or piezoelectric diaphragms have been explored. However, these actuators face challenges in achieving displacement in higher cavity pressure variations, which require them to operate at resonance. Compact designs using moving coil transducers have been developed [224], though these remain bulky, with conventional submerged pumps offering better yields at comparable sizes.

Using piezoelectric diaphragms can lead to ultra-thin SJ designs, as evidenced by their use in commercial ASJDs [233]. Recently, Kang et al. [254] presented a piezoelectric-based LSJD designed to improve heat transfer in microchannels. While their setup achieved a heat transfer coefficient of 0.57 W/(cm^2·K), it required a relatively high operating voltage of 240 V—likely a consequence of adapting ASJD manufacturing methods to function with liquid. Specifically, their approach involved clamping a piezoelectric diaphragm with metallic plates by bolts, producing a clamped boundary condition that, based on our insight, typically results in reduced deflection output. For additional information on past and present SJD manufacturing approaches, refer to second Chapter.

This chapter introduces the application of LSJ impingement to enhance single-phase immersion cooling. Utilizing an adhesive-based manufacturing approach, a thinner device design was achieved, enabling greater diaphragm deflection at lower applied voltage levels. This advancement represents a significant improvement over traditional clamping methods, providing an efficient cooling solution with reduced power consumption. We investigated LSJDs under various conditions, including different drive frequencies, applied voltages, and distances from a localized heat source. Our findings underscore the potential of LSJDs as a transformative approach to single-phase immersion cooling. With their low-power, high-efficiency performance, LSJDs offer a promising solution for reducing the environmental impact of data centers, leading to more sustainable and cost-effective thermal management strategies. The 4 mm-thick LSJDs manufactured for this study operated with minimal power (0.045 - 0.17 W), produced jet velocities exceeding 1 m/s, and achieved an impressive heat transfer coefficient of up to 1.52

W/(cm^2·K) with DI water, marking one of the highest heat removal rates per unit of electrical power reported to date

3.2 Concept, Development of Model, and Manufacturing of Liquid Synthetic Jet Device

3.2.1 Theory and Fundamentals

Figure 3.1(a) depicts LSJD for on-demand cooling. The LSJD is composed of a body producing a cavity that is open to a free stream of coolant on one side and equipped with an electromechanical diaphragm on the other. The diaphragm is made up of a thin metallic shim bonded to a piezo-ceramic element. Subject to sine DC voltage, the piezoelectric material experiences strain due to the indirect piezoelectric effect. This strain generates a bending moment in the diaphragm, resulting in cyclic deflection. The deflection induces high-frequency changes in the cavity volume, resulting in pressure variations that lead to fluid ejection and suction through the orifice. During the outflow phase, a fluid jet (or puff) is generated, accompanied by the formation of a vortex ring around it. Under certain conditions, the jet and vortex ring move downstream due to their velocity, extending into the distant field as the outflow weakens and transitions into the inflow phase. During inflow, the cavity draws fluid from the vicinity of the shed vortex ring, creating a stable downstream flow field. The vortex surrounding the jet allows it to travel uninterrupted toward the heated surface, even in the presence of normal crossflow. The impingement of this quasi-steady jet significantly disrupts the boundary layer, enhancing heat transfer. The locally heated fluid is then displaced away from the cavity region and replaced by cold crossflow through a buoyancy-driven or forced flow field. An analytical model can be developed for the proposed LSJD building upon Sharma's [215] fluid-dynamics-based model for ASJDs. This model is presented in Appendix A and also discussed in Chapter 2. First change is to the speed of the sound in Equation A.2 where in liquids we have:

$$U_{sound} = \sqrt{\frac{K}{\rho_\infty}} \tag{3.1}$$

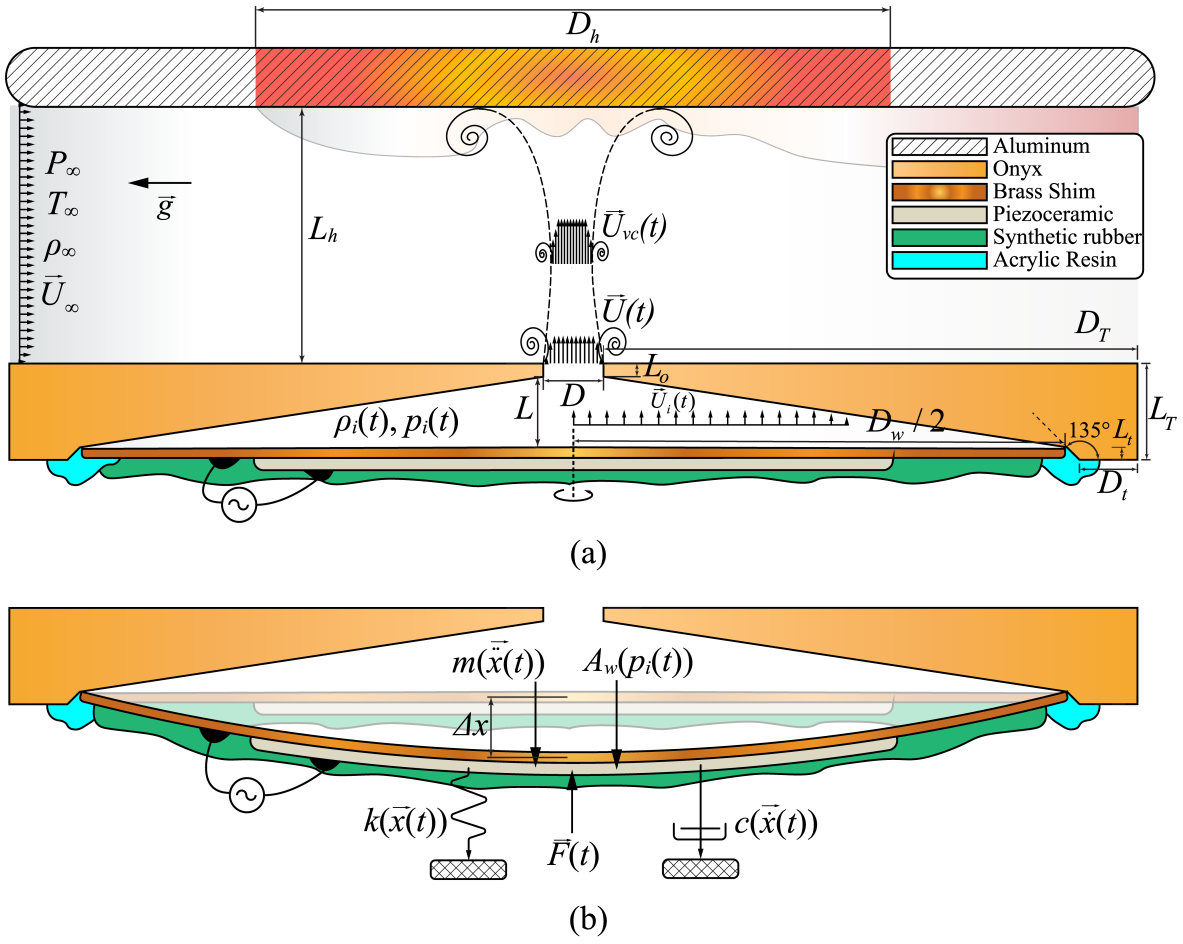

Figure 3.1: (a) Schematic illustration of LSJD for on-demand cooling, and (b) simplified diagram of the diaphragm, depicting its deflection.

where K is bulk modulus (2.2×10^9 Pa for water). Next instead of Assuming isentropic contraction, the equation for the bulk modulus can be used to replace Equation A.7:

$$K = -\rho_\infty \frac{\Delta P}{\Delta \rho} \rightarrow \frac{d\rho_i(t)}{dt} = -\frac{\rho_\infty}{K}\frac{d(p_i(t))}{dt} \tag{3.2}$$

Since, in low-inertia actuation, the Mach number does not fall within the compressibility range, Equation 3.2 can be used. This substitution allows for LEM equations to be closed in liquid case whith more details published in [255]. Now combining Equation A.6 and 3.2 into A.5:

$$-\rho_i A_w \dot{x}_{eq}(t) - \frac{V_0 \rho_\infty}{K}\frac{d(p_i(t))}{dt} = -\rho_\infty A U(t) \rightarrow -A_w \dot{x}_{eq}(t) + \frac{V_0}{K}\frac{d(p_i(t))}{dt} = -AU(t) \tag{3.3}$$

Furthermore combining Equation A.14 with Equation 3.3 we can obtain the modified A.15 as:

$$\ddot{U} + \frac{1-\beta^4}{L_e C_d^4}|U|\dot{U} + \frac{AK}{V_0 \rho_\infty L_e}U = \frac{A_w K}{V_0 \rho_\infty L_e}\dot{x}_{eq} \tag{3.4a}$$

$$\ddot{U} + \frac{1-\beta^4}{L_e C_d^4}|U|\dot{U} + \omega_h^2 U = \frac{A_w}{A}\omega_h^2 \dot{x}_{eq} \tag{3.4b}$$

as $\omega_h = \sqrt{k_h/m_h} = \sqrt{(K/\rho_\infty)/(V_0 L_e/A)} = U_{sound}\sqrt{A/(V_0 L_e)}$ where ω_h is Helmholtz frequency for a liquid system. Thus, the system of ODEs will be modified as:

$$\begin{cases} \dot{p}_i(t) = \frac{A_w K}{V_0}\dot{x}_{eq}(t) - \frac{AK}{V_0}U(t) \\ \dot{x}_{eq}(t) = \frac{d(x_{eq}(t))}{dt} \\ \ddot{x}_{eq}(t) = \frac{F(t)}{m} - \frac{p_i(t)A_w}{m} - 2\zeta\omega_w \dot{x}_{eq}(t) - \omega_w^2 x_{eq}(t) \\ \dot{U}(t) = \frac{d(U(t))}{dt} \\ \ddot{U}(t) = -\frac{1-\beta^4}{L_e C_d^4}|U(t)|\dot{U}(t) - \omega_h^2 U(t) + \frac{A_w}{A}\omega_h^2 \dot{x}_{eq}(t) \end{cases} \tag{3.5}$$

The provided model offers a compelling insight into the behavior of LSJDs compared to ASJDs. Three notable changes can be expected when moving from air to liquid: (1) A significant increase in m_f, which will substantially reduce the diaphragm's resonance and deflection. Thus,

an increase in voltage is necessary and a reduction in velocity can be expected. (2) The significant increase in the speed of sound will lead to a rise in Helmholtz resonance, making it impossible to drive the diaphragm in Helmholtz mode or achieve mode matching to enhance system output (unless a microscale system is being produced). (3) The reduced velocity output will tighten the frequency bandwidth in which the SJ formation criterion can be met [201, 202].

It is possible to assume particular values needed to solve ODE systems numerically by using experimental data collected in the lab. Table 1 displays these values along with the actuator model that was taken into consideration. This allows for a comparison of how the identical device behaves differently in the water and the air. Sharma's model was solved for air and Equation 3.5 was solved for water. The code for single frequency solution is provided in Appendix D. For frequency sweep refer to Appendix A. Figure 3.2 presents the results,

Device	fr_w (Hz)	$k \times 10^4$(N/m)	F_{max} (N)	C_l	C_d	m_w(gr)	D_w(mm)	Diaphragm Model
LSJD	125	24	4	0.9	0.6	3.2	35	PUI Audio. AB3526B-LW100-R
ASJD	1360	24	4	0.9	0.6	3.2	35	PUI Audio. AB3526B-LW100-R

Table 3.1: Characteristics for LSJD and AJSD.

with diaphragm displacement shown in Figure 3.2(a) and maximum area averaged ejection velocity in Figure 3.2(b). Moving from air to water, the wall resonance frequency decreased from 1360 Hz to 125 Hz. Similarly, the deflection at resonance dropped by more than 50%. In terms of velocity behavior, in air, the Helmholtz effect is noticeable around the 3000 Hz range. For water, the maximum U occurs at 160 Hz. The device provides jets in limited frequency bandwidth. Helmholtz resonance is not observed in the shown frequency range.

3.2.2 Manufacturing and Experimental Study

Several LSJD was manufactured in the lab, with a detailed process description in Chapter 2. In short, The Markforged X7 industrial carbon fiber 3D printer was used to print the body of the LSJD. The piezoelectric bender disc is then placed on a 45° edge of the 3D printed body, secured with a temporary clamp, and then attached to the 3D printed structure with acrylic

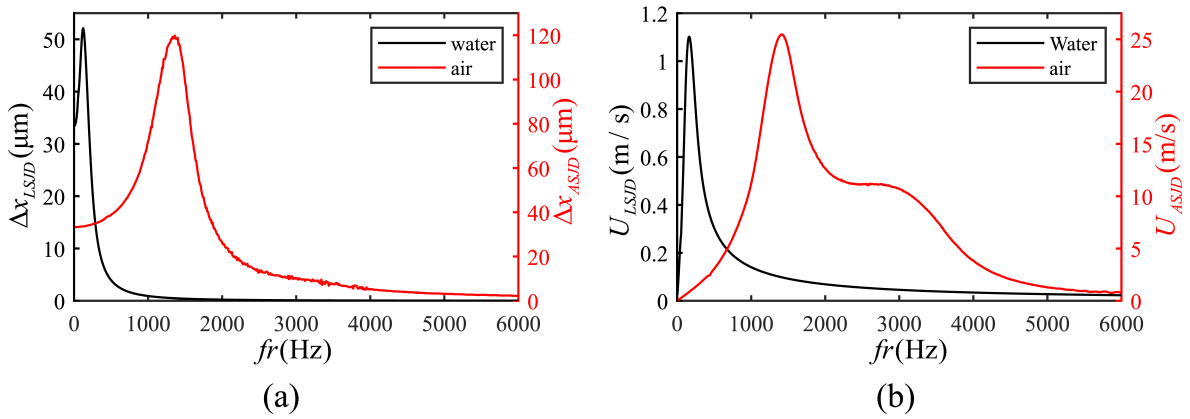

Figure 3.2: Comparison of analytical solutions showing (a) central deflection and (b) maximum ejection velocity for LSJD (left axis) and ASJD (right axis).

adhesive. Piezoceramic is changed to PUI Audio. AB3526B-LW100-R with 35 mm diameter and nominal resonance in air of 2600 Hz. This buzzer has a thicker ceramic thickness of 0.28 mm. An additional step was taken to insulate the high voltage on the piezoceramic from the liquid by covering the piezoceramic and shim with a layer of air-dried synthetic rubber. This ensured no current leakage and made the device safe to operate even in conductive liquids. The diaphragm is driven at peak-to-peak voltages of 120, 140, 160, and 180 V. Due to the significant damping effect of the liquid, these applied voltages ensured the device's safe operation, as the ceramic deflection remained within acceptable limits. Cavity was designed as conical, reducing the fluid volume inside and thus the acoustic mass. This design also enhances fluid guidance for vortex generation and coherent ejection. Parameters defining the geometry of the LSJD are presented in Table 3.3. LSJD was controlled using a custom LabView program. The Siglent

D (mm)	D_w (mm)	D_T (mm)	D_t (mm)	L_{eq} (mm)	L_o (mm)	L_t (mm)	L_T (mm)	V_0 (mm^3)
5	35	18.1	2.5	3	0.5	0.5	4	942

Table 3.2: Axisymmetric cut plane view of manufactured SJDs with a conical cavity.

SDG 2042X function generator generated sine signals which were amplified by a Trek PZD700 High Voltage Amplifier to a peak-to-peak voltage of 120, 140, 160, and 180 V. The voltage and current through the LSJD were measured by connecting the Trek PZD700 analog input to the digital voltage converter NI–9205. Measurements were done at 4kHz for 250 ms during

experiments. 1/200 voltage monitor and 0.1 V/mA voltage output were used to evaluate the current and voltage characteristics of LSJDs. The power consumption rate (P_{in}) calculation was done by integrating the absolute value of the product of voltage and current over a second of operation.

To understand the effectiveness of LSJ impingement and its ability to target localized heat generation zones a thermos-fluidic controlled liquid cooling tank with a specialized heater/measurement unit was built. The configuration of the tank can be seen on Figure 3.3. The tank's

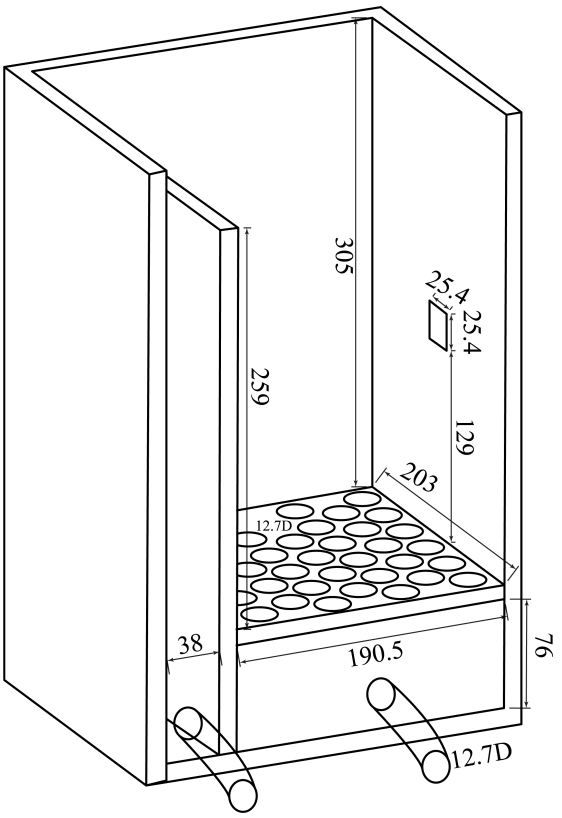

Figure 3.3: Geometric details of the liquid cooling tank test system.

bottom section of 190.5 × 203 mm^2 receives DI water from a half-inch flexible piping and was regulated by 97 half-inch circular outlets. The tank itself is made of waterjet cut half-inch acrylic sheets. Coolant (DI water) travels up to the 259 mm wall and then returns to the circulation system. A half-inch by half-inch heated aluminum surface was positioned 129 mm away from the diffuser plate. The studied flow rates to the tank were 0.5, 1, and 1.5 GPM. This will lead to flow velocities of 0.8, 1.6, and 2.4 mm/s. These values can be considered in the range of immersion cooling tests. Shinde et al. [256] performed an immersion cooling test using

technical grade white mineral oil at inlet oil temperature ranging from 25°– 45°C with volumetric flow rates used for the testing were 0.5 GPM and 1 GPM. M. Muneeshwaran et al. [257] studied single-phase immersion cooling of FC-40 dielectric liquid at flow rate of 1 – 3 lpm with the inlet fluid temperature of 15 – 35 °C. Chhetri et al. [258] showed that the velocity of flow over densely packed immersion cooling servers using dielectric fluid for a volume flow rate of 0.5 lpm is 0.001045 m/s and for a volume flow rate of 2.5 lpm is 0.005223 m/s. To provide a

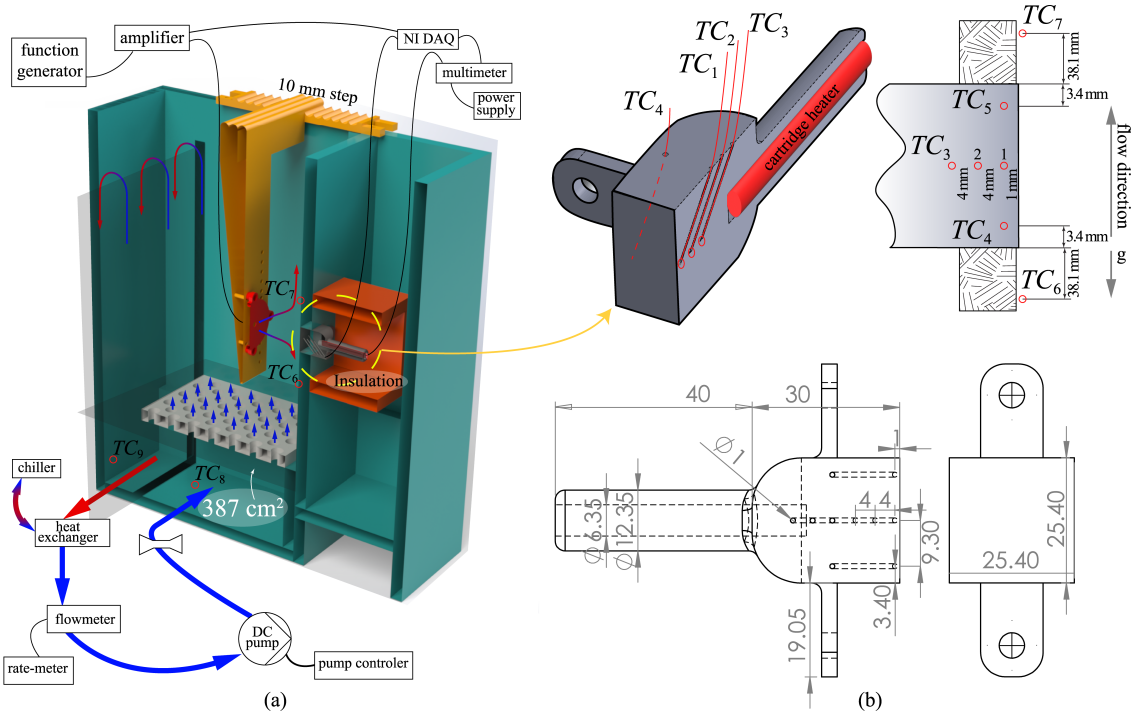

Figure 3.4: (a) Schematic illustration of immersion cooling setup; (b) detailed information on heated block and thermocouple placement.

heated surface inside the immersion cooling tank, a custom aluminum block was machined and polished to provide a heated surface and to hold the cartridge heater and thermocouples. Figure 3.4(b) depicts the block's arrangement. The block was CNC cut and fastened with two bolts to the design area inside the tank. Five T-type thermocouples (Omega 5TC-TT-T-30-36-ROHS) were positioned inside the block, with TC1, TC5, and TC4 near the 1 mm surface and TC2, and TC3 4 mm behind TC1. Omega's cartridge heater (CIR 1020) was used with a power rating of 150 W and a quarter-inch diameter. The heater was powered by an Amrel SPS300-10-K0E1 power supply.

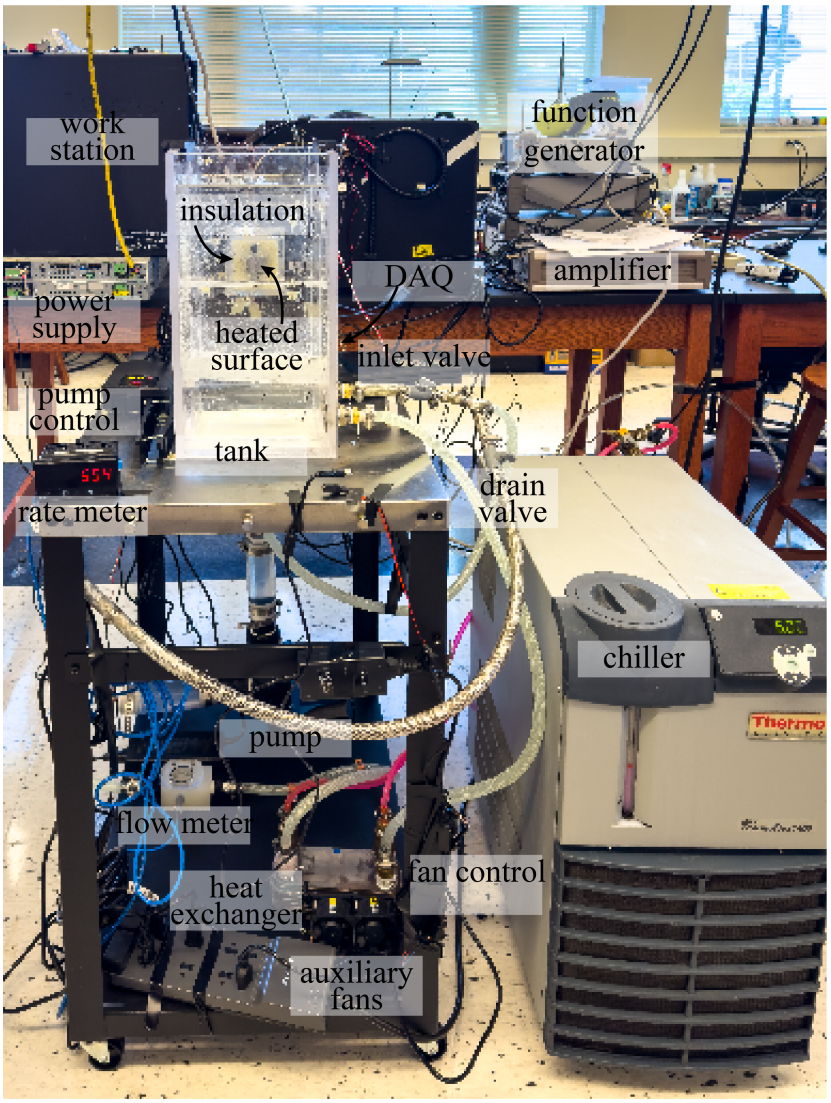

Figure 3.5: Overview of the experimental setup in the laboratory environment.

The heater assembly was insulated with quick-cure foam. Figure 3.4(a) shows a half-inch acrylic enclosure molded with cured polyurethane foam sealant measuring 75 × 75 mm^2. Two TCs, TC7 and TC8, were also located at the 38 mm top and bottom of the heater, as shown in Figure 3.4(b). TC8 was at the inlet, while TC9 was at the outlet. TC10 was used to measure the outside temperature of the insulation foam, as shown in Figure 3.6. TCs were monitored every 6 seconds with the LabVIEW program via the NI data acquisition (DAQ) system. Flow inside the system was provided by an off-the-shelf DC 36 V pump with a variable frequency controller. The flow rate was measured prior to pump entry using an Omega FPR302 flow rate meter with a calibration K factor of 634.3 PPG. The pulse rate was measured and converted using the Omega DPF20-HV rate meter. The inlet temperature was controlled by a ThermoFlex1400 chiller and a flat plate heat exchanger (GEA Heat Exchangers model FP3X8-14). To improve the heat exchange at room temperature, two auxiliary fans were installed in front of the heat exchanger. Details of utilized equipment can be seen in Table 3.3. In Table 3.3, T_f is based

Variable	Temperature dependent (T_f(K)) correlation
μ (Pa.s)	$1.3800 - 0.021224(T_f) + 0.00013605(T_f^2) - 0.0000004645(T_f^3)$ $+8.904 \times 10^{-10}(T_f^4) - 9.079 \times 10^{-13}(T_f^5) + 3.846 \times 10^{-16}(T_f^6)$
c_p (J/kg-K)	$12010 - 80.41(T_f) + 0.3099(T_f^2) - 0.0005382(T_f^3) + 0.000003625(T_f^4)$
ρ (kg/m^3)	$-950.7 + 18.92(T_f) - 0.06037(T_f^2) + 0.0006309(T_f^3)$
k_{th} (W/m-K)	$-0.8691 + 0.008949(T_f) - 0.00001584(T_f^2) + 0.00000007974(T_f^3)$
β (1/K)	$-6.43 \times 10^{-5} + 1.7 \times 10^{-5}(T_f - 273.15) - 2.02 \times 10^{-7}(T_f - 273.15)^2$

Table 3.3: Correlation used to obtain thermophysical properties of DI water [259, 260]

on the average temperature of the surface (T_s) and downstream temperature measured by TC6 (see Figure 3.4(b)):

$$T_f = (T_s + TC_6)/2 \tag{3.6}$$

Referring to Fourier's law, three equally spaced consecutive thermocouples near the surface (TC1, TC2, and TC3) can be used to evaluate heat flux normal to the surface and obtain T_s. The Taylor series expansion was used to calculate the second-order accurate slope:

$$T_s \approx \frac{-TC_1 + 4TC_2 - 3TC_3}{2}\frac{(1\text{ mm})}{(4\text{ mm})} + TC_1 \tag{3.7}$$

Considering the thermal conductivity of aluminum (237 W/(m·K)), the heat flux by conduction can be evaluated as:

$$q''_{cond} \approx 237\,(\text{W/m-K})\frac{-TC_1 + 4TC_2 - 3TC_3}{2(0.004\,\text{m})} \tag{3.8}$$

Due to the small surface area of the heater, surface temperature of the heater remained constant during experiments and one can use natural convection correlation for the heated surface in the vertical direction at constant surface temperature using [261]:

$$\text{Nu}_{NatConv} = \left\{ 0.825 + \frac{0.387\text{Ra}^{1/6}}{\left[1 + \left(\frac{0.492}{\text{Pr}}\right)^{9/16}\right]^{8/27}} \right\}^2 \tag{3.9}$$

Where $\text{Ra} = \text{Gr} \cdot \text{Pr} = \frac{g\beta(T_s - T_m)D_h^3}{\nu^2} \cdot \text{Pr}$, g is gravitational acceleration, T_{in} is temperature from TC8, D_h is 25.4 mm, and ν is kinematic viscosity at film temperature (see Table 3.3). By evaluating the Richardson number, Ri, its value is in the fully natural convection range and Equation 3.8 can be accepted.

The calibration experiment took 3 hours to perform. The chiller's temperature was set to 6 °C, and the heater's power was at 15.34 W. This led to an inlet temperature of 10.5 °C, with the heater temperature reaching a steady state, equal to room temperature, as seen in Figure 3.6. Heat transfer characteristics of the heater during the calibration phase can be evaluated independently using Equations 3.8 and 3.9. This way, one can decide whether these assumptions and heat flux calculations based on Equation 3.8 provide a good estimate of normal heat flux toward coolant, even though heat loss will occur towards the acrylic sheet tightly holding the heater. The results of the calibration phase shown in Fig. 8 indicate a maximum of 7% differ-

Flow rate (GPM)	Re	Gr	Ri
0.5	18.6	432326	1242
1	37.24	424716	306
1.5	55.36	393602	128

Table 3.4: Ri number evaluation in different volume flow rates.

ence in calculation based on Equation 3.8, and Equation 3.9 to evaluate normal heat flux from

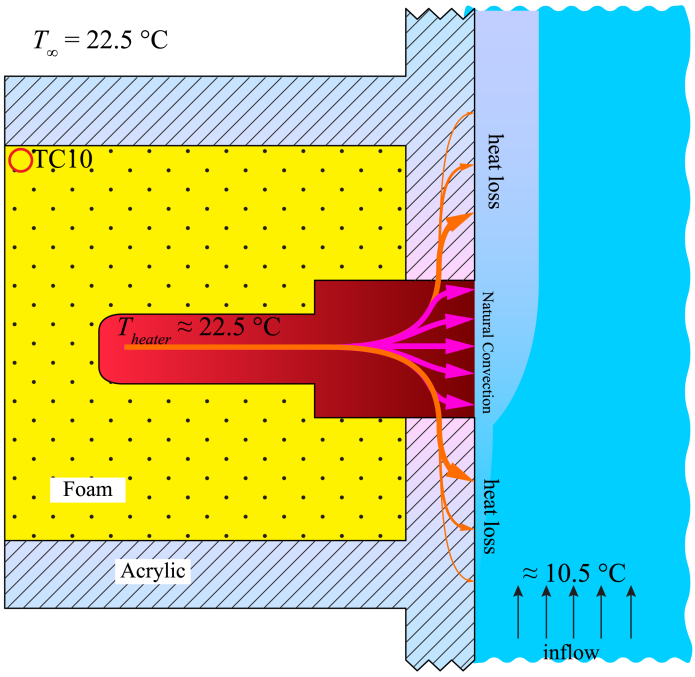

Figure 3.6: Illustration of the calibration phase

the heater to the liquid. Heat flux at the calibration phase based on Equation 3.8 shown with the green linear fit (q''_{cond}) and based on Equation 3.9 shown with the red linear fit ($q''_{NatConv}$). The linear fit in Figure 3.7 and later results are based on robust fitting. Outliers of recorded ex-

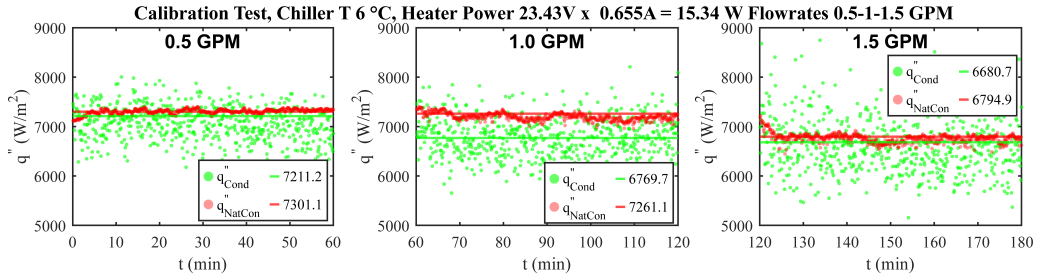

Figure 3.7: Evaluated heat flux at calibration phase based on Equation 3.8 shown with green linear fit and based on Equation 3.9 shown with red linear fit.

perimental values (due to (1) sensor noise, (2) results before reaching a steady state prior to the earlier steady state condition, (3) environmental disturbances, or (4) user errors) were mitigated by using this fitting. Standard linear regression methods, such as ordinary least squares, can be overly sensitive to such outliers, producing biased results that do not accurately reflect the

underlying trend. This regression fitting was done with MATLAB's robustfit function. More results of calibration process can be found in Appendix E.

3.2.3 Particle Image Velocimetry

The MODULE4G-2DPIV particle image velocimetry (PIV) system from TSI measures the instantaneous global velocity field in a flowing fluid. PIV tests are performed at 155 Hz, with a 160 V. The CCD camera is set to f/8 and 50% zoom. 14-micron seed particles of Gls-Hlw-Ag were used. The impinging distance is set, yielding $L_h/D = 10.9$. The PIV frame mode is straddle, which means that two single-exposure images will be captured and compared. Laser pulse repetition rate (the difference between laser pulse sequences is set to 1.81 Hz). The laser pulse delay time is set to 397.5 μs. This determines the amount of time to wait between the start of the pulse sequence and the first laser pulse. The pulse separation is determined to match the flow velocity (with less than 16-pixel displacement for each acquisition). It is set to 100 – 200 μs, depending on vector analysis results. The first frame of the camera is open for 405 μs, known as PIV exposure. The laser power is set to 240. The captured images are framed into 2814 by 1976-pixel frames and calibrated using the measured size of the LSJD within the image. The INSIGHT software processed images.

3.2.4 Design of Experiments

Before conducting performance evaluations of the LSJD and sweeping various parameters, the heater was set to 49.6 W, and the immersion cooling system was established with a flow rate of 0.5 GPM and an inlet temperature of 22.5°C. Surface temperatures were monitored to confirm that steady-state conditions had been reached prior to activating the LSJD. Once the LSJD was powered, parametric adjustments were made, including variations in the distance to the heated surface, operating frequency, applied voltage, and immersion cooling flow rate. Each parameter adjustment was assessed over a 15-minute interval. Typically, steady-state operation was achieved within the first 2-3 minutes of each cycle. Nusselt number and heat transfer

coefficients were obtained based on Equation 3.8. Thermal resistance was obtained based on:

$$R = \frac{q'' A_h}{T_s - T_{in}} \tag{3.10}$$

3.3 Results

3.3.1 Frequency Sweep

Figure 3.8(a), (b), (c), and (d) shows the surface temperature of the heated surface, Nu, heat transfer coefficient, and thermal resistance for a 3-hour continuous test period, respectively. The LSJD was not effective at 95 Hz, resulting in a surface temperature (T_s) of 45.3°C, a heat transfer coefficient (h) of 0.14 W/(cm^2·K), a Nu number of 59.8, and a thermal resistance (R) of 0.45 K/W. An improvement in heat removal was observed between 105 Hz and 125 Hz, with a more enhancement at 135 Hz. The performance peaked between 145 Hz and 165 Hz, before dropping again between 185 Hz and 195 Hz, and showing almost no improvement at 205 H. The optimal performance was achieved at 165 Hz, where the Nu number reached 605.6, the surface temperature dropped to 27.1°C, the heat transfer coefficient increased to 1.52 W/(cm$\hat{2}$·K), and the thermal resistance decreased to 0.08 K/W. The overall trend of performance improvement with varying frequencies is summarized in Figure 3.9.

3.3.2 Distance to Heater Effect

In the second set of tests, the LSJD was positioned at various dimensionless height-to-diameter ratios (L_h/D) ranging from 2 (10 mm) to 24 (120 mm) with a flow rate of 0.5 GPM in an immersion cooling tank. The inlet flow temperature was maintained at 22.5°C, with the heater power set to 49.6 W. The LSJD operated at 160 Vpp at the frequency of 155 Hz. After the heater reached a steady-state condition, the L_h/D ratio was incrementally increased from 2 to 24 in steps of 2. The results of these tests are presented in Figure 3.10.

Similar to Figure 3.9, Figure 3.11 presents the performance behavior of LSJDs. The LSJD was immediately effective, reducing the surface temperature from 45.1°C to 27.6°C within minutes. At steady state, Nu number reached 646.3, h was 1.53 W/(cm^2·K), and was 0.1 K/W.

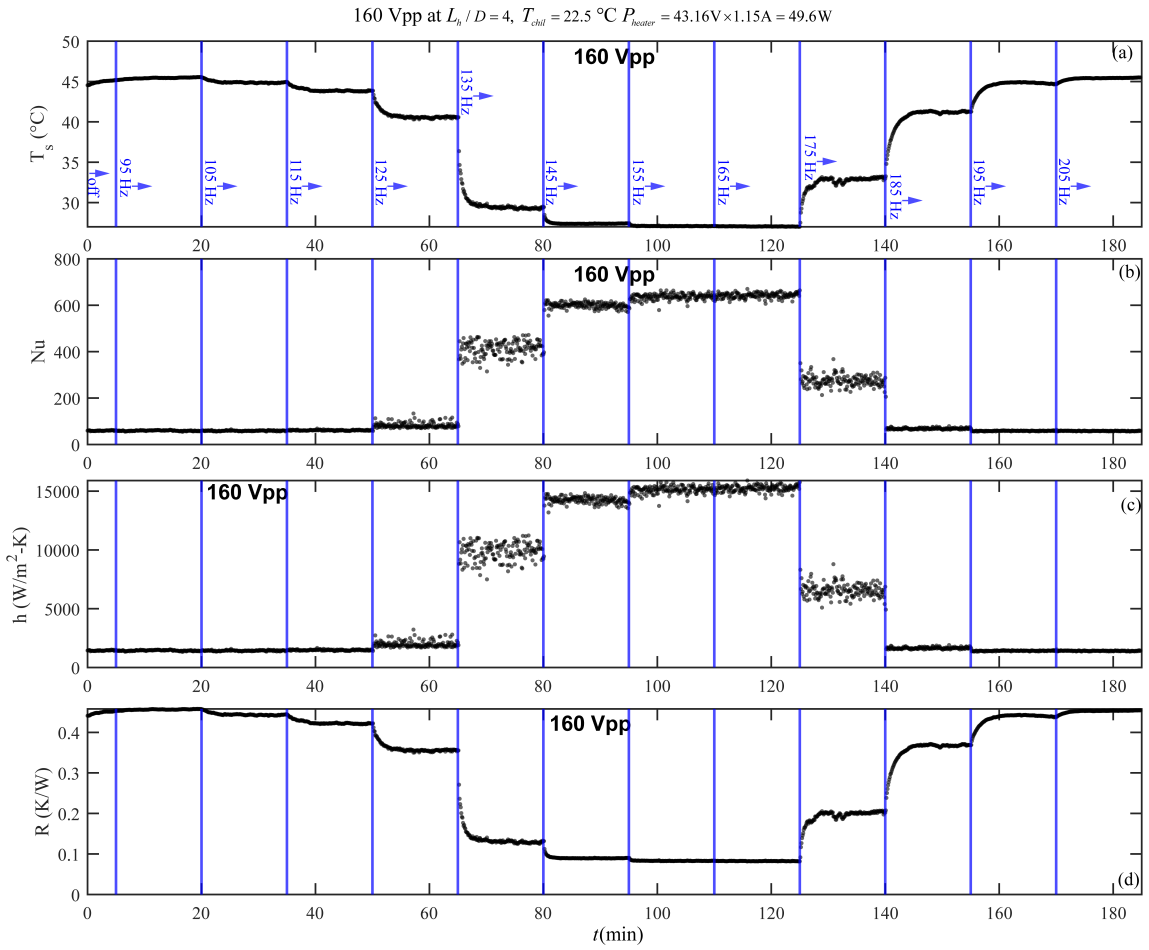

Figure 3.8: Three-hour measurement results for the frequency sweep at a flow rate of 0.5 GPM, an inlet temperature of 22.5°C, a heater power of 49.6 W, an operating voltage of 160 V, and an L_h/D ratio of 4.

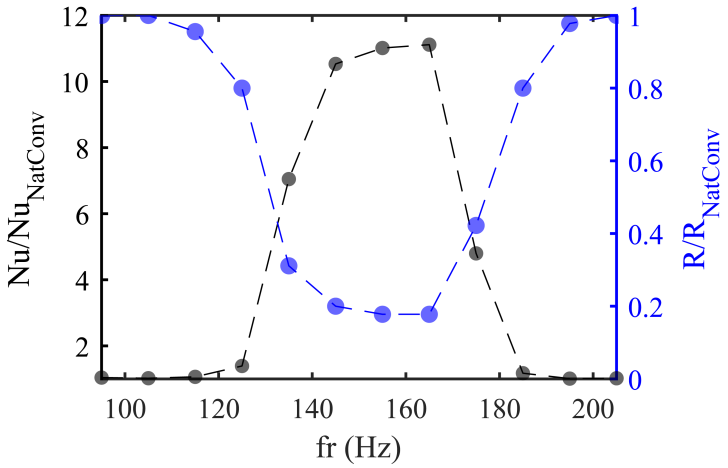

Figure 3.9: The overall trend of performance improvement over natural convection with varying frequencies at a flow rate of 0.5 GPM, an inlet temperature of 22.5°C, a heater power of 49.6 W, an operating voltage of 160 V, and an L_h/D ratio of 4.

These values further improved to 26.9°C, 648, 1.54 W/(cm^2·K), and 0.08 K/W, respectively, at an L_h/D ratio of 4. Beyond this point, the jet strength decreased; however, it remained effective up to an L_h/D of 24, with a surface temperature of 31.6°C, a Nu of 205, a heat transfer coefficient of 0.49 W/(cm^2·K), and a thermal resistance of 0.18 K/W. The overall trend of performance improvement with varying distances is illustrated in Figure 3.11. Further thermal analysis can be found in Appendix F.

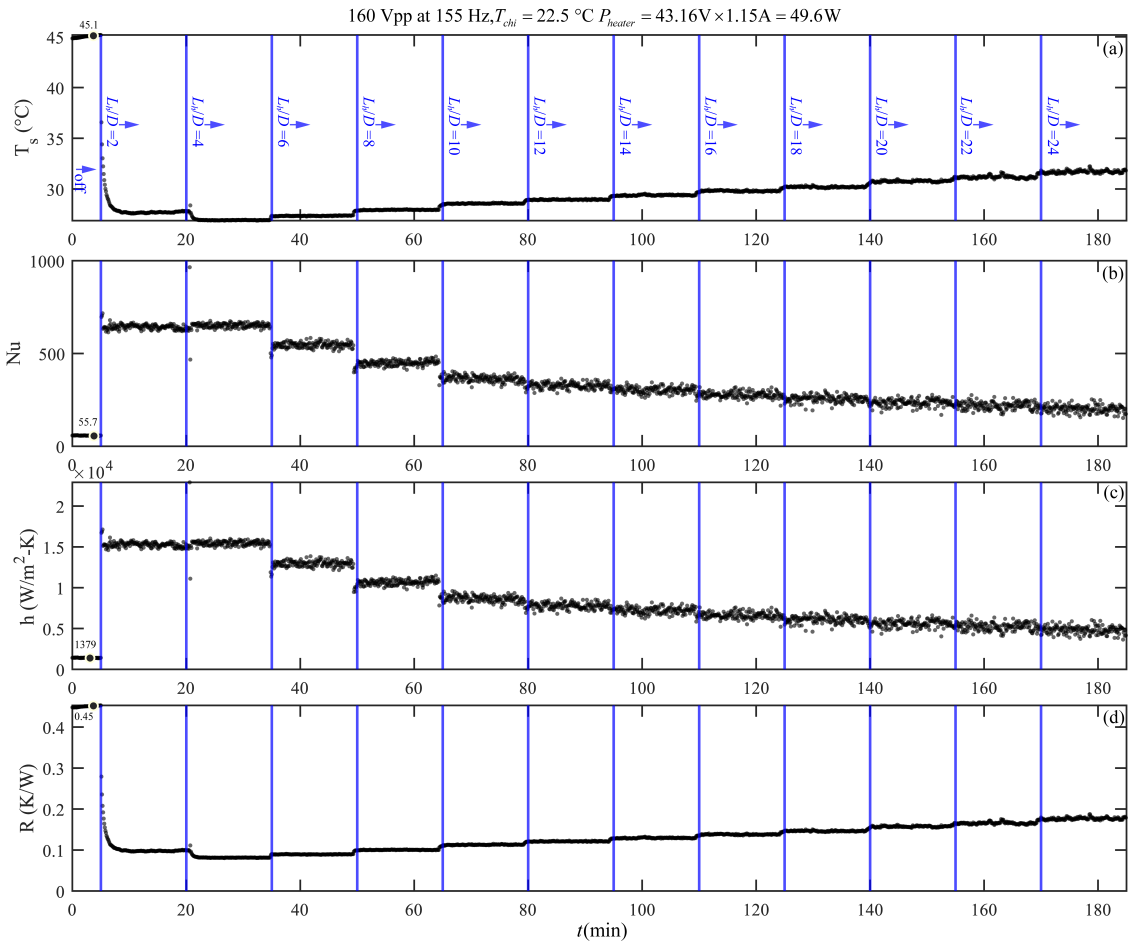

Figure 3.10: Three-hour measurement results for the distance sweep at a flow rate of 0.5 GPM, an inlet temperature of 22.5°C, a heater power of 49.6 W, an operating voltage of 160 at 155 Hz.

3.3.3 Power Consumption Study

The trendline of power consumption for the LSJD at different peak-to-peak voltages across various frequencies is shown in Figure 3.12. The power consumption of the diaphragm is primarily related to its capacitance, the square of the applied voltage, and the operating frequency.

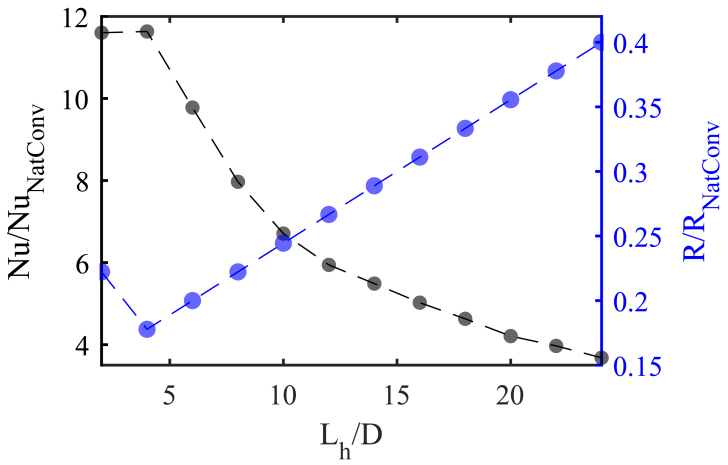

Figure 3.11: Overall trend of performance improvement over natural convection with varying distance to heater at a flow rate of 0.5 GPM, an inlet temperature of 22.5°C, a heater power of 49.6 W, an operating voltage of 160 V, at 155 Hz.

A typical increase in power consumption by an increase in applied voltage and frequency can be seen. At 95 Hz, the power consumption values are 0.045 W, 0.063 W, 0.086 W, and 0.111 W for voltage levels of 120, 140, 160, and 180 Vp, respectively. As the frequency increases to 155 Hz, these values rise to 0.065 W, 0.089 W, 0.120 W, and 0.155 W, respectively. At 165 Hz, the power consumption further increases to 0.065 W, 0.09 W, 0.121 W, and 0.160 W for the same voltage levels. The trend shows a gradual decrease and then an increase in power consumption, reaching a maximum of 0.170 W at 215 Hz at 180 V. An increase in power consumption at resonance is due to larger diaphragm deflection, which induces internal strain and modifies the piezoelectric material's dielectric properties through strain-dependent permittivity. Additionally, this deflection can slightly alter the effective electrode separation and overlap area, impacting capacitance. Although this effect is usually minimal, it can become significant with large deflections due to mechanical deformation.

3.3.4 Effect of cross-flow from immersion cooling tanks

The flow rate from the immersion cooling tank did not affect the performance of the LSJD. Extensive studies were conducted at different applied voltage levels, various distances from the heater, and three immersion cooling flow rates. Sample results are presented in Figure 3.13, which shows the heat transfer coefficient achieved at a distance ratio of 10, at a frequency

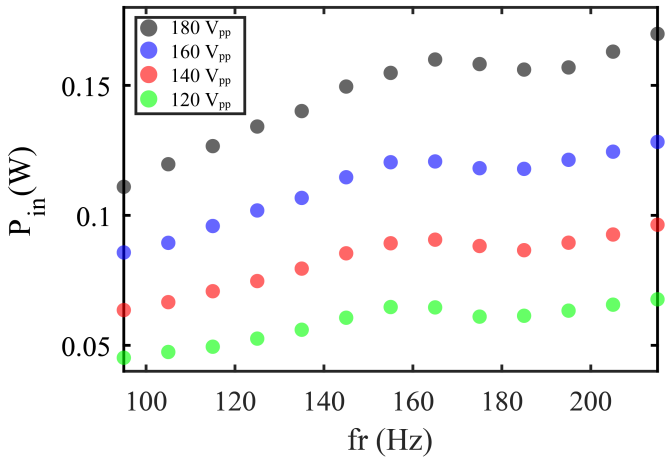

Figure 3.12: Power consumption efficiency of LSJD.

of 155 Hz, and different applied voltage levels. It can be observed that the results follow similar trendlines, even though the LSJD was positioned a long distance from the surface. Despite this distance, the LSJs were able to reach the surface with an effective impact upon impingement. This aligns with previous numerical studies, which demonstrated that vortical structures generated by synthetic jets can penetrate more effectively into crossflow compared to continuous jets [192].

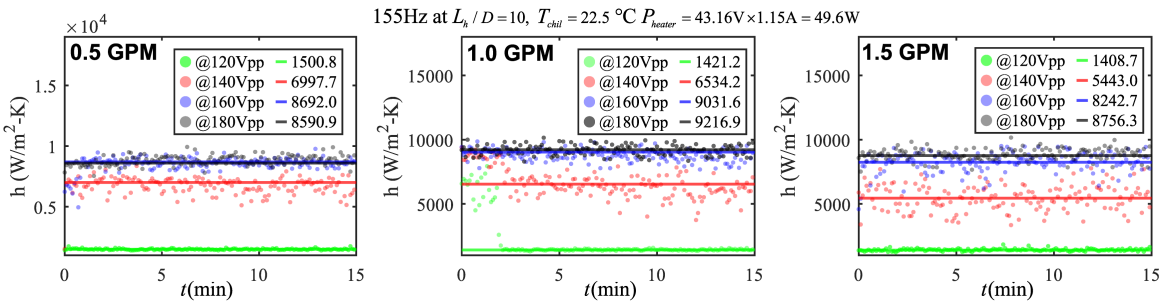

Figure 3.13: Heat transfer coefficient measurement for immersion flow rate sweep at a flow rate of 0.5 to 1.5 GPM, an inlet temperature of 22.5°C, a heater power of 49.6 W, an operating voltage of 120 to 180 V at 155 Hz.

3.3.5 PIV Results

Figure 3.14 displays the results of the PIV analysis. LSJD was positioned on the right side of the frame, with the impinging wall located on the left. The device was operated at 155 Hz and 160 Vpp. The orifice was positioned 57 mm from the wall; however, the vector calculations exclude

the area near the orifice due to high oscillatory behavior of the liquid. The maximum flow velocity upstream of the orifice is observed at an ratio of 4, which aligns with the maximized performance noted in the heat transfer study. The approximate jet spreading behavior is also evident, allowing us to estimate the jet exit velocity to be between 0.8 and 1.2 m/s. Additionally, the stagnation point upon impingement is visible, accompanied by vortex sweeping in some of the figures.

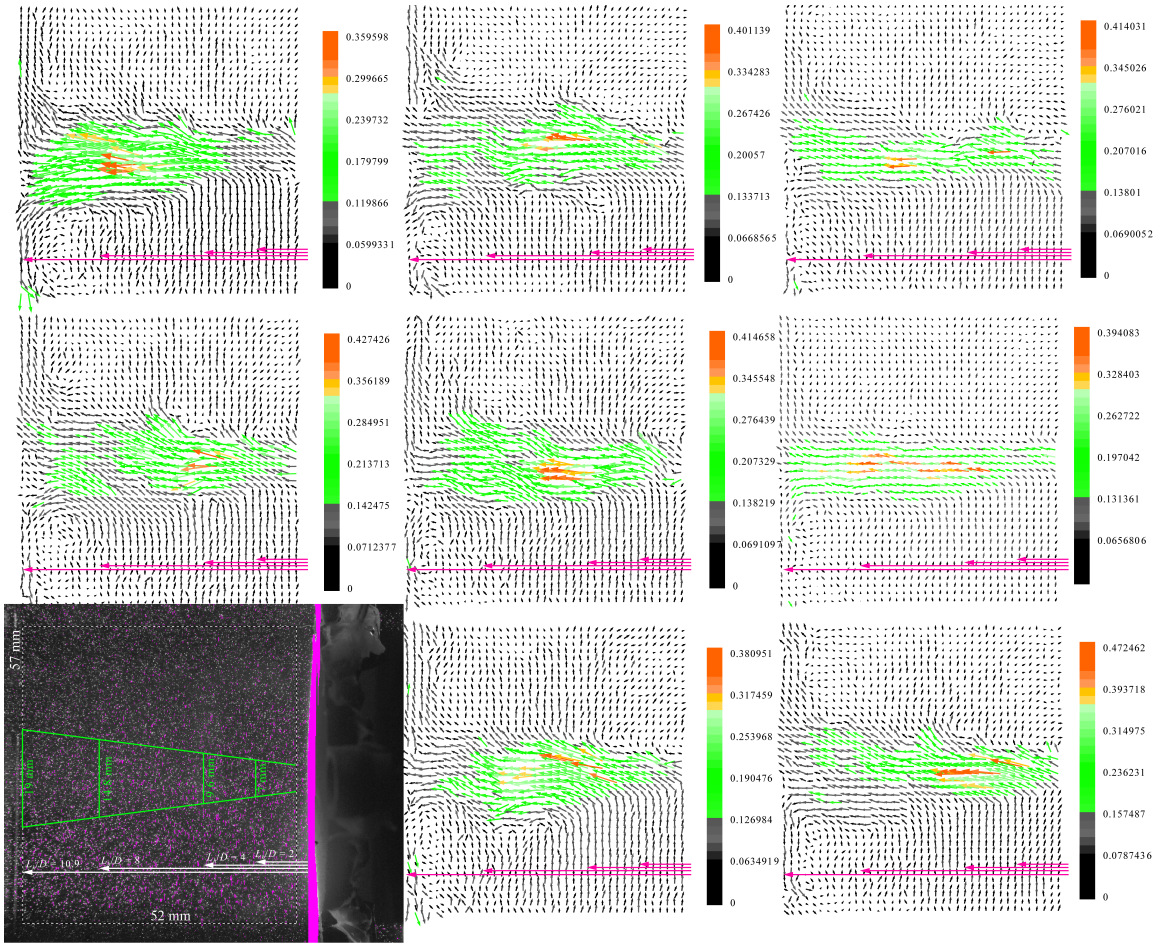

Figure 3.14: Results of the PIV analysis showcasing eight sample vector fields of liquid LSJD in action at 155 Hz and 160 V, positioned 57 mm from the wall. The counter values are expressed in meters per second (m/s).

3.3.6 Discussion and Conclusions

This chapter presents an analytical model, a manufacturing method, thermo-fluidic, and power performance of liquid synthetic jet devices. Frequency-based experimental results reveal a

strong correlation between the device's thermal performance and the analytical model predictions, further supported by comparisons with particle image velocimetry results. Recording diaphragm deflection while submerged posed a challenge, as existing sensors are designed for air environments and lack the precision needed to detect micron-scale oscillations in liquids.

From a heat transfer perspective, complex coupled effects merit further investigation. For example, a greater heat removal was observed at a surface-to-orifice-diameter distance ratio of 4 compared to 2, likely due to reduced mixing of local hot water into the cavity at increased distances. Particle image velocimetry results also indicate peak velocities at a distance ratio of 4, suggesting that optimal spacing enhances performance. Other factors, including vortex shedding frequency and stroke length of the liquid synthetic jets, vary across scenarios, highlighting the intricate interactions affecting thermal performance. While this article introduces these findings, further exploration is needed to fully understand the underlying fluidic phenomena and thermal impacts. To establish a baseline for understanding and to compare with established research on water immersion cooling, it is essential to highlight findings from recent investigations using water as a coolant. Birbarah et al. [262] introduced a method of waterproofing servers using a 1 μm Parylene C coating, which enabled direct immersion in water. Using single-phase natural convection, they achieved a heat transfer coefficient of up to 0.92 W/(cm^2·K) at the higher end of surface temperature rise, near boiling. It is important to note that, similar to this study, the immersion bath temperature was maintained at 22 °C. However, the thermal pads in their study varied in size from 5 mm × 7 mm to 7 mm × 10 mm, significantly smaller than the current study at 25.4 mm × 25.4 mm. The most important highlight of this study is the low liquid velocity in the immersion cooling tank which was 1 mm/s. As discussed earlier, even with flow circulation inside tanks, velocities rarely exceed 5 mm/s and are often parallel to the heated surface. Therefore, a method like liquid synthetic jets, which can enhance velocities ¿100 times higher near the heated surface, can significantly improve heat transfer. In a more recent study [263], researchers explored DI water jet impingement cooling using a central pump and manifold array, reporting a maximum heat transfer coefficient of 0.23 W/(cm^2·K)—approximately 2.6 times higher than immersion-based cooling. Similar to this study, the heating load was controlled to 60 °C, but the coolant inlet

temperature varied between 18 °C, 22 °C, and 27 °C. Jet distances ranged from 1 cm to 10 cm, and inlet water flow rates for the manifolds were set between 8 L/min and 18 L/min. Recent commercial applications of directed cooling in immersion systems by Intel [209] have also demonstrated advancements. In these applications, traditional immersion cooling heat sinks were replaced with specialized cold plates that draw flow from a pump, direct it onto the lid, and discharge it into the immersion tank. Using PAO4 and PAO6 as coolants, a forced flow rate of 0.8 lpm achieved a 15% improvement, while increasing the flow rate to 1 lpm resulted in a 27% reduction in thermal resistance for a 350 W TDP CPU [264].

In a study focused on enhancing microchannel heat transfer rather than immersion cooling, Kang et al. [254] demonstrated the use of liquid synthetic jet devices. They achieved a heat transfer coefficient of 0.57 W/(cm^2·K), though this required a relatively high voltage of 240 V and resulted in only a 31% improvement in performance. The liquid synthetic jet device design presented in this study shows a significant enhancement in heat transfer performance compared to previous methods. This improvement is primarily due to the higher velocity achieved on the heated surface, enabled by a new manufacturing method. The introduced manufacturing approach enables high-speed liquid synthetic jet impingement, achieving a heat transfer coefficient of 1.53 W/(cm^2·K) at a lower applied voltage of 160 V. Moreover, convective thermal resistance was reduced to 0.08 K/W while consuming less than 0.16 W of electrical power. This represents a substantial improvement over previous methods, showcasing the potential of the introduced devices for highly efficient, low-energy, and silent cooling in immersion environments. Certain limitations and application challenges remain, including the long-term durability of this approach, particularly for prolonged operation in engineered or immersion cooling liquids. Further improvements could be realized by replacing polycrystalline-based diaphragms with electromechanically efficient single-crystal alternatives, such as lead magnesium niobate-lead titanate (PMN-PT) [230]. It's important to highlight that, unlike air-based synthetic jet devices, liquid-based synthetic jet devices operate with little to no noise. Supplementary video recordings are available showing them in operation. Furthermore, proper device priming before use is crucial, as trapped air during liquid operation can significantly reduce performance or even lead to device failure.

Chapter 4

Enhanced Liquid Synthetic Jet Design and Test in Harsh Conditions

This chapter presents further analytical and numerical study with experimental validation of enhanced fully submerged mesoscale liquid synthetic jet device (LSJD) for efficient thermal management in high-flux immersion cooling systems. Thermal testing were performed in same test environment, however manufacturing has been imporved. Results demonstrated heat transfer enhancement, with the LSJD achieving a peak heat transfer coefficient of 1.7 W/(cm^2·K), an 8.7-fold improvement over mixed convection cooling, while maintaining low power consumption (0.22 W). The device cooled a 144 W heated surface from 72 °C to 31.5 °C under a crossflow rate of 2 GPM at 20 °C. Results of Particle Image Velocimetry (PIV) experiments and high-speed videography are also provided. Computational Fluid Dynamics (CFD) simulations, validated by experimental results, enabled the characterization of diaphragm deflection to use analytical lumped element model (LEM) for expanded frequency-domain analysis. This enabled the report on jet formation criterion for water LSJDs, with a value of +6 for circular orifices. By comparing LSJD-assisted cooling with traditional impingement systems, the study highlights the significant energy efficiency and compactness of LSJDs, positioning them as a transformative technology for immersion cooling applications. This chapter has been published in [265].

4.1 Introduction

When the efficiency is essential, nature organically gravitates toward pulsatile zero-net-mass-flux (ZNMF) systems as one of the best solutions for generating momentum in fluids. These

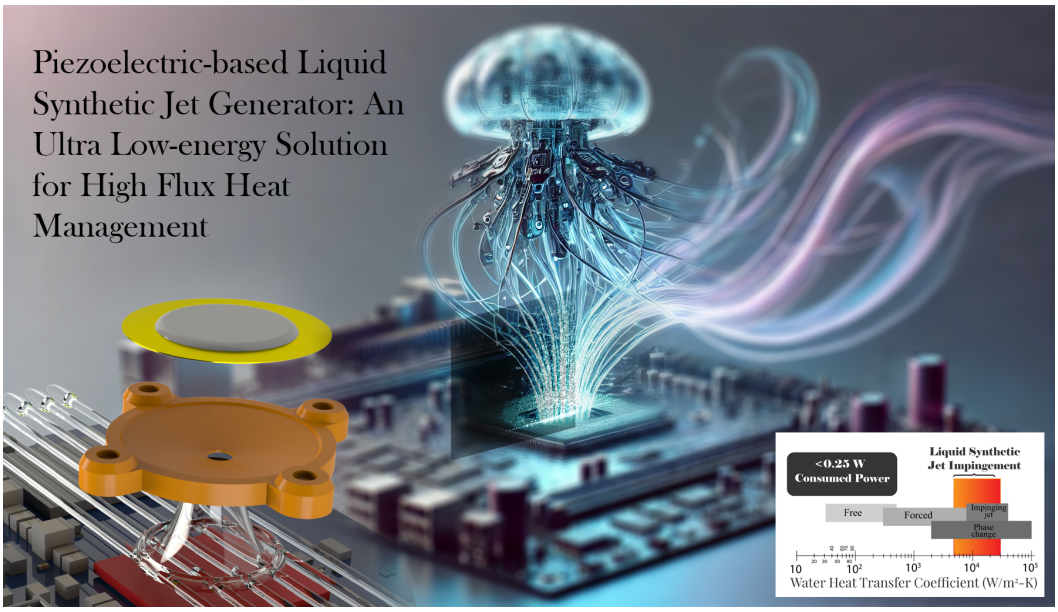

Figure 4.1: Solid state liquid jet impingement concept.

systems reflect a design philosophy that minimizes energy consumption while producing an effective fluidic jet. Consider breathing, nature minimizes energy consumption for this essential process while ensuring that stale air is adequately expelled, making room for fresh, oxygen-rich air intake. Margaria et al. [266] report that, in a resting human, the total mechanical power required for breathing ranges from 0.04 to 0.1 W. Similarly, consider the swimming of the most energy-efficient animal, jellyfish [267, 268]. In 2020, a bio-hybrid jellyfish robot was found to require 10 to 1000 times less power per unit mass to swim in comparison to conventional aquatic robots [269].

Natural ZNMF systems rely on soft diaphragm motion. Engineers face challenges when attempting to replicate these natural actuators [270]. However, with low input powers, piezo-electrically actuated thin metallic disc benders have been shown to mimic diaphragm motion with a relatively high deflection amplitude. These composite diaphragms are typically made of brass/steel, with a piezoceramic patch attached to one or both sides. This leads to the question of whether these can yield efficient ZNMF systems for liquid cooling.

As seen in the previous two chapters, the short answer is yes, however, previous attempts from other researchers were not in large fluidics, but rather in microfluidics. For example, Liu et al. [271] designed and developed a novel micromixer driven by two valveless piezoelectric

pumps, integrating microchannel structures such as diffuser/nozzle tubes and Tesla tubes to achieve multi-stage mixing. At 65 Hz and 120 V, the design achieved a maximum flow rate of 0.20 ml/min. Numerical simulations showed a maximum velocity of 8 mm/s in the middle of a 0.725 mm wide channel. This is all while the piezoelectric diaphragm was in contact with liquid in a chamber of 15 mm diameter and an effective depth of 0.05 mm, while the other side of the diaphragm was in contact with air. As discussed in prevuous chapter, Kang et al. [189] introduced a piezoelectric-based LSJD connected with a 0.5 mm orifice diameter to a microchannel heat sink with a hydraulic diameter of 1.82 mm. Their setup achieved a heat transfer coefficient of 0.57 W/(cm^2·K), resulting in a 31% improvement in heat transfer performance at an operating voltage of 240 V. The design featured a piezoelectric diaphragm clamped between metallic plates, which created a boundary condition that likely reduced diaphragm deflection and, consequently, limited performance.

As presented in Chapter 2, a new method of manufacturing both for air and liquid SJDs yielded a better performance. As seen in Chapter 3, in DI water, the new design was positioned in front of a heated aluminum surface in an immersion cooling tank. Despite the cross-flow between the LSJD and the heated surface, localized, high-velocity jet impingement was achieved leading to a heat transfer coefficient of up to 1.52 W/(cm^2·K). This marked one of the highest reported heat removal per unit of consumed power using a mesoscale fluidic device.

In this Chapter, manufacturing is improved and device is tested in a harshened thermal environment and cross flow. The crossflow rate increased from 0.5 GPM to 2 GPM (limit of the pump) and heated surface power increased from 49.6 W to 144 W (limit of the heater). With the stiffer attachment of the diaphragm to the LSJD body, its resonance frequency was enhanced from 155–165 Hz to 210–220 Hz. The flow field was analyzed using Particle Image Velocimetry (PIV) tests, further supported by high-speed videography for detailed flow visualization. Numerical simulations with a deforming mesh approach were conducted, offering estimations of diaphragm deflection amplitude in submerged conditions. The final results were cross-validated against a previously developed analytical lumped element model (LEM) of the LSJD system. Lastly, power consumption measurements were conducted to evaluate the system's energy efficiency.

4.2 Methodology

4.2.1 Refined Manufacturing of the Liquid Synthetic Jet Device

Extensive details on the manufacturing process of LSJD can be found in previous two chapters. The LSJD body is fabricated using an industrial-grade carbon fiber 3D printer. A 35 mm diameter commercial piezoelectric bender disc is then affixed to the 45° slanted edge of the body (see Figure 4.2). The attachment is based on acrylic resin. Unlike previous chapters, the acrylic application is carried out in two stages, ensuring that the piezo disc is exclusively in contact with the acrylic. This approach eliminates voids and potential wobbling caused by direct contact between the disc and the LSJD body, resulting in a more secure and rigid attachment. Consequently, the system's resonance frequency increased from 155–165 Hz to 210–220 Hz. To prevent current leakage and waterproof the piezoelectric diaphragm, air-dried synthetic rubber is applied to the top surface of the device. The diaphragm is driven at a peak-to-peak voltage of 180 V, with the device (when submerged) capable of withstanding up to 250 V. After being submerged, the LSJD cavity is flushed with liquid to remove any trapped air. Finally, four small bolts securely mounted the device to the holder arm. Parameters defining the geometry of the LSJD are presented in Table 3.3. When comparing results with Chapter 3, the enhanced LSJD herein is referred to as LSJD-2, whereas the devices tested in the previous chapter are referred to as LSJD-1. When no comparison exists, the device is referred to as LSJD.

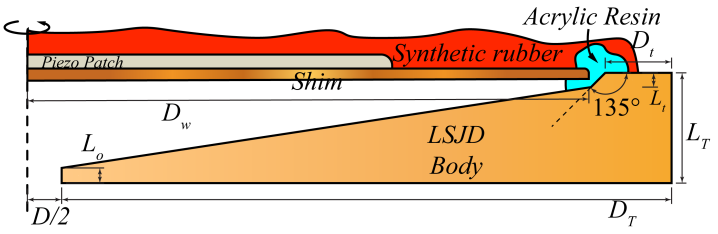

Figure 4.2: Axisymmetric cut plane view of modified manufactured LSJD with a conical cavity.

4.2.2 Power Measurment and Comparison with Previous Design

A sine signal was supplied to the piezo disc using a Siglent SDG 2042X function generator, amplified by a Trek PZD700 high-voltage amplifier. Voltage and current measurements were conducted via the amplifier's analog sense input, connected to a digital voltage converter (NI–9205). Data acquisition occurred at 10 kHz for 500 ms. A 1/200 voltage monitor, and a 0.1 V/mA voltage output were utilized to characterize the voltage and current behavior of the LSJD. The maximum uncertainties in voltage and current measurements were approximately 0.64 V and 0.057 mA, respectively. The power consumption against operating frequency (fr) at 180 V for the LSJD-2 submerged in DI water is presented in Figure 4.3. Comparative trends from the previous chapter, LSJD-1, at 180 V and 160 V are also provided. The diaphragm's power consumption is determined primarily by its capacitance, the square of the applied voltage, and the operating frequency. At 155 Hz resonance, LSJD-1 consumes 0.120 W and 0.155 W. At 240 Hz, the power consumption of LSJD-2 reaches a peak of 0.225 W. However, at 210 Hz, it consumes approximately 0.21 W of power. At the same operating voltages, both devices exhibit a similar pattern of power consumption before reaching resonance due to the use of the same type of piezoelectric bender. However, because of the improved manufacturing method in LSJD-2, it achieves resonance at a higher resonance frequency.

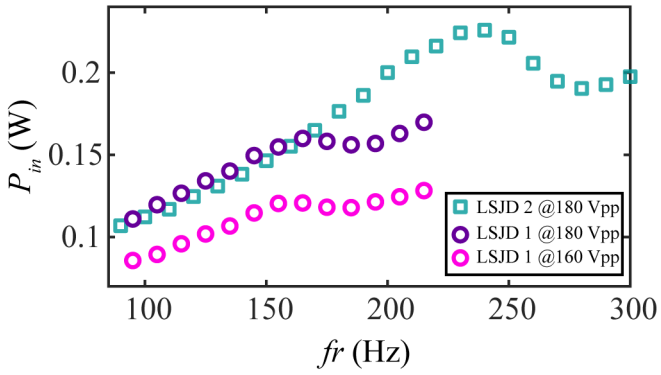

Figure 4.3: Variation of power consumption for LSJD-1 and LSJD-2 for a range of voltages.

4.2.3 Assisted Immersion Cooling With Jet Impingement

Immersion cooling is among attractive high-density solutions for high flux electronics cooling. However, immersion cooling faces challenges with upcoming high heat flux devices due to the no local control on the flow field that necessitates lower inlet temperatures and increased pumping power. In immersion cooling tanks, flow over heated chips is parallel to the surface, with flow over the parallel surface rarely exceeding 10 mm/s [256, 257, 258]. This is why we have observed an increase in the concept of jet-assisted immersion cooling [263, 264, 272]. Such implementations rely on rotary pumps with low power efficiencies ranging from 42% to 83% for large pumps, and often less than 30% for smaller ones [250]. Frictional losses in complex networks of couplings, piping, manifolds, cold plates or nozzles, and heat exchangers reduce efficiency even further. In other words, dynamic pressure is generated upstream and directed to target surfaces via frictional losses. In contrast, LSJD can be used to generate dynamic pressure exactly where and when it is needed. Furthermore, it produces flow in the form of jets, eliminating the need for expensive cold-plates and simplifying the design and manufacture of immersion-cooled equipment. Figure 4.4 illustrates the concept. This method has the advantage of being inexpensive, silent, compact, and it only requires a low-frequency signal to drive a piezoelectric diaphragm using low-current wiring.

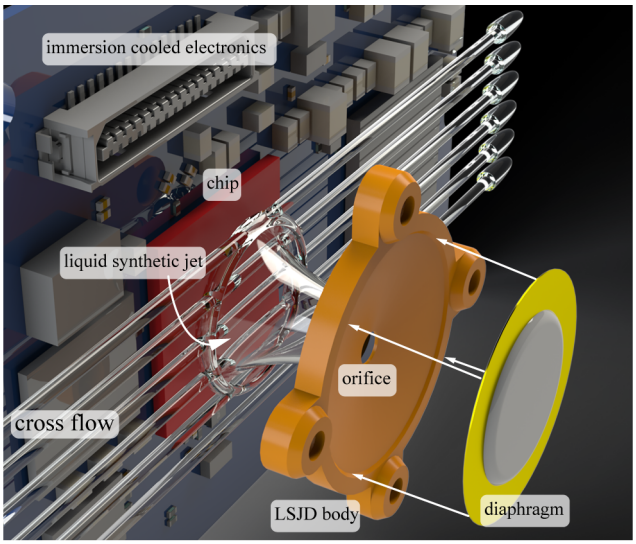

Figure 4.4: Visualization of the concept of liquid synthetic jet-assisted immersion cooling.

Thermal tests were carried out in a forced DI water immersion tank. An insulated cartridge heater heats up a 25.4 × 25.4 mm^2 polished aluminum surface to 72 °C with regulated inlet coolant from the bottom of the tank at 19.7 °C and a rate of 7.57 lit/min (2 GPM). Given a characteristic length of 25.4 mm, the Nusselt (Nu) number is evaluated 86 (up from 60 in previous tests in Chapter 3). The normal heat flux to the liquid is evaluated from three equally spaced consecutive thermocouples near the surface based on Taylor series expansion to calculate the second-order accurate temperature gradient. The LSDJ's 5 mm diameter orifice was positioned 20 mm from the heated surface ($L_h/D = 4$), which has previously been shown to achieve the highest thermal performance. The thermal performance of the LSJD was then evaluated over three hours of operation while changing the frequency of operation from 170 Hz to 280 Hz. Picture from the experimental set up is provided in Figure 4.5.

4.2.4 PIV Tests and High-Speed Videography

The MODULE4G-2D PIV particle image velocimetry (PIV) system from TSI was utilized for the experiments. PIV measurements were conducted at 180 to 240 Hz frequencies, using 14-micron Gls-Hlw-Ag seed particles. Additional details regarding the PIV setup can be found in Chapter 3. In Chapter 3, PIV results were presented over arbitrary time intervals of the flow field. This approach was adopted because the jet formation required several cycles after diaphragm activation to achieve a quasi-steady state. Later high-speed videography of the flow field showed that the quasi-steady state did not exist, and the flow field was unpredictable and exhibited extreme turbulence. Furthermore, a vaiable phase lag persisted between the jet exit behavior and diaphragm deflection. This rendered the external triggering of the PIV setup unreliable for producing phase-locked results. Chaotic bursts of jets from the cavity are documented in high-speed videography shown in supplementary videos. The videography was performed at 2000 fps (frame per second) using a Phantom v310 high speed camera. Observations indicated that the LSJ flow field could be divided into three distinct regions as shown in Figure 4.6.

- Inflow zone: We observed a continuous and low-velocity inflow of liquid from the sides into the cavity.

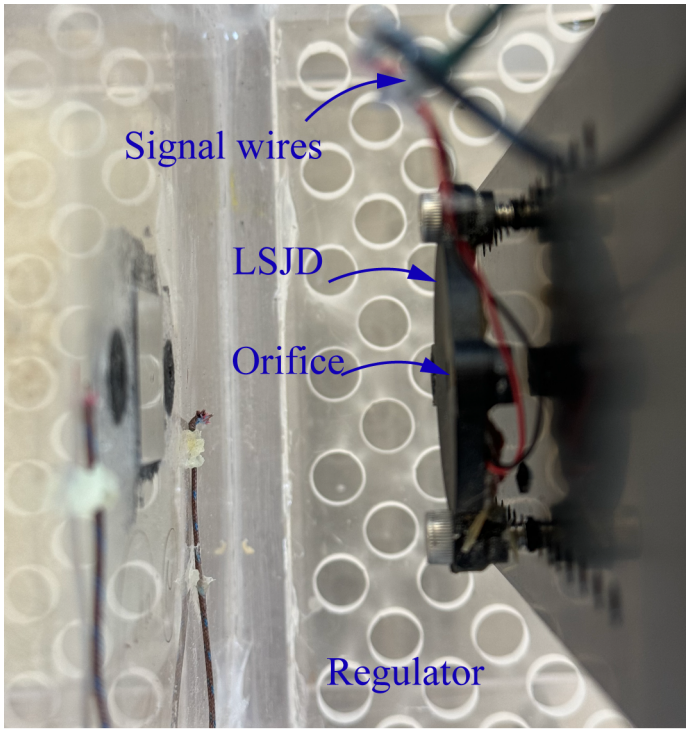

(a) top view

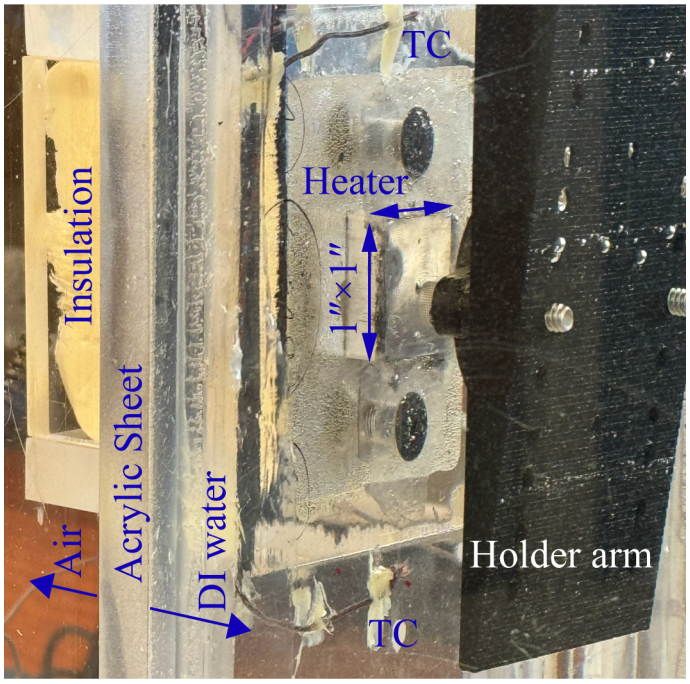

(b) side view

Figure 4.5: View of the experimental system (a) top view, and (b) side view of the thermal experiment

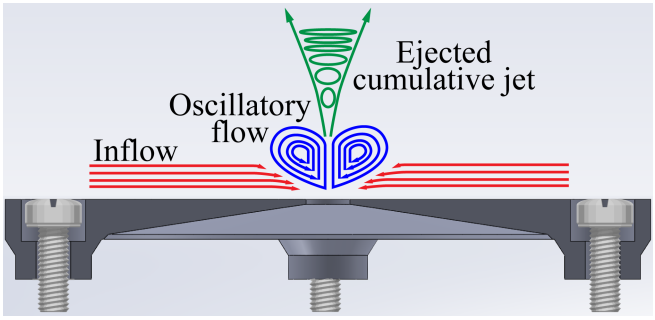

Figure 4.6: Three distinct flow field regions.

- Oscillatory flow zone: There is an oscillatory flow field in the vicinity of the orifice, where high velocity back and force direction changing flow were evident in the same frequency as the diaphragm's oscillations.

- Ejected cumulative jet zone: Through this oscillatory region, variable velocity jets of liquid were generated.

This distinguishes air-based and liquid-based SJs. During air synthetic jet (ASJ) generation, coherent vortex rings form at the orifice wall, cushioning ejected air puffs from the center of the orifice. In contrast, in LSJs, it seems as if the vortex rings were not ejected (or collapsed immediately), but through them, the liquid jets emerge in the form of small-scale cumulative jets. These jets either traveled downstream at velocities slower than the oscillatory flow near the orifice or were suddenly ejected at higher velocities. We call this region an ejected cumulative jet zone. In part, such observation reports can be found in the literature for ASJDs. For example Mallinson et al. [197] reports on standing vortex at orifice where flow oscillations introduced by the device cause a much greater entrainment of fluid, however, they were dampened out very close to the orifice, and disappeared when the self-similar flow is established. However, in liquid systems because of higher turbulence intensity, self-similar flow was not established.

As shown in Figure 4.7, a sample PIV vector field analysis demonstrates our ability to resolve the vector field in the far field. However, the available zoom was insufficient to resolve the finer details of the oscillatory flow zone near the orifice. Furthermore, this zone was not relevant to the current article because the upper flow field was responsible for jet cooling. To capture the behavior of this zone that also did not align with the diaphragm's oscillation

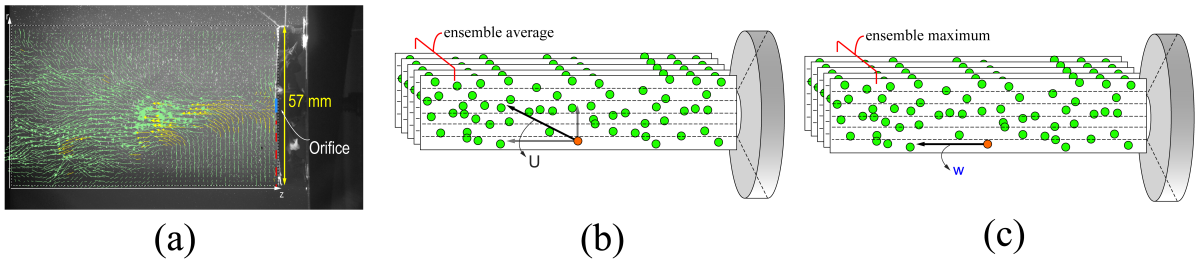

Figure 4.7: (a) A sample PIV vector field analysis, and description of the ensembled analysis of vector field for (b) averaging the velocity magnitude (U), and (c) maximum value of the jet exit velocity in the z-direction (w).

frequency, a new approach to PIV analysis was implemented. PIV experiments were conducted across a range of frequencies from 180 Hz to 240 Hz, with 50 to 200 analyses performed for each case. Some of the data for analysis are provided in Appendix G. A custom MATLAB code was developed to perform an ensemble study of the resulting velocity fields (Appendix G). In the first set of results (Figure 4.7(b)), the MATLAB code was used to calculate the ensemble average of the velocity magnitude (U). In the second analysis, the code extracted the maximum value of the jet exit velocity in the ejected z-direction (w) at each location (Figure 4.7(c)). Ensemble analysis was performed on sets of 50 vector fields while excluding outlier vectors from PIV tests(results were practically identical when the set number increased or changed, indicating the report's reliability).

4.2.5 Free Liquid Synthetic Jet Generation, CFD Simulations, and Comparison with Analytical Analysis

An SJ formation, evolution, and impingement can be considered turbulent flow due to its highly transient pressure variation, strong shear stresses at the orifice, and vortical flow field. White [273] describes turbulence as a "spatially varying mean flow with superimposed three-dimensional random fluctuations that are self-sustaining and enhance mixing, diffusion, entrainment, and dissipation." Based on time averaging of these fluctuations, Reynolds [274] obtained equations of motion and energy balance for an incompressible turbulent flow which is the basis of investigation in this research. By considering flow property as mean value plus a superimposed random fluctuation one can obtain unsteady Reynolds-averaged Navier–Stokes

equations (uRANS equations). To apply and numerically solve uRANS equations governing the fluid flow of this study computational fluid dynamic (CFD) studies are performed with the Fluent 2021 R2 package. Physical assumptions must be used for the problem: Newtonian single-phase, single-species, non-reacting, and incompressible flow while neglecting thermal radiation and body forces due to gravity. Furthermore, turbulent field is considered isotropic (i.e. the statistically averaged properties are invariant under the rotation of the coordinate system, or under reflection with respect to a coordinate plane). Moreover, the turbulent flow field is considered homogeneous, that is if the turbulent fluctuations have the same structure everywhere.

Derived from the core conservation principles, and based on the Eulerian description of fluid flow with u_i represent the Cartesian velocity components at a specific point in space and time for flow with the density of ρ, the pressure of p, dynamic viscosity of μ, thermal conductivity of k, thermal diffusivity of α and specific heat of c_p one can write one can write:

$$\frac{\partial \rho}{\partial t} + \frac{\partial(\rho \overline{u_i})}{\partial x_i} = 0 \tag{4.1}$$

$$\frac{D(\rho \overline{u_i})}{Dt} = -\frac{\partial \overline{p}}{\partial x_i} + \frac{\partial}{\partial x_j}\left[\mu\left(\frac{\partial \overline{u_i}}{\partial x_j} + \frac{\partial \overline{u_j}}{\partial x_i} - \frac{2}{3}\delta_{ij}\frac{\partial \overline{u_l}}{\partial x_l}\right)\right] + \frac{\partial}{\partial x_j}(-\rho\overline{u_i' u_j'}) \tag{4.2}$$

$$\frac{D(\rho c_p \overline{T})}{Dt} = -\frac{\partial}{\partial x_j}(\overline{q_j''} + \rho c_p \overline{T' u_j'}), \overline{q_j''} = \rho c_p\left(-\alpha\frac{\partial \overline{T}}{\partial x_j} + \overline{T' u_j'}\right) \tag{4.3}$$

Mean values are represented with a bar above the variable, while superimposed random fluctuations are denoted with a prime symbol. It can be seen that Reynolds stresses,$-\rho\overline{u_i' u_j'}$, must be modeled to close the momentum equation. As first proposed by Boussinesq, the cross-correlation of fluctuating velocity components in turbulent flow is proportional to the mean velocity gradient, with the proportionality coefficient defined as the turbulent viscosity μ_{tu}:

$$-\rho\overline{u_i' u_j'} = \mu_{tu}\left(\frac{\partial \overline{u_i}}{\partial x_j} + \frac{\partial \overline{u_j}}{\partial x_i}\right) - \frac{2}{3}\left(\rho k + \mu_{tu}\frac{\partial \overline{u_k}}{\partial x_k}\right)\delta_{ij} \tag{4.4}$$

then turbulent viscosity can be expressed as a function of turbulence kinetic energy (K) and its dissipation rate (ϵ), while they can be modeled as transport property and solved numerically. This relationship forms the basis for many turbulence models, including the widely used $K-\epsilon$

and $K-\omega$ frameworks where transport equations solve for the turbulence K and the rate of its dissipation, ϵ, or specific dissipation rate, ω. A hybrid SST $k-\omega$ uses a blending function to allow these models to be combined effectively. Specifically, the standard $K-\omega$ model can be applied in the near-wall region, where it excels at resolving boundary layer phenomena, while the transformed $K-\epsilon$ model can be used in the freestream, where it is more efficient:

$$\frac{\partial}{\partial t}(\rho K)+\frac{\partial}{\partial x_j}(\rho K\overline{u_i})=\frac{\partial}{\partial x_j}\left(\Gamma_k\frac{\partial K}{\partial x_j}\right)+\widetilde{G}_K-Y_K \tag{4.5}$$

$$\frac{\partial}{\partial t}(\rho \omega)+\frac{\partial}{\partial x_j}(\rho \omega\overline{u_j})=\frac{\partial}{\partial x_j}\left(\Gamma_\omega\frac{\partial K\omega}{\partial x_j}\right)+G_\omega-Y_\omega \tag{4.6}$$

where, Γ_k, and Γ_ω represents effective diffusivity of K, and ω, respectively, $\widetilde{G}_K$ represent the generation of turbulent kinetic energy due to mean velocity gradient, G_ω represents the generation rate of ω and Y_K, and Y_ω are dissipation of K, and ω, respectively. Lastly, turbulent viscosity can be defined as:

$$\mu_{tu}=\frac{\rho k}{\omega}\frac{1}{\max\left[1/\alpha^*, SF_2/\alpha_1\omega\right]} \tag{4.7}$$

where the right-hand side is the function to dampen turbulent viscosity at low Reynolds (Re) numbers. Lastly, it needs to be noted that The enhanced wall function, specific to ANSYS Fluent, is naturally applied in models which is aimed to reduce errors in the buffer region of the boundary layer [275]. It utilizes a continuous blending function that smoothly transitions between the viscous sublayer and the logarithmic region based on Ref. [276]. It is important to note that, based on the enhanced wall function, the calculated $y+$ should be either less than 2 or greater than 30 as a rule of thumb. This condition is implemented in the simulation by applying inflation layers in the mesh along no-slip walls. Furthermore, to accommodate diaphragm motion, dynamic mesh motion is defined using a user-defined function. As discussed in Chapter 2, the behavior of the diaphragm can be modeled as:

$$z(r)=\Delta z\frac{1-4(r/D_w)^2}{2\pi\cdot fr\cdot t} \tag{4.8}$$

Where Δz is deflection at center amplitude that will be decided based on experimental verification with altering its value from 30 to 50 μm, D_w is the diameter of the diaphragm, and fr is the frequency of operation that is considered constant at 155 or 210 Hz. As the diaphragm motion alters the domain geometry over time, the volume mesh is automatically updated by ANSYS Fluent at each time step based on the new boundary positions. This approach allows the velocity term in the convective derivative of all fields to be extracted from the mesh velocity associated with the moving mesh.

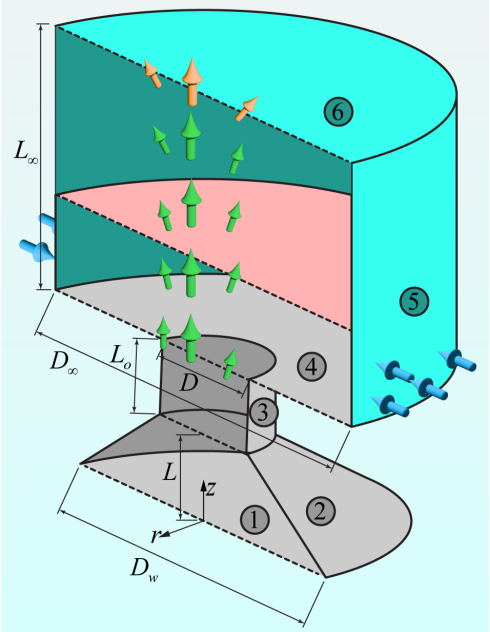

Figure 4.8: CFD model details (gray surfaces representing walls, blue surfaces representing pressure outlets, and red surfaces representing a sample imaginary surface for data analysis).

Parameter	L_∞	D_∞	L_o	D	L	D_w
Value	50	45	0.5	5	3	35

Table 4.1: Parametric definition of the CFD simulations.

Parametric naming of the model geometry is shown in Figure 4.8 and their values are provided in 4.1. Boundary conditions are also marked in Figure 4.8 and are defined in Table 4.2 along with the meshing details of each face with numbers. Simulations were designed to understand the deflection amplitude. LSJD was open to ambient to find the matching deflection of the diaphragm that can lead to approximately similar results with PIV test results. Mesh

	Face size in mm (growth rate)						
	Face 1	Face 2	Face 4	Face 5	Face 6	Total	Cell no
Coarse	1.5(1.1)	1.5(1.1)	0.1(1.1)	2(1.2)	2(1.2)	2(1.2)	564k
Medium	1(1.1)	1(1.1)	0.075(1.1)	1.25(1.2)	1.25(1.2)	1.25(1.2)	859k
fine	0.8(1.1)	0.8(1.1)	0.06(1.1)	1(1.2)	1(1.2)	1(1.2)	1.1M
Extra fine	0.5(1.1)	0.5(1.1)	0.05(1.1)	0.9(1.2)	0.9(1.2)	0.9(1.2)	1.2M
B.C.	UDF	Wall	Wall	Wall	P out	P out	-

Table 4.2: Description of considered mesh structures and boundary conditions in simulations.

dependency tests are also performed in these series to understand the required mesh refinement in near and far field regions.

A pressure-based solver was utilized, employing a second-order upwind scheme for spatial discretization and an implicit first-order time integration for temporal discretization. The SIMPLE algorithm was selected for pressure-velocity coupling. All equations were solved iteratively for each time step until the convergence criteria were met, with absolute residual criteria reduced to one-tenth of the default values. Prior to solving, hybrid initialization was applied to the domain (solving for potential flow). The time steps were defined such that the time domain for each deflection cycle was divided into 40 intervals. A total of 4000-time steps were solved, resulting in a semi-steady behavior of the flow field. After estimating the diaphragm displacement, the previously developed analytical lumped element model (LEM) was tuned based on the determined force on the wall and its deflection. Then obtained velocity behavior at the orifice exit between CFD and LEM was compared. This will help expand the analysis from a single 210 Hz frequency case to a spectrum of operation in different frequencies without the requirement for time-consuming CFD simulations.

4.2.6 Impinging Liquid Synthetic Jet CFD Simulations

After deciding on the deflection of the diaphragm, LSJ impingement models were also performed. Figure 4.9 depicts the parametric naming of the model geometry, with values provided in Table 4.3. Boundary 1 is a deforming wall and has a constant surface temperature of 300 K, along with boundary walls 2–4. Boundary wall 6 is insulated with wall 7 at 350 K. Velocity inlet 5 is half of the cylindrical domain above the orifice exit, with x-direction velocity values

of 10, 30, and 50 mm/s. Pressure outlets are located at boundaries 8 and 9. A mesh dependency test was performed. Prior to solving, hybrid initialization was applied to the domain (solving for potential flow). Next, constant temperature of 300 K is patched to whole domain. The domain was then solved for 15 iterations or more as needed with a time step of 0.2 s without the use of LSJD. This lays the groundwork for heat transfer performance using only cross-flow. The diaphragm is then activated, and the domain is solved for 5000 additional iterations at a much finer time step of $1/(20fr)$. This allows it to be determined how much improvement LSJD can achieve after a total of 250 diaphragm deflections. It should be noted that cross-flow continues to enter the domain even after the diaphragm is actuated. Frequencies of 155 and 210 Hz were modeled.

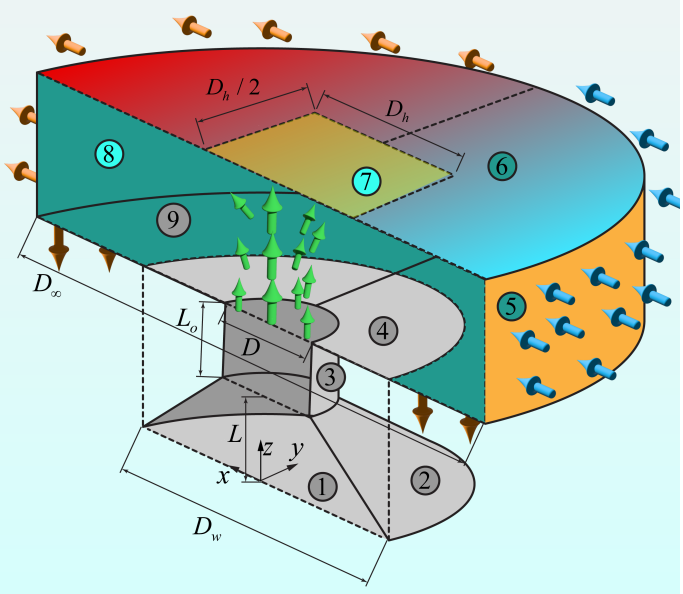

Figure 4.9: Parametric definition of the impingement CFD simulations.

Parameter	D_h	L_h	D_∞	L_o	D	L	D_w
Value	25.4	20	65	0.5	5	3	35

Table 4.3: Parametric definition of the CFD simulations.

4.3 Results

4.3.1 Thermal Experiments

Figure 4.10 demonstrates the thermal behavior of a one-square-inch heater at 144 W, cooled by a crossflow of DI water at 2 GPM from below, while natural convection aids in heat removal. In the initial state, the surface temperature stabilizes at 72°C, which corresponds to a mixed heat transfer coefficient of 0.2 W/(cm^2·K). At this juncture, the LSJD positioned 20 mm from the center of the heated surface is activated, impinging normal jets onto the surface at an initial frequency of 170 Hz. This results in a pronounced drop in surface temperature, which stabilizes at 53.8°C after 5 minutes of operation. After 15 minutes of operation in each frequency, the diaphragm operation frequency increases in increments of 10 Hz. LSJD demonstrates peak performance at 210-220 Hz, where the heat transfer coefficient reaches 1.7 W/(cm^2·K), and the corresponding Nu number climbs to 740 (in previous chapter maximum Nu was 648). Temperature rise drops from 52.4 C to 12 C. This represents an 8.7-fold Nu number enhancement compared to mixed convection without the LSJD assisted impingement. Beyond 210-220 Hz, performance declines significantly. At 240 Hz a sharp reduction in heat transfer performance can be seen. By 270 Hz, effective jet generation ceases entirely, and the surface temperature reverts to its pre-impingement steady state. This is all while, as shown in Supplementary Video, jet generation occurs until 270 Hz, but because its strength is reduced, it cannot penetrate the crossflow and has no effect on disturbing the thermal boundary layer. A view of the impact of the driving frequency on Nu number profile is presented in the subfigure, with the characteristic length based on the heater dimensions to standardize comparisons against unassisted cooling. It is noteworthy that LSJD assisted cooling outperforms forced parallel convection but achieves performance on par with traditional water jet impingement cooling, while consuming orders of magnitude less electrical power. This can be seen in Figure 4.11. For conventional jet impingement systems, reported power consumption values often solely consider the nozzle's pressure drop, ignoring additional losses from system components such as piping, pumps, and the pump's inherent inefficiencies. In contrast, the LSJD power consumption reported here reflects the direct electrical power input to the device (excluding losses during AC-to-amplified

sine DC conversion). Despite this exclusion, the coefficient of performance (COP) achieved by the LSJD can be ranked among the highest recorded in the literature. This positions LSJD technology as a highly efficient, low-power alternative for advanced thermal management applications.

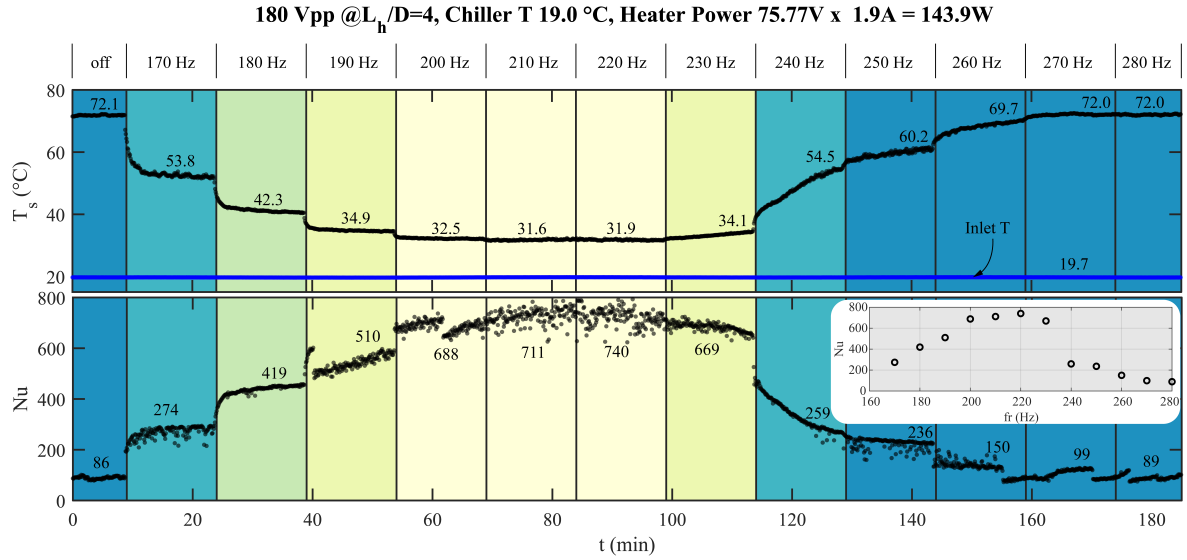

Figure 4.10: A continuos measurement results for the frequency sweep at a crossflow rate of 2 GPM, an inlet temperature of 19.7°C, a heater power of 144 W, an LSJD operating voltage of 180 V, and a distance to heater surface of 20 mm.

4.3.2 Fluidic Study

Figure 4.12(a) shows the distribution of w (velocity component in the positive z-direction) along the central line of the modeled geometry ($r = 0$), where the central deflection of the diaphragm in the simulation varies between 40 and 60 microns at 210 Hz. The results are reported after 4000-time steps of simulation, equivalent to 100 cycles of deflection, when the fluidic system reaches a quasi-steady-state behavior. The velocity profile in the far field matches the ensemble-averaged maximum values of w from the PIV tests. However, in the near field (the region close to the orifice), PIV results fail to accurately represent the high-velocity behavior. This limitation is previously discussed in the method section. Despite this, we can see that the location of the vena contracta shifts forward as diaphragm deflection increases. This issue is also highlighted in Figure 4.13, where it is clear that the location of the vena contracta shifts in tandem with the frequency of operation. Further comparisons of the reported velocities

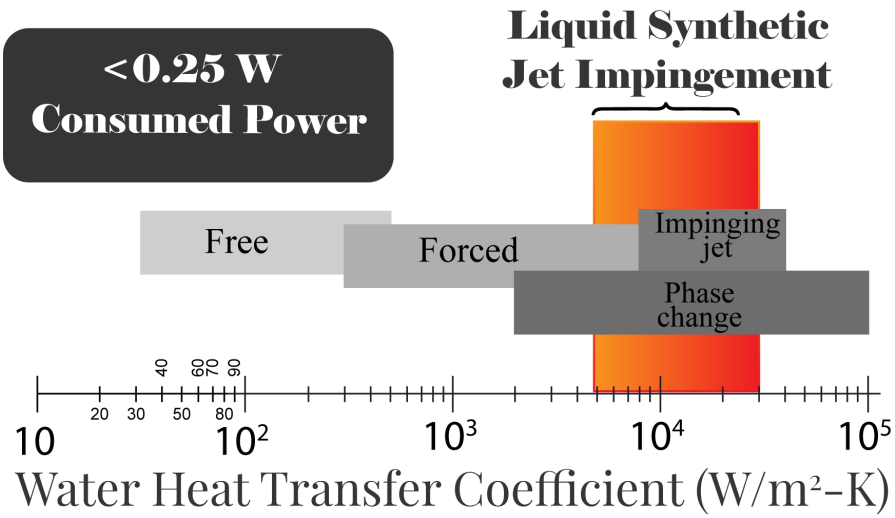

Figure 4.11: Range of heat transfer coefficient for different cooling methods [277] and comparison with water SJ impingement.

in Figure 4.12(a) are consistent with the high-speed videography analysis. Additionally, it is evident that a 40-micron diaphragm deflection results in almost no LSJ generation, with the liquid ejected from the orifice being sucked back in. Figure 4.14 shows that at 40 μm and 210 Hz, there is almost no jet output in the far field, despite relatively high velocities at the jet exit (at the oscillatory flow zone). LSJs can be successfully ejected at 50 and 60 micron central deflection.

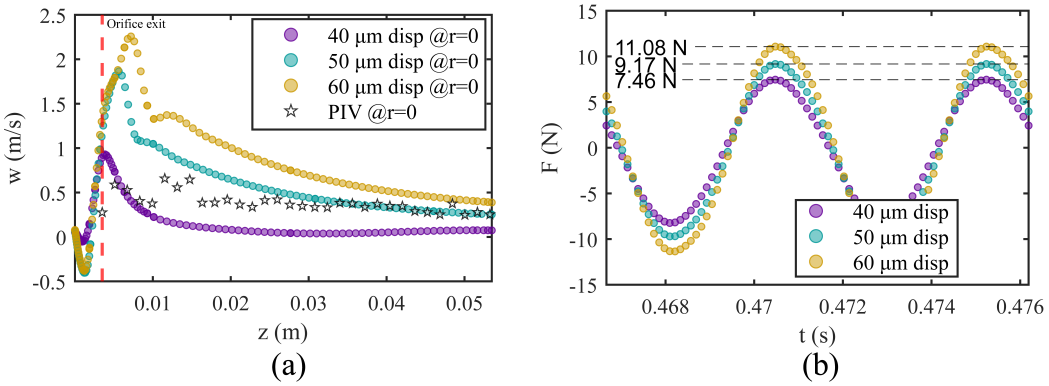

Figure 4.12: (a) Distribution of w on the central line of the LSJD after 100 cycles of operation, with the red dashed line indicating the position of the orifice exit. (b) The total force acting on an oscillating diaphragm in a sample data set to capture the entire oscillation cycle.

Figure 4.13 presents the results of the ensembled analysis of the PIV test. A sample view of the vector field in the PIV imaging is shown at the top, with the orifice location highlighted

by a red dotted line, extending into the bottom vector field. The device itself is also visible. The bottom vector field illustrates the jet exit behavior, with averaged velocity displayed on the left and maximum ejection velocity on the right. To enhance visualization of the vector field, the results are plotted as x-y graphs on the left side of each vector field for five parallel lines near the orifice. These plots show the location and values of the maximum velocities. It is evident that as the jet exit velocity increases, the location of the vena contracta shifts. Overall, the ensemble maximum analysis captures the behavior of the jet exit velocity in the far field, validated through high-speed videography and CFD simulation.

Figure 4.14 depicts the w velocity distribution after 100 cycles at various distances from the orifice exit for three different diaphragm oscillations. For a diaphragm displacement of 40 microns at 210 Hz, it can be observed that there is almost no jet output in the far field, despite relatively large velocities being present at the jet exit. A consistent jet spreading is observed starting from 5 mm at the jet exit, extending to 20 mm within a 40 mm downstream travel. Results also show minimal change in results of simulation with different mesh sizing.

A comparison of PIV and CFD simulations enables considering that the diaphragm's central deflection is within the 50-micron range. Later, by analyzing the force acting on the diaphragm at this deflection, LEM model can be tuned to study the system in a wider frequency domain. As shown in Figure 4.12(b), the force on the diaphragm at a 50-micron displacement is calculated to be 9.17 N. By incorporating this value into the LEM model, we have determined the diaphragm's stiffness and the two required constants, as summarized in Table 4.4.

$K \times 10^6$ (N/m)	F_{max} (N)	C_l	C_d	m_w (gr)
1.2	9.17	3	0.6	3.2

Table 4.4: Stiffness and mass of the socilation wall, the force acting on it, and the constants needed to tune the orifice jet outlet for LEM.

It's important to note that LEM focuses on area-averaged jet exit velocity ($\overline{U}$), not far-field behavior. Solving LEM equations at 210 Hz and comparing the results to CFD simulations reveals good agreement between the two models, as shown in Figure 4.15(a). These findings show that at 210 Hz, the LSJD can displace 0.42 liters per minute in one direction or 0.84 liters per minute in both directions. This is all done while consuming only 0.21 W. This is within the

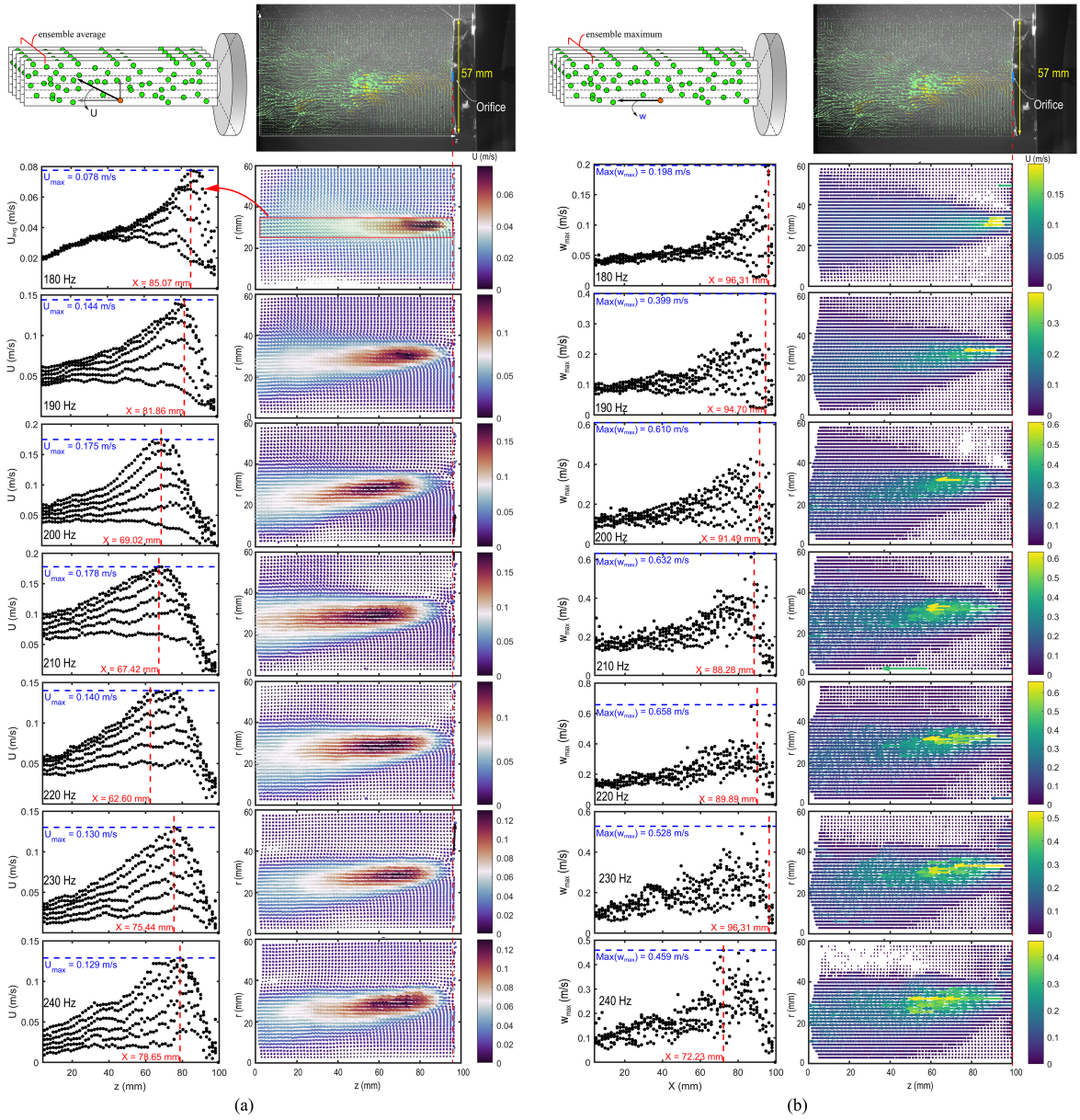

Figure 4.13: Ensemble averaged vector field analysis of PIV tests. The results on the left show the ensemble averaging of velocity vectors. The results on the right showed only the maximum ensembling of the ejection z velocity vectors.

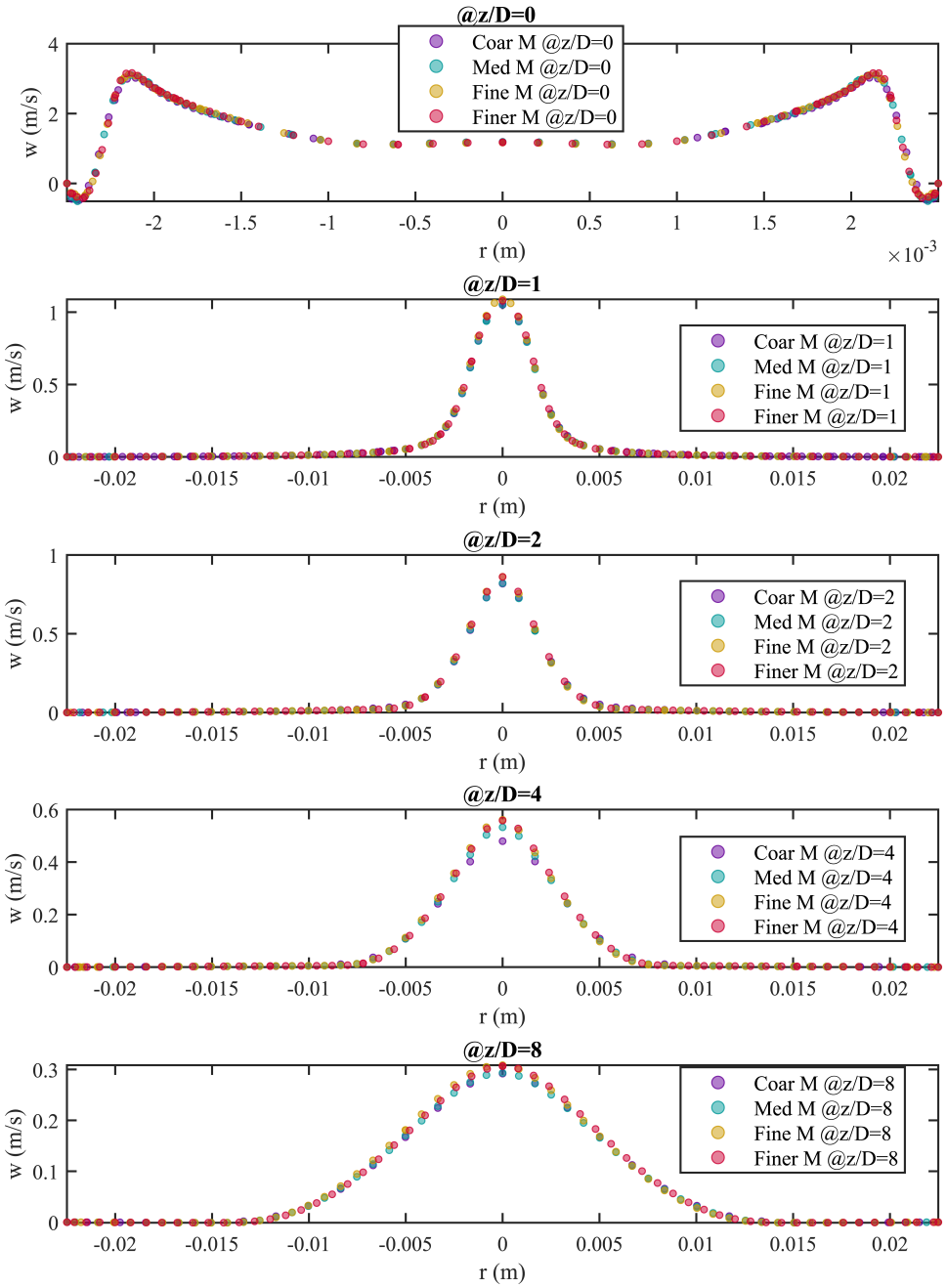

Figure 4.14: Distribution of w along parallel lines to the orifice exit at various distances for three different wall deflection amplitudes at 210 Hz.

range of small-scale (5-10 W) rotary pumps. However, as previously discussed, not all of the displaced liquid can be ejected as jets into the far field. As previously discussed, part of the jet's central region ejects into the downstream, but this ejection is not uniform and predictable, as highlighted in the high-speed videography. An important advantage of the LEM model is that

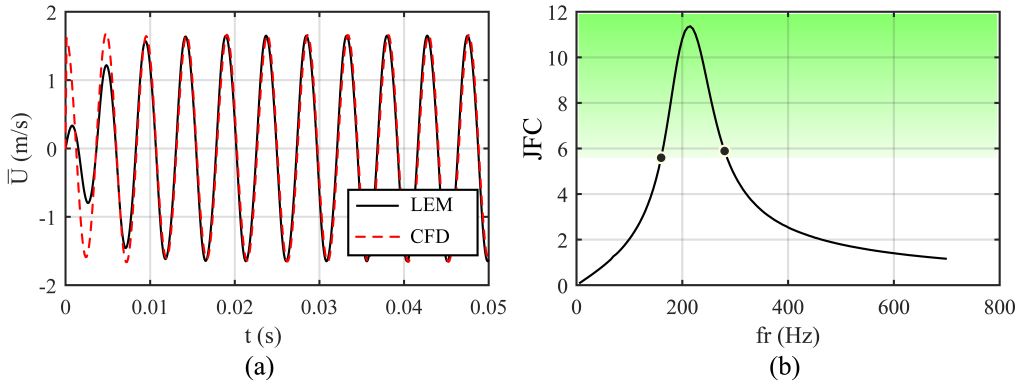

Figure 4.15: (a) Comparison of area-averaged jet exit velocity between LEM and CFD modes, and (b) JFC distribution in various frequencies of operation predicted by LEM.

it solves the coupled behavior of flow and diaphragm. In other words, we can solve the tuned LEM model for a wide range of frequencies while ensuring that displacement behavior of the diaphragm and jet exit velocities are taken care of during the solution, as we have previously shown in Chapter 2.This way one can determine a value for LSJ formation criteria. In comparison to air, in water, this value increases significantly, resulting in an approximate value of 6. The green bond in Fig. 10(b) can also be seen in Supplementary Video, which shows the LSJD operation over a frequency range of 170 Hz to 280 Hz. This video shows that SJ formation occurs between 170 and 270 Hz. By comparing this videography to the plotted JFC-fr relation provided by LEM, it is clear that K^* falls into the +6 range.

Figure 4.16 plots a normalized ensemble-averaged velocity field, ensemble-maximum ejection velocity, piezoceramic power consumption, and Nu number enhancement on the same plot with a fourth-order polynomial fit. It can be seen that diaphragm resonance occurred at 239 Hz, while maximum heat transfer performance was achieved at 211 Hz (between 210 and 220 Hz). Maximum velocity values were observed at slightly lower frequencies, highlighting a

phase mismatch between the maximum thermal response, diaphragm dynamics, and fluid behavior. Such phase lag was also observed in ASJDs, however, we can highlight some major differences between the two concepts of ASJD and LSJDs.

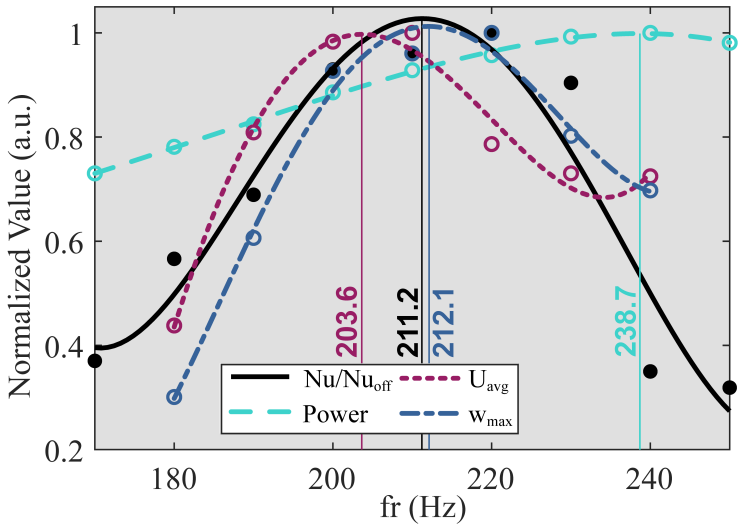

Figure 4.16: Normalized comparison of diaphragm dynamics, flow field, and impingement characteristics.

The dynamics of SJDs in air and liquid media are shaped by the interplay of fluid properties, including compressibility, viscosity, density, and momentum diffusion. ASJDs benefit from air's compressibility, which enables smooth energy transmission and the formation of predictable vortex rings, resulting in consistent and self-similar flows. In contrast, LSJDs exhibit irregular velocity patterns due to the distinct properties of liquids, such as higher viscosity, inertia, momentum diffusion, and incompressibility. In the near field, we have observed a standing vortex (constantly accelerating and deceleration zone near orifice) and high turbulence and in the far field we have observed chaotic jet patterns and increased jet spreading (CFD simulation shows jet spreading of 20 mm at 40 mm distance from the orifice – see Figure 4.17). This indeed causes varying pressure conditions at jet formation zone leading to alternating bursts of high-speed flow followed by periods of reduced speed flow. In air-based systems, compressibility allows for the elastic storage and release of energy during diaphragm oscillations, facilitating the periodic ejection of coherent vortex rings. This leads to Helmholtz resonance where device performance can be further improved by mode matching between wall and Helmholtz resonance. Conversely, the incompressibility of liquids directly transmits pressure disturbances,

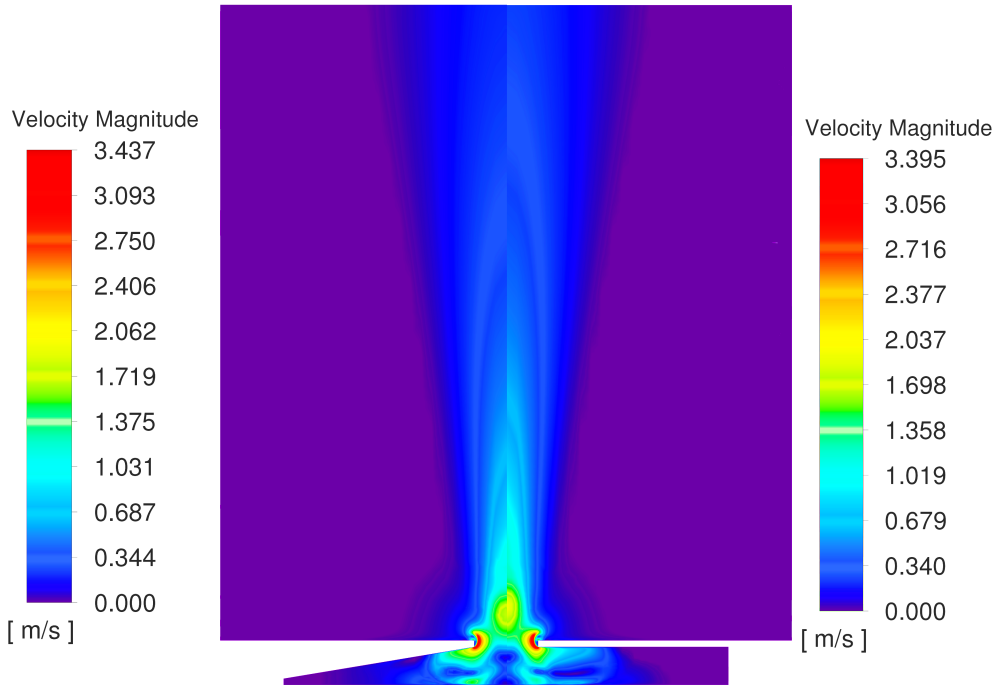

Figure 4.17: Velocity magnitude contour for simulation at 210 Hz with 50-micron displacement at the diaphragm.

further hindering the formation of stable vortex structures (see Figure 4.18 for flow oscillation in near and far fields).

Figure 4.18 illustrates the maximum w velocity component (in the ejection direction) at various distances from the orifice exit. In the initial cycles, the SJ is not yet formed. Instead, after three cycles, accumulated jets are abruptly pushed into regions with no velocity, leading to a sudden rise in velocities. It is also evident that the SJ requires some time to travel from the orifice exit to the far field. Following this, the flow field transitions to a quasi-steady-state behavior, with minor frequency variations in the jet dynamics. These fluctuations are attributed to the incompressibility of the liquid, where the diaphragm oscillations continue to influence the jet even at the far field. This behavior is corroborated by high-speed videography, which reveals oscillations in the inflow to the orifice, clearly visible in the recordings. Additionally, mesh-independency tests confirm that the fine mesh used provides accurate predictions of the flow field, yielding consistent results with Finer mesh.

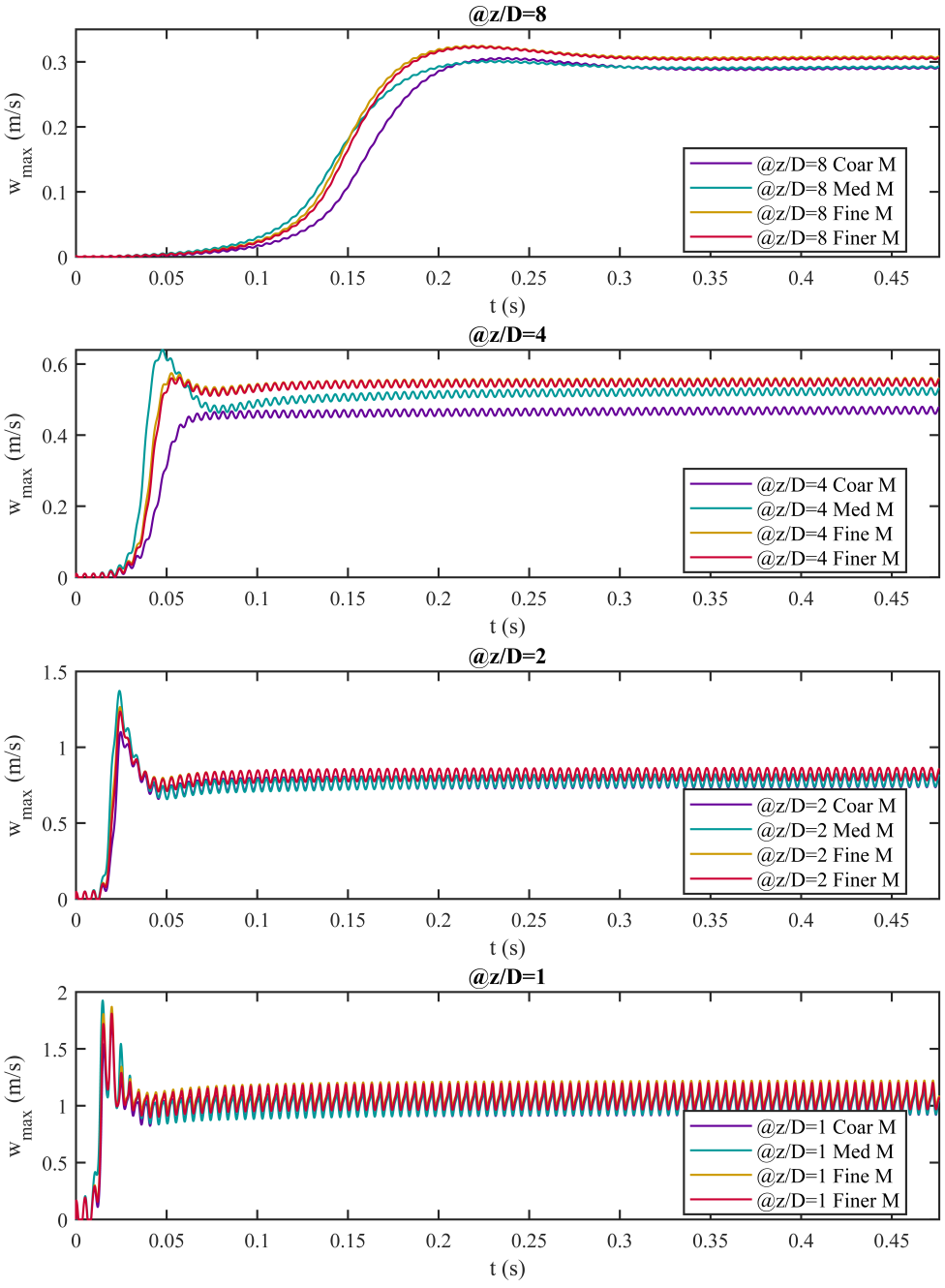

Figure 4.18: Mesh dependency analysis evaluating the maximum w velocity at various distances from the orifice exit over time, from the start to the end of the simulation.

While propagation and generation of coherent structures can't be seen in LSJs, they offer enhanced mixing and heat transfer. Interestingly, upon a burst of high-velocity jets, we observed vortex creation after impingement to the heated surface followed by vortex sweeping. Furthermore, the higher heat capacity of liquids and rapid dissipation prevent the localization of heated areas, and the cavity is constantly refreshed with cold inlet liquid. Operationally, LSJDs operate at lower frequencies than ASJDs due to the higher density and inertia of liquids. Furthermore, they need more force (2-3 times more than ASJDs) to maintain oscillatory motion. Still, the diaphragm operates at reduced deflection, resulting in increased reliability. Furthermore, lower operation frequency and deflection offer a significantly lower noise level, almost silent.

In the Figure 4.18, the velocity distributions of semi–steady-state liquid synthetic jets are presented side-by-side for conical (left) and cylindrical (right) cavity geometries. Although both configurations produce a jet with comparable peak velocities at the orifice exit, the cylindrical cavity tends to focus the flow more narrowly along the centerline, resulting in a longer region of high velocity extending upwards. In contrast, inside the cavity, the cylindrical cavity generates a broader circulation zone.

This contrast in flow patterns suggests that the cylindrical cavity may be advantageous, but as previously discussed, our goal was to reduce fluidic mass inside the cavity in order to increase diaphragm deflection. Because adhesive application in manufacturing is done by hand, a side-by-side experimental study between two geometries is not possible, and fine manufacturing methods are required to capture such minor differences between two designs.

4.3.3 Impingement Thermofluidic Study

Figure 4.19(a), (b) provides streamlines of the jet from the front view and side view, with velocity magnitude shown in Figure 4.19(d) for a device in a quasi-steady state at 210 Hz operation with inflow of 50 mm/s while heated surface is at 50 C higher temperature boundary condition than rest of the system. We can divide the fluidic behavior into three zones. Upon impingement, flow separates into two regions. When impinged flow spreads in the direction of inflow, it travels downstream without generating significant vortical structure. However,

spreading in the opposite direction of the inflow creates a recirculation area. As shown in Figure 4.19(c) and (e), this results in the mixing of heated liquid with upcoming jets; however, unlike ASJDs, the heated flow does not find a passage into the cavity and instead travels to the outlet via inflow. As a result, the cavity is almost at the cold temperature conditions. This also demonstrates the advantage of distancing the device at L_h/D of 4, which has been shown to provide the best thermal performance. If the device is positioned in a location that is known to be in the path of this heated recirculated flow, heated liquid can be sucked into the cavity, reducing the effectiveness of the jets and creating a positive feedback loop for cavity heating. Another important aspect is that a higher inflow rate leads to deflection of the jet from its central impingement, and due to the inclination of the jets, the values of heat flux can be reduced. Figure 4.20 presents quantitative simulation results highlighting how much heat can be removed

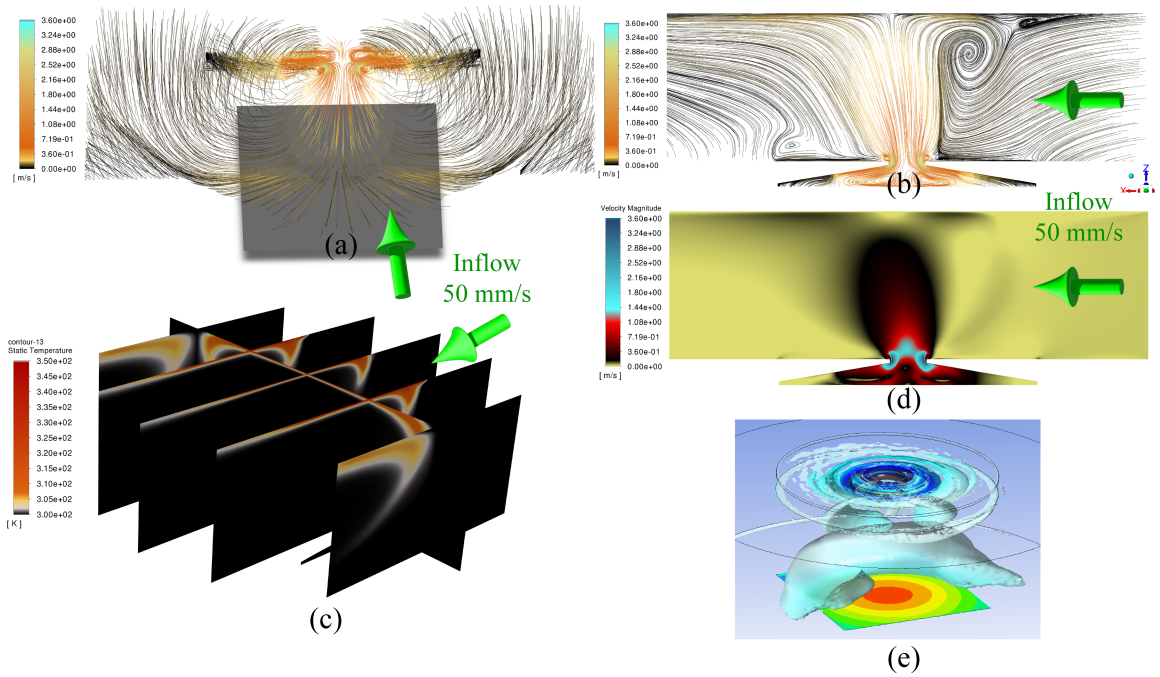

Figure 4.19: Streamlines of jet from front view and (b) side view, (c) temperature distribution of flow on a half-inch parallel surface above the heated surface, (d) velocity distribution from the side, and (e) Q-criterion isosurface and heat flux distibution on heated surface.

with a 50 °C temperature difference between the LSJ and the heated surface. These findings are directly compared to the baseline cross-flow-only case. As previously observed in Figure 4.18, the onset of LSJ generation involves a brief delay, followed by an accumulation of slower initial jets that eventually transition into fully developed synthetic jets. Once these jets impinge on the

heated surface, a sharp increase in both the maximum local heat flux and the total heat removed is evident in Figures 4.20(a) and (b).

In examining the maximum local heat flux at different cross-flow velocities, the values at 210 Hz and 155 Hz are relatively close, peaking at 158 $\mathrm{W}/(\mathrm{cm}^2 \cdot \mathrm{K})$ and 140 $\mathrm{W}/(\mathrm{cm}^2 \cdot \mathrm{K})$, respectively. After the system reaches a quasi-steady state, these values decrease to approximately 35, 45, and 43 $\mathrm{W}/(\mathrm{cm}^2 \cdot \mathrm{K})$ at 210 Hz for cross-flow velocities of 10, 30, and 50 mm/s, respectively. At 155 Hz, the corresponding values stabilize at 37, 36, and 33.5 $\mathrm{W}/(\mathrm{cm}^2 \cdot \mathrm{K})$. By comparison, before LSJ impingement, the local heat flux was only 14, 21, and 27 $\mathrm{W}/(\mathrm{cm}^2 \cdot \mathrm{K})$ for cross-flow velocities of 10, 30, and 50 mm/s, respectively.

A similar trend is observed in terms of total heat removal. Prior to LSJ impingement, the system removes 15.7, 26.5, and 33.7 W for cross-flow velocities of 10, 30, and 50 mm/s, respectively. With the introduction of LSJ at 210 Hz, these values jump to 342.3, 348.7, and 334.4 W, while at 155 Hz they reach 281.2, 268, and 269 W. Eventually, they stabilize at 147.7, 197, and 176 W for 210 Hz, and 167.7, 152.1, and 127.2 W for 155 Hz, respectively, demonstrating the substantial influence of both frequency and cross-flow velocity on the heat removal performance.

The presence of a cross flow is known to significantly affect the heat transfer characteristics of impinging jets, consistent with the findings of Goldstein *et al.* [278]. Their results can be summarized in three main points:

- **Large jet-to-plate spacing** $(L/D = 12)$: Cross flow diminishes the peak heat transfer coefficient by deflecting the jet further downstream and increasing jet–cross-flow mixing, thus lowering the approach velocity at the wall.

- **Small jet-to-plate spacing** $(L/D = 6)$: Cross flow can enhance the peak heat transfer coefficient, particularly at higher blowing rates $(M > 9)$, due to increased turbulence intensity along the jet centerline caused by the mixing of the cross-flowing stream.

- **Location of the maximum Nusselt number**: The jet's symmetry is disrupted by the cross flow, causing the peak local Nusselt number to shift downstream from the geometric center as M decreases.

In the context of our simulations, it can be seen that at 155Hz, cross flow of 10 mm/s, and at 210 Hz, cross flow of 30 mm/s are showing best performance. This reavels a complex interplay between jet frequency, cross-flow velocity, and jet-to-plate spacing requiring further test and analysis.

Looking at the local heat flux profile on the heater's centerline in Figure 4.20(c), the influence of recirculation is clearly evident on the left side of the graph (where the inflow begins). Here, the impinging jet, after spreading radially, is forced back onto the heated plate by the cross flow, reducing the local heat flux. This "folding-back" effect becomes more pronounced as the cross-flow velocity increases, effectively creating a localized stagnation point on one side of the heated surface. Furthermore, at lower jet frequencies (155 Hz), the jet is weaker compared to 210 Hz; as a result, a cross-flow velocity of 50 mm/s can bend the jet from its normal impingement path, thereby reducing the maximum achievable heat flux upon impingement.

Figure 4.20(d) depicts the w-velocity profile along the center axis of the LSJD. Notably, at 210 Hz, the cross flow can enhance the velocity component normal to the heated plate at the center line of the simulation, as part of the cross-flow momentum merges with the jet stream and increases its impingement velocity. However, at 155 Hz, the weaker jet is more easily deflected by the cross flow, causing a reduction in the normal velocity component and, in turn, diminishing its overall heat transfer effectiveness.

Figure 4.21 illustrates the surface heat flux distribution on the heated plate for two jet frequencies (155 Hz in the top row and 210 Hz in the bottom row) and three cross-flow velocities (10, 30, and 50 mm/s from left to right). Several key observations can be drawn from these contour plots.

At lower cross-flow velocities (10 mm/s), the heat flux contours appear nearly axisymmetric with peak in the central region of impingement. This indicates that the synthetic jet can maintain a relatively normal trajectory to the surface, resulting in a high local heat flux where the jet core impinges. As the cross-flow velocity increases to 30 and 50 mm/s, there is a subtle shift in the high-flux region and a broader spread in the contour levels, reflecting the cross flow's growing influence on jet trajectory. Comparing the top row (155 Hz) to the bottom row (210 Hz) highlights the effect of operating frequency on heat transfer performance.

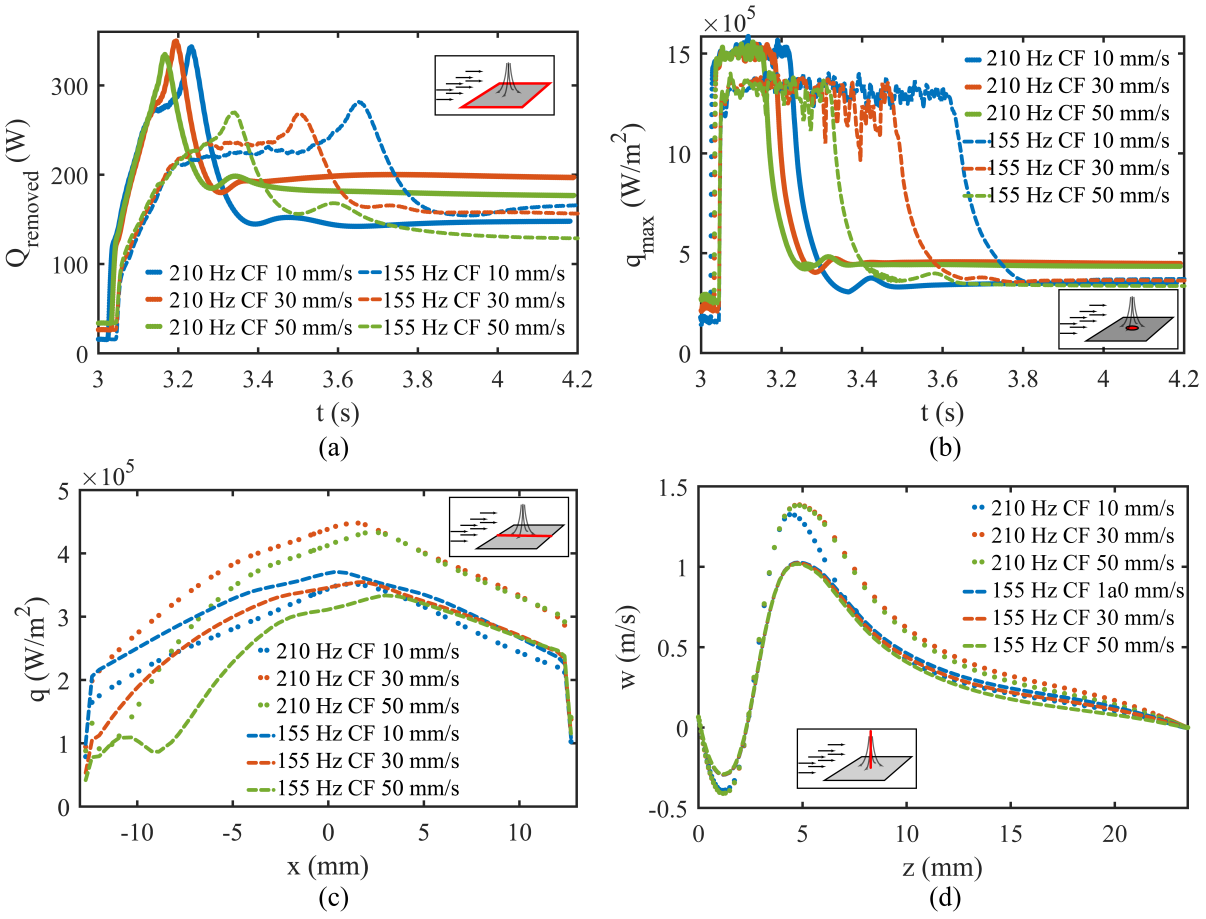

Figure 4.20: (a) Integrated total heat removal, (b) maximum heat removal flux, (c) heat flux distribution on the central line of the heated surface, and (d) ejection velocity in the z direction on the normal line from the center of the device to the heated surface, for the device at 210 Hz and various inflow rates.

In general, the 210 Hz jet exhibits a more pronounced peak heat flux near the center, consistent with a stronger synthetic jet that better resists cross-flow deflection. At 155 Hz, the jet is weaker and more susceptible to bending or diffusion by the cross flow, leading to a slightly reduced maximum heat flux and a more radially dispersed contour pattern. As the cross-flow velocity increases from 10 to 50 mm/s, the jet is progressively deflected downstream. Although the center of the impingement region remains roughly in the middle of the plate, the area of high heat flux grows asymmetrical, especially at the lower frequency of 155 Hz. This effect arises because the weaker jet cannot fully counteract the momentum of the cross flow, which promotes additional mixing and recirculation regions (notice the crescent at 155 Hz). In contrast, at 210 Hz, the jet retains more of its axial momentum, so while there is still some bending, the central peak remains relatively pronounced. These distributions underscore the importance of matching jet frequency and cross-flow velocity to the desired cooling objective. A higher-frequency synthetic jet (e.g., 210 Hz) can produce a sharper and more intense impingement zone, which may be advantageous for cooling highly localized hot spots. Conversely, a slightly lower frequency in conjunction with moderate cross flow could offer more uniform coverage, potentially beneficial for broader surfaces requiring more even heat removal.

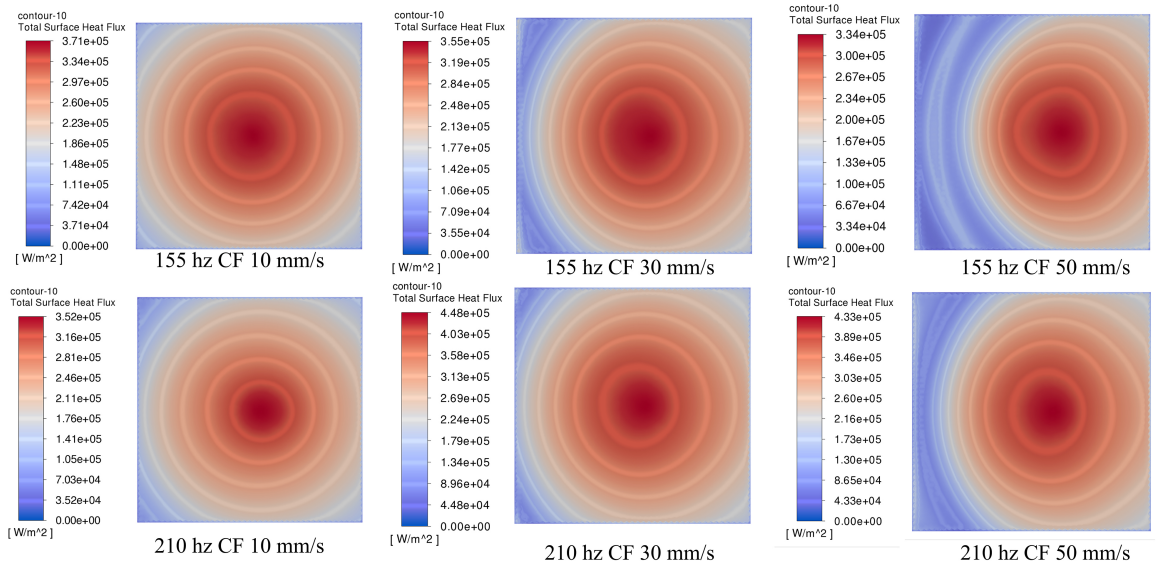

Figure 4.21: surface heat flux distribution on the heated plate for two synthetic jet frequencies (155 Hz in the top row, 210 Hz in the bottom row) and three cross-flow velocities (10, 30, and 50 mm/s from left to right).

4.4 Conclusions and Future Work

This research presents a proof-of-concept study demonstrating the feasibility of Liquid Synthetic Jet Devices (LSJDs) for high-performance immersion cooling. LSJDs can increase the COP of immersion cooling tanks by up to 12 times by introducing jet impingements at speeds of up to 0.5 m/s. Experiments highlight that using a single DI water LSJD, an average heat transfer coefficient of up to 1.7 W/cm²·K can be achieved on a polished one-square-inch aluminum surface. Power consumption is almost negligible at less than 0.25 W, which is significantly lower than traditional rotary pumps at comparable flow rates that consume 5-10 W. LSDJs are solid-state devices with no moving parts that operate almost silently and are dependable in harsh thermal or vibration environments. 3D CFD simulations show that LSJD-assisted immersion cooling can remove 200 W of heat even in the harshest fluidic conditions. Further improvement can be seen using metal foams and enhanced surfaces. Best thermal performance is achieved when the heat source is sufficiently close to the surface and there is no local mixing into the cavities. Increased inflow rate, on the other hand, can reduce the effect of jet impingement by folding the heated liquid back onto the heated surface and inclining the jet upon impingement. LSJDs operate at lower frequencies than ASJDs due to liquid density and inertia.

Although this study provides an understanding of how to build and implement liquid synthetic jets for heat transfer augmentation of immersion cooling systems, several avenues remain open for further investigation:

- Building a low-cost and high-efficiency voltage amplifier to drive the synthetic jets more effectively. Future work should focus on designing amplifier circuits that minimize power losses while delivering a stable output voltage over a selected frequency range of less than 300 Hz. This research could explore innovative semiconductor materials and circuit topologies, and consider integrating digital control strategies to precisely regulate voltage.

- Studying the system when impinging on enhanced surfaces to assess its performance with different macro and micro sized fins. Enhanced surfaces, featuring micro- or even

nano-structured coatings, have the potential to significantly modify local heat transfer characteristics. Future investigations should include both detailed simulations and experimental analyses to understand how different surface textures and material properties affect the liquid syntheit jet impingement dynamics and the resultant heat flux.

- Investigating the impact of different angles of jet impingement relative to the cross flow, as well as varying jet frequencies and cross-flow rates, to optimize heat transfer performance. By exploring a wider range of impingement angles, researchers can determine how directional control of the jet interacts with cross-flow effects to enhance or diminish the cooling performance. Systematic studies should aim to correlate variations in operating frequency and cross-flow velocity with changes in the thermal boundary layer, ultimately identifying optimal configurations for specific cooling scenarios.

- Exploring configurations involving multiple synthetic jets to evaluate the benefits of impingement in array setups. The interaction of multiple jets could lead to synergistic effects that enhance overall cooling efficiency. Future work should investigate the spatial arrangement, phase synchronization, and spacing between jets, using both numerical simulations and experimental methods, to determine the most effective array configurations that maximize heat removal without detrimental jet-to-jet interference.

- Evaluating the effects of positioning synthetic jets at different locations around the target surface (e.g., from four different sides parallel to the heated surface) to achieve more uniform cooling. Altering the positioning and orientation of jets can help create a more homogeneous temperature distribution across the surface. Detailed studies are needed to quantify how different configurations influence the local heat transfer and to develop design guidelines for achieving optimal thermal uniformity, which is critical in applications like electronic cooling.

- Improving the cavity and manufacturing design to enhance the detachment of the ejected jet from the orifice before re-ingestion into the cavity. Future research should focus on optimizing the cavity geometry and orifice design to promote clean jet detachment. This

might involve advanced CFD analyses and experimental validation, targeting modifications in shape or operation frequency that ensure the jet remains effective in impingement and does not suffer from premature re-ingestion, thereby maximizing cooling performance.

- Utilizing CNC machining and machine-based manufacturing techniques to reduce fabrication uncertainties and ensure consistent device performance. Adopting precision manufacturing methods can minimize dimensional variations and defects, leading to improved repeatability and scalability of the synthetic jet devices. Future studies should develop standardized production processes specifically in adhesive application to ultimately enhancing the overall performance and commercial viability of the system. Furthermore, new more efficient piezoelectric ceramics must be employed to reduce the operating voltage of the system.

- Testing the system in real immersion cooling tanks to simulate operational conditions and validate its practical applicability. Immersion cooling environments introduce additional complexities, such as fluid compatibility. Conducting experiments in realistic cooling tanks will provide critical data on the performance of synthetic jets under true operational conditions, paving the way for their application in industrial and commercial cooling solutions.

- Conducting prolonged reliability tests of the piezoelectric diaphragm during extended operation to assess durability. Long-term endurance studies are essential to ensure that the piezoelectric components can withstand the mechanical, thermal, and electrical stresses encountered during continuous operation. Future work should involve rigorous lifetime testing and failure analysis, which will inform design improvements aimed at enhancing durability and reducing maintenance requirements.

- Investigating the system's performance in two-phase immersion cooling environments to explore its potential for advanced thermal management applications. Two-phase cooling, involving both liquid and vapor phases, offers enhanced heat transfer capabilities that

could be leveraged in high-power density applications. Future research should examine how synthetic jets interact with phase-change phenomena, such as boiling and condensation, and optimize the system to efficiently manage the thermal loads associated with two-phase cooling. Orifice design, and spacing must be optimized to prevent bubble injestion inside the cavity.

- Employing higher-fidelity simulations (e.g., Large Eddy Simulation or Direct Numerical Simulation) could offer deeper insights into the turbulent structures and unsteady flow features that govern heat transfer performance.

- Extended Applications: Beyond electronics cooling, the principles demonstrated here could be adapted to other thermal management challenges (e.g., gas turbine blade cooling, high-temperature heat exchangers, or chemical process equipment) where localized heat removal is critical.

By pursuing these directions, future studies can build upon the present work to develop more robust, efficient, and application-specific cooling strategies that leverage the unique characteristics of liquid synthetic jet devices thermally critical environments.

Bibliography

[1] Mohammad Azarifar, Mehmet Arik, and Je-Young Chang. Liquid cooling of data centers: A necessity facing challenges. *Applied Thermal Engineering*, page 123112, 2024. publisher: Elsevier.

[2] Eric Masanet, Arman Shehabi, Nuoa Lei, Sarah Smith, and Jonathan Koomey. Recalibrating global data center energy-use estimates. *Science*, 367(6481):984–986, feb 28 2020. publisher: American Association for the Advancement of Science.

[3] Data Centers and Servers. https://www.energy.gov/eere/buildings/data-centers-and-servers. [Online; accessed 2023-09-17].

[4] An Inefficient Truth | greenict.org.uk. https://www.greenict.org.uk/an-inefficient-truth. [Online; accessed 2023-05-06].

[5] Beth Whitehead, Deborah Andrews, Amip Shah, and Graeme Maidment. Assessing the environmental impact of data centres part 1: Background, energy use and metrics. *Building and Environment*, 82:151–159, dec 1 2014.

[6] Mark Haranas. Covid-19 Spurs Record Data Center Spending By Amazon, Google, Microsoft. https://www.crn.com/news/data-center/covid-19-spurs-record-data-center-spending-by-amazon-google-microsoft, jan 5 2021. [Online; accessed 2023-08-22].

[7] Data Center - Worldwide | Statista Market Forecast, January 2025. [Online; accessed 20. Jan. 2025].

[8] Ian Bremmer. Technology Companies, Digital World Order Will Replace Unipolar Model, July 2023.

[9] Advanced Small Modular Reactors (SMRs), January 2025. [Online; accessed 20. Jan. 2025].

[10] Standard Power Chooses NuScale's Approved SMR Technology and ENTRA1 Energy to Energize Data Centers | NuScale Power, January 2025. [Online; accessed 20. Jan. 2025].

[11] Samuel K. Moore. Keeping Moore's Law Going Is Getting Complicated. *IEEE Spectrum*, May 2023.

[12] Jan van Schoot. This Machine Could Keep Moore's Law on Track. *IEEE Spectrum*, August 2023.

[13] Samuel K. Moore. The node is nonsense. *IEEE Spectrum*, 57(8):24–30, 8 2020. event-title: IEEE Spectrum.

[14] Shien-Yang Wu, C.H. Chang, M.C. Chiang, C.Y. Lin, J.J. Liaw, J.Y. Cheng, J.Y. Yeh, H.F. Chen, S.Y. Chang, K.T. Lai, M.S. Liang, K.H. Pan, J.H. Chen, V.S. Chang, T.C. Luo, X. Wang, Y.S. Mor, C.I. Lin, S.H. Wang, M.Y. Hsieh, C.Y. Chen, B.F. Wu, C.J. Lin, C.S. Liang, C.P. Tsao, C.T. Li, C.H. Chen, C.H. Hsieh, H.H. Liu, P.N. Chen, C.C. Chen, R. Chen, Y.C. Yeo, C.O. Chui, W. Chang, T.L. Lee, K.B. Huang, H.J. Lin, K.W. Chen, M.H. Tsai, K.S. Chen, X.M. Chen, Y.K. Cheng, C.H. Wang, W. Shue, Y. Ku, S. M. Jang, M. Cao, L.C. Lu, and T.S. Chang. A 3nm cmos finflex™ platform technology with enhanced power efficiency and performance for mobile soc and high performance computing applications. In *2022 International Electron Devices Meeting (IEDM)*. IEEE, December 2022.

[15] Dr. Ian Cutress. 'Better Yield on 5nm than 7nm': TSMC Update on Defect Rates for N5, August 2020.

[16] Tsmc Expands Advanced Technology Leadership with N4P Process. http://pr.tsmc.com/english/news/2874, oct 26 2021. [Online; accessed 2023-05-05].

[17] Amd: Addressing the challenge of energy-efficient computing. https://venturebeat.com/data-infrastructure/amd-addressing-the-challenge-of-energy-efficient-computing/, jul 6 2022. [Online; accessed 2023-05-05].

[18] NVIDIA Hopper GPU Architecture, January 2025. [Online; accessed 20. Jan. 2025].

[19] NVIDIA Ada Lovelace Architecture, January 2025. [Online; accessed 20. Jan. 2025].

[20] Intel® Core™ Processors, FPGAs, GPUs, Networking, Software, January 2025. [Online; accessed 20. Jan. 2025].

[21] AMD EPYC™ 4th Gen 9004 & 8004 Series Server Processors – Details, January 2025. [Online; accessed 20. Jan. 2025].

[22] Yingbo Zhang, Kui Shan, Xiuming Li, Hangxin Li, and Shengwei Wang. Research and Technologies for next-generation high-temperature data centers – State-of-the-arts and future perspectives. *Renewable and Sustainable Energy Reviews*, 171:112991, jan 1 2023.

[23] Nicola Jones. How to stop data centres from gobbling up the world's electricity. *Nature*, 561(7722):163–166, sep 12 2018. Bandiera_abtest: a Cg_type: News Feature number: 7722 publisher: Nature Publishing Group Subject_term: Energy, Engineering, Research data, Computer science.

[24] Ali Habibi Khalaj and Saman K. Halgamuge. A Review on efficient thermal management of air- and liquid-cooled data centers: From chip to the cooling system. *Applied Energy*, 205:1165–1188, nov 1 2017.

[25] Dongmei Huang, Chao Yang, and Bang Li. *Rack-Level Cooling and Server-Level Cooling*, pages 227–237. John Wiley & Sons, Ltd, 2021. section: 14 _eprint: https://onlinelibrary.wiley.com/doi/pdf/10.1002/9781119597537.ch14 DOI: 10.1002/9781119597537.ch14.

[26] Ali Heydari, Bahareh Eslami, Vahideh Radmard, Fred Rebarber, Tyler Buell, Kevin Gray, Sam Sather, and Jeremy Rodriguez. Power Usage Effectiveness Analysis of a

High-Density Air-Liquid Hybrid Cooled Data Center. *ASME Digital Collection*, December 2022.

[27] ASHRAE Technical Committee 9.9, Mission Critical Facilities, Data Centers, Technology Spaces and Electronic Equipment. Water-Cooled Servers Common Designs, Components, and Processes [White paper]. Technical report, 2019.

[28] Malik Megdiche, Jay Park, and Sarah Hanna. *Data Center Electrical Design*, pages 441–481. John Wiley & Sons, Ltd, 2021. section: 25 _eprint: https://onlinelibrary.wiley.com/doi/pdf/10.1002/9781119597537.ch25 DOI: 10.1002/9781119597537.ch25.

[29] ASHRAE Data Center Resources, January 2025. [Online; accessed 20. Jan. 2025].

[30] Hwaiyu Geng. *Data Center Handbook*. John Wiley & Sons, Inc., apr 20 2021.

[31] I. K. M. User. 2022 Best Practice Guidelines for the EU Code of Conduct on Data Centre Energy Efficiency. https://e3p.jrc.ec.europa.eu/publications/2022-best-practice-guidelines-eu-code-conduct-data-centre-energy-efficiency, mar 14 2022. [Online; accessed 2023-08-25].

[32] Bill Tschudi and Otto VanGeet. Best Practices Guide for Energy-Efficient Data Center Design. Technical Report NREL/BR-7A40-47201, mar 1 2011.

[33] Lubnnia Souza, Kádna Camboim, and Fernanda Alencar. A systematic literature review about integrating dependability attributes, performability and sustainability in the implantation of cooling subsystems in data center. *The Journal of Supercomputing*, 78(14):15820–15856, sep 1 2022.

[34] Yanan Liu, Xiaoxia Wei, Jinyu Xiao, Zhijie Liu, Yang Xu, and Yun Tian. Energy consumption and emission mitigation prediction based on data center traffic and PUE for global data centers. *Global Energy Interconnection*, 3(3):272–282, jun 1 2020.

[35] Daehoon Kang, Jooyoung Lee, Anirban Chakraborty, Sang-Eui Lee, Gildong Kim, and Choongho Yu. Recent Advances in Two-Phase Immersion Cooling with Surface Modifications for Thermal Management. *Energies*, 15(3):1214, 1 2022. number: 3 publisher: Multidisciplinary Digital Publishing Institute.

[36] Uptime Institute's 2022 Global Data Center Survey Reveals Strong Industry Growth as Operators Brace for Expanding Sustainability Requirements, January 2025. [Online; accessed 20. Jan. 2025].

[37] Jinkyun Cho, Taesub Lim, and Byungseon Sean Kim. Viability of datacenter cooling systems for energy efficiency in temperate or subtropical regions: Case study. *Energy and Buildings*, 55:189–197, dec 1 2012.

[38] Best Practices for Data Centers: Lessons Learned from Benchmarking 22 Data Centers, January 2025. [Online; accessed 20. Jan. 2025].

[39] PE Roger Schmidt PhD. Ashrae's Data Center Thermal Guidelines-Air-Cooled Evolution. *ASHRAE Journal*, 64(5):54–60, 2022. publisher: American Society of Heating, Refrigeration and Air Conditioning Engineers, Inc.

[40] Tony Evans. The Different Technologies for Cooling Data Centers [White Paper]. Technical report, Schneider Electric – Data Center Science Center. [Online; accessed 2023-08-28].

[41] Jun Dai, Michael M. Ohadi, Diganta Das, and Michael G. Pecht. *Principal Cooling Methods*, pages 47–69. Springer, New York, NY, 2014. DOI: 10.1007/978-1-4614-5602-5_4.

[42] Ruolan Zhao, Yahui Du, Xiaochen Yang, Zhihua Zhou, Wufan Wang, and Xueqing Yang. A critical review on the thermal management of data center for local hotspot elimination. *Energy and Buildings*, page 113486, aug 22 2023.

[43] Zongwei Han, Haotian Wei, Xiaoqing Sun, Chenguang Bai, Da Xue, and Xiuming Li. Study on influence of operating parameters of data center air conditioning system based on the concept of on-demand cooling. *Renewable Energy*, 160:99–111, nov 1 2020.

[44] Nosayba El-Sayed, Ioan A. Stefanovici, George Amvrosiadis, Andy A. Hwang, and Bianca Schroeder. Temperature management in data centers: why some (might) like it hot. *ACM Conferences*, 40(1):163–174, June 2012.

[45] Mir Seyed Mohammad Mohsen Emamat, Saif Wakeel, Maghsoud Amiri, Shafi Ahmad, and Sedat Bingol. A novel approach based on grey simplified best–worst method and grey possibility degree for evaluating materials in semiconductor industries. *Soft Computing*, 27(22):17043–17062, nov 1 2023.

[46] Longfei Wang and Zhong Lin Wang. Advances in piezotronic transistors and piezotronics. *Nano Today*, 37:101108, apr 1 2021.

[47] Litton Power. The Ongoing Value of Hard Disk Drives in Data Centers | ESF. https://www.enterprisestorageforum.com/news/hard-disk-drives-data-centers/, sep 10 2021. [Online; accessed 2023-09-01].

[48] Martijn Koot and Fons Wijnhoven. Usage impact on data center electricity needs: A system dynamic forecasting model. *Applied Energy*, 291:116798, jun 1 2021.

[49] Why HDDs Dominate Hyperscale Cloud Architecture | Seagate US, January 2025. [Online; accessed 20. Jan. 2025].

[50] Andy Pearson. Carbon dioxide—new uses for an old refrigerant. *International Journal of Refrigeration*, 28(8):1140–1148, dec 1 2005.

[51] Change Is on the Horizon in Data Center Cooling Refrigerants, May 2018. [Online; accessed 20. Jan. 2025].

[52] James M. Calm. The next generation of refrigerants – Historical review, considerations, and outlook. *International Journal of Refrigeration*, 31(7):1123–1133, nov 1 2008.

[53] U.S. Environmental Protection Agency. Phasing out HCFC refrigerants to protect the ozone layer. Technical Report EPA-430-F-09-080.

[54] Mark O. McLinden, J. Steven Brown, Riccardo Brignoli, Andrei F. Kazakov, and Piotr A. Domanski. Limited options for low-global-warming-potential refrigerants. *Nature Communications*, 8(1):14476, feb 17 2017. number: 1 publisher: Nature Publishing Group.

[55] Canada, Environment and Climate Change. Regulatory amendments on hydrofluorocarbons: Frequently asked questions. https://www.canada.ca/en/environment-climate-change/services/canadian-environmental-protection-act-registry/ozone-regulations-amendments-questions.html, nov 6 2017. Last Modified: 2022-12-09.

[56] OAR US EPA. Substitutes in Centrifugal Chillers. https://www.epa.gov/snap/substitutes-centrifugal-chillers, nov 5 2014. [Online; accessed 2023-08-28].

[57] F. Molés, J. Navarro-Esbrí, B. Peris, A. Mota-Babiloni, and K. Kontomaris. Thermodynamic analysis of a combined organic Rankine cycle and vapor compression cycle system activated with low temperature heat sources using low GWP fluids. *Applied Thermal Engineering*, 87:444–453, 2015.

[58] David A. Didion and Donald B. Bivens. Role of refrigerant mixtures as alternatives to CFCs. *International Journal of Refrigeration*, 13(3):163–175, may 1 1990.

[59] Leelananda Rajapaksha. Influence of special attributes of zeotropic refrigerant mixtures on design and operation of vapour compression refrigeration and heat pump systems. *Energy Conversion and Management*, 48(2):539–545, feb 1 2007.

[60] Kazuaki Yazawa, Supriya Dharkar, Orkan Kurtulus, and Eckhard A. Groll. Optimum design for thermoelectric in a sub-cooled trans-critical CO2 heat pump for data center cooling. In *2015 31st Thermal Measurement, Modeling & Management Symposium (SEMI-THERM)*, pages 19–24, 3 2015. ISSN: 1065-2221.

[61] Junyuan Liao, Chunxin Yang, and Han Yang. Experimental study and information entropy analysis on periodic performance of a PCM thermal management system for blade servers in data centers. *International Journal of Thermal Sciences*, 188:108216, jun 1 2023.

[62] Srikanth Rangarajan, Scott Schiffres, and Bahgat Sammakia. A Review of Recent Developments in "On-Chip" Embedded Cooling Technologies for Heterogeneous Integrated Applications. *Engineering*, apr 13 2023. [Online; accessed 2023-06-04].

[63] D. W. Anderson, F. J. Sparacio, and R. M. Tomasulo. The IBM System/360 Model 91: Machine Philosophy and Instruction-Handling. *IBM Journal of Research and Development*, 11(1):8–24, 1 1967.

[64] Avram Bar-Cohen and Karl J. L. Geisler. Cooling the Electronic Brain. *Mechanical Engineering*, 133(04):38–41, apr 1 2011.

[65] Thomas J. Breen, Ed J. Walsh, Jeff Punch, Amip J. Shah, and Cullen E. Bash. From chip to cooling tower data center modeling: Part I Influence of server inlet temperature and temperature rise across cabinet. In *2010 12th IEEE Intersociety Conference on Thermal and Thermomechanical Phenomena in Electronic Systems*, pages 1–10, 6 2010. ISSN: 1087-9870.

[66] Ed J. Walsh, Thomas J. Breen, J. Punch, Amip J. Shah, and Cullen E. Bash. From chip to cooling tower data center modeling: Part II Influence of chip temperature control philosophy. In *2010 12th IEEE Intersociety Conference on Thermal and Thermomechanical Phenomena in Electronic Systems*, pages 1–7, 6 2010. ISSN: 1087-9870.

[67] Nuoa Lei and Eric Masanet. Statistical analysis for predicting location-specific data center PUE and its improvement potential. *Energy*, 201:117556, jun 15 2020.

[68] White Paper: Liquid Immersion Cooling Reduces Power Use and Drives Sustainability Efforts in Data Centers, April 2024. [Online; accessed 20. Jan. 2025].

[69] *Maintaining Datacom Rack Inlet Air Temperatures With Water Cooled Heat Exchanger*, volume Advances in Electronic Packaging, Parts A, B, and C of *International Electronic Packaging Technical Conference and Exhibition*, 07 2005.

[70] Ali Almoli, Adam Thompson, Nikil Kapur, Jonathan Summers, Harvey Thompson, and George Hannah. Computational fluid dynamic investigation of liquid rack cooling in data centres. *Applied Energy*, 89(1):150–155, jan 1 2012.

[71] *Feasibility Study of Rear Door Heat Exchanger for a High Capacity Data Center*, volume ASME 2022 International Technical Conference and Exhibition on Packaging and Integration of Electronic and Photonic Microsystems of *International Electronic Packaging Technical Conference and Exhibition*, 10 2022.

[72] Ramendra Kumar and Sanjeev Jain. Performance analysis of an in-situ data centre. *Energy and Buildings*, 209:109679, feb 15 2020.

[73] Jetsadaporn Priyadumkol and Chawalit Kittichaikarn. Application of the combined air-conditioning systems for energy conservation in data center. *Energy and Buildings*, 68:580–586, jan 1 2014.

[74] Hongjie Lu, Zhongbin Zhang, and Liu Yang. A review on airflow distribution and management in data center. *Energy and Buildings*, 179:264–277, nov 15 2018.

[75] *Performance of Temperature Controlled Perimeter and Row-Based Cooling Systems in Open and Containment Environment*, volume Volume 8B: Heat Transfer and Thermal Engineering of *ASME International Mechanical Engineering Congress and Exposition*, 11 2015.

[76] Ben Cutler, Spencer Fowers, Jeffrey Kramer, and Eric Peterson. Dunking the data center. *IEEE Spectrum*, 54(3):26–31, 3 2017. event-title: IEEE Spectrum.

[77] Patrick Kennedy. Microsoft Project Natick Gen 3 Undersea Azure AZ. https://www.servethehome.com/microsoft-project-natick-gen-3-undersea-azure-az/, jul 11 2020. [Online; accessed 2024-02-29].

[78] Adesh Kumar, Gaurav Verma, Vijay Nath, and Sushabhan Choudhury. Ic Packaging: 3d IC Technology and Methods. In Vijay Nath, editor, *Proceedings of the International Conference on Nano-electronics, Circuits & Communication Systems*, Lecture Notes in Electrical Engineering, pages 303–317, Singapore, 2017. Springer.

[79] E. J. Rymaszewski, J. L. Walsh, and G. W. Leehan. Semiconductor Logic Technology in IBM. *IBM Journal of Research and Development*, 25(5):603–616, 9 1981. event-title: IBM Journal of Research and Development.

[80] Andrew Kearney, Li Li, and Sean Sanford. Interaction between TIM1 and TIM2 for mechanical robustness of integrated heat spreader. In *2009 25th Annual IEEE Semiconductor Thermal Measurement and Management Symposium*, pages 293–298, 3 2009. ISSN: 1065-2221.

[81] Memory Cooling MX4 - CoolIT Systems, June 2021. [Online; accessed 21. Jan. 2025].

[82] Ali Heydari, Ahmad R. Gharaibeh, Mohammad Tradat, Qusai soud, Yaman Manaserh, Vahideh Radmard, Bahareh Eslami, Jeremy Rodriguez, and Bahgat Sammakia. Experimental evaluation of direct-to-chip cold plate liquid cooling for high-heat-density data centers. *Applied Thermal Engineering*, 239:122122, feb 15 2024.

[83] Girish Kini, Choong-Un Kim, H. Madanipour, Je-Young Chang, Amitesh Saha, Aravindha Antoniswamy, Iolanda Klein, Michael Jorgensen, Minseok Ha, Peng Li, Berhanu Wondimu, and Dev Kulkarni. Corrosion in Liquid Cooling Systems with Water-Based Coolant – Part 1: Flow Loop Design for Reliability Tests. In *2020 19th IEEE Intersociety Conference on Thermal and Thermomechanical Phenomena in Electronic Systems (ITherm)*, pages 422–428, 7 2020. ISSN: 2577-0799.

[84] Choong-Un Kim, Geng Ni, Girish Kini, Je-Young Chang, Amitesh Saha, Aravindha Antoniswamy, Iolanda Klein, Michael Jorgensen, Minseok Ha, Peng Li, Berhanu Wondimu, and Dev Kulkarni. Corrosion in Liquid Cooling Systems with Water-Based Coolant – Part 2: Corrosion Reliability Testing and Failure Model. In *2020 19th IEEE*

Intersociety Conference on Thermal and Thermomechanical Phenomena in Electronic Systems (ITherm), pages 429–434, 7 2020. ISSN: 2577-0799.

[85] Ali C. Kheirabadi and Dominic Groulx. Cooling of server electronics: A design review of existing technology. *Applied Thermal Engineering*, 105:622–638, 7 2016.

[86] Sreya Sarkar, Rohit Gupta, Tamal Roy, Ranjan Ganguly, and Constantine M. Megaridis. Review of jet impingement cooling of electronic devices: Emerging role of surface engineering. *International Journal of Heat and Mass Transfer*, 206:123888, 6 2023.

[87] S. M. Sohel Murshed and C. A. Nieto de Castro. A critical review of traditional and emerging techniques and fluids for electronics cooling. *Renewable and Sustainable Energy Reviews*, 78:821–833, October 2017.

[88] S M Sohel Murshed. Introductory chapter: Electronics cooling — an overview. In S M Sohel Murshed, editor, *Electronics Cooling*, chapter 1. IntechOpen, Rijeka, 2016.

[89] Weinan Zhou, Kaijun Dong, Qin Sun, Weimin Luo, Bobo Zhang, Shengli Guan, and Guangwu Wang. Research progress of the liquid cold plate cooling technology for server electronic chips: A review. *International Journal of Energy Research*, 46(9):11574–11595, 2022. _eprint: https://onlinelibrary.wiley.com/doi/pdf/10.1002/er.7979.

[90] Nicholas Gilmore, Victoria Timchenko, and Chris Menictas. Manifold microchannel heat sink topology optimisation. *International Journal of Heat and Mass Transfer*, 170:121025, 5 2021.

[91] Yuhui Pan, Rui Zhao, Yongle Nian, and Wenlong Cheng. Study on the flow and heat transfer characteristics of pin-fin manifold microchannel heat sink. *International Journal of Heat and Mass Transfer*, 183:122052, feb 1 2022.

[92] D.B. Tuckerman and R.F.W. Pease. High-performance heat sinking for VLSI. *IEEE Electron Device Letters*, 2(5):126–129, 5 1981. event-title: IEEE Electron Device Letters.

[93] W. Escher, B. Michel, and D. Poulikakos. A novel high performance, ultra thin heat sink for electronics. *International Journal of Heat and Fluid Flow*, 31(4):586–598, aug 1 2010.

[94] Stephen M. Walsh, Bernard A. Malouin, Eric A. Browne, Kevin R. Bagnall, Evelyn N. Wang, and James P. Smith. Embedded Microjets for Thermal Management of High Power-Density Electronic Devices. *IEEE Transactions on Components, Packaging and Manufacturing Technology*, 9(2):269–278, 2 2019. event-title: IEEE Transactions on Components, Packaging and Manufacturing Technology.

[95] Direct-to-Chip Liquid Cooling Technology | JetCool, December 2024. [Online; accessed 21. Jan. 2025].

[96] On-Chip Semiconductor Liquid Cooling Solutions | JetCool. https://jetcool.com/semiconductor-liquid-cooling/, sep 12 2023. [Online; accessed 2023-09-18].

[97] Press Release - Imec demonstrates efficient cost-effective cooling solution for high performance chips, January 2025. [Online; accessed 21. Jan. 2025].

[98] Sreejith Kochupurackal Rajan, Ankit Kaul, Thomas Sarvey, Gary S. May, and Muhannad S. Bakir. Design Considerations, Demonstration, and Benchmarking of Silicon Microcold Plate and Monolithic Microfluidic Cooling for 2.5d ICs. In *2021 IEEE 71st Electronic Components and Technology Conference (ECTC)*, pages 1418–1426, 6 2021. ISSN: 2377-5726.

[99] Phillip E. Tuma. The merits of open bath immersion cooling of datacom equipment. In *2010 26th Annual IEEE Semiconductor Thermal Measurement and Management Symposium (SEMI-THERM)*, pages 123–131, 2 2010. ISSN: 1065-2221.

[100] Jordan Mizerak, Bernard Malouin, and Jetcool Technologies Inc. Microjet-Cooled Flanges for Electronic Devices, May 2020. [Online; accessed 21. Jan. 2025].

[101] Je-Young Chang, Devdatta Kulkarni, Ravi Mahajan, Michael Jorgensen, Nick Neal, Rich Dischler, Aravind Dasu, Sandeep Ahuja, and Rajiv Mongia. Package-Level Integration of Liquid Cooling Technology with Microchannel IHS for High Power Cooling. In *2021 20th IEEE Intersociety Conference on Thermal and Thermomechanical Phenomena in Electronic Systems (iTherm)*, pages 18–23, 6 2021. ISSN: 2694-2135.

[102] Shankar Earni, Steve Greenberg, and Walker Johnson. The Installation of Direct Water-Cooling Systems to Reduce Cooling Energy Requirements for High-Performance Computing Centers, August 2020. [Online; accessed 20. Jan. 2025].

[103] Shankar Earni and Steve Greenberg. The Installation of Direct Water-Cooling Systems to Reduce Cooling Energy Requirements for High-Performance Computing Centers. Technical report, Lawrence Berkeley National Lab. (LBNL), Berkeley, CA (United States), sep 28 2020. DOI: 10.20357/B7RC8M.

[104] Alfonso Capozzoli and Giulio Primiceri. Cooling Systems in Data Centers: State of Art and Emerging Technologies. *Energy Procedia*, 83:484–493, dec 1 2015.

[105] B. Kroposki, D. Mooney, T. Markel, and B. Lundstrom. Energy systems integration facilities at the national renewable energy laboratory. In *2012 IEEE Energytech*, pages 1–4, 5 2012.

[106] Sanjay K. Roy and Individual. Active cold plate/heat sink, November 2000. [Online; accessed 21. Jan. 2025].

[107] Mike Holden, Seyed Kamaleddin Mostafavi Yazdi, Randy Kubik, and CoolIT Systems Inc. Cooling module with leak detector and related systems, September 2022. [Online; accessed 21. Jan. 2025].

[108] H262-Z62 (rev. 100) | High Density Servers - GIGABYTE U.S.A., January 2025. [Online; accessed 21. Jan. 2025].

[109] Li Ling, Quan Zhang, Yuebin Yu, and Shuguang Liao. A state-of-the-art review on the application of heat pipe system in data centers. *Applied Thermal Engineering*, 199:117618, nov 25 2021.

[110] Using Thermosyphon Hybrid Cooling System to Optimize Data Center Water Efficiency. Technical Report DOE/GO-102019-5172, may 24 2019.

[111] Yuwei Zheng, Zhen Li, Xiaohua Liu, Zhen Tong, and Rang Tu. Retrofit of Air-Conditioning System in Data Center Using Separate Heat Pipe System. In Angui Li, Yingxin Zhu, and Yuguo Li, editors, *Proceedings of the 8th International Symposium on Heating, Ventilation and Air Conditioning*, Lecture Notes in Electrical Engineering, pages 685–694, Berlin, Heidelberg, 2014. Springer.

[112] Tao Ding, Xiaoxuan Chen, Hanwen Cao, Zhiguang He, Jianmin Wang, and Zhen Li. Principles of loop thermosyphon and its application in data center cooling systems: A review. *Renewable and Sustainable Energy Reviews*, 150:111389, oct 1 2021.

[113] Aranya Chauhan and Satish G. Kandlikar. Characterization of a dual taper thermosiphon loop for CPU cooling in data centers. *Applied Thermal Engineering*, 146:450–458, jan 5 2019.

[114] Raffaele L. Amalfi, Filippo Cataldo, Jackson B. Marcinichen, and John R. Thome. Experimental Characterization of a Server-Level Thermosyphon for High-Heat Flux Dissipations. In *2020 19th IEEE Intersociety Conference on Thermal and Thermomechanical Phenomena in Electronic Systems (ITherm)*, pages 402–409, 7 2020. ISSN: 2577-0799.

[115] Nicolas Lamaison, Jackson Braz Marcinichen, and John Richard Thome. Two-Phase Flow Control of Electronics Cooling With Pseudo-CPUs in Parallel Flow Circuits: Dynamic Modeling and Experimental Evaluation. *Journal of Electronic Packaging*, 135(030908), jul 24 2013. [Online; accessed 2023-09-26].

[116] Simiao Fan and Fei Duan. A review of two-phase submerged boiling in thermal management of electronic cooling. *International Journal of Heat and Mass Transfer*, 150:119324, apr 1 2020.

[117] Bharath Ramakrishnan, Cong Hiep Hoang, Sadegh Khalili, Yaser Hadad, Srikanth Rangarajan, Arvind Pattamatta, and Bahgat Sammakia. Experimental Characterization of Two-Phase Cold Plates Intended for High-Density Data Center Servers Using a Dielectric Fluid. *Journal of Electronic Packaging*, 143(020904), mar 5 2021. [Online; accessed 2023-09-25].

[118] Ebullient Introduces Revolutionary "Waterless" Liquid Cooling Technology, September 2023. [Online; accessed 21. Jan. 2025].

[119] R. R. Schmidt and B. D. Notohardjono. High-end server low-temperature cooling. *IBM Journal of Research and Development*, 46(6):739–751, 11 2002. event-title: IBM Journal of Research and Development.

[120] Akasit Poachaiyapoom, Rattapon Leardkun, Jirawat Mounkong, and Somchai Wongwises. Miniature vapor compression refrigeration system for electronics cooling. *Case Studies in Thermal Engineering*, 13:100365, mar 1 2019.

[121] H. M. Hu, T. S. Ge, Y. J. Dai, and R. Z. Wang. Experimental study on water-cooled thermoelectric cooler for CPU under severe environment. *International Journal of Refrigeration*, 62:30–38, feb 1 2016.

[122] Ihtesham Chowdhury, Ravi Prasher, Kelly Lofgreen, Gregory Chrysler, Sridhar Narasimhan, Ravi Mahajan, David Koester, Randall Alley, and Rama Venkatasubramanian. On-chip cooling by superlattice-based thin-film thermoelectrics. *Nature Nanotechnology*, 4(4):235–238, 4 2009. number: 4 publisher: Nature Publishing Group.

[123] A. Bar-Cohen, M. Arik, and M. Ohadi. Direct Liquid Cooling of High Flux Micro and Nano Electronic Components. *Proceedings of the IEEE*, 94(8):1549–1570, 8 2006. event-title: Proceedings of the IEEE.

[124] Yiping Wang, Chen Wen, Qunwu Huang, Xue Kang, Miao Chen, and Huilin Wang. Performance comparison between ethanol phase-change immersion and active water cooling for solar cells in high concentrating photovoltaic system. *Energy Conversion and Management*, 149:505–513, oct 1 2017.

[125] Charlotte Roe, Xuning Feng, Gavin White, Ruihe Li, Huaibin Wang, Xinyu Rui, Cheng Li, Feng Zhang, Volker Null, Michael Parkes, Yatish Patel, Yan Wang, Hewu Wang, Minggao Ouyang, Gregory Offer, and Billy Wu. Immersion cooling for lithium-ion batteries – A review. *Journal of Power Sources*, 525:231094, mar 30 2022.

[126] Yunpeng Zhang, S. L. Ho, and Weinong Fu. Applying Response Surface Method to Oil-Immersed Transformer Cooling System for Design Optimization. *IEEE Transactions on Magnetics*, 54(11):1–5, 11 2018. event-title: IEEE Transactions on Magnetics.

[127] Oktay Sevgin. Multi-liquid heat transfer. https://patents.google.com/patent/US3406244A/en, oct 15 1968. [Online; accessed 2023-09-29].

[128] Richard C. Chu and John H. Seely. Immersion cooling system for modularly packaged components. https://patents.google.com/patent/US3512582A/en, may 19 1970. [Online; accessed 2023-09-29].

[129] Nugroho Agung Pambudi, Alfan Sarifudin, Ridho Alfan Firdaus, Desita Kamila Ulfa, Indra Mamad Gandidi, and Rahmat Romadhon. The immersion cooling technology: Current and future development in energy saving. *Alexandria Engineering Journal*, 61(12):9509–9527, dec 1 2022.

[130] Research Markets. The Worldwide Immersion Cooling Industry is Expected to Reach $700 Million by 2026 at a CAGR of 23.6% from 2021. https://www.globenewswire.com/news-release/2021/07/26/2268720/28124/en/The-Worldwide-Immersion-Cooling-Industry-is-Expected-to-Reach-700-Million-by-2026-at-a-CAGR-of-23-6-from-2021.html, jul 26 2021. [Online; accessed 2023-05-05].

[131] Steven C. Sherwood, Vishal Dixit, and Chryséis Salomez. The global warming potential of near-surface emitted water vapour. *Environmental Research Letters*, 13(10):104006, 9 2018. publisher: IOP Publishing.

[132] Patrick Birbarah, Tarek Gebrael, Thomas Foulkes, Andrew Stillwell, Alexandra Moore, Robert Pilawa-Podgurski, and Nenad Miljkovic. Water immersion cooling of high power density electronics. *International Journal of Heat and Mass Transfer*, 147:118918, feb 1 2020.

[133] Saeed Moghaddam and Ken Kiger. Physical mechanisms of heat transfer during single bubble nucleate boiling of FC-72 under saturation conditions. II: Theoretical analysis. *International Journal of Heat and Mass Transfer*, 52(5):1295–1303, feb 1 2009.

[134] Z. Li and E. Gariboldi. Review on the temperature-dependent thermophysical properties of liquid paraffins and composite phase change materials with metallic porous structures. *Materials Today Energy*, 20:100642, jun 1 2021.

[135] Björn Nienborg, Stefan Gschwander, Gunther Munz, Dominik Fröhlich, Tobias Helling, Rafael Horn, Helmut Weinläder, Felix Klinker, and Peter Schossig. Life Cycle Assessment of thermal energy storage materials and components. *Energy Procedia*, 155:111–120, nov 1 2018.

[136] DOWSIL™ 550 Fluid, January 2025. [Online; accessed 21. Jan. 2025].

[137] B Brandt, Evelin Kletzer, Harald Pilz, Dariya Hadzhiyska, and P Seizov. Siliconchemistry carbon balance—an assessment of greenhouse gas emissions and reductions, 2013.

[138] Other Oils and Fluids | Shell Global, January 2025. [Online; accessed 21. Jan. 2025].

[139] Hiroki Shigemune, Kittamet Pradidarcheep, Yu Kuwajima, Yumeta Seki, Shingo Maeda, and Vito Cacucciolo. Wireless Electrohydrodynamic Actuators for Propulsion and Positioning of Miniaturized Floating Robots. *Advanced Intelligent Systems*, 3(7):2100004, 2021. _eprint: https://onlinelibrary.wiley.com/doi/pdf/10.1002/aisy.202100004.

[140] Omidreza Ghaffari, Francis Grenier, Jean-François Morissette, Martin Bolduc, Simon Jasmin, and Julien Sylvestre. Pool Boiling Experiment of Dielectric Liquids and Numerical Study for Cooling a Microprocessor. In *2019 18th IEEE Intersociety Conference on Thermal and Thermomechanical Phenomena in Electronic Systems (ITherm)*, pages 540–545, 5 2019. ISSN: 2577-0799.

[141] 3M™ Novec™ 7100 Engineered Fluid, January 2025. [Online; accessed 21. Jan. 2025].

[142] Phillip E. Tuma. Design considerations relating to non-thermal aspects of passive 2-phase immersion cooling. In *2011 27th Annual IEEE Semiconductor Thermal Measurement and Management Symposium*, pages 1–9, 3 2011. ISSN: 1065-2221.

[143] Kawsar Haghshenas, Brian Setz, Yannis Blosch, and Marco Aiello. Enough hot air: the role of immersion cooling. *Energy Informatics*, 6(1):14, aug 9 2023.

[144] Wendy Luiten. Single phase passive hydrocarbon immersion cooling of high-power ics. In *2021 27th International Workshop on Thermal Investigations of ICs and Systems (THERMINIC)*, pages 1–6. IEEE, 2021.

[145] Base Specification for Immersion Fluids Revision 1.0, Version 1.0. Technical report, dec 1 2022.

[146] Yongping Huang, Junlei Ge, Yongping Chen, and Chengbin Zhang. Natural and forced convection heat transfer characteristics of single-phase immersion cooling systems for data centers. *International Journal of Heat and Mass Transfer*, 207:124023, jun 15 2023.

[147] Jimil M. Shah, Richard Eiland, Pavan Rajmane, Ashwin Siddarth, Dereje Agonafer, and Veerendra Mulay. Reliability Considerations for Oil Immersion-Cooled Data Centers. *Journal of Electronic Packaging*, 141(2), apr 10 2019. [Online; accessed 2023-05-05].

[148] S.M. Sohel Murshed and C.A. Nieto De Castro. A critical review of traditional and emerging techniques and fluids for electronics cooling. *Renewable and Sustainable Energy Reviews*, 78:821–833, 10 2017.

[149] Alex Alley Have say. Asperitas and Shell announce new cooling platform and immersion liquid. https://www.datacenterdynamics.com/en/news/asperitas-and-shell-announce-new-cooling-platform-and-immersion-liquid/, may 13 2020. [Online; accessed 2023-10-09].

[150] Peter Judge Have say. Alibaba Cloud to test Shell China's cooling fluid. https://www.datacenterdynamics.com/en/news/alibaba-cloud-to-use-shell-chinas-cooling-fluid/, feb 24 2023. [Online; accessed 2023-10-09].

[151] Immersion Cooling at Scale | SmartPod Platform | Submer | Immersion, January 2025. [Online; accessed 21. Jan. 2025].

[152] Riot Platforms, Inc. https://www.riotplatforms.com, oct 4 2023. [Online; accessed 2023-10-09].

[153] Shao-Wen Chen, Fang-Chin Liu, Hsiao-Jou Lin, Pei-Syuan Ruan, Yu-Ting Su, Yu-Chi Weng, Jong-Rong Wang, Jin-Der Lee, and Wei-Keng Lin. Experimental test and empirical correlation development for heat transfer enhancement under ultrasonic vibration. *Applied Thermal Engineering*, 143:639–649, oct 1 2018.

[154] Sir James Lighthill. Acoustic streaming. *Journal of Sound and Vibration*, 61(3):391–418, dec 8 1978.

[155] Rahim Aytug Ozer, Bayram Sahin, and Ibrahim Ates. Effect of the acoustic manipulation on single phase immersion cooling performance of discretely heated vertical plate. *International Journal of Heat and Mass Transfer*, 217:124649, dec 15 2023.

[156] Masoud Asadi, Gongnan Xie, and Bengt Sunden. A review of heat transfer and pressure drop characteristics of single and two-phase microchannels. *International Journal of Heat and Mass Transfer*, 79:34–53, dec 1 2014.

[157] Sambhaji T. Kadam and Ritunesh Kumar. Twenty first century cooling solution: Microchannel heat sinks. *International Journal of Thermal Sciences*, 85:73–92, 11 2014.

[158] Majid Jalili, Ioannis Manousakis, Íñigo Goiri, Pulkit A. Misra, Ashish Raniwala, Husam Alissa, Bharath Ramakrishnan, Phillip Tuma, Christian Belady, Marcus Fontoura, and Ricardo Bianchini. Cost-Efficient Overclocking in Immersion-Cooled Datacenters. In *2021 ACM/IEEE 48th Annual International Symposium on Computer Architecture (ISCA)*, pages 623–636, 6 2021. ISSN: 2575-713X.

[159] Yaser Nabavi Larimi, Omidreza Ghaffari, Alireza Ganjali, Chady Al Sayed, Francis Grenier, Simon Jasmin, Luc Fréchette, and Julien Sylvestre. Multi-Scale Electroplated Porous Coating for Immersion Cooling of Electronics. In *2022 21st IEEE Intersociety Conference on Thermal and Thermomechanical Phenomena in Electronic Systems (iTherm)*, pages 1–7, 5 2022. ISSN: 2694-2135.

[160] Guohui Zhou, Jingzhi Zhou, Xiulan Huai, Feng Zhou, and Yawen Jiang. A two-phase liquid immersion cooling strategy utilizing vapor chamber heat spreader for data center servers. *Applied Thermal Engineering*, 210:118289, jun 25 2022.

[161] Ashish Raniwala. Bringing 2-Phase Immersion Cooling to Hyperscale Cloud. In *Optical Fiber Communication Conference (OFC) 2022 (2022), paper Tu2A.4*, page Tu2A.4. Optica Publishing Group, mar 6 2022. [Online; accessed 2023-10-09].

[162] Fábio N. Leão and Ian R. Pashby. A review on the use of environmentally-friendly dielectric fluids in electrical discharge machining. *Journal of Materials Processing Technology*, 149(1):341–346, jun 10 2004.

[163] OA US EPA. Epa Proposes Designating Certain PFAS Chemicals as Hazardous Substances Under Superfund to Protect People's Health. https://www.epa.gov/newsreleases/epa-proposes-designating-certain-pfas-chemicals-hazardous-substances-under-superfund, aug 26 2022. [Online; accessed 2023-10-10].

[164] Linda G. T. Gaines. Historical and current usage of per- and polyfluoroalkyl substances (PFAS): A literature review. *American Journal of Industrial Medicine*, 66(5):353–378, 2023. _eprint: https://onlinelibrary.wiley.com/doi/pdf/10.1002/ajim.23362.

[165] A Billion New Air Conditioners Will Save Lives But Cook the Planet. *Bloomberg.com*, may 17 2023. [Online; accessed 2023-11-03].

[166] Mohammad Azarifar, Faisal Ahmed, and Mehmet Arik. Vortex-enhanced jet impingement and the role of impulse generation rate in heat removal using additively manufactured synthetic jet devices. *Applied Thermal Engineering*, 259:124914, jan 15 2025.

[167] Johannes Jörg, Silvano Taraborrelli, Garikoitz Sarriegui, Rik W. De Doncker, Reinhold Kneer, and Wilko Rohlfs. Direct Single Impinging Jet Cooling of a mosfet Power Electronic Module. *IEEE Transactions on Power Electronics*, 33(5):4224–4237, 5 2018. event-title: IEEE Transactions on Power Electronics.

[168] Beomjin Kwon, Thomas Foulkes, Tianyu Yang, Nenad Miljkovic, and William P. King. Air Jet Impingement Cooling of Electronic Devices Using Additively Manufactured Nozzles. *IEEE Transactions on Components, Packaging and Manufacturing Technology*, 10(2):220–229, 2 2020.

[169] Dominik Hofer, Michael Krieger, and Martin Kirchhofer. Particle image velocimetry and constant temperature anemometer measurements of the jet produced by a centrifugal fan. *Physics of Fluids*, 33(6):065126, jun 1 2021.

[170] Shun-Chang Yen and Jung-Hsuan Liu. Piv MEASUREMENTS OF EXIT FLOW FIELD OF CENTRIFUGAL FANS WITH CONDITIONAL SAMPLING. *Journal of Marine Science and Technology*, 15(3), jun 15 2007. [Online; accessed 2024-04-02].

[171] USPTO.report. Piezoelectric MEMS-based active cooling for heat dissipation in compute devices. https://uspto.report/patent/grant/10,943,850. [Online; accessed 2024-04-08].

[172] Jinjun Wang and Lihao Feng, editors. *Synthetic Jet*, pages 168–205. Cambridge Aerospace Series. Cambridge University Press, Cambridge, 2018. DOI: 10.1017/9781316676448.009.

[173] B. L. Smith and A. Glezer. Jet vectoring using synthetic jets. *Journal of Fluid Mechanics*, 458:1–34, 5 2002. publisher: Cambridge University Press.

[174] Ari Glezer and Michael Amitay. Synthetic Jets. *Annual Review of Fluid Mechanics*, 34(1):503–529, 2002. _eprint: https://doi.org/10.1146/annurev.fluid.34.090501.094913.

[175] Louis N. Cattafesta and Mark Sheplak. Actuators for Active Flow Control. *Annual Review of Fluid Mechanics*, 43(1):247–272, 2011. _eprint: https://doi.org/10.1146/annurev-fluid-122109-160634.

[176] D. A. Tamburello and M. Amitay. Active manipulation of a particle-laden jet. *International Journal of Multiphase Flow*, 34(9):829–851, sep 1 2008.

[177] H. Wang and S. Menon. Fuel-Air Mixing Enhancement by Synthetic Microjets. *AIAA Journal*, 39(12):2308–2319, 12 2001. publisher: American Institute of Aeronautics and Astronautics.

[178] Mangesh Chaudhari, Bhalchandra Puranik, and Amit Agrawal. Heat transfer characteristics of synthetic jet impingement cooling. *International Journal of Heat and Mass Transfer*, 53(5):1057–1069, feb 1 2010.

[179] Anna Pavlova and Michael Amitay. Electronic Cooling Using Synthetic Jet Impingement. *Journal of Heat Transfer*, 128(9):897–907, feb 20 2006.

[180] L. Marchitto, G. Valentino, M. Chiatto, and L. Luca. Water Spray Flow Characteristics Under Synthetic Jet Driven By a Piezoelectric Actuator. *Journal of Physics: Conference Series*, 778(1):012005, 1 2017. publisher: IOP Publishing.

[181] Anna A. Pavlova, Kiyoshi Otani, and Michael Amitay. Active control of sprays using a single synthetic jet actuator. *International Journal of Heat and Fluid Flow*, 29(1):131–148, feb 1 2008.

[182] Babak A. Parviz, Khalil Najafi, Michael O. Muller, Luis P. Bernal, and Peter D. Washabaugh. Electrostatically driven synthetic microjet arrays as a propulsion method for micro flight. *Microsystem Technologies*, 11(11):1214–1222, oct 1 2005.

[183] Tiffany J. Finley and Kamran Mohseni. Micro Pulsatile Jets for Thrust Optimization. pages 725–733. American Society of Mechanical Engineers Digital Collection, mar 24 2008. [Online; accessed 2023-11-29].

[184] Kiyoshi Otani, Joseph Moore, William Gressick, and Michael Amitay. Active Yaw Control of a Ducted Fan-Based MAV using Synthetic Jets. *International Journal of Flow Control*, 1(1):29–42, 3 2009.

[185] Charles E. Seeley, Yogen Utturkar, Mehmet Arik, and Tunc Icoz. Fluid-Structure Interaction Model for Low-Frequency Synthetic Jets. *AIAA Journal*, jul 11 2012. [Online; accessed 2024-01-04].

[186] Jivtesh Garg, Mehmet Arik, Stanton Weaver, Todd Wetzel, and Seyed Saddoughi. Meso Scale Pulsating Jets for Electronics Cooling. *Journal of Electronic Packaging*, 127(4):503–511, apr 20 2005.

[187] Tomáš Vít. Investigation of the Effect of a Synthetic Jet on the Heat Transfer Coefficient. jan 1 2017. [Online; accessed 2024-01-11].

[188] Xin He, Jason A. Lustbader, Mehmet Arik, and Rajdeep Sharma. Heat transfer characteristics of impinging steady and synthetic jets over vertical flat surface. *International Journal of Heat and Mass Transfer*, 80:825–834, jan 1 2015.

[189] Mehmet Arik. An investigation into feasibility of impingement heat transfer and acoustic abatement of meso scale synthetic jets. *Applied Thermal Engineering*, 27(8):1483–1494, jun 1 2007.

[190] Mehmet Arik, Rajdeep Sharma, Jason Lustbader, and Xin He. Steady and Unsteady Air Impingement Heat Transfer for Electronics Cooling Applications. *Journal of Heat Transfer*, 135(111009), sep 23 2013. [Online; accessed 2024-01-11].

[191] Hussein M. Maghrabie. Heat transfer intensification of jet impingement using exciting jets - A comprehensive review. *Renewable and Sustainable Energy Reviews*, 139:110684, 4 2021.

[192] Mohammad Azarifar and Mehmet Arik. Direct Numerical Simulation of Synthetic Jet Coupled to Forced Convection Cooling in a Channel Flow. In *2023 22nd IEEE Intersociety Conference on Thermal and Thermomechanical Phenomena in Electronic Systems (ITherm)*, pages 1–8, 5 2023. ISSN: 2694-2135.

[193] Adeel Arshad, Mark Jabbal, and Yuying Yan. Synthetic jet actuators for heat transfer enhancement – A critical review. *International Journal of Heat and Mass Transfer*, 146:118815, jan 1 2020.

[194] Muhammad Ikhlaq, Muhammad Yasir, Mehmet Demiroğlu, and Mehmet Arik. Synthetic Jet Cooling Technology for Electronics Thermal Management—A Critical Review. *IEEE Transactions on Components, Packaging and Manufacturing Technology*, 11(8):1156–1170, 8 2021. event-title: IEEE Transactions on Components, Packaging and Manufacturing Technology.

[195] Pawan Sharma, Pushpanjay K. Singh, Santosh K. Sahu, and Harekrishna Yadav. A Critical Review on Flow and Heat Transfer Characteristics of Synthetic Jet. *Transactions of the Indian National Academy of Engineering*, 7(1):61–92, mar 1 2022.

[196] Gopal Krishan, Kean C. Aw, and Rajnish N. Sharma. Synthetic jet impingement heat transfer enhancement – A review. *Applied Thermal Engineering*, 149:1305–1323, 2 2019.

[197] S. G. Mallinson, J. A. Reizes, and G. Hong. An experimental and numerical study of synthetic jet flow. *The Aeronautical Journal*, 105(1043):41–49, 1 2001.

[198] B.L. Smith and A. Glezer. The formation and evolution of synthetic jets. *Physics of Fluids*, 10(9):2281–2297, 1998.

[199] S. Menon and J.-H. Soo. Simulation of vortex dynamics in three-dimensional synthetic and free jets using the large-eddy lattice Boltzmann method. *Journal of Turbulence*, 5(1):032, 8 2004.

[200] Norbert Didden. On the formation of vortex rings: Rolling-up and production of circulation. *Zeitschrift für angewandte Mathematik und Physik ZAMP*, 30(1):101–116, jan 1 1979.

[201] Ryan Holman, Yogen Utturkar, Rajat Mittal, Barton L. Smith, and Louis Cattafesta. Formation Criterion for Synthetic Jets. *AIAA Journal*, 43(10):2110–2116, 10 2005. publisher: American Institute of Aeronautics and Astronautics.

[202] Yogen Utturkar, Ryan Holman, Rajat Mittal, Bruce Carroll, Mark Sheplak, and Lou Cattafesta. *A Jet Formation Criterion for Synthetic Jet Actuators*. Aerospace Sciences Meetings. American Institute of Aeronautics and Astronautics, jan 6 2003. DOI: 10.2514/6.2003-636.

[203] Yao-Hsien Liu, Shu-Yao Tsai, and Chi-Chuan Wang. Effect of driven frequency on flow and heat transfer of an impinging synthetic air jet. *Applied Thermal Engineering*, 75:289–297, jan 22 2015.

[204] Mangesh Chaudhari, Bhalchandra Puranik, and Amit Agrawal. Effect of orifice shape in synthetic jet based impingement cooling. *Experimental Thermal and Fluid Science*, 34(2):246–256, feb 1 2010.

[205] Ari Glezer. The formation of vortex rings. *The Physics of Fluids*, 31(12):3532–3542, dec 1 1988.

[206] Luis Silva-Llanca and Alfonso Ortega. Vortex dynamics and mechanisms of heat transfer enhancement in synthetic jet impingement. *International Journal of Thermal Sciences*, 112:153–164, feb 1 2017.

[207] Carlo Salvatore Greco, Gennaro Cardone, and Julio Soria. On the behaviour of impinging zero-net-mass-flux jets. *Journal of Fluid Mechanics*, 810:25–59, 1 2017.

[208] Yang Xu and LiHao Feng. Influence of orifice-to-wall distance on synthetic jet vortex rings impinging on a fixed wall. *Science China Technological Sciences*, 56(7):1798–1806, jul 1 2013.

[209] Yang Xu and Jin Jun Wang. Flow structure evolution for laminar vortex rings impinging onto a fixed solid wall. *Experimental Thermal and Fluid Science*, 75:211–219, jul 1 2016.

[210] P. Valiorgue, T. Persoons, A. McGuinn, and D. B. Murray. Heat transfer mechanisms in an impinging synthetic jet for a small jet-to-surface spacing. *Experimental Thermal and Fluid Science*, 33(4):597–603, apr 1 2009.

[211] Z. Trávníček and T. Vít. Impingement heat/mass transfer to hybrid synthetic jets and other reversible pulsating jets. *International Journal of Heat and Mass Transfer*, 85:473–487, jun 1 2015.

[212] Tim Persoons, Alan McGuinn, and Darina B. Murray. A general correlation for the stagnation point Nusselt number of an axisymmetric impinging synthetic jet. *International Journal of Heat and Mass Transfer*, 54(17):3900–3908, aug 1 2011.

[213] Eoin Fanning, Tim Persoons, and Darina B. Murray. Heat transfer characteristics of a pair of impinging synthetic jets: Effect of orifice spacing and impingement distance. *Journal of Physics: Conference Series*, 395(1):012025, 11 2012.

[214] D. McCormick. *Boundary layer separation control with directed synthetic jets*. Aerospace Sciences Meetings. American Institute of Aeronautics and Astronautics, jan 10 2000. DOI: 10.2514/6.2000-519.

[215] Rajnish N. Sharma. Fluid-Dynamics-Based Analytical Model for Synthetic Jet Actuation. DOI: 10.2514/1.25427.

[216] Quentin Gallas, Guiqin Wang, Melih Papila, Mark Sheplak, and Lou Cattafesta. *Optimization of Synthetic Jet Actuators*. American Institute of Aeronautics and Astronautics, Reno, Nevada, jan 6 2003. [Online; accessed 2024-04-24].

[217] Quentin Gallas, Ryan Holman, Toshikazu Nishida, Bruce Carroll, Mark Sheplak, and Louis Cattafesta. Lumped Element Modeling of Piezoelectric-Driven Synthetic Jet Actuators. *AIAA Journal*, 41(2):240–247, 2003. publisher: American Institute of Aeronautics and Astronautics _eprint: https://doi.org/10.2514/2.1936.

[218] Louis N. Cattafesta Oyarzun, Matias. *Design of Synthetic Jets*. CRC Press, 2014. number-of-pages: 50.

[219] J. P. Den Hartog. *Mechanical vibrations*. McGraw-Hill, 1st ed. edition, 1934.

[220] Tyler Van Buren, Edward Whalen, and Michael Amitay. Synthetic Jet Actuator Cavity Acoustics: Helmholtz Versus Quarter-Wave Resonance. *Journal of Vibration and Acoustics*, 137(054501), oct 1 2015. [Online; accessed 2024-04-08].

[221] Michael T. Sheng, Scott M. Keller, Anthony Mickalauskas, David Menicovich, Michael Amitay, and Christopher S. Lynch. Hybrid Lumped-Element and Finite Element Model for Novel Synthetic Jet Actuator Shapes. *AIAA Journal*, 61(9):3923–3934, 2023. publisher: American Institute of Aeronautics and Astronautics _eprint: https://doi.org/10.2514/1.J062755.

[222] Thomas M. Crittenden and Ari Glezer. A high-speed, compressible synthetic jet. *Physics of Fluids*, 18(1):017107, jan 1 2006.

[223] Kamran Mohseni. Zero-mass pulsatile jets for unmanned underwater vehicle maneuvering. In *AIAA 3rd "Unmanned Unlimited" Technical Conference, Workshop and Exhibit*.

[224] Janhavi Agashe, David Arnold, and Louis Cattafesta. Development of Compact Electrodynamic Zero-Net Mass-Flux Actuators. In *47th AIAA Aerospace Sciences Meeting including The New Horizons Forum and Aerospace Exposition*, jan 5 2009. [Online; accessed 2024-02-05].

[225] Paweł Gil. Synthetic jet Reynolds number based on reaction force measurement. *Journal of Fluids and Structures*, 81:466–478, aug 1 2018.

[226] J. E. Huber, N. A. Fleck, and M. F. Ashby. The selection of mechanical actuators based on performance indices. *Proceedings of the Royal Society of London. Series A: Mathematical, Physical and Engineering Sciences*, 453(1965):2185–2205, oct 8 1997. publisher: Royal Society.

[227] R. Mahalingam, S. Heffington, L. Jones, and M. Schwickert. Newisys server processor cooling augmentation using synthetic jet ejectors. In *Thermal and Thermomechanical Proceedings 10th Intersociety Conference on Phenomena in Electronics Systems, 2006. ITHERM 2006.*, pages 705–709, 5 2006. ISSN: 1087-9870.

[228] Raghavendran Mahalingam and Samuel Heffington. Synthetic jet cooling system for LED module. https://patents.google.com/patent/US7932535B2/en, apr 26 2011. [Online; accessed 2024-04-02].

[229] Fang-Jenq Chen, Chungsheng Yao, George Beeler, Robert Bryant, and Robert Fox. *Development of synthetic jet actuators for active flow control at NASA Langley*. Fluid Dynamics and Co-located Conferences. American Institute of Aeronautics and Astronautics, jun 19 2000. DOI: 10.2514/6.2000-2405.

[230] Baris Gungordu, Mark Jabbal, and Atanas A. Popov. Enhancing Jet Velocity and Power Conversion Efficiency of Piezoelectric Synthetic Jet Actuators. *AIAA Journal*, 61(10):4321–4331, 2023. publisher: American Institute of Aeronautics and Astronautics _eprint: https://doi.org/10.2514/1.J062930.

[231] Matteo Chiatto, Francesco Capuano, Gennaro Coppola, and Luigi De Luca. Lem Characterization of Synthetic Jet Actuators Driven by Piezoelectric Element: A Review. *Sensors*, 17(6):1216, 6 2017. number: 6 publisher: Multidisciplinary Digital Publishing Institute.

[232] Stephen Timoshenko. *Theory of plates and shells*. Engineering societies monographs. McGraw-Hill Book Company, Inc., 1st ed. edition, 1940.

[233] H. Peter de Bock, Pramod Chamarthy, Jennifer L. Jackson, and Bryan Whalen. Investigation and application of an advanced dual piezoelectric cooling jet to a typical electronics cooling configuration. In *13th InterSociety Conference on Thermal and Thermomechanical Phenomena in Electronic Systems*, page 1387–1394. IEEE, May 2012.

[234] Jonathan R. Bost. A New Type of Tweeter Horn Employing a Piezoelectric Driver. *Journal of the Audio Engineering Society*, 23(10):796–801, dec 1 1975. publisher: Audio Engineering Society.

[235] Arya Ayaskanta, Longzhong Huang, Terrence Simon, Taiho Yeom, Mark North, and Tianhong Cui. Heat Transfer Enhancement of a Heat Sink by Inclined Synthetic Jets for Electronics Cooling. American Society of Mechanical Engineers Digital Collection, dec 21 2013. [Online; accessed 2024-04-08].

[236] Jivtesh Garg, Mehmet Arik, Stanton Weaver, and Seyed Saddoughi. Micro Fluidic Jets for Thermal Management of Electronics. pages 647–654. American Society of Mechanical Engineers Digital Collection, feb 24 2009. [Online; accessed 2024-02-15].

[237] Itimad D. J. Azzawi, Artur J. Jaworski, and Xiaoan Mao. An Overview of Synthetic Jet Under Different Clamping and Amplitude Modulation Techniques. *Journal of Fluids Engineering*, 143(031501), dec 4 2020. [Online; accessed 2024-04-08].

[238] Mehmet Arik and Yogen V. Utturkar. A Computational and Experimental Investigation of Synthetic Jets for Cooling of Electronics. *Journal of Electronic Packaging*, 137(021005), jun 1 2015. [Online; accessed 2024-02-19].

[239] Zdenek Travnicek and Z. Antosova. Synthetic jet actuators with rigid and temporally variable nozzles. Begel House Inc., 2023. [Online; accessed 2024-02-19].

[240] Omidreza Ghaffari, Stephen A. Solovitz, and Mehmet Arik. An investigation into flow and heat transfer for a slot impinging synthetic jet. *International Journal of Heat and Mass Transfer*, 100:634–645, sep 1 2016.

[241] Tyler Van Buren, Edward Whalen, and Michael Amitay. Achieving a High-Speed and Momentum Synthetic Jet Actuator. *Journal of Aerospace Engineering*, 29(2):04015040, mar 1 2016. publisher: American Society of Civil Engineers.

[242] Satoshi Yuura, Yasumasa Watanabe, Katsushi Furutani, and Taro Handa. Ultrasonic-driven synthetic-jet actuator: High-efficiency actuator creating high-speed and high-frequency pulsed jet. *Sensors and Actuators A: Physical*, 353:114231, apr 16 2023.

[243] Pushpanjay K. Singh, M. Renganathan, Harekrishna Yadav, Santosh K. Sahu, Prabhat K. Upadhyay, and Amit Agrawal. An experimental investigation of the flow-field and thermal characteristics of synthetic jet impingement with different waveforms. *International Journal of Heat and Mass Transfer*, 187:122534, may 15 2022.

[244] Yiran Lu and Jinjun Wang. Numerical investigation of synthetic jets generated by various signals in quiescent ambient. *Physics of Fluids*, 35(1):015107, 01 2023.

[245] Ceb-44d06. `https://www.digikey.com/en/products/detail/same-sky-formerly-cui-devices/CEB-44D06/446282`. [Accessed 10-02-2025].

[246] M. K. Swaminathan, G. W. Rankin, and K. Sridhar. A note on the response equations for hot-wire anemometry. *Journal of Fluids Engineering*, 108(1):115–118, 03 1986.

[247] Jason Stafford, Ed Walsh, and Vanessa Egan. The effect of global cross flows on the flow field and local heat transfer performance of miniature centrifugal fans. *International Journal of Heat and Mass Transfer*, 55(7):1970–1985, mar 1 2012.

[248] Jason Stafford, Ed Walsh, and Vanessa Egan. Local heat transfer performance and exit flow characteristics of a miniature axial fan. *International Journal of Heat and Fluid Flow*, 31(5):952–960, oct 1 2010.

[249] Mohammad Azarifar and Mehmet Arik. Liquid synthetic jets for high flux electronics cooling. *Applied Thermal Engineering*, 261:125007, feb 15 2025.

[250] Durmuş Kaya, Fatma Çanka Kılıç, and Hasan Hüseyin Öztürk. *Energy Efficiency in Pumps*, pages 329–374. Springer International Publishing, Cham, 2021. DOI: 10.1007/978-3-030-25995-2_11.

[251] Jivtesh Garg, Mehmet Arik, Avram Bar-Cohen, Rex Wolf, Bojan Vukasinovic, James G. Hartley, and Ari Glezer. Synthetic jet enhancement of natural convection and pool boiling in a dielectric liquid. In *Proceeding of International Heat Transfer Conference 12*. Begellhouse, 2002.

[252] A. Polsenberg-Thomas, J. Burdick, and K. Mohseni. An Experimental Study of Voice-Coil Driven Synthetic Jet Propulsion for Underwater Vehicles. *Proceedings of OCEANS 2005 MTS/IEEE*, pages 1–5, 2005. event-title: OCEANS 2005 MTS/IEEE ISBN: 9780933957343 publisher-place: Washington, DC, USA publisher: IEEE.

[253] Lingbo Geng, Zhiqiang Hu, and Yang Lin. Hydrodynamic characteristic of synthetic jet steered underwater vehicle. *Applied Ocean Research*, 70:1–13, jan 1 2018.

[254] Ying Kang, Zhi-xun Xia, Zhen-bing Luo, Xiong Deng, Yin-xin Zhu, and Can Peng. Experimental study on a dual synthetic jets liquid cooling device. *Applied Energy*, 372:123865, oct 15 2024.

[255] Mohammad Azarifar, Faisal Ahmed, Muhammad Ikhlaq, and Mehmet Arik. Development of a Novel Analytical Model for Liquid Synthetic Jets and Introduction of Their Application in Immersion Cooling Systems. In *2024 23rd IEEE Intersociety Conference on Thermal and Thermomechanical Phenomena in Electronic Systems (ITherm)*, pages 1–11. IEEE, 2024. [Online; accessed 2024-10-29].

[256] Pravin A. Shinde, Pratik V. Bansode, Satyam Saini, Rajesh Kasukurthy, Tushar Chauhan, Jimil M. Shah, and Dereje Agonafer. Experimental Analysis for Optimization of Thermal Performance of a Server in Single Phase Immersion Cooling. [Online; accessed 2024-08-13].

[257] M. Muneeshwaran, Yueh-Cheng Lin, and Chi-Chuan Wang. Performance analysis of single-phase immersion cooling system of data center using FC-40 dielectric fluid. *International Communications in Heat and Mass Transfer*, 145:106843, jun 1 2023.

[258] Aditya Chhetri, Devendra Kashyap, Arvind Mali, Chaitanya Agarwal, Caroline Ponraj, and N. Gobinath. Numerical simulation of the single-phase immersion cooling process using a dielectric fluid in a data server. *Materials Today: Proceedings*, 51:1532–1538, jan 1 2022.

[259] Bruce E. Poling, John M. Prausnitz, and John P. O'Connell. *Properties of Gases and Liquids*. McGraw-Hill Education, 5th edition edition, 2001. [Online; accessed 2024-08-26].

[260] Calvin F. Spencer and Stanley B. Adler. A critical review of equations for predicting saturated liquid density. *Journal of Chemical & Engineering Data*, 23(1):82–89, jan 1 1978. publisher: American Chemical Society.

[261] Theodore L. Bergman, Adrienne S. Lavine, Frank P. Incropera, and David P. DeWitt. *Fundamentals of Heat and Mass Transfer, 8th Edition*. Wiley, Hoboken, NJ, USA, December 2018.

[262] Patrick Birbarah, Tarek Gebrael, Thomas Foulkes, Andrew Stillwell, Alexandra Moore, Robert Pilawa-Podgurski, and Nenad Miljkovic. Water immersion cooling of high power density electronics. *International Journal of Heat and Mass Transfer*, 147:118918, feb 1 2020.

[263] Linhui Yuan, Yu Wang, Risto Kosonen, Zhengchao Yang, Yingying Zhang, and Xincheng Wang. Comparative Study on Heat Dissipation Performance of Pure Immersion and Immersion Jet Liquid Cooling System for Single Server. *Buildings*, 14(9):2635, 9 2024. number: 9 publisher: Multidisciplinary Digital Publishing Institute.

[264] Satyam Saini, Eric McAfee, Casey Carte, Drew Damm, Suchismita Sarangi, Jessica Gullbrand, and Mark MacDonald. Cooling Capability Enhancement in Single-Phase

Immersion using Targeted Flow. In *2024 23rd IEEE Intersociety Conference on Thermal and Thermomechanical Phenomena in Electronic Systems (ITherm)*, pages 1–6, 5 2024. ISSN: 2694-2135.

[265] Mohammad Azarifar and Mehmet Arik. Mesoscale solid-state liquid jet generation: A nature-inspired path to efficient liquid cooling. 2025.

[266] R. Margaria, G. Milic-Emili, J. M. Petit, and G. Cavagna. Mechanical work of breathing during muscular exercise. *Journal of Applied Physiology*, 15(3):354–358, 5 1960. publisher: American Physiological Society.

[267] Brad J. Gemmell, John H. Costello, Sean P. Colin, Colin J. Stewart, John O. Dabiri, Danesh Tafti, and Shashank Priya. Passive energy recapture in jellyfish contributes to propulsive advantage over other metazoans. *Proceedings of the National Academy of Sciences*, 110(44):17904–17909, oct 29 2013. publisher: Proceedings of the National Academy of Sciences.

[268] John H. Costello, Sean P. Colin, John O. Dabiri, Brad J. Gemmell, Kelsey N. Lucas, and Kelly R. Sutherland. The Hydrodynamics of Jellyfish Swimming. *Annual Review of Marine Science*, 13(Volume 13, 2021):375–396, jan 3 2021. publisher: Annual Reviews.

[269] Nicole W. Xu and John O. Dabiri. Low-power microelectronics embedded in live jellyfish enhance propulsion. *Science Advances*, 6(5):eaaz3194, jan 29 2020. publisher: American Association for the Advancement of Science.

[270] Babar Jamil, Namsoo Oh, Jin-Gyu Lee, Haneol Lee, and Hugo Rodrigue. A Review and Comparison of Linear Pneumatic Artificial Muscles. *International Journal of Precision Engineering and Manufacturing-Green Technology*, 11(1):277–289, jan 1 2024.

[271] Guojun Liu, Meng Wang, Pengfei Li, Xiaodong Sun, Luntao Dong, and Peiqing Li. A micromixer driven by two valveless piezoelectric pumps with multi-stage mixing characteristics. *Sensors and Actuators A: Physical*, 333:113225, jan 1 2022.

[272] Chendong Liu, Yongping Huang, and Chengbin Zhang. Efficient jet-assisted single-phase immersion liquid cooling for high heat-flux servers. *Applied Thermal Engineering*, 259:124935, jan 15 2025.

[273] Frank M. White and Joseph Majdalani. *Viscous fluid flow*, volume 3. McGraw-Hill New York, 2006. [Online; accessed 2024-07-25].

[274] Osborne Reynolds. Iv. On the dynamical theory of incompressible viscous fluids and the determination of the criterion. *Philosophical Transactions of the Royal Society of London. (A.)*, 186:123–164, 1 1997. publisher: Royal Society.

[275] ANSYS FLUENT 12.0 Theory Guide - 4.12.4 Enhanced Wall Treatment, February 2025. [Online; accessed 21. Feb. 2025].

[276] B. A. Kader. Temperature and concentration profiles in fully turbulent boundary layers. *International Journal of Heat and Mass Transfer*, 24(9):1541–1544, sep 1 1981.

[277] S.M. Sohel Murshed and C.A. Nieto De Castro. A critical review of traditional and emerging techniques and fluids for electronics cooling. *Renewable and Sustainable Energy Reviews*, 78:821–833, 10 2017.

[278] R.J. Goldstein and A.I. Behbahani. Impingement of a circular jet with and without cross flow. *International Journal of Heat and Mass Transfer*, 25(9):1377–1382, 1982.

[279] Frank M. White. *Fluid mechanics*. Mcgraw-Hill series in mechanical engineering. McGraw-Hill, New York, NY, 6th ed edition, 2009.

[280] Quick cure polyurethane foam sealant. `https://www.touch-n-seal.com/quick-cure.html`. [Accessed 10-02-2025].

[281] Yunus A. Cengel and Afshin J. Ghajar. *Heat and Mass Transfer: Fundamentals and Applications*. McGraw-Hill Education, 6th edition, 2020. SI Units Edition.

[282] Avraham Shitzer. Wind-chill-equivalent temperatures: regarding the impact due to the variability of the environmental convective heat transfer coefficient. *International Journal of Biometeorology*, 50(4):224–232, mar 1 2006.

[283] Abdul-Jabbar N Khalifa. Natural convective heat transfer coefficient – a review: I. Isolated vertical and horizontal surfaces. *Energy Conversion and Management*, 42(4):491–504, mar 1 2001.

[284] Yifan Fan, Yongling Zhao, Juan F. Torres, Feng Xu, Chengwang Lei, Yuguo Li, and Jan Carmeliet. Natural convection over vertical and horizontal heated flat surfaces: A review of recent progress focusing on underpinnings and implications for heat transfer and environmental applications. *Physics of Fluids*, 33(10):101301, oct 5 2021.

[285] Subho Samanta and Abhijit Guha. A similarity theory for natural convection from a horizontal plate for prescribed heat flux or wall temperature. *International Journal of Heat and Mass Transfer*, 55(13):3857–3868, jun 1 2012.

Appendices

Appendix A

Air LEM Model and Verification

The objective of LEM model is to make a connection between $U(t)$ based on the driving force $F(t)$ exerted by an input voltage $v(t)$. This LEM is introduced by Sharma [215]. The system has a mass (m), damping coefficient (c), and stiffness (k). $m = m_w + m_f$, includes mass of the oscillating wall m_w (mass of shim and piezoelectric ceramic) and added acoustic mass of fluid m_f. The damping coefficient (c) consists of the damping of the (c_w) and the acoustic radiation damping factor (c_f). In the context of a circular piston vibrating within an infinite baffle at a radian frequency of the added acoustic mass and damping terms are [50]:

$$m_f = \frac{2\rho_x A_v U_{sound} H_1(y)}{y\omega} = \frac{4\rho_x A_v U_{sound}}{\pi\omega} y \left(\frac{1}{3} - \frac{y^2}{3^2 \cdot 5} + \frac{y^4}{3^2 \cdot 5^2 \cdot 7} - ... \right) \tag{A.1a}$$

$$c_f = \rho_x A_v U_{sound} \left(1 - \frac{2J_1(y)}{y} \right) = \rho_x A_v U_{sound} y^2 \left(\frac{1}{2 \cdot 4} - \frac{y^2}{2 \cdot 4^2 \cdot 6} + \frac{y^4}{2 \cdot 4^2 \cdot 6^2 \cdot 8} - ... \right) \tag{A.1b}$$

$$y = \frac{\omega D}{U_{sound}} \tag{A.1c}$$

Where ρ_∞, A_w, U_{sound}, H_1, J_1, and D_w are unperturbed fluid density (initial density, or density outside the cavity), the surface area of the oscillating wall, speed of sound, Struve function of the first kind, Bessel function of the first kind, and diameter of the oscillating wall (herein we assume its equal to the diameter of the cavity), respectively. Moreover, speed of sound is:

$$U_{sound} = \sqrt{\gamma \frac{P_\infty}{\rho_\infty}}, \quad \gamma = c_p/c_v \tag{A.2}$$

where γ, c_p, c_v, and P_∞ are ratios of specific heat ($\approx$1.4 for air), specific heat in constant pressure, and constant volume, and initial cavity pressure (or pressure outside the cavity), respectively. During actuation, the gauge pressure inside the cavity, $p_i(t)$, undergoes fluctuations around a zero-mean value. One can assume that the cavity pressure is approximately equal to the pressure outside the cavity ($p_i(t) \approx P_\infty$). An equation governing the dynamics of the flexible membrane can be derived as:

$$m\ddot{x}_{eq}(t) + c\dot{x}_{eq}(t) + kx_{eq}(t) = F(t) - p_i(t)A_w \tag{A.3}$$

in which $A_w = \pi D^2/4$. Assuming the actuation begins with $x_{eq}(t = 0) = \dot{x}_{eq}(t = 0) = \ddot{x}_{eq}(t = 0) = 0$ thus, $F(t)$ can be defined as $F(t) = F_{max} \sin(\omega t)$. Concerning the system

introduced in Equation. A.3, $\omega_w = \sqrt{k/m}$ represents the wall's resonance frequency. Additionally, the damping ratio for the wall can be defined as $\zeta = \frac{c}{2\sqrt{mk}}$. Consequently, we can express Equation. A.3 as:

$$\ddot{x}_{eq}(t) + 2\zeta\omega_w\dot{x}_{eq}(t) + \omega_w^2 x_{eq}(t) = \frac{F(t) - p_i(t)A_w}{m} \tag{A.4}$$

At any given instant in time, the internal pressure in the cavity can be considered uniform (except near the orifice), under the condition that the wavelength of the pressure oscillations is significantly greater than a typical dimension L (length) of the actuator cavity. Provided by continuity, the rate of change of mass inside the cavity concerning the change in cavity volume is equal to the mass flow rate out of the cavity with an area of A and a velocity of $U(t)$:

$$\frac{d(\rho_i(t)V(t))}{dt} = -\rho_\infty AU(t) \rightarrow \rho_i\frac{d(V(t))}{dt} + V_0\frac{d(\rho_i(t))}{dt} = -\rho_\infty AU(t) \tag{A.5}$$

Where $V(t) = V_0 - A_w x_{eq}(t) \approx V_0$ is the volume of the cavity, thus:

$$\frac{d(V(t))}{dt} = \frac{d(V_0 - A_w x(t))}{dt} = -A_w\dot{x}_{eq}(t) \tag{A.6}$$

Assuming isentropic contraction:

$$\frac{P_i(t)}{\rho_i^\gamma(t)} = \frac{P_\infty}{\rho_\infty^\gamma(t)} \rightarrow \gamma\frac{\rho_i^{\gamma-1}(t)d\rho_i(t)}{dt} = \frac{\rho_\infty^\gamma(t)}{P_\infty}\frac{d(P_i(t))}{dt} \tag{A.7}$$

Again, assuming $\rho_i(t) \approx \rho$ then Equation A.7 can be simplified to:

$$\frac{d(\rho_i(t))}{dt} = \frac{\rho_\infty}{\gamma}\frac{d(p_i(t))}{dt} \tag{A.8}$$

Incorporating Equation A.6, and A.8 into Equation A.5, the following expression is derived:

$$-\rho_i A_w\dot{x}_{eq}(t) + \frac{V_0\rho_\infty}{\gamma}\frac{d(p_i(t))}{dt} = -\rho_\infty AU(t) \rightarrow -A_w\dot{x}_{eq}(t) + \frac{V_0}{\gamma}\frac{d(p_i(t))}{dt} = -AU(t) \tag{A.9}$$

Now, the unsteady Bernoulli equation is considered from a point inside the cavity where the flow begins to contract into the orifice and extends to the point of vena contracta. Here, it is assumed that streamlines are in the x-direction, and the velocity inside the cavity before contraction into the orifice is negligible.

$$\begin{aligned} P_i(t) + \frac{1}{2}\rho_i(t)U_i^2(t) = P_\infty + \frac{1}{2}\rho U_{vc}^2(t) + C_L\frac{1}{2}\rho U^2(t) \\ + \int_{start\ of\ flow\ contraction\ in\ cavity}^{vena\ contracta} \frac{1}{2}\rho_\infty\frac{dU(t, x_{eq})}{dt}dx_{eq} \end{aligned} \tag{A.10}$$

where viscous dissipations due to sudden contraction in the orifice are considered as$C_L 1/2_\infty U^2(t)$. Here, C_L represents the sudden contraction loss coefficient of flow at the orifice entrance, and it is assumed to be constant and not changing with time, given by $C_L = 0.42(1 - \beta^2)$. Additionally, assuming cavity velocity is negligible and simplifying the integral section with an effective length of the air jet/slug at the orifice (L_e), which is the sum of the actual orifice length

(L_o) and end corrections quantified using the inertia coefficient C_l as $L_e = L_o + C_l\sqrt{A}$, thus:

$$P_i = P_\infty + \frac{1}{2}\rho U_{vc}^2(t) + C_L\frac{1}{2}\rho_\infty U^2(t) + \rho_\infty L_e\frac{\partial U(t)}{\partial t} \tag{A.11}$$

Now, the vena contracta velocity can be exchanged with the orifice exit velocity using the contraction coefficient as:

$$p_i = \left(C_L + \frac{1}{C_c^2}\right)\frac{1}{2}\rho_\infty U^2(t) + \rho_\infty L_e\frac{\partial U(t)}{\partial t} \tag{A.12}$$

where C_c is the contraction coefficient, representing the area ratio of A_{vc}/A and will vary with the characteristics and strength of the vena contracta. Based on Bernoulli's obstruction theory [279]:

$$A_w U_i(t) = AU_{vc}(t) \tag{A.13a}$$

$$\begin{aligned} P_i(t) + \frac{1}{2}\rho_i(t)U_i^2(t) &= P_{vc} + \frac{1}{2}\rho_\infty U_{vc}^2(t) \\ &\rightarrow U_{vc}(t) \approx \left[\frac{2(P_i(t) - P_{vc})}{\rho_\infty(1 - A_{vc}^2/A_w^2)}\right]^{1/2} \\ &\rightarrow U(t) \approx C_d\left[\frac{2(P_i(t) - P_{vc})}{\rho_\infty(1-\beta^4)}\right]^{1/2} \end{aligned} \tag{A.13b}$$

$$\begin{aligned} P_i(t) - P_{vc} &\approx \frac{1}{2}\rho_\infty(U_{vc}^2(t) - 0) + C_L\frac{1}{2}\rho_\infty U^2(t) \\ &= \frac{1}{2}\rho_\infty[U_{vc}^2(t) + C_L U^2(t)] \\ &\approx \frac{1}{2}\rho_\infty\left[\frac{1}{C_c^2} + C_L\right]U^2(t) \end{aligned} \tag{A.13c}$$

where $\frac{1}{C_c^2} + C_L = \frac{1-\beta^4}{C_d^4}$. Thus Equation A.11 11 can be written while assuming U is positive for outflow and negative for inflow as:

$$p_i(t) = \frac{1}{2}\rho_\infty\left[\left(\frac{1-\beta^4}{C_d^4}\right)U(t)|U(t)| + L_e\frac{dU(t)}{dt}\right] \tag{A.14}$$

It should be noted that $\beta = D/D_w$ and $C_d = f(,\mathrm{Re}_D)$, where $\mathrm{Re}_D = U_i(t)D_w/\nu_\infty$. For small β, C_d is approximated as 0.6. Combining second and third principal equations reveal the second resonance of the system:

$$\ddot{U} + \frac{1-\beta^4}{L_e C_d^4}|U|\dot{U} + \frac{\gamma A P_\infty}{V_0\rho_\infty L_e}U = \frac{\gamma A_w P_\infty}{V_0\rho_\infty L_e}\dot{x}_{eq} \tag{A.15a}$$

$$\ddot{U} + \frac{1-\beta^4}{L_e C_d^4}|U|\dot{U} + \omega_h^2 U = \frac{A_w}{A}\omega_h^2\dot{x}_{eq} \tag{A.15b}$$

Here $\omega_h = U_{sound}\sqrt{A/V_0 L_e}$ represents the Helmholtz frequency. Given the preceding discussion, a system of five nonlinear ordinary differential equations (ODEs) requires a numerical

approach to solve:

$$\begin{cases} \dot{p}_i(t) = \frac{\gamma A_w P_\infty}{V_0}\dot{x}_{eq}(t) - \frac{\gamma A P_\infty}{V_0}U(t) \\ \dot{x}_{eq}(t) = \frac{d(x_{eq}(t))}{dt} \\ \ddot{x}_{eq}(t) = \frac{F(t)}{m} - \frac{p_i(t)A_w}{m} - 2\zeta\omega_w\dot{x}_{eq}(t) - \omega_w^2 x_{eq}(t) \\ \dot{U}(t) = \frac{d(U(t))}{dt} \\ \ddot{U}(t) = -\frac{1-\beta^4}{L_e C_d^4}|U(t)|\dot{U}(t) - \omega_h^2 U(t) + \frac{A_w}{A}\omega_h^2\dot{x}_{eq}(t) \end{cases} \tag{A.16}$$

Each ODE is broken down into manageable steps, enabling the approximation of solutions by the six-stage, fifth order, Runge-Kutta method in MATLAB. Validation of the calculation can be seen in Fig. 22 with the comparison of between behavior of piezoelectric-driven SJD that was studied and experimentally verified by Gallas et al. [217], and later by Sharma [215].

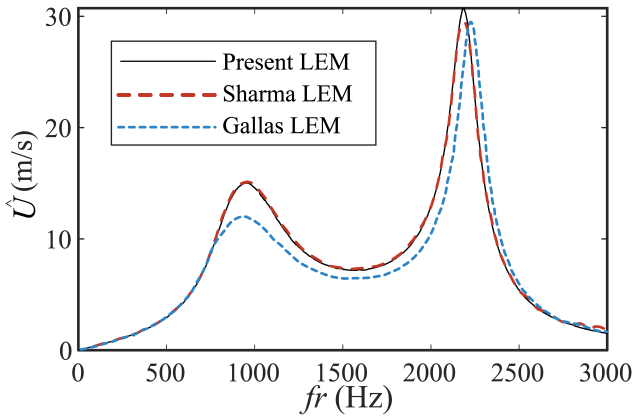

Figure A.1: Maximum area averaged jet exit velocity $\hat{U}$ in the frequency range of 50 to 3000 Hz.

A sample MATLAB code is presented here:

```
clc
clear
%Code by Mohammad Azarifar at Auburn University. Use by Referencing
    Only
%%%%% Parameter Definitions for Piezoelectric Actuator System
% Units are SI unless otherwise specified

% --- Physical Constants and Ambient Conditions ---
T_inf_C = 20; % Room Temperature in Celsius
T_inf = 273.15 + T_inf_C; % Ambient Temperature in Kelvin
P_inf = 101325; % Ambient Pressure in Pascals

% --- Geometric Parameters (in meters) ---
D_w = 35/1000; % Diaphragm Diameter
D_piezo = 25/1000; % Piezo Ceramic Diameter
D_o = 5E-3; % Orifice Diameter
thickness_shim = 0.25/1000; % Brass Shim Thickness
```

```
thickness_piezo = 0.28/1000; % Piezo Ceramic Thickness
L = 1.5E-3; % Cavity Length (Note: Half for Conical Cavity Design)
L_o = 0.5E-3; % Orifice Length

% --- Material Properties ---
dens_shim = 8700; % Density of Brass (kg/m^3)
dens_piezo = 7700; % Density of Piezo Ceramic (kg/m^3)
C_l = 0.9; % Inertia Coefficient for Effective Orifice Length
C_d = 0.6; % Discharge Coefficient for Orifice Flow

% --- System Parameters ---
F_max = 4; % Maximum Force at end of each stroke (N)
k = 300000 * 0.8; % Stiffness of Diaphragm (N/m), reduced by a
    factor
Increase_in_Force_water = 10; % Force Increase for Water (Not Used
    in Air Calculation)
Increase_in_Force_oil = 10; % Force Increase for Oil (Not Used in
    Air Calculation)

% --- Calculated Geometric Properties ---
A_o = pi / 4 * D_o^2; % Area of Orifice
A_w = pi * D_w^2 / 4; % Area of Diaphragm
A_piezo = pi * D_piezo^2 / 4; % Area of Piezo Ceramic
L_e = L_o + C_l * sqrt(A_o); % Effective Length of Orifice
V_0 = (A_w + A_o) * L; % Volume of Cavity (Note: L is half for
    conical cavity)

% --- Mass Calculation ---
m_w = A_w * thickness_shim * dens_shim + A_piezo * thickness_piezo
    * dens_piezo; % Mass of Diaphragm Assembly

% --- Loss Coefficient ---
K = (1 - (A_o / A_w)^2) / C_d^4; % Effective Loss Coefficient


%%%%%%%%%%%%%%%%%%%%%%%%%%%%%%%%%%%%%%%%%%%%%%%%%%%%%%%%%%%%%%%%
%%%%% Air Properties and System Dynamics Calculation
%%%%%%%%%%%%%%%%%%%%%%%%%%%%%%%%%%%%%%%%%%%%%%%%%%%%%%%%%%%%%%%%

F_max_air = F_max; % Maximum Force for Air Case (N)

% Frequency Range for Analysis
f_values = 50:50:5000; % Frequencies in Hz
distance = [1, 2, 5, 10, 20]; % Distances for Nu Calculation

% Initialize arrays to store maximum values over frequencies
max_Xdot1_values = zeros(size(f_values)); % Max dP/dt
max_Xdot2_values = zeros(size(f_values)); % Max Displacement
max_Xdot3_values = zeros(size(f_values)); % Max Velocity of
    Diaphragm
```

```
max_Xdot4_values = zeros(size(f_values)); % Max Velocity of Orifice
max_Xdot5_values = zeros(size(f_values)); % Max Acceleration of
    Orifice

% Loop through each frequency value
for i = 1:length(f_values)

    % --- Air Property Calculation at T_inf ---
    mu_inf = -0.000000838278 + 0.0000000835717342 * T_inf^1 -
        0.0000000000769429583 * T_inf^2 + 4.6437266E-14 * T_inf^3 -
        1.06585607E-17 * T_inf^4; % Dynamic Viscosity
    Cp_inf = 1047.63657 - 0.372589265 * T_inf^1 + 0.000945304214 *
        T_inf^2 - 0.000000602409443 * T_inf^3 + 0.00000000012858961
        * T_inf^4; % Specific Heat at Constant Pressure
    dens_inf = P_inf * 0.02897 / 8.3145 / T_inf; % Density (Ideal
        Gas Law)
    nu_inf = mu_inf / dens_inf; % Kinematic Viscosity
    cond_inf = -0.00227583562 + 0.000115480022 * T_inf^1 -
        0.0000000790252856 * T_inf^2 + 0.0000000000411702505 *
        T_inf^3 - 7.43864331E-15 * T_inf^4; % Thermal Conductivity
    Exp_coeff_inf = 1 / T_inf; % Expansion Coefficient (Ideal Gas)
    Prandtl_inf = mu_inf * Cp_inf / cond_inf; % Prandtl Number
    Cp_ratio = 1.4; % Ratio of Specific Heats for Air
    U_sound = sqrt(Cp_ratio * P_inf / dens_inf); % Speed of Sound
        in Air

    gamma = 1.4; % Heat Capacity Ratio for Air
    f = f_values(i); % Current Frequency
    omega = f * 2 * pi; % Angular Frequency

    % --- Fluidic Mass and Damping Calculation ---
    y = dens_inf * D_w / U_sound; % Non-dimensional frequency
        parameter
    H1 = y / 3; % Approximation for H1 function (complex part of
        impedance)
    for j = 2:10 % Iterative summation for H1 for better accuracy
        H1 = H1 + (-1)^(j + 1) * y^(2 * j - 1) * (factorial(j * 2 +
            1) / factorial(j) / 2^j)^-1;
    end
    J1 = besselj(1, y); % Bessel function of first kind, order 1
    m_f = 4 * dens_inf * A_w * U_sound * H1 * pi / omega; % Fluidic
        mass
    c_f = dens_inf * A_w * U_sound * (1 - 2 * J1 / y); % Fluidic
        damping

    % --- System Mass, Damping, and Stiffness ---
    m = m_f + m_w; % Total effective mass
    omega_w = sqrt(k / m); % Natural frequency of diaphragm
    c_crtic = 2 * sqrt(m * omega_w); % Critical damping coefficient
```

```
96      c_w = 0.03 * c_crtic; % Structural damping (assumed 3% of
            critical damping)
97      c = c_f + c_w; % Total damping
98      zeta = c / c_crtic; % Damping ratio
99
100     % --- System Parameters for ODE ---
101     a1 = gamma * A_w * P_inf / V_0;
102     a2 = gamma * A_o * P_inf / V_0;
103     a3 = 1 / dens_inf / L_e;
104     a4 = K / 2 / L_e;
105     a6 = A_w / m;
106     a7 = zeta * 2 * omega_w;
107     a8 = omega_w^2;
108     omega_h = U_sound * sqrt(A_o / L_e / V_0); % Helmholtz
            resonance frequency
109     fr_h = omega_h / 2 / pi; % Helmholtz resonance frequency in Hz
110     fr_w = omega_w / 2 / pi; % Natural frequency of diaphragm in Hz
111     a11 = omega_h^2;
112     a12 = A_w / A_o * a11;
113
114     % --- Parameter Structure for ODE Function ---
115     params.a1 = a1;
116     params.a2 = a2;
117     params.a3 = a3;
118     params.a4 = a4;
119     params.a5 = F_max_air / m; % Force per unit mass
120     params.a6 = a6;
121     params.a7 = a7;
122     params.a8 = a8;
123     params.a9 = f; % Frequency for forcing function
124     params.a11 = a11;
125     params.a12 = a12;
126
127     % --- ODE Simulation ---
128     t_end = 1/f*50+1/f/4; % Simulation time: 50 cycles + 1/4 cycle
            for settling
129     [t, X] = ode45(@(t, X) system_equations(t, X, params), [0,
            t_end], [0, 0, 0, 0, 0]);
130
131     % --- Post-processing and Max Value Extraction ---
132     mid_index = round(size(X, 1) / 1.5); % Index to start analysis
            after initial transient
133     u_squared = X(mid_index:end, 4).^2; % Square of orifice velocity
134     momnetum(i) = trapz(t(mid_index:end, 1), u_squared) .* dens_inf
            * A_o / (25/2) * f; % Momentum calculation (scaled)
135     u_avg = abs(X(mid_index:end, 4)); % Absolute orifice velocity
136     Massflow(i) = trapz(t(mid_index:end, 1), u_avg) .* dens_inf *
            A_o / (25/2) * f; % Mass flow rate calculation (scaled)
137
138     % --- Store Maximum Values for Plotting ---
```

```
    max_Xdot1_values(i) = max(X(mid_index:end, 1));
    max_Xdot2_values(i) = max(X(mid_index:end, 2));
    max_Xdot3_values(i) = max(X(mid_index:end, 3));
    max_Xdot4_values(i) = max(X(mid_index:end, 4));
    max_Xdot5_values(i) = max(X(mid_index:end, 5));
    U_air(i) = max_Xdot4_values(i); % Max Orifice Velocity
    Disp_air(i) = max_Xdot2_values(i); % Max Diaphragm Displacement
    Phase_air(i) = X(end, 4) / max_Xdot4_values(i) * 2 * pi; %
       Phase of Orifice Velocity (Not consistently used, review if
       phase is needed at end time)
    Phase_air_disp(i) = X(end, 2) / max_Xdot2_values(i) * 2 * pi; %
       Phase of Displacement (Not consistently used, review if
       phase is needed at end time)
    Phase_air_vel(i) = (X(end, 4) .* X(end, 3)) ./
       (max_Xdot4_values(i) .* max_Xdot3_values(i)); % Combined
       Phase Term (Review Physical Meaning)


    for q = 1:length(distance) % Loop for different distances for
       Nusselt Number
        Re_air(i) = max_Xdot4_values(i) * D_o / pi / nu_inf; %
           Reynolds Number Calculation
        Nu_air(i, q) = 1.007 * Prandtl_inf^0.42 * Re_air(i)^0.485 *
           (omega / omega_w)^(-1/500) * (0.0001 / A_o)^(-0.214) *
           (distance(q))^-0.914; % Nusselt Number Calculation
           (Empirical Correlation)
    end
end


%%%%%%%%%%%%%%%%%%%%%%%%%%%%%%%%%%%%%%%%%%%%%%%%%%%%%%%%%%%%%%%%
%%%%% Plotting Results
%%%%%%%%%%%%%%%%%%%%%%%%%%%%%%%%%%%%%%%%%%%%%%%%%%%%%%%%%%%%%%%%

% --- Orifice Velocity vs Frequency ---
fig1 = figure('Units', 'centimeters', 'Position', [0, 0, 9, 6]);
plot(f_values, U_air, 'k-', 'LineWidth', 1);
hold on;
ax = gca;
ax.GridLineStyle = '-';
ax.FontName = 'Times New Roman';
ax.FontSize = 10;
ax.XLabel.String = 'Frequency (Hz)';
ax.YLabel.String = 'Orifice Velocity U_{air} (m/s)';
ax.LineWidth = 1;
legend('U_{air}');
title([]);
grid on;
ax.Box = 'on';
ax.LineWidth = 1;
```

```
178
179
180 % --- Diaphragm Displacement vs Frequency ---
181 fig2 = figure('Units', 'centimeters', 'Position', [0, 0, 9, 6]);
182 plot(f_values, Disp_air * 1000000, 'k-', 'LineWidth', 1); %
       Displacement in micrometers
183 ax = gca;
184 ax.GridLineStyle = '-';
185 ax.FontName = 'Times New Roman';
186 ax.FontSize = 10;
187 ax.XLabel.String = 'Frequency (Hz)';
188 ax.YLabel.String = 'Diaphragm Displacement (\mum)';
189 ax.LineWidth = 1;
190 legend('Disp_{air}');
191 title([]);
192 grid on;
193 ax.Box = 'on';
194 ax.LineWidth = 1;
195
196
197 % --- Phase Lag vs Frequency ---
198 fig3 = figure('Units', 'centimeters', 'Position', [0, 0, 9, 6]);
199 plot(f_values, (1 - Phase_air_vel) .* 90, 'k-', 'LineWidth', 1); %
       Phase Lag (scaled to degrees - review scaling factor)
200 ax = gca;
201 ax.GridLineStyle = '-';
202 ax.FontName = 'Times New Roman';
203 ax.FontSize = 10;
204 ax.XLabel.String = 'Frequency (Hz)';
205 ax.YLabel.String = 'Phase Lag';
206 ax.LineWidth = 1;
207 legend('Phase Lag');
208 title([]);
209 grid on;
210 ax.Box = 'on';
211 ax.LineWidth = 1;
212 ylim([-10 180]) % Set Y-axis limits
213
214
215 % --- Momentum vs Frequency ---
216 fig4 = figure('Units', 'centimeters', 'Position', [0, 0, 9, 6]);
217 plot(f_values, momnetum, 'k-', 'LineWidth', 1);
218 ax = gca;
219 ax.GridLineStyle = '-';
220 ax.FontName = 'Times New Roman';
221 ax.FontSize = 10;
222 ax.XLabel.String = 'Frequency (Hz)';
223 ax.YLabel.String = 'Momentum';
224 ax.LineWidth = 1;
225 legend('Momentum');
```

```
title([]);
grid on;
ax.Box = 'on';
ax.LineWidth = 1;


% --- Volume Flow Rate vs Frequency ---
fig8 = figure('Units', 'centimeters', 'Position', [0, 0, 9, 6]);
plot(f_values, Massflow ./ dens_inf .* 3600, 'k-', 'LineWidth', 1);
    % Volume flow rate in m^3/hour
ax = gca;
ax.GridLineStyle = '-';
ax.FontName = 'Times New Roman';
ax.FontSize = 10;
ax.XLabel.String = 'Frequency (Hz)';
ax.YLabel.String = 'Volume flow rate (m^3/hour)';
ax.LineWidth = 1;
legend('Volume flow rate');
title([]);
grid on;
ax.Box = 'on';
ax.LineWidth = 1;


%%%%%%%%%%%%%%%%%%%%%%%%%%%%%%%%%%%%%%%%%%%%%%%%%%%%%%%%%%%%
%%%%% ODE Function Definition
%%%%%%%%%%%%%%%%%%%%%%%%%%%%%%%%%%%%%%%%%%%%%%%%%%%%%%%%%%%%

function Xdot = system_equations(t, X, params)
    %SYSTEM_EQUATIONS Defines the set of ODEs for the piezoelectric
       actuator system.
    %   Xdot = system_equations(t, X, params) returns the
       derivatives of the state
    %   variables X at time t, given the parameters in the struct
       'params'.
    %   State variables X are:
    %   X(1): Pressure in cavity (P) - actually derivative of
       Pressure dP/dt
    %   X(2): Diaphragm Displacement (x_w)
    %   X(3): Diaphragm Velocity (x_w_dot)
    %   X(4): Orifice Velocity (u)
    %   X(5): Orifice Acceleration (u_dot)


    pressure_flow_coeff = params.a1;    % a1 = gamma * A_w * P_inf /
       V_0;
    pressure_orifice_coeff = params.a2; % a2 = gamma * A_o * P_inf
       / V_0;
    orifice_velocity_pressure_coeff = params.a3; % a3 = 1 /
       dens_inf / L_e;
```

```
268     orifice_loss_coeff = params.a4;       % a4 = K / 2 / L_e;
269     driving_force_amplitude_coeff = params.a5; % a5 = F_max_air / m;
270     diaphragm_pressure_coeff = params.a6;     % a6 = A_w / m;
271     diaphragm_damping_coeff = params.a7;      % a7 = zeta * 2 *
            omega_w;
272     diaphragm_stiffness_coeff = params.a8;    % a8 = omega_w^2;
273     f = params.a9;                            % f = frequency
274     orifice_pressure_term_coeff = params.a11; % a11 = omega_h^2;
275     orifice_diaphragm_term_coeff = params.a12; % a12 = A_w / A_o *
            a11;
276
277
278     Xdot = zeros(5, 1);  % Initialize Xdot as a column vector
279
280     % --- Define the ODEs ---
281     Xdot(1) = pressure_flow_coeff * X(3) - pressure_orifice_coeff *
            X(4);         % dP/dt equation
282     Xdot(3) = driving_force_amplitude_coeff * cos(f * 2 * pi * t) -
            diaphragm_pressure_coeff * X(1) - diaphragm_damping_coeff *
            X(3) - diaphragm_stiffness_coeff * X(2); % Diaphragm
            acceleration equation
283     Xdot(2) = X(3);

            % Diaphragm velocity equation
284     Xdot(4) = X(5);

            % Orifice velocity equation
285     Xdot(5) = -2 * orifice_loss_coeff * abs(X(4)) * X(5) -
            orifice_pressure_term_coeff * X(4) +
            orifice_diaphragm_term_coeff * X(3); % Orifice acceleration
            equation
286
287 end
```

Listing A.1: Frequency Sweep of LEM on Air

Appendix B

Air Impingement Heater Unit Design and Calibration

The proposed experiments require the construction of a specialized heater/measurement unit. This unit is designed to provide a surface heat flux on a 30 mm × 30 mm area on the top surface of a 30 mm × 30 mm × 2.25 mm aluminum block. The arrangement of the unit can be seen in the exploded view in Figure B.1(a) and the assembled view in Figure B.1(b). Eleven holes are drilled 15 mm into the center of the block with 2.5 mm distance from each other using CNC machining. These holes are then filled with thermal conductive paste. Array of thermocouples inserted into the sensor block, just below 0.5 mm from its top surface.
As shown in Figure B.1(c), eleven T type beaded thermocouples (TCs) from Omega (5TC-TT-T-30-36-ROHS), each with a wire gauge of 30 and total thickness of 0.5 mm insulated with PFA plastic (perfluoroalkoxy with added thickness 3 mil or 0.0762 mm increasing total diameter of the TC to around 0.7-0.8 mm), are inserted into the holes. The tip of each thermocouple is positioned at the end of its respective hole. The thermocouples are connected to a temperature input module NI-9213. Temperature reading from each thermocouple is denoted as $\text{TC}_1, TC_2, toTC_{11}$.

To provide heat source to the aluminum block, a self-adhesive polyimide flexible surface heater (model KHLVA-101(1) from Omega) is installed on the bottom of the aluminum block. Power to the heater is supplied by Agilent E3633A DC power supply. Furthermore, the voltage across the heater is monitored by Hewlett 34401A multimeter.
To hold heater, thermocouple and insulate the aluminum block, the unit is insulated with quick cure Polyurethane foam sealant [280]. To do this, as shown in Figure B.2(a), aluminum block is placed securely on a work bench. Next the plastic mold cup is positioned above the heater block with center alignment. Next, as shown in Figure B.2(b) from the hole in top of the plastic cup insulating foam is ejected into the cup and is waited to be cured. After the foam is cured, as shown in Figure B.2(c) heater block, TC sensors, and plastic cup are all assembled and kept in please by insulation foam. Heater control and data acquisition is performed using custom LabView program. These custom programs involve data acquisition controlled by a for-loop with a specified number of iterations and delay between measurements.
As illustrated in Figure B.3(a), the thermal resistance network of the heater can be simplified into two major heat paths.

- The first path is from the top side of the surface heater that is attached to the aluminum block.

  In the first path, there are two thermal resistances: from the heater to the other side of the aluminum block (denoted asR_b), and from the surface of the aluminum block to the air

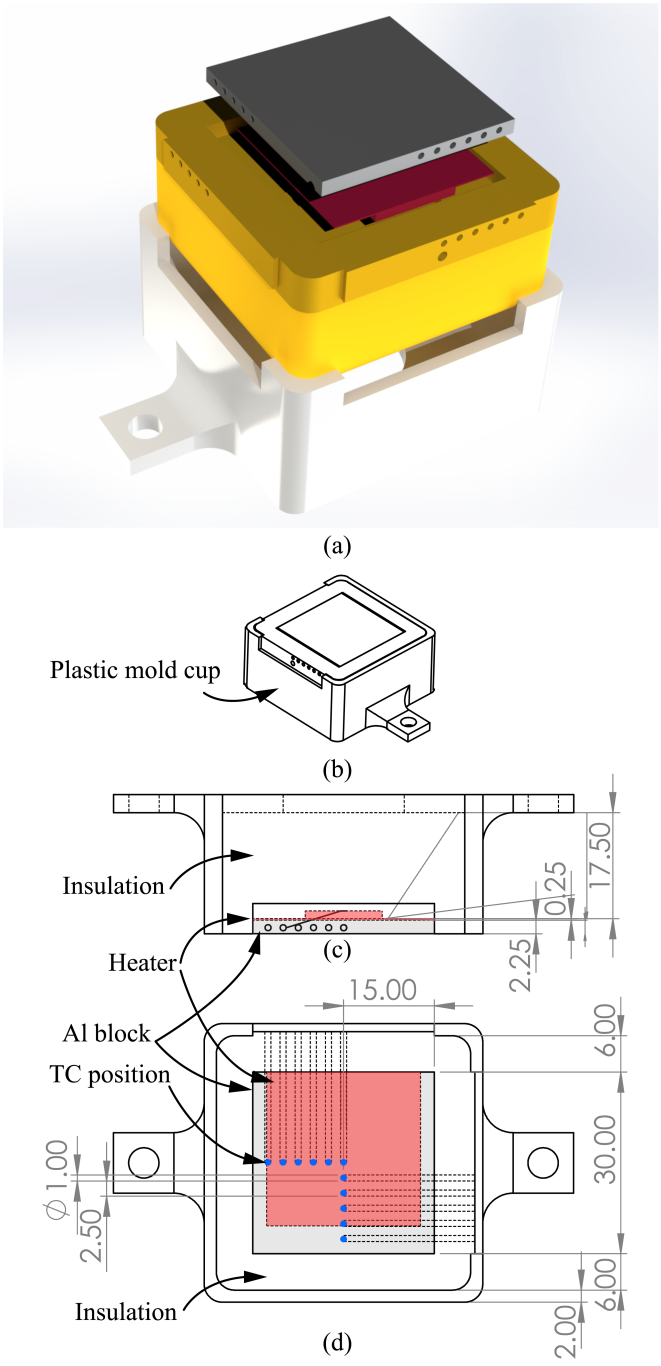

Figure B.1: (a) 3D explode view, (b) assembled view (c) and detailed view of the heater unit. (Dimensions are in mm.)

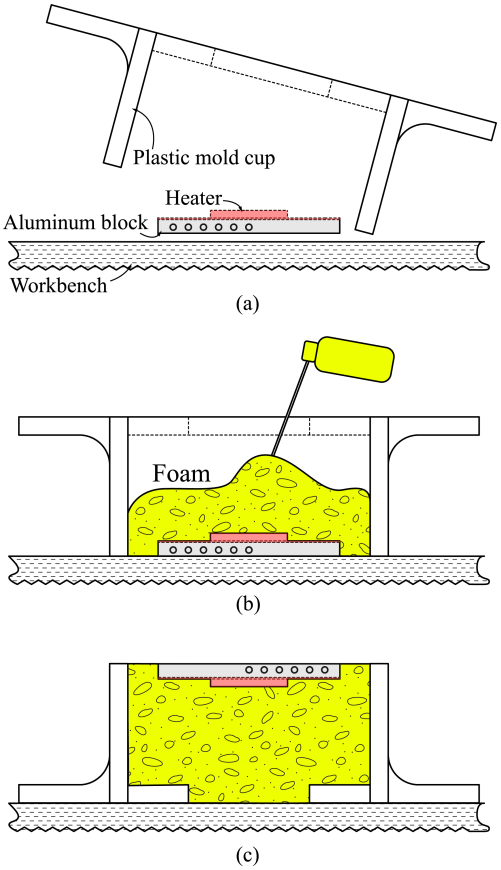

Figure B.2: (a) 3D explode view, (b) assembled view (c) and detailed view of the heater unit (Dimensions are in mm).

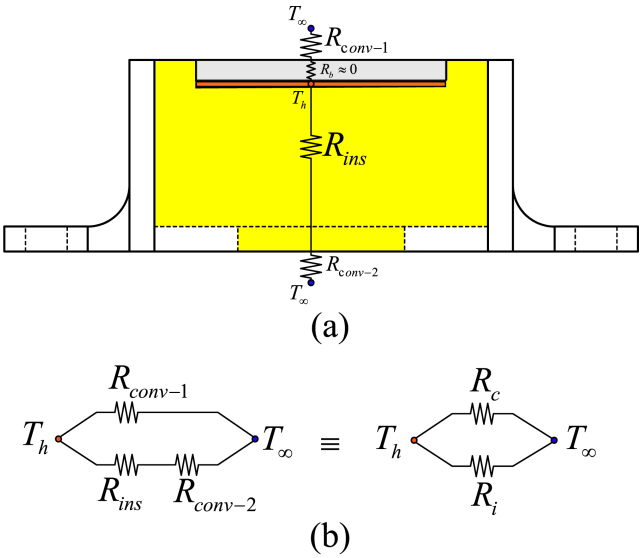

Figure B.3: (a) Thermal resistance of the heater unit, and (b) simplified thermal resistance network.

(denoted as R_{conv-1}). (It's important to note that due to the heater and heat source being similar in size, the heat spreading from heater the aluminum block can be neglected. Additionally, due to the thin profile of the aluminum block, the resistance between both sides of the block is almost zero (0.0125 K/W) and can also be neglected ($R_b = 0$).)

- The Second heat path is opposite side of the surface heater that is being covered by insulation foam. On the second path, heat spreads into the insulation foam and then reaches to the plastic cup, which is denoted as Rins. Next, convection to air occurs which is denoted as R_{conv-2}. As shown in B.3(b), we can denote thermal resistance of the first path to R_c, which represents the convection on top of the aluminum block. Next for the second path, thermal resistance is denoted as $R_i = R_{ins} + R_{conv-2}$, which controls the total heat loss of the system. R_c and Ri are in parallel configurations.

It is important to note that in study being performed on the heater, it is expected that R_i to be constant while R_c to be changed in different conditions, including different surface temperature, or different cooling methods being applied on the top of the heater. The reason the R_i is going to be considered as constant is that during natural convection studies done on the heater, which is going to be discussed next, surface temperature rise of the insulation around the heater is almost negligible. Furthermore, the small surface area makes convective heat transfer from sides of the heater negligible and R_{conv-2} is mainly due to conduction to air and natural convection effect is almost zero. This, way if one can calibrate and know the value of R_i through calibration studies, then R_c and consequently combined convective and radiative heat transfer coefficient on top surface the heater block can be evaluated as:

$$\frac{R_c R_i}{R_c + R_i} = \left(\sum_{i=1}^{11} TC_i/11 - TC_{air} \right) /P \tag{B.1}$$

$$h = \left(\frac{P}{\sum_{i=1}^{11} TC_i/11 - TC_{air}} - \frac{1}{R_i} \right) /A_{heater} \tag{B.2}$$

Where$A_{heater} = 0.0009(\mathrm{m}^2)$ is surface area of the heater and P is input source power which can be evaluated as $P = V_{heater} \cdot I_{heater}$ where Iheater and Vheater are applied current, and measured voltage of the heater, respectively.

To determine R_i, the heater was tested under horizontal natural convection conditions at five different current levels: $I_{heater} = 0.111, 0.117, 0.122, 0.127, and 0.132$ (A). For each current level measurements continue to reach steady state. The total duration of the calibration test was 18000 seconds (5 hours). The experimental results revealed that the temperatures of all 11 thermocouples were the same, with negligible deviation. This indicates that the surface temperature of the heater remained constant during natural convection. This can be seen in Fig. 26. B.4 presents the temporal variation of temperature for all eleven thermocouples in current level of $I = 0.132$ (A) in 1000 second snapshot duration recorded in steady state conditions. TCs positioned in the center show slightly higher temperatures in comparison to TCs positioned in the edges due to thermal boundary layer formation in the center of the heater. Furthermore, presented results ensure the factory calibration of the TCs where deviation of temperature in between neighboring TCs are below the error of the measurement.
Since the temperature of the thermocouples are almost the same and we are observing a uniform temperature in the heater, results for the calibration test will be performed based on the average value of all 11 thermocouples. The time-dependent average surface temperature of the

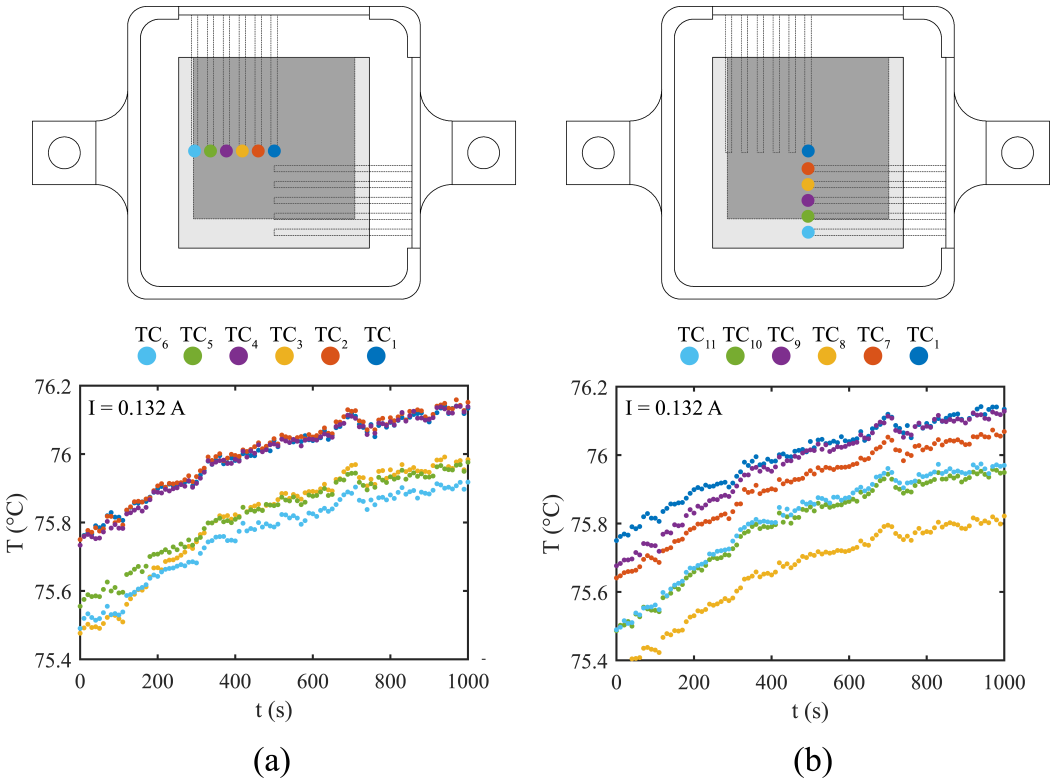

(a) (b)

Figure B.4: Temporal variation of temperature for all eleven thermocouples in current level of $I_{heater} = 0.132$ (A) for (a) thermocouple number 1 to 6, and (b) thermocouple number 1, 7 to 11 in 1000 second duration recorded in steady state conditions.

heater, the temperature of the air, and the temperature rise of the heater are all shown in Figure B.5. From Figure B.5(a), it can be observed that the heater reaches a steady state within the first 1000 seconds (17 minutes) of each power level. However, to ensure the accuracy of the measurements, the measurements were continued. In Figure B.5(a) one can observe a fluctuation in the surface temperature of the heater, which is due to temperature variation of the air in the lab environment, which can be seen in Figure B.5(b). In Figure B.5(b) the temperature of the air in the laboratory fluctuates between 21.5 and 23 °C. It should be noted that the test is performed on winter at atmospheric pressure of 1.02 bar.
The power level of the heater, as shown in Figure B.5(c), appears to be quite uniform during the simulations. However, if we plot the resistance of the heater versus time, an increase in its resistance over time can be observed, while this fluctuation does not seem effective, however we can detect a pattern between thermal resistance of the heater and aluminum block temperature as shown Fig. 27(a) (for instance compare Figure B.5(a) and Figure B.5(d) at t = 3000 (s) or at t = 10000 (s)). Thus, time dependent heat generation (P) in the heater is considered in calculations. To determine whether the system reaches a steady state, we need to note that heat removal from the top surface can be affected by the fluctuation of air temperature. If one subtracts the surface temperature of the heater from the air temperature, steady state conditions can be seen which is shown in Figure B.5(e). The results confirm the accuracy of the measurements. Due to the long duration of the experiment, steady state condition might not be visible in Figure B.5(e), so the results the last 1000 seconds of each measurement is provided in Figure B.5(f), where the steady state condition can be observed. With having the results in hand for heater unit performance in natural convection condition facing upwards, thermal resistance of the insulation can be evaluated as:

$$R_i = \left(\frac{P}{\sum_{i=1}^{11} TC_i/11 - TC_{air}} - \frac{1}{hA_{heater}} \right)^{-1} \tag{B.3}$$

It can be seen that value of h is the only unknown in right hand side of Equation B.3. To evaluate h, heat transfer correlation in natural convection needs to be revisited. The simple empirical correlations for the average Nusselt number Nu in natural convection are of the form:

$$Nu = \frac{hL_c}{k} = C(Gr \cdot Pr)^n = CRa^n \tag{B.4}$$

Where k, Pr, Gr, and Ra are thermal conductivity, Prandtl, Grashof, and Rayleigh number of the air in film temperature, respectively. Furthermore, L_c is characteristic length, which for heated plates facing upward is usually the ratio of surface area to the perimeter which is $L_c = 7.5$ (mm) in here. $C1$ is constant and depends on the geometry of the surface and the flow regime. In most cases usually n is 0.25 for laminar flow (Gr $< 10^9$) [281]. Ra number represents the ratio of buoyancy forces to both thermal diffusivity and momentum diffusivity and can be evaluated as:

$$Ra = \frac{gc_p\beta(T_s - T_\infty)L_c^3}{\mu k} \tag{B.5}$$

Where g, c_p, , are standard acceleration of gravity, specific heat in constant pressure, thermal expansion coefficient ($1/T_f$), and dynamic viscosity in film temperature ($T_f = (T_s + T_\infty)/2$). Based on the time-dependent behavior of the air film temperature, the time-dependent Rayleigh number of the system is developed in Figure B.5(g). This calculation is based on the temperature-dependent behavior of the air that alters the density, viscosity, specific heat,

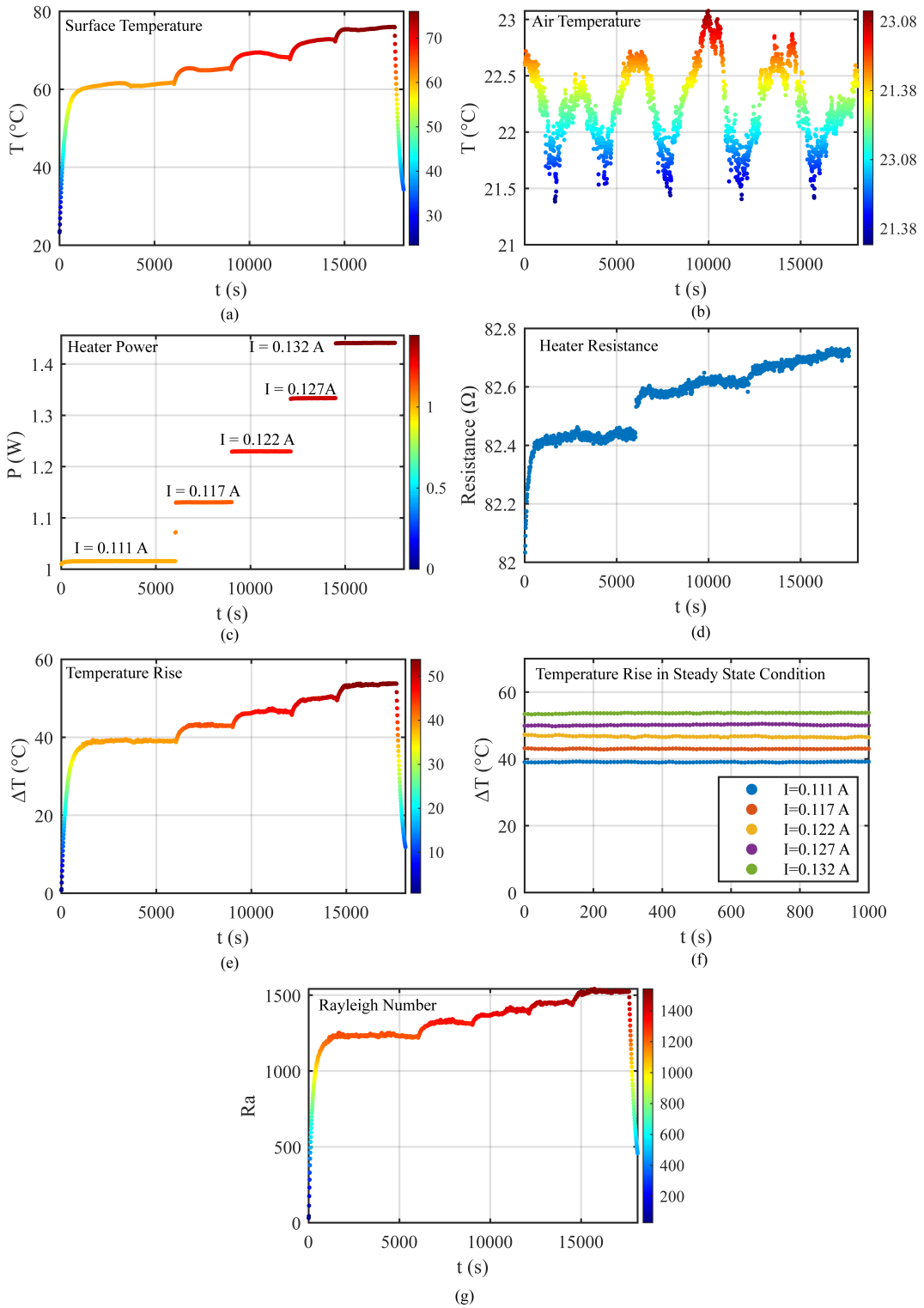

Figure B.5: (a) averaged surface temperature of 11 TCs, (b) air temperature, (c) input heater power, (d) heater resistance, (e) average surface temperature rise, (f) average surface temperature rise in steady state condition, and (g) Rayleigh number vs time in calibration test study.

thermal conductivity, and thermal expansion coefficient, which are calculated based on a forth order polynomial fittings for air properties in atmospheric pressure [282]. Rayleigh number is between 1000 to 1500 for current test case. This Ra number value range is well below validity range of empirical correlations for the average Nusselt number for natural convection over constant temperature horizontal surfaces (typically Ra104). The reason for such low Ra number is that small size of the surface area. If one examines the natural convection correlations for isolated horizontal surfaces in literature we can see that almost all of the test specimen surface are relatively large in comparison to our study [283, 284]. Low Rayleigh number in current case reflects that buoyancy driven flow is weak. Thus, for accurate heat transfer coefficient evaluation, three-dimensional computational fluid dynamic simulations is needed to be performed. As discussed in previous section, since the heater has a small surface area, the Rayleigh number is in lower limit of proposed empirical correlations for natural convection correlations from. It is also discussed that as surface area becomes smaller it's expected that the role of natural convection reduces. This brings the necessity of CFD simulations to understand the flow field and heat removal to air from the aluminum block. For this purpose, the surrounding air is modeled to understand non-isothermal buoyancy driven laminar flow characteristics around the heater. The configuration of the simulation is shown in Figure B.6(a) and (b). As shown in B.6(a) it can be seen that domain around the heater can be cut into 1/8th because of existing symmetry in the model, while considering laminar flow due to low Gr number. A total of 8 surfaces are identified for simulation. Surface ID (1) is the constant temperature zone. Constant temperature is selected, since all 11 thermocouples in the heater as shown in B.4 approved this assumption for this surface. Considered temperatures for this surface are 39.05, 42.99, 46.67, 50.15, and 53.69 °C, respectively for current levels of 0.111, 0.117, 0.122, 0.127, and 0.132 (A) of the heaters. These temperatures are the average surface temperature of the aluminum block in steady state conditions evaluated from an average of 11 thermocouple readings in last 1000 seconds of each test current.

Surface ID (2) and (3), account for the insulation around the heater and considered as insulated wall. It needs to be noted that the insulation provides a step-like structure around the heater, which might affect the incoming flow from surrounding. This incoming flow is considered from Surface ID (8) at 8 mm distant from the side of the heater with assigned boundary condition of pressure inlet. The gauge pressure value in this surface is linearly varying and is defined based on the height of each cell, which is given in Table 9. Surface ID 4 is considered as insulated wall and is the base where heater unit sits on. Surface ID (6) and (7) are considered as symmetry planes. Finally, Surface ID (5) is a pressure outlet with gauge pressure of 0. The transient natural convection phenomenon was investigated using ANSYS Fluent v2021.R2. The computational domain was filled with air modeled as an incompressible ideal gas with an operating pressure and temperature of 1 atm and 22°C, respectively. Numerical convergence was achieved by setting the residual targets to 10^{-8} for the continuity and momentum equations and 10^{-10} for the energy equation.

Gravity was incorporated through the consideration of a body force term. Pressure based solver with pressure-velocity coupling scheme is employed. Mass flux type of Rhie-Chow: distance based is used. For the spatial discretization of the convection terms in the solution, for pressure correction, the body force weighted scheme was preferred. Higher-order discretization was utilized for density, momentum, and energy using the second-order upwind scheme with pseudo-transient formulation. Flow is solved in a pseudo-transient fashion. The pseudo-transient approach introduces an artificial "time-like" variable by iteratively updating the flow

variables over "pseudo-time steps.". Steady state condition is controlled by controlling the average surface heat flux on Surface ID (1) for each time step. A summary of boundary conditions assigned for each surface ID can be seen in Table **??**.

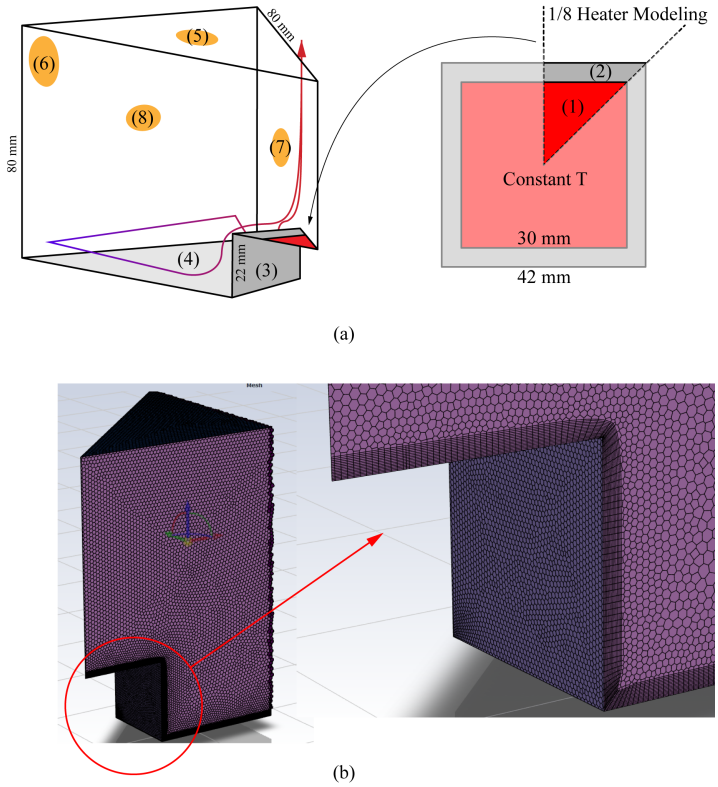

Figure B.6: (a) averaged surface temperature of 11 TCs, (b) air temperature, (c) input heater power, (d) heater resistance, (e) average surface temperature rise, (f) average surface temperature rise in steady state condition, and (g) Rayleigh number vs time in calibration test study.

Meshing is performed using Fluent Meshing. The meshing method is selected as poly-hexacore with 3 buffer layers and 1 peel layer. A total of 15 uniform inflation layers are used on the walls with first layer height of 0.1 mm and growth rate of 1.02. This selection is based on evaluation of boundary layer thickness which is evaluated based on a scaling analysis for laminar boundary layer in natural convection yields to [285]:

$$\delta = \mathrm{Gr}^{-0.2} L_c \tag{B.6}$$

Where δ, is boundary layer thickness. Calculation of boundary layer thickness lead to approximate thermal boundary layer thickness of 1.6 mm. This thickness is covered by the inflation layers in the meshing as shown In Fig. 28(b). Furthermore, as shown in Table B.1, mesh face size is considered 0.5 mm for surface ID (1 to 4) and 1 mm for surface ID (5 to 8). Figure B.7(a) and (b) present the temperature, and velocity vector field of in central plane of the heater for the lowest power level. It can be seen that the step structure of the heater barely effects the natural convective current above the heater while velocities are highest in the center line of the heater above the heater where convective currents are merging together. This is more visible in 3D view of the air streamlines in Figure B.7(c). Overall there is a fairly low velocity field in the domain for studied power levels. For current levels of 0.111, 0.117, 0.122, 0.127, and 0.132 (A),

	Surface ID number							
	1	2	3	4	5	6	7	8
Thermal BC	Constant T	Insulated			295.15 K	Sym		295.15 K
Momentum BC	Wall				p = 0	Sym		p = g(0.08[m]-z)(1.2[kg/m^3])
Mesh face size	0.5 mm				1 mm	1 mm		
Inflation Layers number	15				N/A			
First Height/growth rate of inflation layer	0.1 mm / 1.02				N/A			

Table B.1: Summary of applied boundary conditions and meshing configuration for studied models.

respectively, calculated heat transfer to air from fluent simulations are 299.36, 3332.92, 363.18, 403.89, 433.66 W/m^2. Taking into account that average temperature rise for these numbers are 39.05, 42.99, 46.67, 50.15, and 53.69 K, heat transfer coefficients can be evaluated as 7.56, 77, 7.81, 7.95, and 8.05 W/(m^2·K). This shows a relatively lower Nusselt number of Nu = 2.06 for lowest surface temperature to Nu = 2.15 for highest surface temperature. From other perspective, results show a 35% reduction in natural convection effectiveness in comparison to higher Ra ranges where most of the empirical correlations are obtained (famous Nusselt correlation that can be obtained from Nu = 0.54 Ra$^{0.25}$, which is valid for Ra range of 104-107 [167]).

Revisiting Equation B.3, one can now determine the thermal resistance of the insulation in the heater, and the obtained results are presented in the last line of Table **??**. Notably, a fairly constant value of thermal resistance is observed for the heater, as expected. Through experimental observation, it is seen that the surface temperature of the insulation around the heater barely rises to a level where convection from the sides of the heater contributes significantly to convective heat transfer. The primary heat transfer from the sides of the heater is predominantly due to conduction to air. This is the reason why insulation thermal resistance is constant. Therefore, based on the findings, and noting that the later experiments will be performed in similar power ranges and with higher heat transfer coefficient on the aluminum plate, it is reasonable to consider that the thermal resistance of the heater insulation is 51.7 K/W. This implies that the insulation around the heater effectively resists the flow of heat, maintaining a relatively constant thermal resistance value across varying conditions in the experiments.

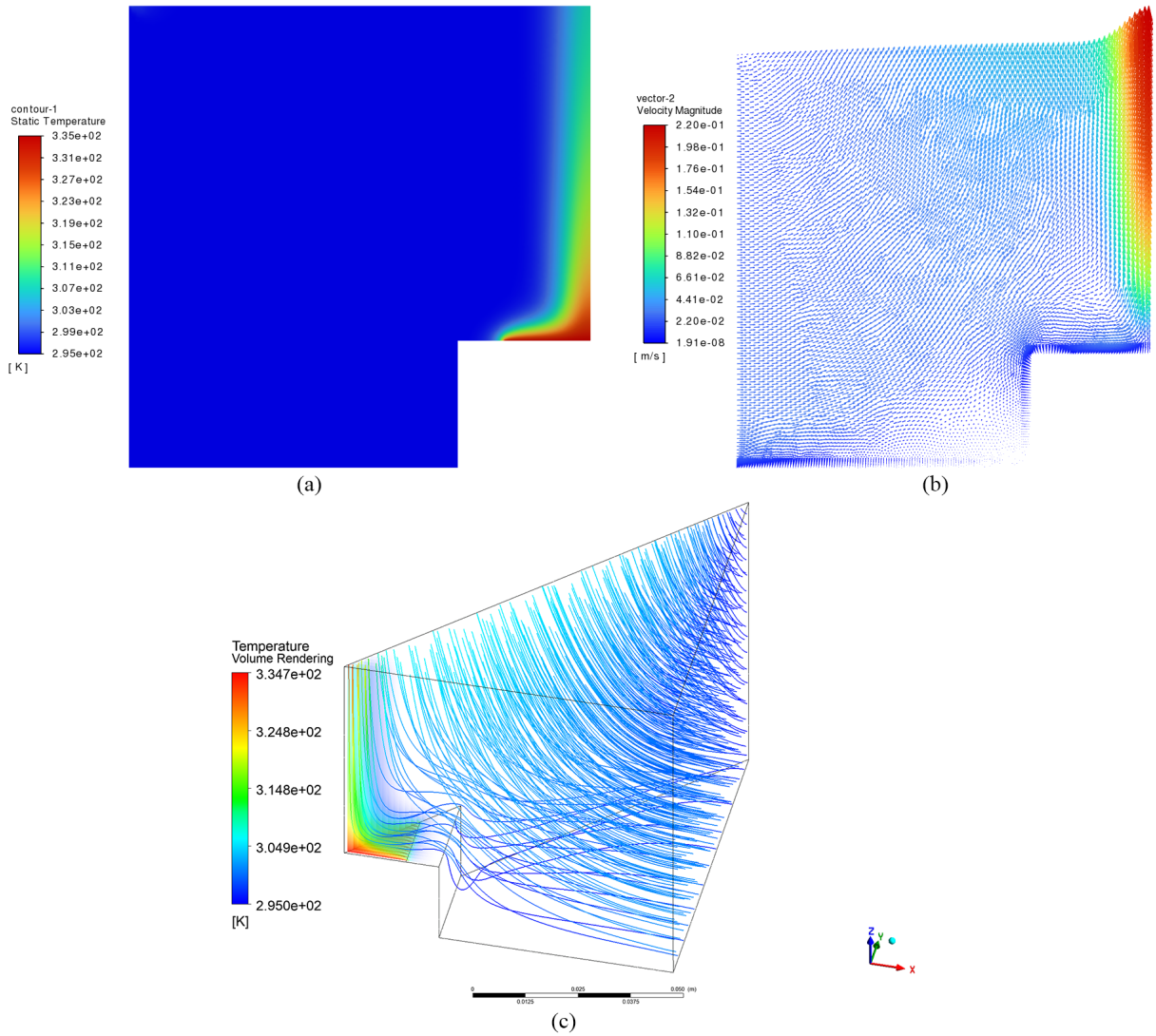

Figure B.7: (a) temperature distribution (b), and velocity vector field on central cut plane of the air. (c) 3D streamlines starting from pressure inlet and transparent volumetric temperature distribution of air over heater. The current level is 0.111 A.

P (W)	1.072	1.131	1.229	1.333	1.441
T_s (°C)	61.54	65.19	68.44	72.75	75.86
Ra	1226.74	1317.6	1401.44	1450.87	1523.49
q_{conv} (W/m^2)	299.36	332.92	363.18	403.89	433.66
h (W/m^2-K)	7.56	7.70	7.81	7.95	8.05
Nu	2.06	2.09	2.11	2.13	2.15
R_i (K/W)	48.65	51.72	51.70	51.7	51.08

Table B.2: Results of simulation and calculated behavior of natural convection and thermal resistance of heater insulation.

Appendix C

Deflection measurement and LEM tuning Results at Higher Voltage Level

This section contains the results obtained from SJDs operating at 140 Vpp. During these experiments, SJD 1, 2, and 6 failed due to the diaphragm's extremely high deflection. It should be noted that this failure did not occur suddenly. These devices failed after a few hours of operation at the wall resonance frequency. Thus, for the remainder of the experiments, voltage levels are reduced to 100 Vpp. When compared to 100 Vpp results, it is clear that SJDs operated at different voltages exhibit slightly different behavior, indicating the nonlinearity of such systems. In other words, the results from one voltage cannot be directly correlated to the device's behavior at higher or lower operating voltages.

		Deflection Experiment						LEM				
SJD	Cavity	fr_{min} (Hz)	Δx μm	fr_w (Hz)	Δx (μm)	fr_H(Hz)	Δx (μm)	k x 10^4(N/m)	F_{max}(N)	C_l	C_d	fr_H(Hz)
1	con	25	133	525	287	1600-1800	65	7.77	3.69	1.5	0.6	1304
2	cyl	25	130	600	344	1400-1600	70	10.14	7.06	1.5	0.6	1304
3	con	25	109	625	388	1600-1800	77	9.43	3.00	2	0.6	1370
4	con	25	148	475	301	1600-1800	91	7.49	3.02	2.75	0.6	1610
5	con	25	119	575	296	1500-1700	46	7.65	3.56	0.45	0.6	1555
6	con	25	113	600	279	1500-1800	49	8.33	3.44	0.3	0.6	1600
7	cyl	25	126	650	428	1200-1400	51	7.72	4.82	0.45	0.6	1555

Table C.1: Results of deflection test and LEM tuning at 140 V.

SJD #	fr (Hz)	U (m/s)
1	570	48.3
2	665	67.9
3	620	39.8
4	515	47.8
5	625	48.5
6	655	47.4
7	630	58.3

Table C.2: Predicted maximum area averaged jet exit velocity at 140 V.

Appendix D

MATLAB Code for Liquid LEM

A sample MATLAB code is presented here:

```
clc
clear
% Code by Mohammad Azarifar, Auburn University. Use by Referencing
    Only
%%%%%Define Characters of Device
T_inf = 273.15 + 20;
P_inf = 101325;

D_w = 35 / 1000;           % Diaphragm Dia
D_piezo = 25 / 1000;       % Ceramic Dia
D_o = 5E-3;                % Dia of Orifice

dens_shim = 8700;          % Density of Brass
dens_piezo = 7700;         % Density of Piezo
thickness_shim = 0.25 / 1000; % Thickness of Brass
thickness_piezo = 0.28 / 1000; % Thickness of Piezo

A = pi / 4 * D_o^2;        % Area of Orifice
A_w = pi * D_w^2 / 4;      % Area of Diaphragm
A_piezo = pi * D_piezo^2 / 4; % Area of Ceramic

m_w = A_w * thickness_shim * dens_shim + A_piezo * thickness_piezo
    * dens_piezo; % Mass of Diaphragm

C_l = 3;                   % Inertia coefficient Used to Determine
    Effective Length of Orifice L_e
C_d = 0.6;                 % Discharge Coefficient used in Bernoulli
    Eq

L = 3E-3;                % Length of Cavity (Decided to be Half for
    Conical Cavity)
L_o = 0.5E-3;            % Length of Orifice
L_e = L_o + C_l * sqrt(A);

```

```
V_0 = (A_w + A) * L;       % Volume of the Cavity (L is half for
    conical Cavity)

F_max = 9;                 % Maximum Force at end of each stroke

k = 1200000;               % Stiffness of Diaphragm
K = (1 - (A / A_w)^2) / C_d^4; % This is effective Loss Coefficient

f_values = 210;            % For what frequencies you want to solve it

%%%%%%%%%%%%%%%%%%%%%%%%%%%%%%%%%%%%%%%%%%%%%%%%%%%%%%%%%%%%%%%%%%%%%%%
F_max_water = F_max;

    % Define Liquid Properties
    mu_inf = 0.001002;     % Viscosity
    Cp_inf = 4186;         % Specific Heat
    dens_inf = 998;        % Density
    nu_inf = mu_inf / dens_inf;  % Kinematic Viscosity
    cond_inf = 0.606;      % Thermal Conductivity
    Bulk_mod = 2.2E9;      % Bulk Modulus
    Prandtl_inf = mu_inf * Cp_inf / cond_inf; % Prandtl
    U_sound = sqrt(Bulk_mod / dens_inf);       % Speed of sound

    f = f_values;
    omega = f * 2 * pi;    % Change frequency into angular frequency

    % Evaluate Acoustic Damping and Mass
    y = omega * D_w / U_sound;
    % Evaluate Struve function of the first kind for few summations
    H1 = y / 3;
    for j = 2:10
        H1 = H1 + (-1)^(j + 1) * y^(2 * j - 1) * (factorial(j * 2 +
            1) / factorial(j) / 2^j)^-1;
    end
    J1 = besselj(1, y);    % Evaluated Bessel

    m_f = 4 * dens_inf * A_w * U_sound * H1 / pi / omega; %
        Acoustic Mass
    c_f = dens_inf * A_w * U_sound * (1 - 2 * J1 / y);      %
        Acoustic Damping

    m = m_f + m_w;         % Total mass
    omega_w = sqrt(k / m); % Radial Resonance of Diaphragm
    c_crtic = 2 * sqrt(m * omega_w); % Critical Damping of Diaphragm
    c_w = 0.03 * c_crtic;  % Damping of wall (assumed damping ratio
        0.03)
    c = c_f + c_w;         % Total damping of diaphragm
    zeta = c / c_crtic;    % Damping ratio

    % Coefficients of ODEs
```

```
75      a1 = A_w * Bulk_mod / V_0;
76      a2 = A * Bulk_mod / V_0;
77      a3 = 1 / dens_inf / L_e;
78      a4 = K / 2 / L_e;
79      a6 = A_w / m;
80      a7 = zeta * 2 * omega_w;
81      a8 = omega_w^2;
82      omega_h = U_sound * sqrt(A / V_0 / L_e); % Helmholtz Resonance
83      a11 = omega_h^2;
84      a12 = A_w / A * a11;
85
86      params.a1 = a1;
87      params.a2 = a2;
88      params.a3 = a3;
89      params.a4 = a4;
90      params.a5 = F_max_water / m;
91      params.a6 = a6;
92      params.a7 = a7;
93      params.a8 = a8;
94      params.a9 = f;
95      params.a11 = a11;
96      params.a12 = a12;
97
98      % Define what to solve in 50 cycles of oscillation
99      [t, X] = ode45(@(t, X) FUNCT(t, X, params), [0, 1 / f * 50 + 1
            / f / 4], [0, 0, 0, 0, 0]);
100
101     % Ignore data from first cycles to include steady state
            condition only
102     mid_index = round(size(X, 1) / 1.5);
103
104     % Evaluate Impulse Generation
105     u_squared = X(mid_index:end, 4).^2;
106     momnetum = trapz(t(mid_index:end, 1), u_squared) .* dens_inf *
            A / 25 / 2 * f;
107
108     % Evaluate Mass Flow Rate
109     u_avg = abs(X(mid_index:end, 4));
110     Massflow = trapz(t(mid_index:end, 1), u_avg) .* dens_inf * A /
            25 / 2 * f;
111
112     % Evaluate JFK
113     JFK = Massflow / dens_inf / A / 2 / pi / D_o;
114
115
116     max_Xdot1_values = max(X(mid_index:end, 1));
117     max_Xdot2_values = max(X(mid_index:end, 2));
118     max_Xdot3_values = max(X(mid_index:end, 3));
119     max_Xdot4_values = max(X(mid_index:end, 4));
120     max_Xdot5_values = max(X(mid_index:end, 5));
```

```
121     U_air = max_Xdot4_values;
122     Disp_air = max_Xdot2_values;
123 
124     % Evaluate Phases of jet and diaphragm
125     Phase_air = X(end, 4) / max_Xdot4_values * 2 * pi;
126     Phase_air_disp = X(end, 2) / max_Xdot2_values * 2 * pi;
127     Phase_air_vel = (X(end, 4) * X(end, 3)) / (max_Xdot4_values *
            max_Xdot3_values);
128 
129 %%%%%%%%%%%%%%%%%%%%%%%%%%%%%%%%%%%%%%%%%%%%%%%%%%%%%%%%%%%%%%%%%%%%%%%%
130 fig1 = figure('Units', 'centimeters', 'Position', [0, 0, 9, 6]);
131 plot(t(:), X(:, 4), 'k-', 'LineWidth', 1);
132 xlim([0, 0.05])
133 ax = gca;
134 ax.GridLineStyle = '-';
135 ax.FontName = 'Times New Roman';
136 ax.FontSize = 10;
137 ax.XLabel.String = 'fr (Hz)';
138 ax.YLabel.String = 'U (m/s)';
139 ax.LineWidth = 1;
140 legend('U\_L\_E\_M');
141 title([]);
142 grid on;
143 outerBoundary = findobj(gcf, 'Type', 'axes', 'Tag',
        'OuterPosition');
144 ax.Box = 'on';
145 ax.LineWidth = 1;
146 
147 % Function Matlab
148 function Xdot = FUNCT(t, X, params)
149     a1 = params.a1;
150     a2 = params.a2;
151     a3 = params.a3;
152     a4 = params.a4;
153     a5 = params.a5;
154     a6 = params.a6;
155     a7 = params.a7;
156     a8 = params.a8;
157     f = params.a9;
158     a11 = params.a11;
159     a12 = params.a12;
160 
161     Xdot = zeros(5, 1);  % Initialize Xdot as a column vector
162 
163     Xdot(1) = a1 * X(3) - a2 * X(4);
164     Xdot(2) = X(3);
165     Xdot(3) = a5 * cos(f * 2 * pi * t) - a6 * X(1) - a7 * X(3) - a8
            * X(2);
166     Xdot(4) = X(5);
167     Xdot(5) = -2 * a4 * abs(X(4)) * X(5) - a11 * X(4) + a12 * X(3);
```

```
168 end
```

Listing D.1: Single Frequency of LEM on Liquid

Appendix E

Liquid Synthetic Jet Impingement Set Up Calibration - Additional Figures

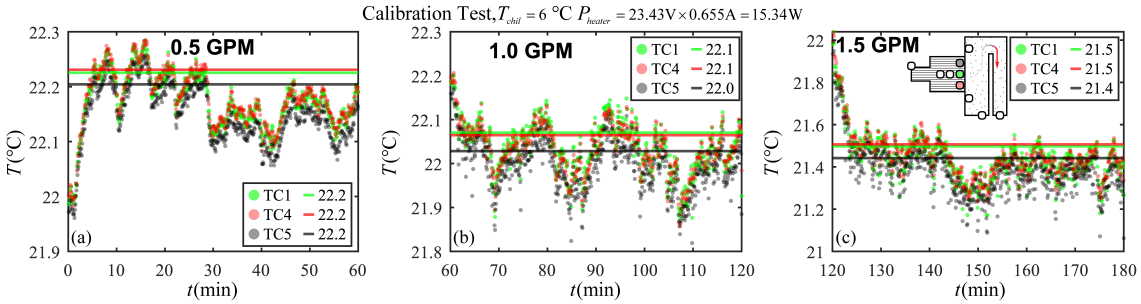

Figure E.1: TC1, 4, and 5 in 3 hour calibration test in three different inlet flow rates.

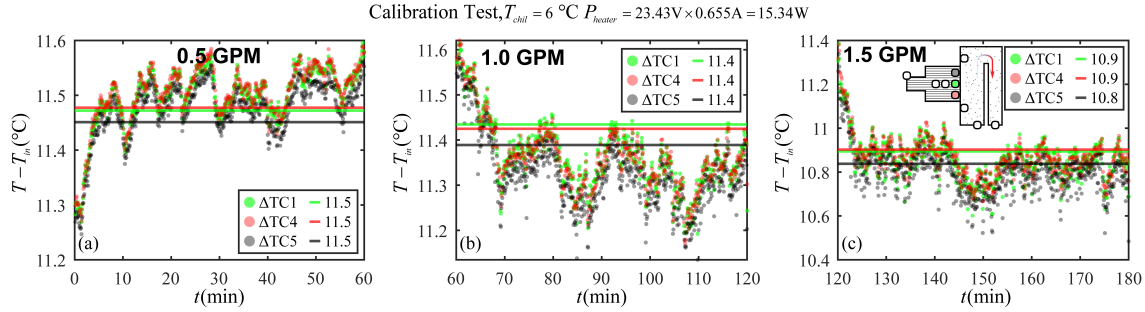

Figure E.2: Temperature rise of TC1, 4, and 5 in 3 hour calibration test in three different inlet flow rates.

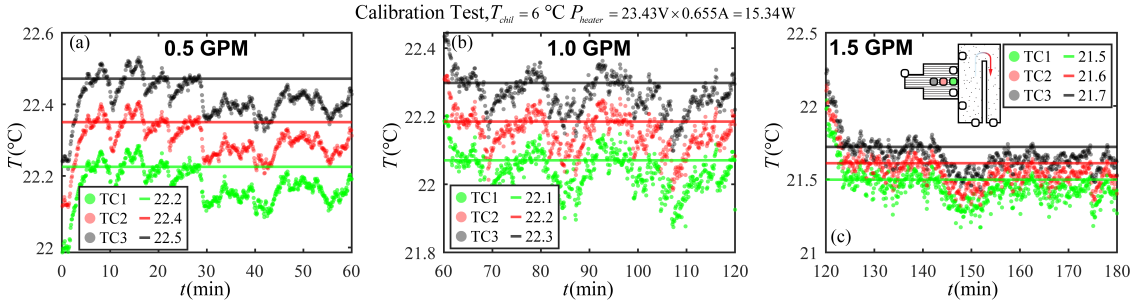

Figure E.3: TC1, 2, and 3 in 3 hour calibration test in three different inlet flow rates.

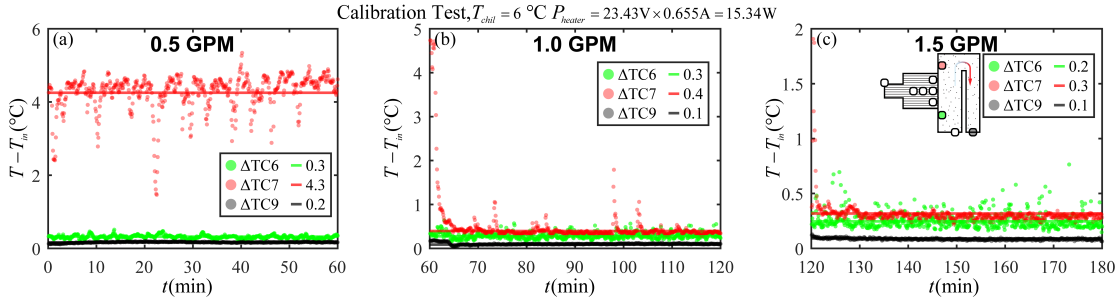

Figure E.4: Temperature rise of TC6, 7, and 9 in 3 hour calibration test in three different inlet flow rates.

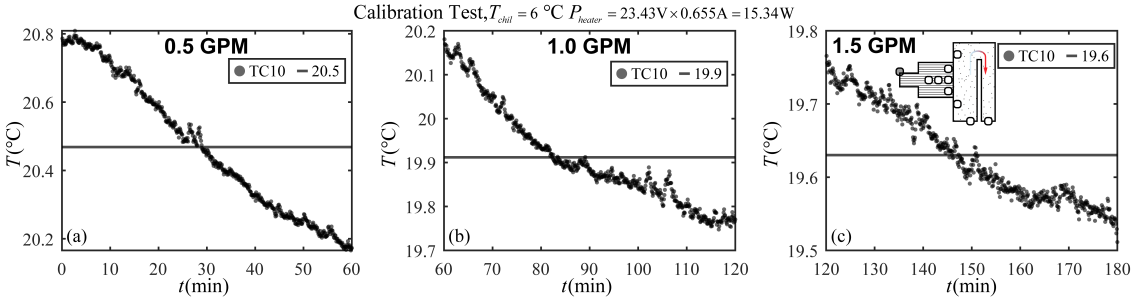

Figure E.5: TC10 in 3 hour calibration test in three different inlet flow rates.

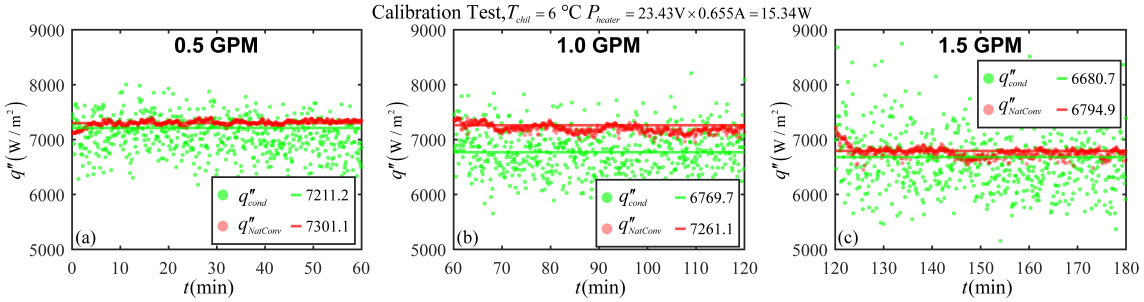

Figure E.6: Heat flux in three different inlet flow rates.

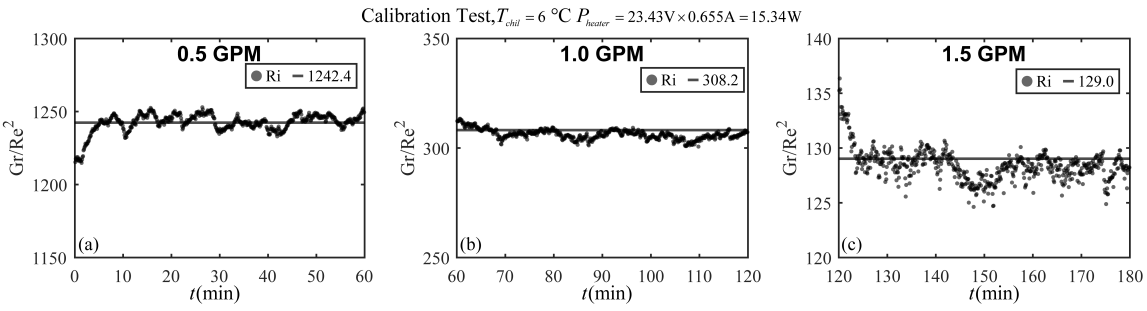

Figure E.7: Ri number in three different inlet flow rates.

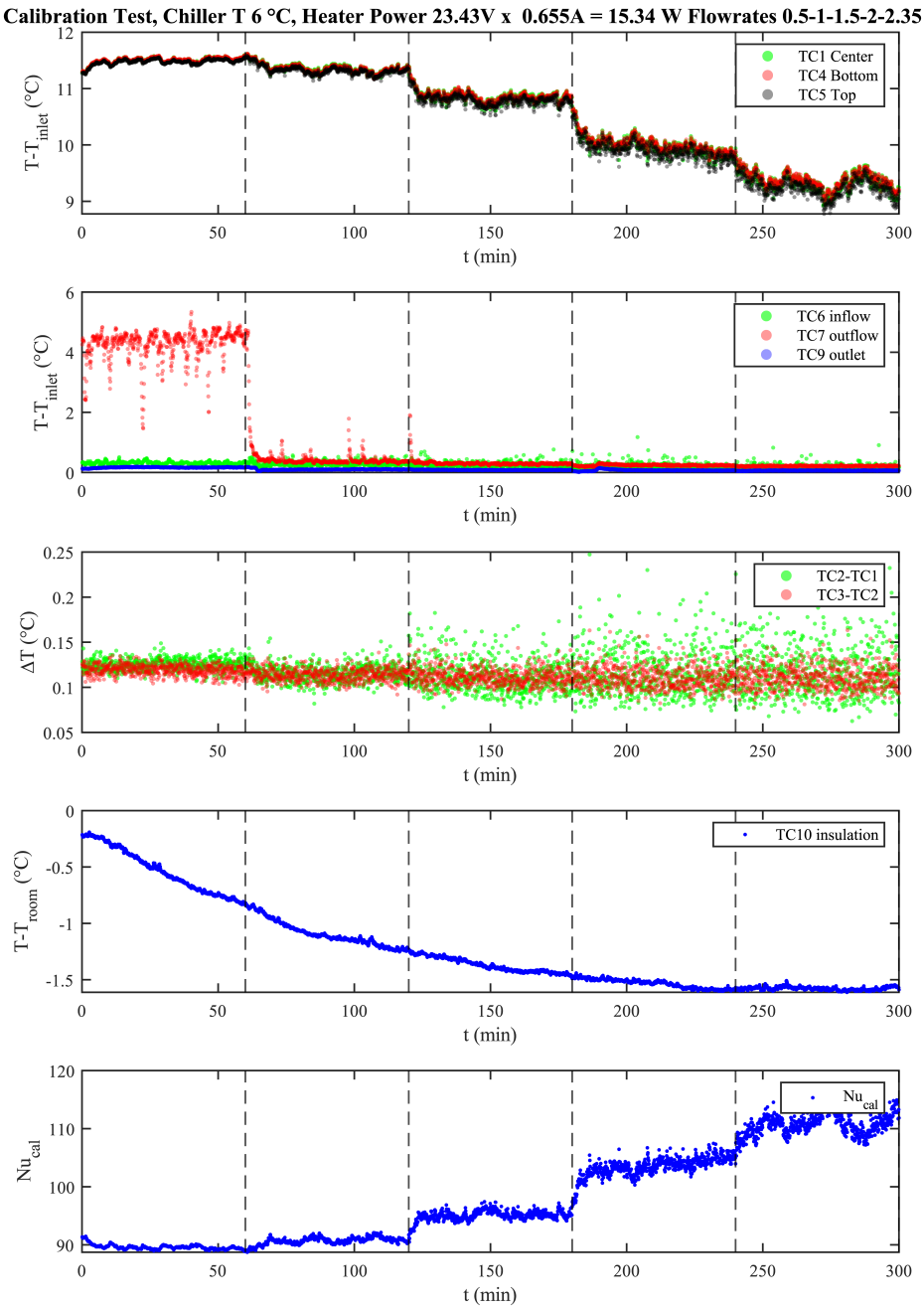

Figure E.8: Calibration data at additional flow rates.

Appendix F

Liquid Synthetic Jet Impingement Tests - Additional Figures

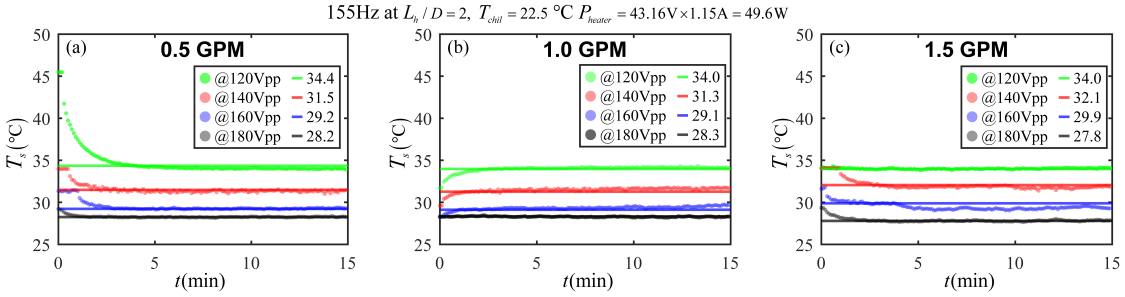

Figure F.1: T_s at $L_h/D = 2$.

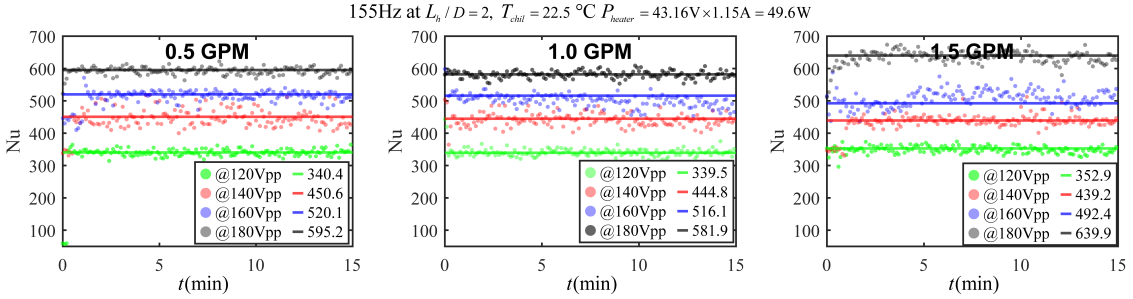

Figure F.2: Nu at $L_h/D = 2$.

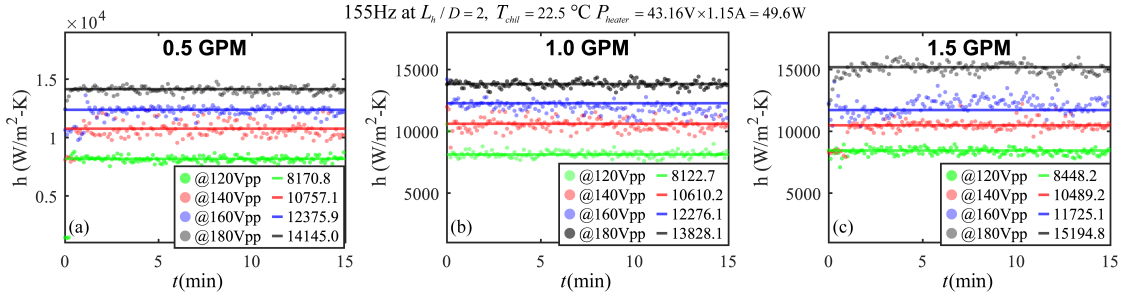

Figure F.3: h at $L_h/D = 2$.

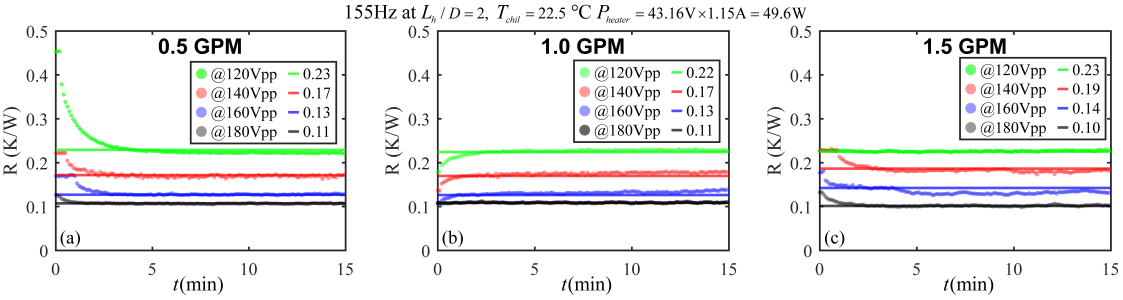

Figure F.4: R at $L_h/D = 2$.

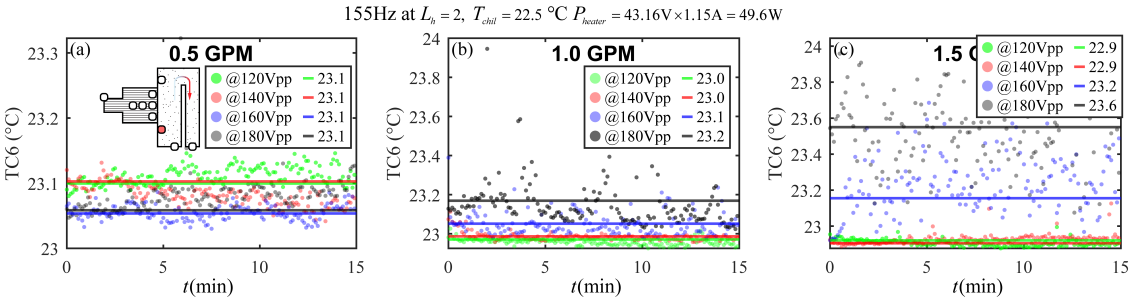

Figure F.5: TC6 at $L_h/D = 2$.

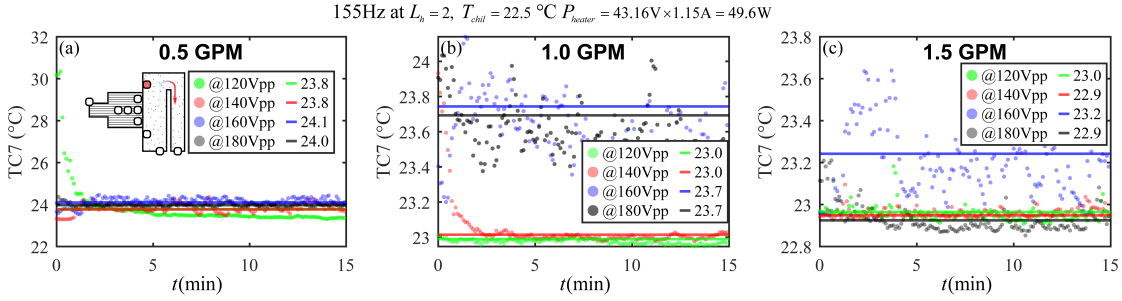

Figure F.6: TC7 at $L_h/D = 2$.

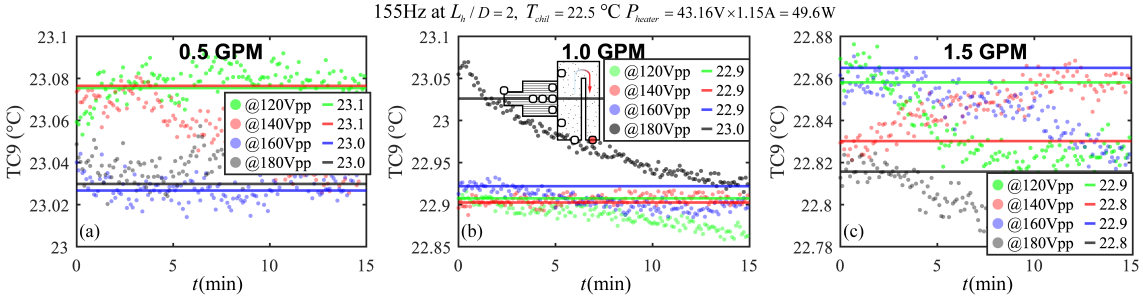

Figure F.7: TC9 at $L_h/D = 2$.

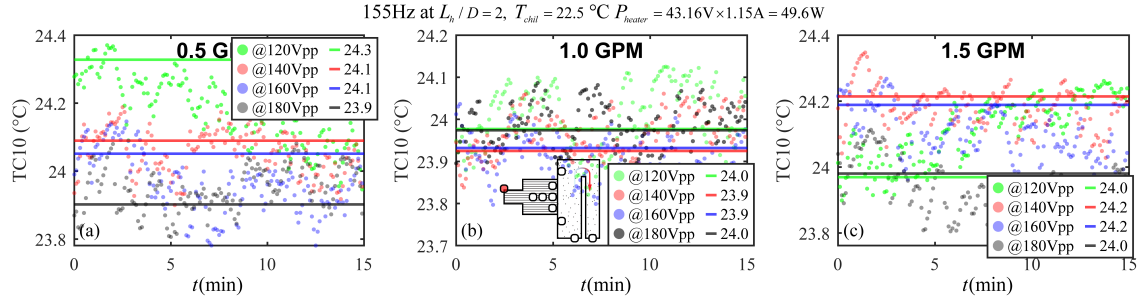

Figure F.8: TC10 at $L_h/D = 2$.

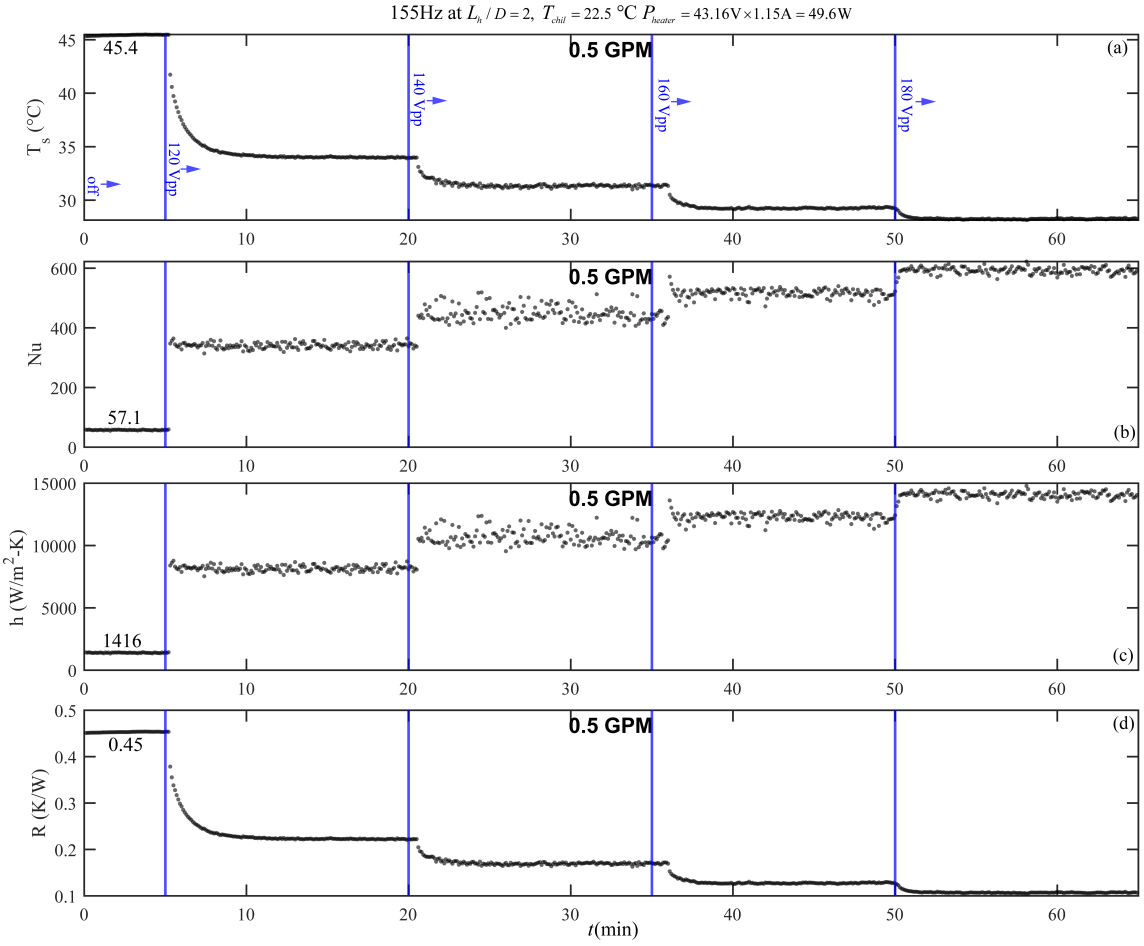

Figure F.9: Data at $L_h/D = 2$.

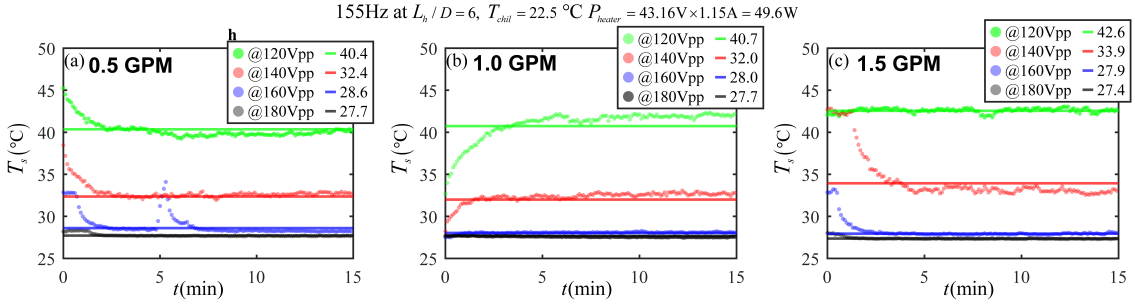

Figure F.10: T_s at $L_h/D = 6$.

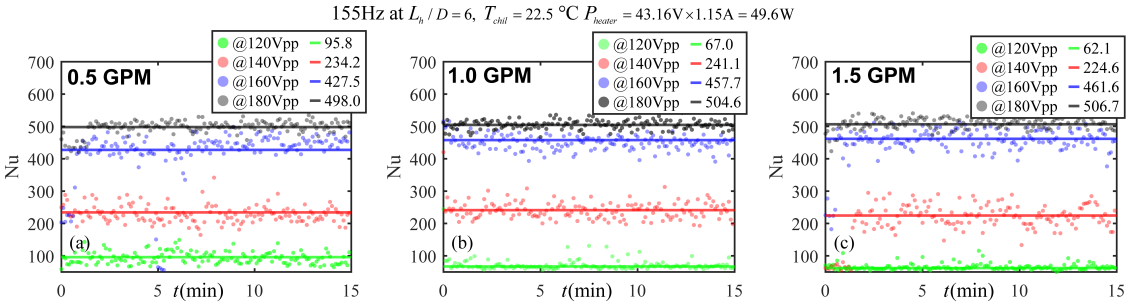

Figure F.11: Nu at $L_h/D = 6$.

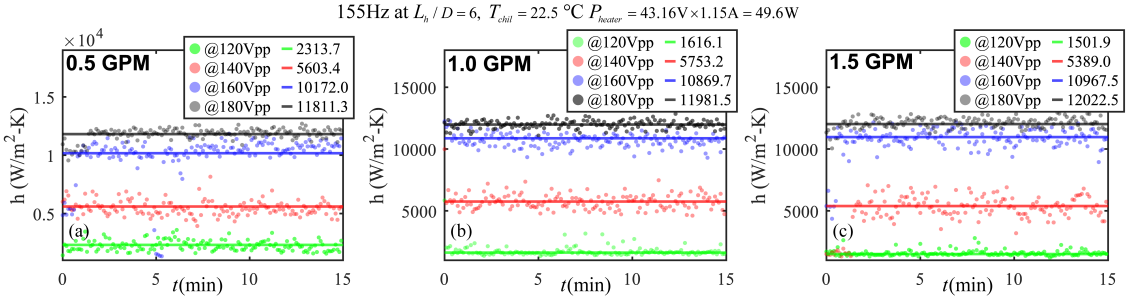

Figure F.12: h at $L_h/D = 6$.

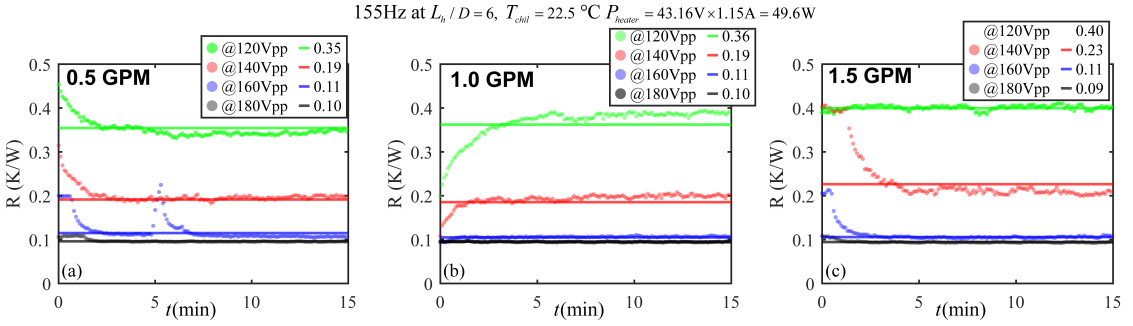

Figure F.13: R at $L_h/D = 6$.

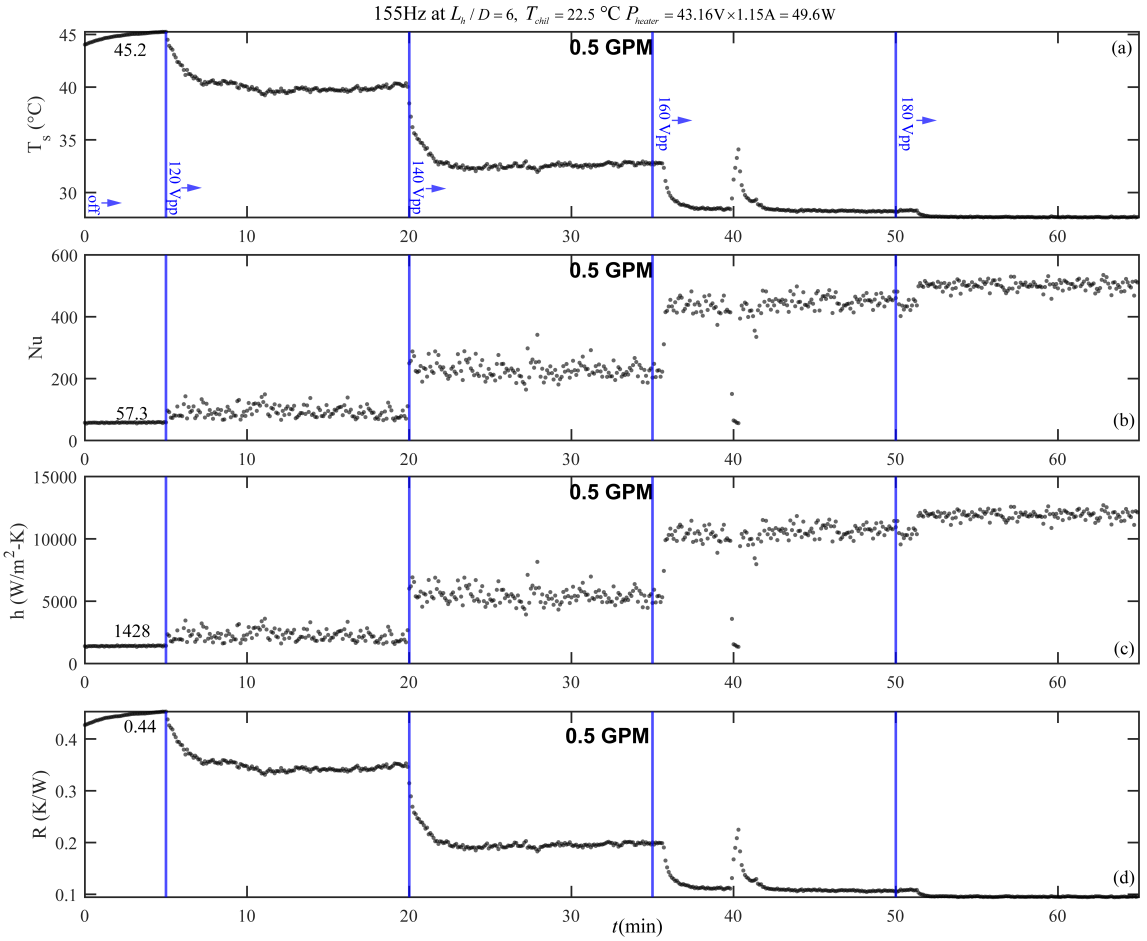

Figure F.14: Data at $L_h/D = 6$.

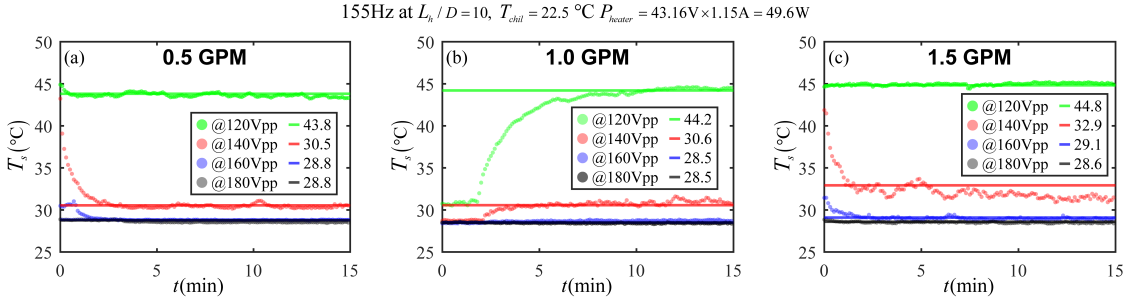

Figure F.15: T_s at $L_h/D = 10$.

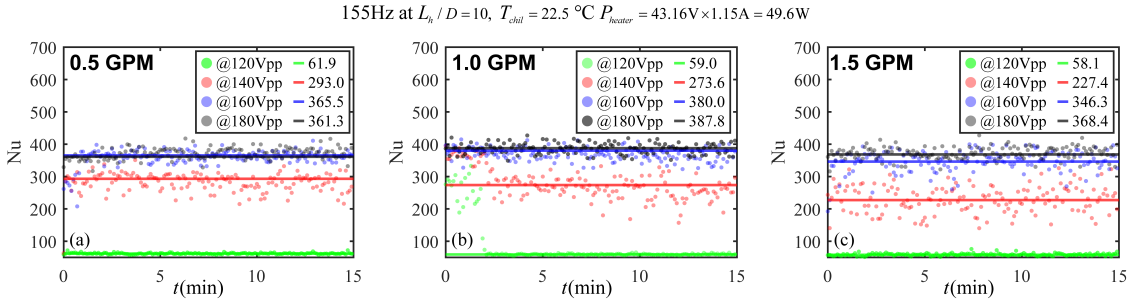

Figure F.16: Nu at $L_h/D = 10$.

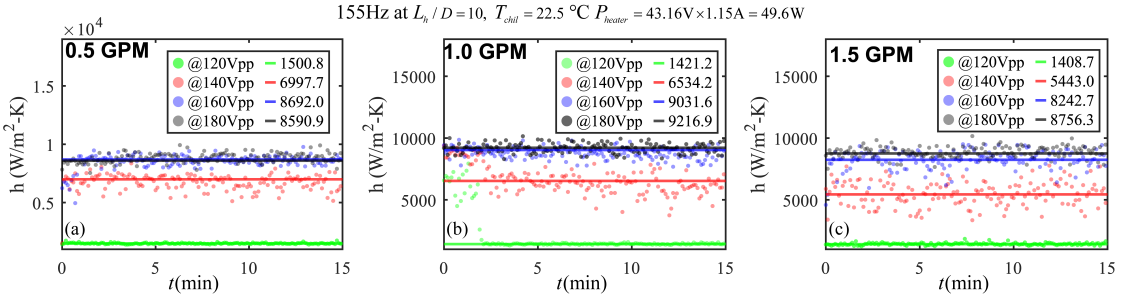

Figure F.17: h at $L_h/D = 10$.

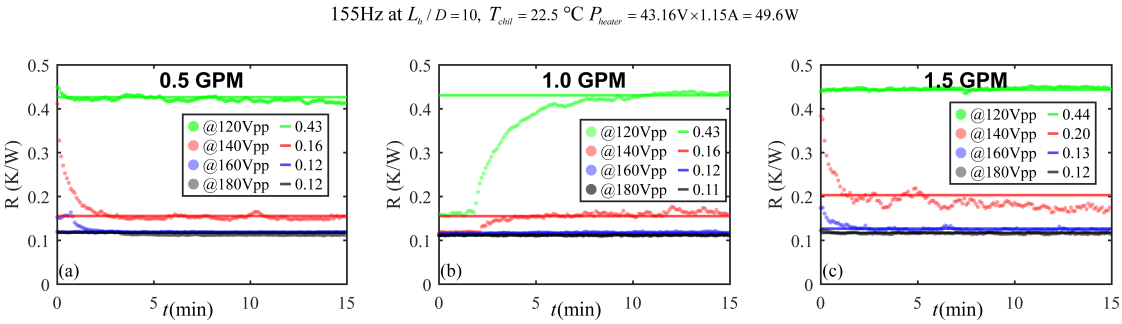

Figure F.18: R at $L_h/D = 10$.

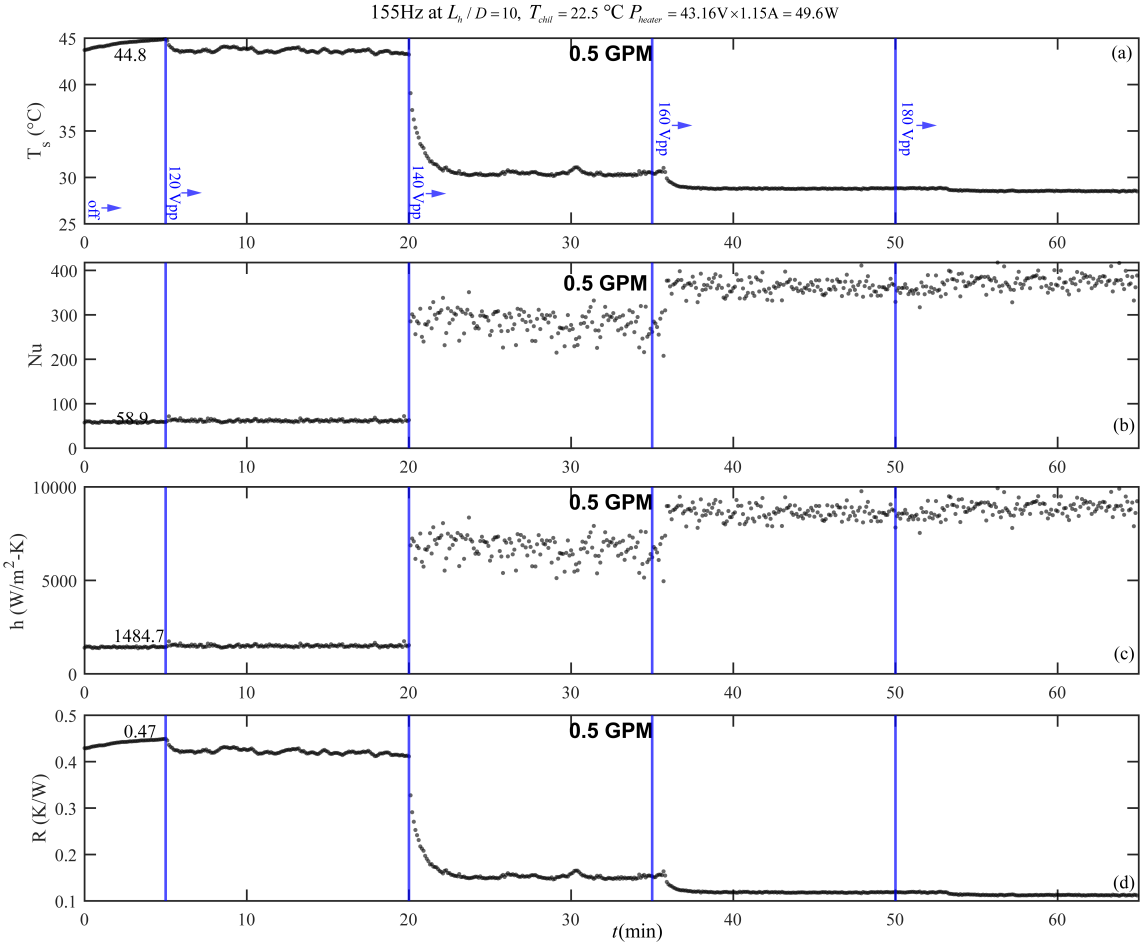

Figure F.19: Data at $L_h/D = 10$.

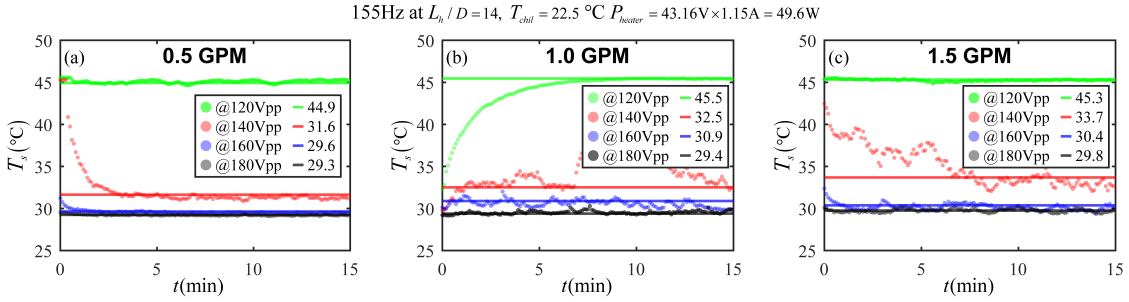

Figure F.20: T_s at $L_h/D = 14$.

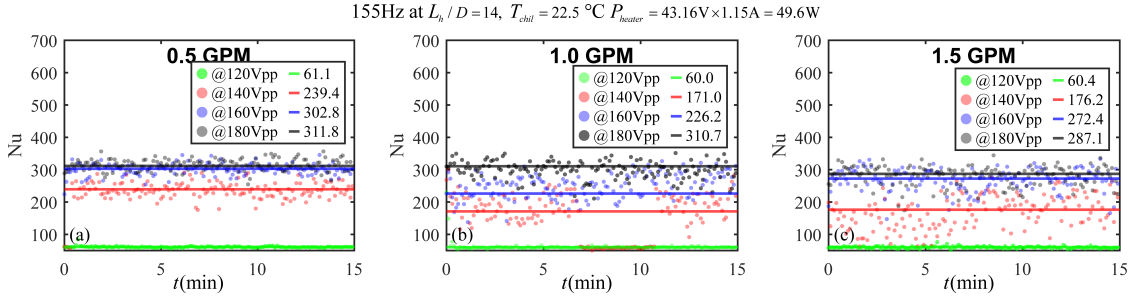

Figure F.21: Nu at $L_h/D = 14$.

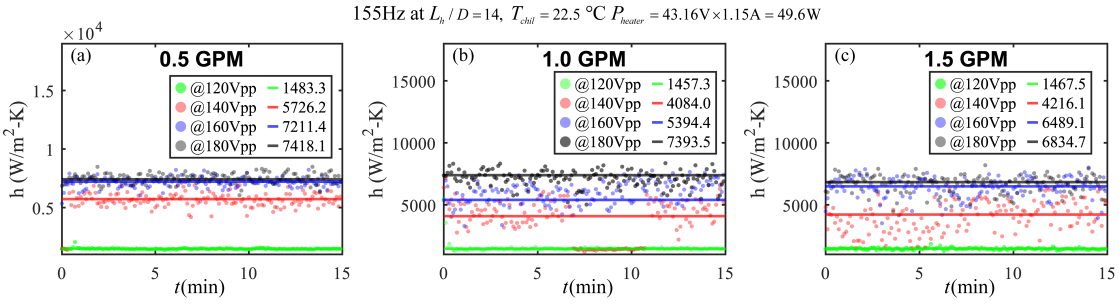

Figure F.22: h at $L_h/D = 14$.

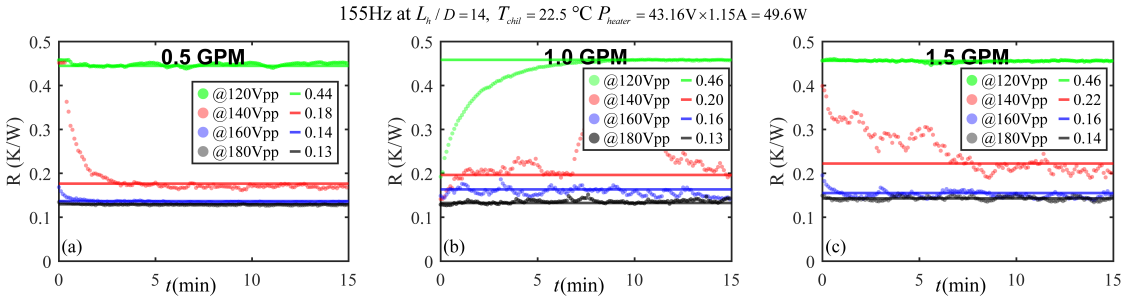

Figure F.23: R at $L_h/D = 14$.

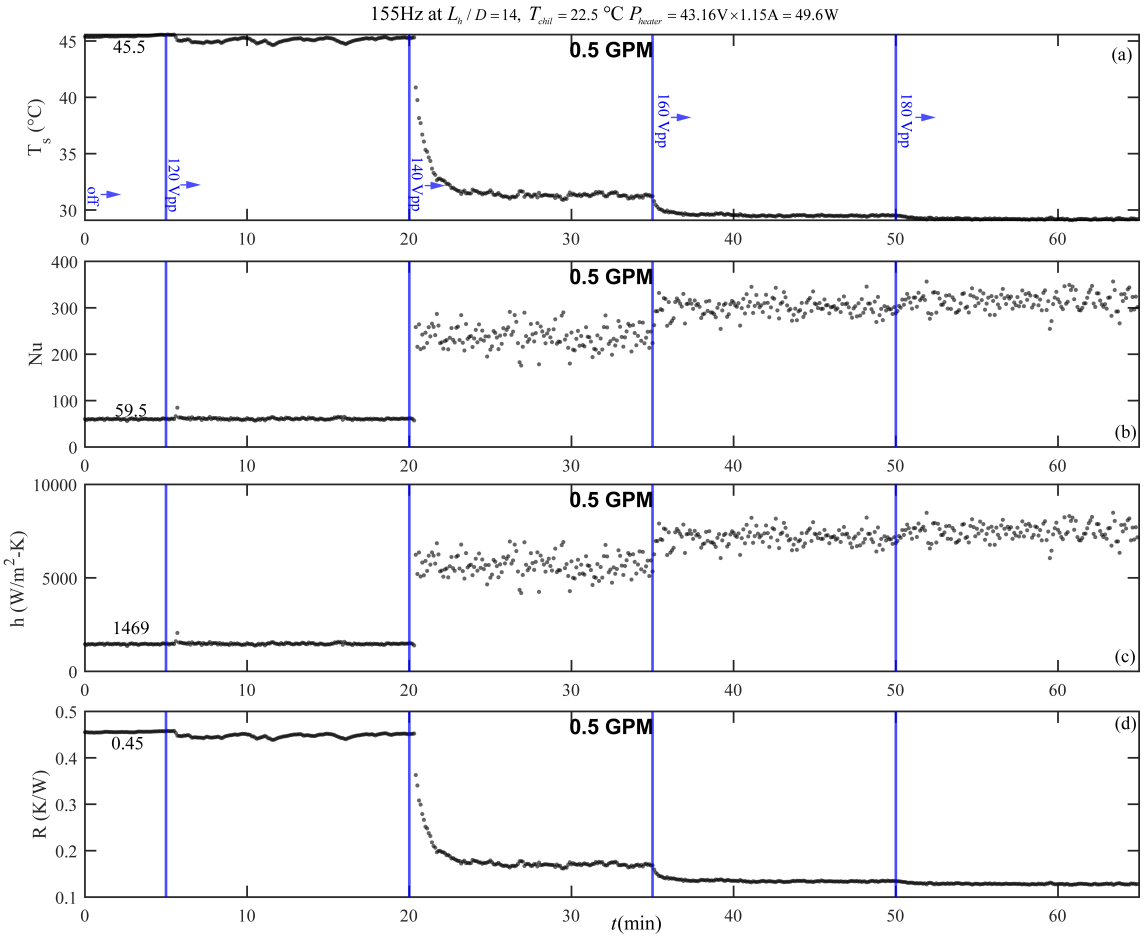

Figure F.24: Data at $L_h/D = 14$.

Appendix G

PIV Results

G.1 Matlab codes for PIV Analysis

A sample MATLAB code is presented here:

```
%Code by Mohammad Azarifar
%Folder containing .VEC files
folder = 'E:\OneDrive - Auburn University\Auburn PHD\';  % folder
    path

% Get a list of all .VEC files in the folder
fileList = dir(fullfile(folder, '*.vec'));

% Initialize variables to accumulate data and squared data
u_sum = [];
v_sum = [];
u_squared_sum = [];
v_squared_sum = [];
fileCount = 0;

% Loop over each file
for i = 1:length(fileList)
    % Full file path
    filename = fullfile(folder, fileList(i).name);

    % Open the file
    fileID = fopen(filename, 'r');

    % Skip header lines if necessary
    headerLines = 1; % Adjust based on your file structure
    for j = 1:headerLines
        fgetl(fileID);
    end

    % Read data (comma-separated values)
    data = textscan(fileID, '%f %f %f %f', 'Delimiter', ',');

```

```
32      % Close the file
33      fclose(fileID);
34
35      % Extract data into variables
36      x = data{1}; % X coordinates (same for all files)
37      y = data{2}; % Y coordinates (same for all files)
38      u = data{3}; % U velocity component
39      v = data{4}; % V velocity component
40
41      % Initialize sums on the first iteration
42      if isempty(u_sum)
43          u_sum = zeros(size(u));
44          v_sum = zeros(size(v));
45          u_squared_sum = zeros(size(u));
46          v_squared_sum = zeros(size(v));
47      end
48
49      % Accumulate sum and squared sum
50      u_sum = u_sum + u;
51      v_sum = v_sum + v;
52      u_squared_sum = u_squared_sum + u.^2;
53      v_squared_sum = v_squared_sum + v.^2;
54      fileCount = fileCount + 1;
55  end
56
57  % Calculate mean u and v values
58  u_avg = u_sum / fileCount;
59  v_avg = v_sum / fileCount;
60
61  % Calculate standard deviation for u and v
62  u_std = sqrt(u_squared_sum / fileCount - u_avg.^2);
63  v_std = sqrt(v_squared_sum / fileCount - v_avg.^2);
64
65  % Calculate the magnitude of average velocity for color coding
66  velocity_magnitude = sqrt(u_avg.^2 + v_avg.^2);
67
68  % Filter out values where the magnitude is greater than 0.2
69  valid_indices = velocity_magnitude <= 0.28;
70  x_filtered = x(valid_indices);
71  y_filtered = y(valid_indices);
72  u_avg_filtered = u_avg(valid_indices);
73  v_avg_filtered = v_avg(valid_indices);
74  velocity_magnitude_filtered = velocity_magnitude(valid_indices);
75
76  % Check if any data points remain after filtering
77  if isempty(x_filtered)
78      warning('No data points remain after filtering. Adjust the
            threshold.');
79      return;
80  end
```

```
81
82 % Set up figure
83 figure('Position', [100, 100, 800, 600]);
84 colormap(jet); % Use jet colormap for a smooth color gradient
85
86 % Set the color axis limits based on actual min and max of the
       filtered values
87 colorbar;
88 caxis([min(velocity_magnitude_filtered),
       max(velocity_magnitude_filtered)]);
89 title(colorbar, 'Velocity Magnitude');
90
91 % Get the colormap data
92 color = jet;
93 num_colors = size(color, 1);
94
95 % Choose a large scale factor for quiver arrows
96 scale_factor = 20;
97
98 % Plot each filtered vector with color based on its actual magnitude
99 hold on;
100 for k = 1:length(x_filtered)
101     % Calculate color index based on actual magnitude
102     color_idx = max(1, min(num_colors,
          round((velocity_magnitude_filtered(k) -
          min(velocity_magnitude_filtered)) / ...
103           (max(velocity_magnitude_filtered) -
              min(velocity_magnitude_filtered)) * (num_colors - 1) +
              1)));
104     arrow_color = color(color_idx, :);
105
106     % Draw arrow with adjusted color and larger scale
107     quiver(x_filtered(k), y_filtered(k), u_avg_filtered(k),
          v_avg_filtered(k), scale_factor, ...
108             'Color', arrow_color, 'MaxHeadSize', 2, 'LineWidth', 2);
109 end
110 hold off;
111
112 % Set axis labels and title
113 xlabel('X (units)');
114 ylabel('Y (units)');
115 title('Ensemble-Averaged PIV Vector Field with Variability
       (Filtered for Magnitude     0.2)');
116
117 % Customize plot appearance
118 set(gca, 'FontSize', 12, 'LineWidth', 1.5);
119 axis equal; % Ensure equal scaling for X and Y axes
120 grid on;
121
122 % Set the x and y axis limits to start from zero
```

```
xlim([0, max(x_filtered)]);
ylim([0, max(y_filtered)]);

end
```

Listing G.1: Ensemble Averaging Code

```
%Code by Mohammad Azarifar
%Folder containing .VEC files
folder = 'C:\Users\burto\OneDrive - Auburn University\Auburn PHD\

% Get a list of all .VEC files in the folder
fileList = dir(fullfile(folder, '*.vec'));

% Initialize variable to track minimum (most negative) u values
u_min = [];

% Loop over each file
for i = 1:length(fileList)
    % Full file path
    filename = fullfile(folder, fileList(i).name);

    % Open the file
    fileID = fopen(filename, 'r');

    % Skip header lines if necessary
    headerLines = 1; % Adjust based on your file structure
    for j = 1:headerLines
        fgetl(fileID);
    end

    % Read data (comma-separated values)
    data = textscan(fileID, '%f %f %f %f', 'Delimiter', ',');

    % Close the file
    fclose(fileID);

    % Extract data into variables
    x = data{1}; % X coordinates (same for all files)
    y = data{2}; % Y coordinates (same for all files)
    u = data{3}; % U velocity component

    % Initialize min array on the first iteration
    if isempty(u_min)
        u_min = u;
    else
        % Update min u values by comparing each new files data
        u_min = min(u_min, u);
    end
end

```

```
% Replace non-negative values with zero
u_min(u_min >= 0) = 0;

% Compute absolute values for color mapping
u_abs = abs(u_min);

% Set up figure for plotting minimum x-direction (u) velocity field with absolute color mapping
figure('Units', 'inches', 'Position', [1, 1, 4.54, 3.5]);  % Adjusted width and height for better visibility
colormap(viridis);
colorbar;
caxis([0, max(u_abs)]);
title(colorbar, 'Vel (m/s)');

% Get colormap and set up color indexing based on absolute values
color = viridis;
num_colors = size(color, 1);

% Choose a scale factor for quiver arrows
scale_factor = 50;

% Plot each vector with color based on the absolute value of u_min
hold on;
for k = 1:length(x)
    % Calculate color index based on the absolute value of u_min
    color_idx = max(1, min(num_colors, round((u_abs(k) - 0) / ...
        (max(u_abs) - 0) * (num_colors - 1) + 1)));
    arrow_color = color(color_idx, :);

    % Draw arrow with direction based on u_min and color based on |u_min|
    quiver(x(k)-min(x), y(k)-min(y)-10, u_min(k), 0, scale_factor, ...
        'Color', arrow_color, 'MaxHeadSize', 0.5, 'LineWidth', 2);
end
hold off;

% Set axis labels and title
xlabel('X (mm)');
ylabel('Y (mm)');
title('180 Hz Max Ejection Vel', 'FontWeight', 'normal');

% Customize plot appearance
set(gca, 'Box', 'on', 'LineWidth', 1.5, 'FontSize', 10);
axis equal;

% Set the x and y axis limits to start from zero
xlim([0, 100]);
```

```
ylim([0, 60]);


% Save the plot in various formats
saveas(gcf, '180maxejectionvelocity_field.svg');
saveas(gcf, '180maxejectionvelocity_field.fig');
print(gcf, '180maxejectionvelocity_field', '-dtiff', '-r300');  % Saves as a TIFF with 300 DPI


% Folder containing your .VEC files
folder = 'C:\Users\burto\OneDrive - Auburn University\Auburn PHD\Master Folder Synthetic Jet Research\13-PIV PAPER\piv\piv\180';

% Get a list of all .VEC files in the folder
fileList = dir(fullfile(folder, '*.vec'));

% Initialize variable to track minimum (most negative) u values
u_min = [];

% Loop over each file
for i = 1:length(fileList)
    % Full file path
    filename = fullfile(folder, fileList(i).name);

    % Open the file
    fileID = fopen(filename, 'r');

    % Skip header lines if necessary
    headerLines = 1; % Adjust based on your file structure
    for j = 1:headerLines
        fgetl(fileID);
    end

    % Read data (comma-separated values)
    data = textscan(fileID, '%f %f %f %f', 'Delimiter', ',');

    % Close the file
    fclose(fileID);

    % Extract data into variables
    x = data{1}; % X coordinates (same for all files)
    y = data{2}; % Y coordinates (same for all files)
    u = data{3}; % U velocity component

    % Initialize min array on the first iteration
    if isempty(u_min)
        u_min = u;
    else
```

```
137         % Update min u values by comparing each new files data
                for the most negative values
138         u_min = min(u_min, u);
139     end
140 end
141
142 % Now plot the most negative (minimum) u values along the central
      y-line
143 % Display the range of y values
144 disp(['Min y: ', num2str(min(y))]);
145 disp(['Max y: ', num2str(max(y))]);
146
147 % Calculate the middle value in the y direction
148 y_mid = (min(y) + max(y)) / 2;
149 disp(['Middle y value (y_mid): ', num2str(y_mid)]);
150
151 % Increase the tolerance to capture points near the middle y line
152 tolerance = 5;  % Adjust this tolerance if necessary
153
154 % Find indices of points near the middle y line
155 middle_line_indices = abs(y - y_mid) < tolerance;
156
157 % Check if middle_line_indices contains any true values
158 if any(middle_line_indices)
159     % Extract x and minimum (most negative) u values along the
          middle y line
160     x_middle_line = x(middle_line_indices);
161     u_min_middle_line = u_min(middle_line_indices);
162
163     % Sort by x values for a clear plot
164     [x_middle_sorted, sort_idx] = sort(x_middle_line);
165     u_min_sorted = u_min_middle_line(sort_idx);
166
167     % Set up figure for plotting
168     figure('Units', 'inches', 'Position', [1, 1, 3.54, 2.5]);  %
          Adjust figure size for publication
169     scatter(x_middle_sorted, abs(u_min_sorted), 12, 'k', 'filled');
            % 'k' sets color to black, 'filled' fills the marker
170
171     % Label axes and title
172     xlabel('X (mm)', 'FontSize', 12, 'FontWeight', 'normal');
173     ylabel('Max Eject Vel Mag (m/s)', 'FontSize', 12, 'FontWeight',
          'normal');
174     title('180 Hz Max Ejection Vel Mag Mid Y', 'FontSize', 10,
          'FontWeight', 'normal');
175
176     % Find the most negative u value and its corresponding x value
177     [min_u, min_idx] = min(u_min_sorted);
178     x_min = x_middle_sorted(min_idx);
179
```

```
    % Plot horizontal and vertical lines at the location of the most negative value
    hold on;
    line([x_min, x_min], ylim, 'Color', 'red', 'LineStyle', '--', 'LineWidth', 1.5);  % Vertical line at x_min
    line(xlim, [abs(min_u), abs(min_u)], 'Color', 'blue', 'LineStyle', '--', 'LineWidth', 1.5);  % Horizontal line at min_u

    % Display the minimum x and u values near the respective lines
    y_limits = ylim;  % Store the y-axis limits
    x_limits = xlim;  % Store the x-axis limits

    text(x_min, y_limits(1), sprintf('X = %.2f mm', x_min), ...
        'VerticalAlignment', 'bottom', 'HorizontalAlignment', 'right', 'FontSize', 10, 'Color', 'red');
    text(x_limits(1)+5, abs(min_u), sprintf('U_{min} = %.3f m/s', abs(min_u)), ...
        'VerticalAlignment', 'top', 'HorizontalAlignment', 'left', 'FontSize', 10, 'Color', 'blue');
    hold off;

    % Customize plot appearance
    set(gca, 'Box', 'on', 'LineWidth', 1.5, 'FontSize', 10);  % Adds box outline, sets thicker line width for visibility
    grid off;
    xlim([4, 100]);

else
    warning('No data points found near the middle y line. Consider increasing the tolerance.');
end

% Save the plot in various formats
saveas(gcf, '180maxejectionvelocityLine.svg');
saveas(gcf, '180maxejectionvelocityLine.fig');
print(gcf, '180maxejectionvelocityLine', '-dtiff', '-r300');  % Saves as a TIFF with 300 DPI
```

Listing G.2: Ensemble Maximizing Code

G.2 Sample Figures of PIV Tests

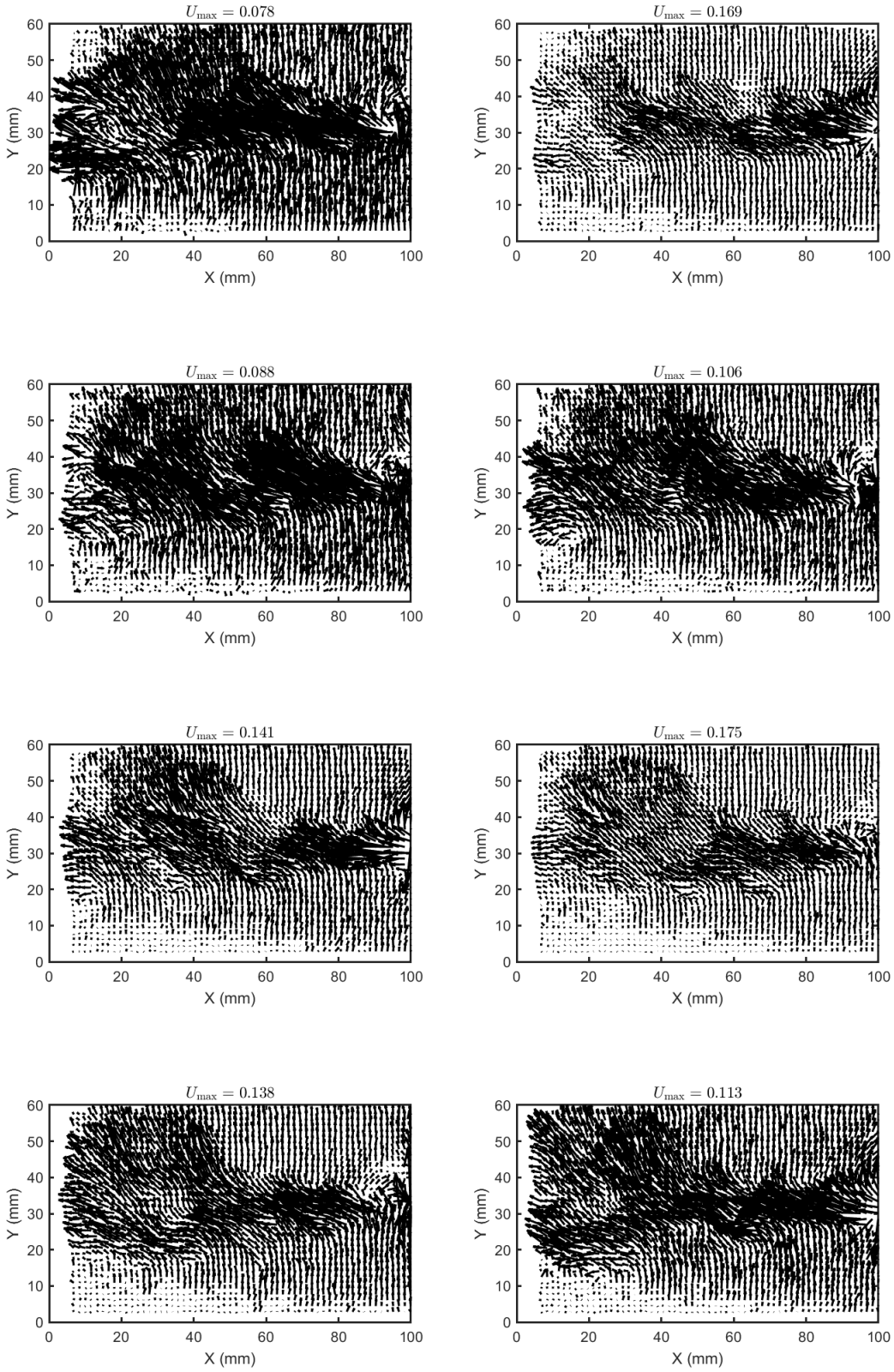

Figure G.1: Uncleaned PIV data at 180 Hz - Image 1

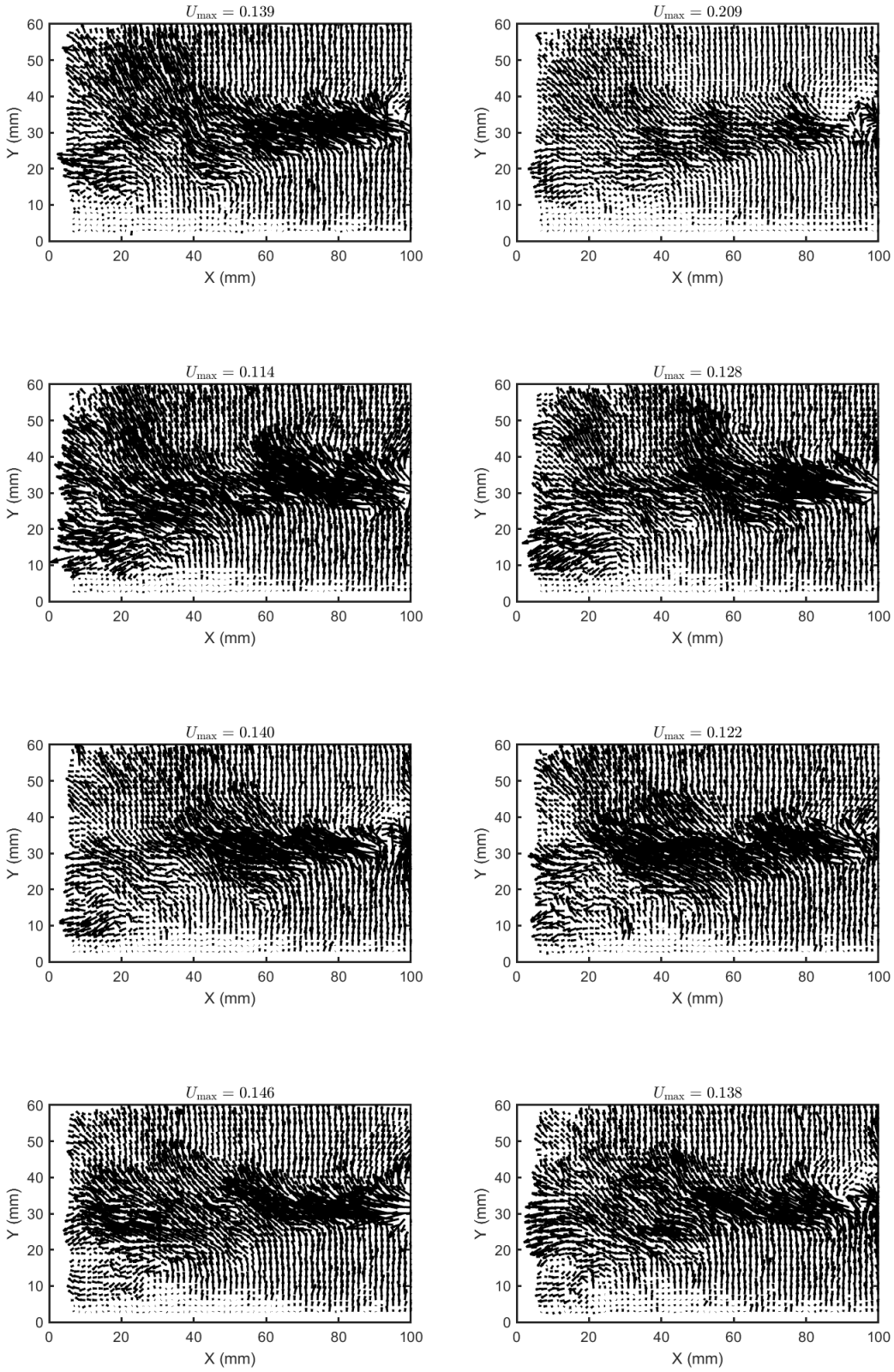

Figure G.2: Uncleaned PIV data at 180 Hz - Image 2

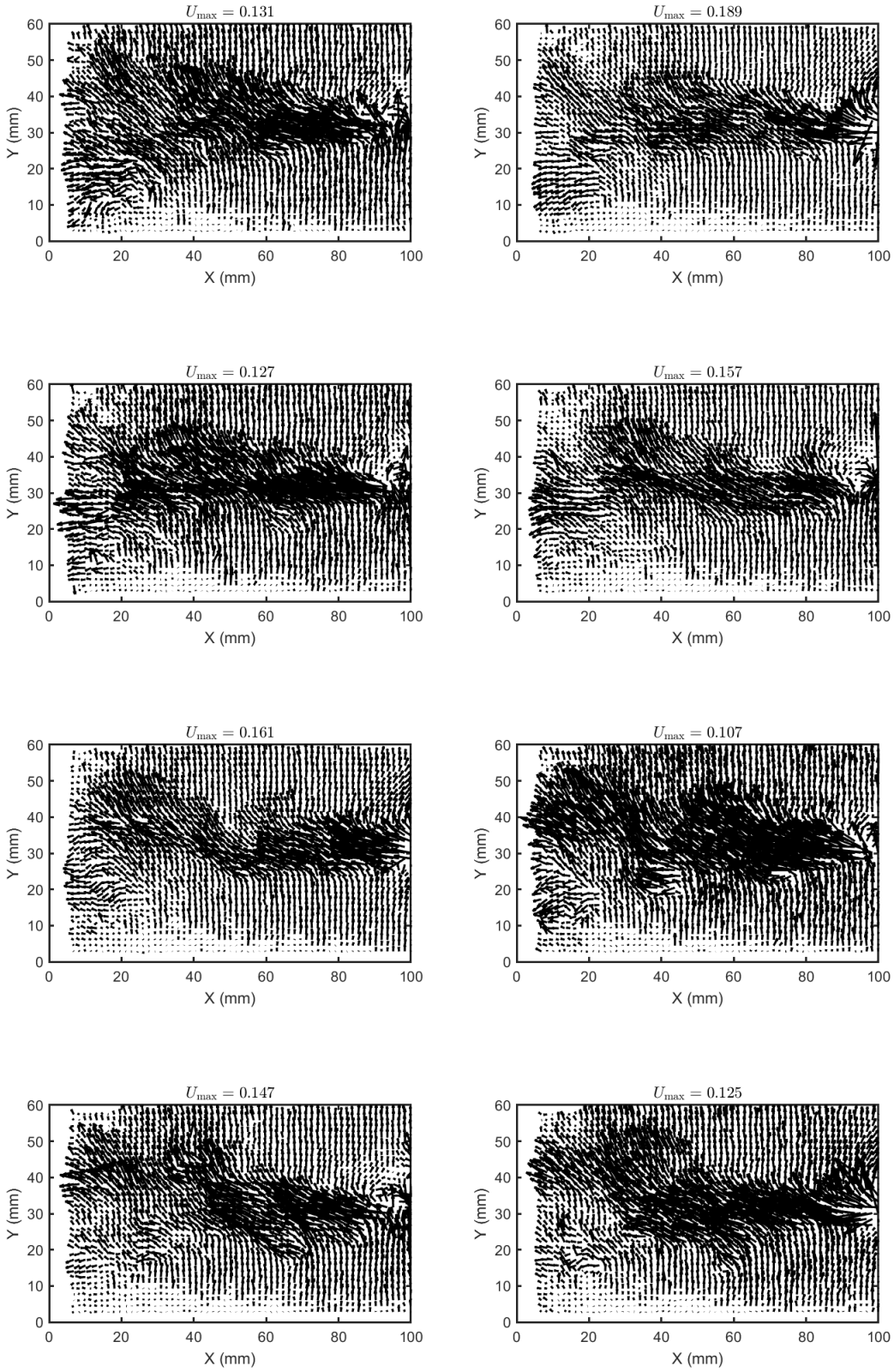

Figure G.3: Uncleaned PIV data at 180 Hz - Image 3

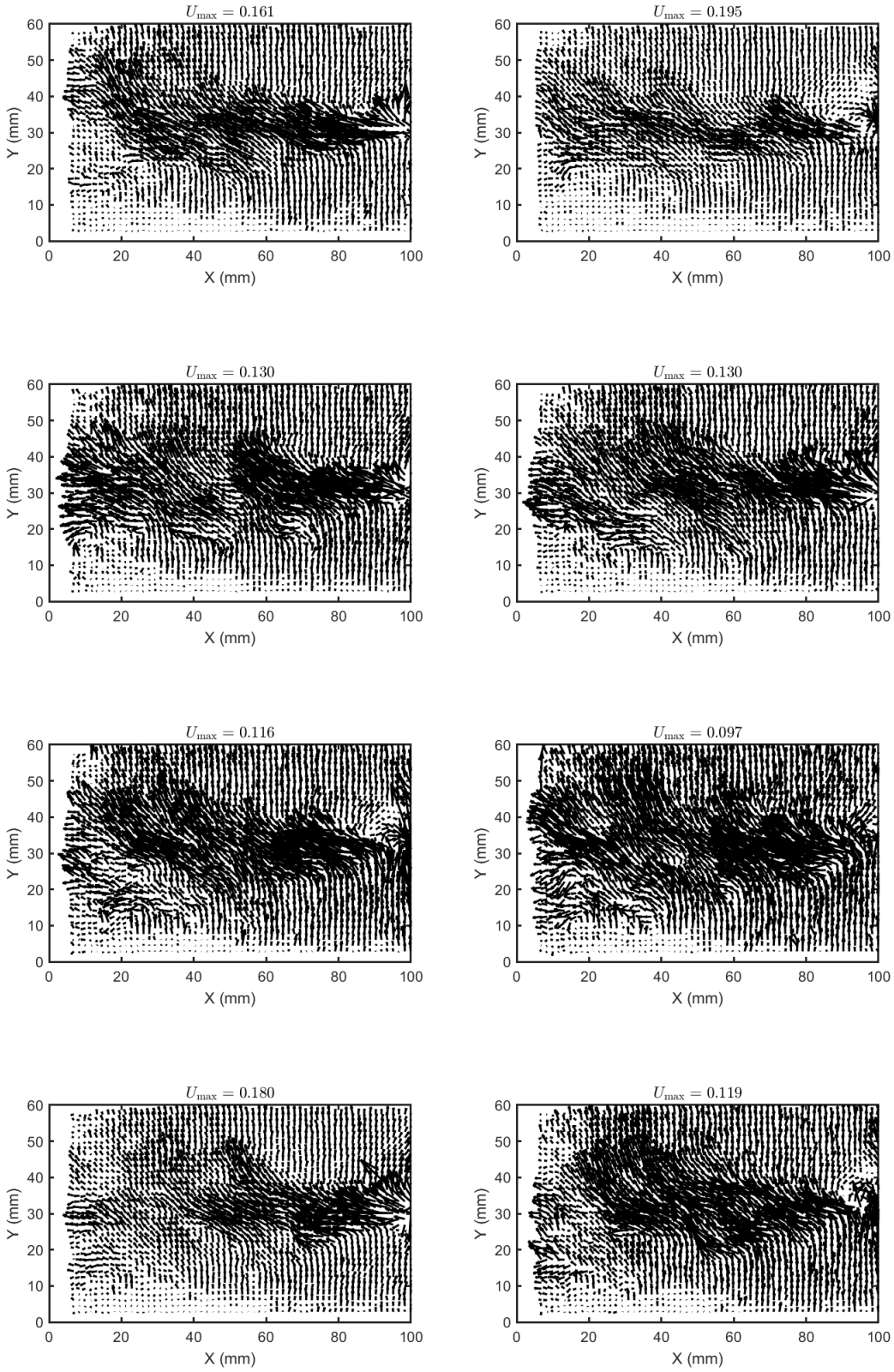

Figure G.4: Uncleaned PIV data at 180 Hz - Image 4

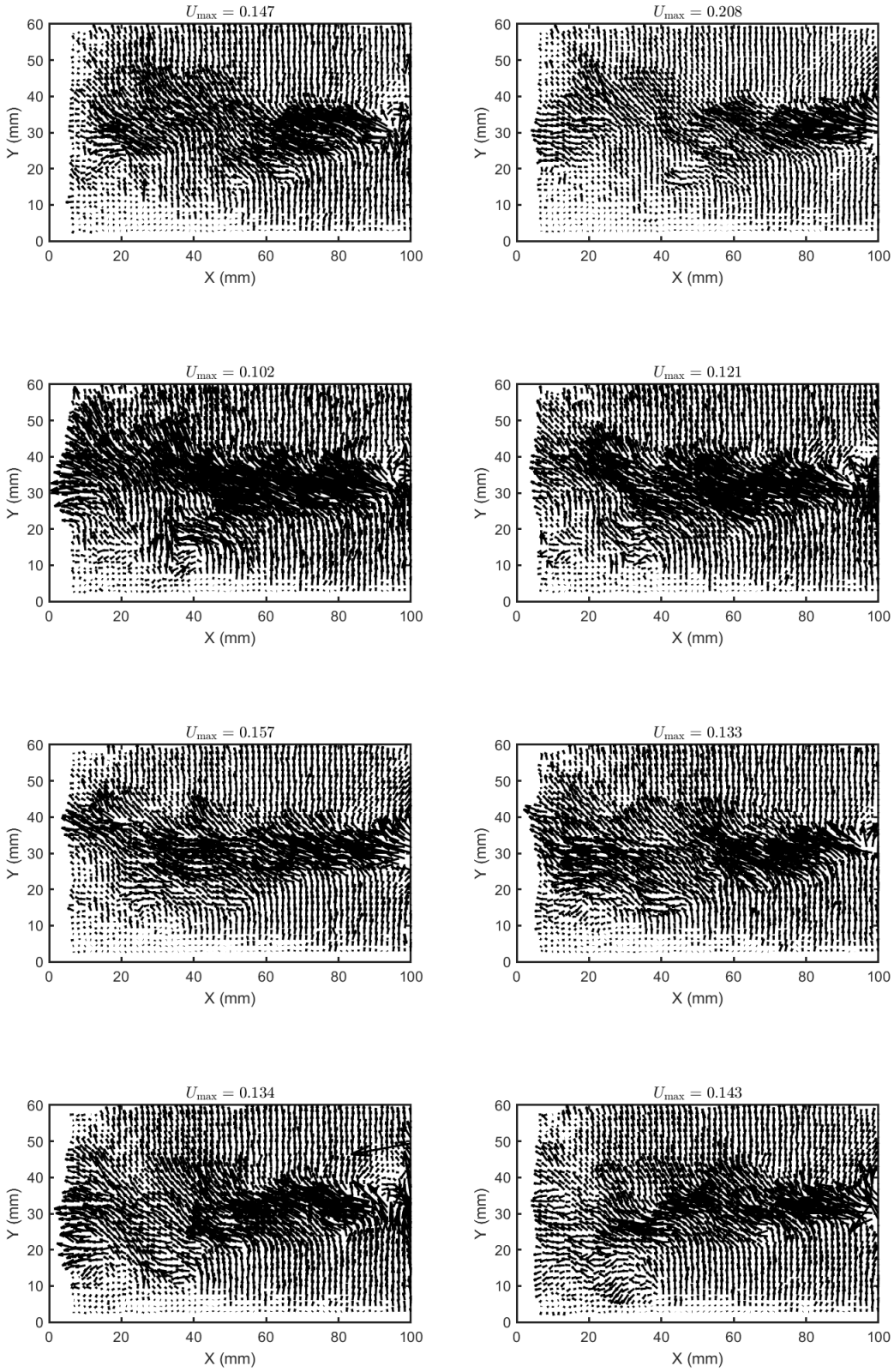

Figure G.5: Uncleaned PIV data at 180 Hz - Image 5

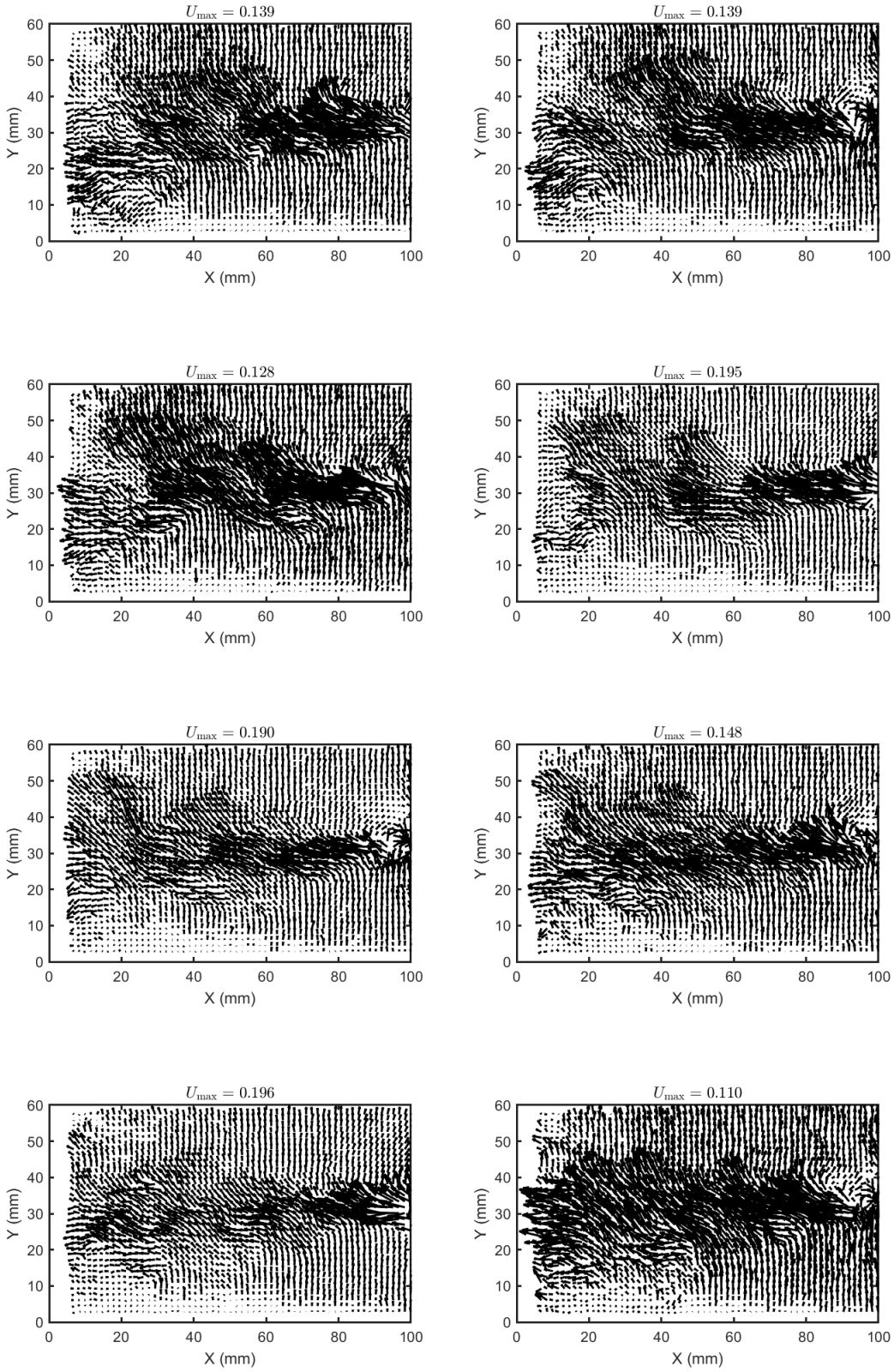

Figure G.6: Uncleaned PIV data at 180 Hz - Image 6

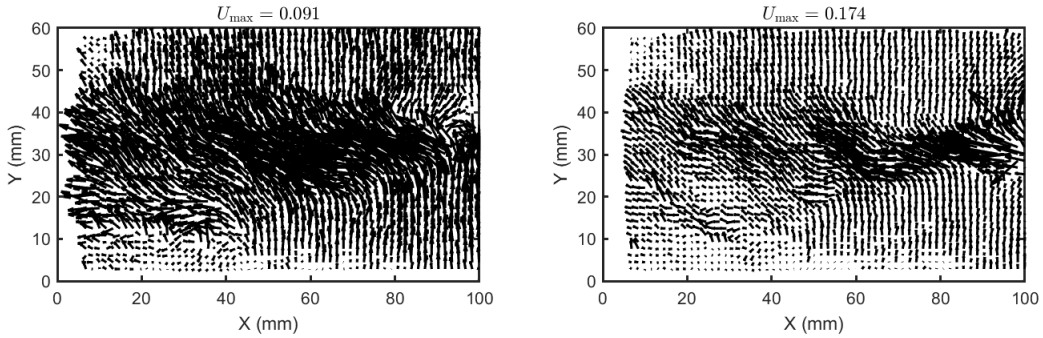

Figure G.7: Uncleaned PIV data at 180 Hz - Image 7

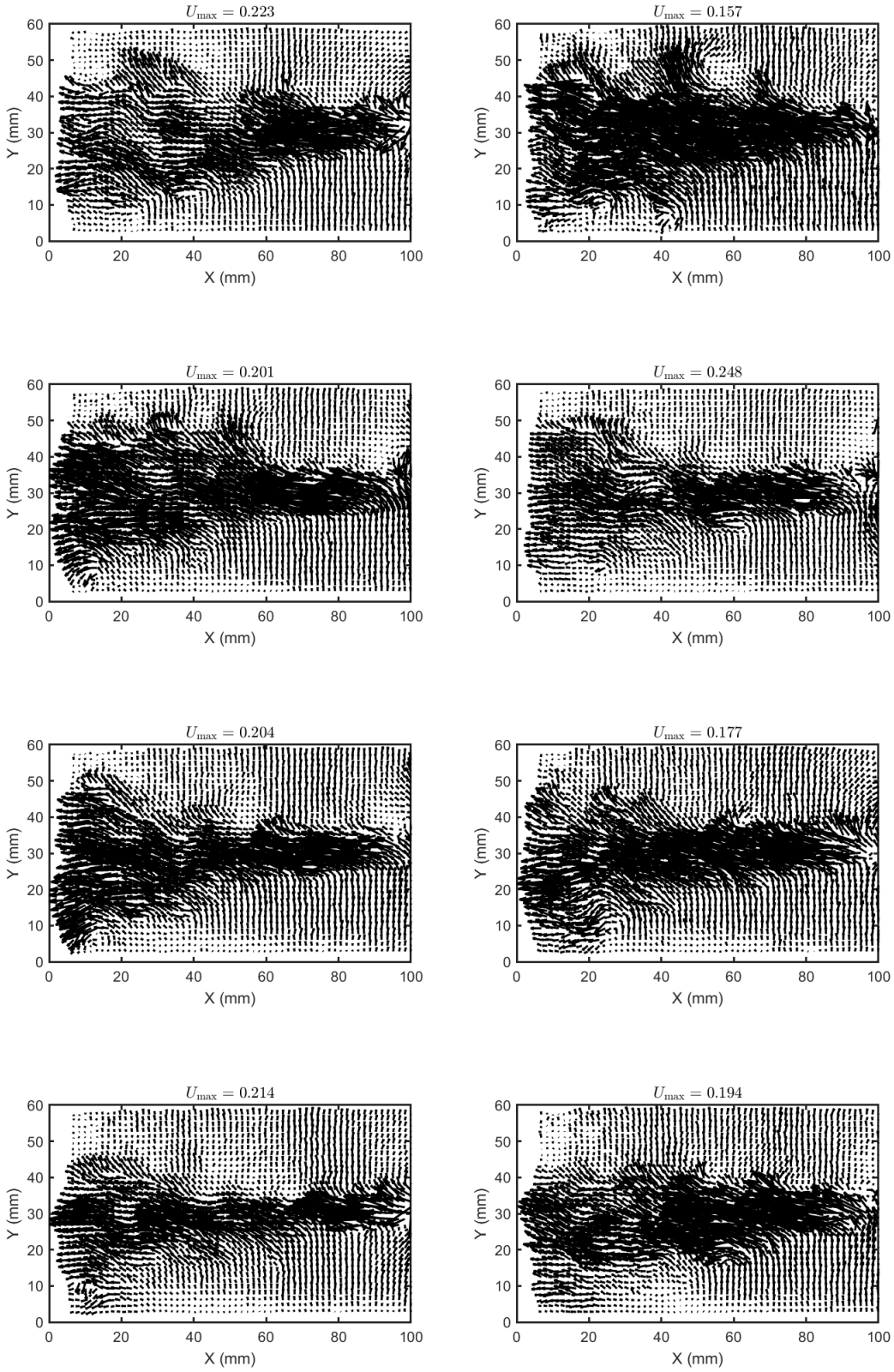

Figure G.8: Uncleaned PIV data at 190 Hz - Image 1

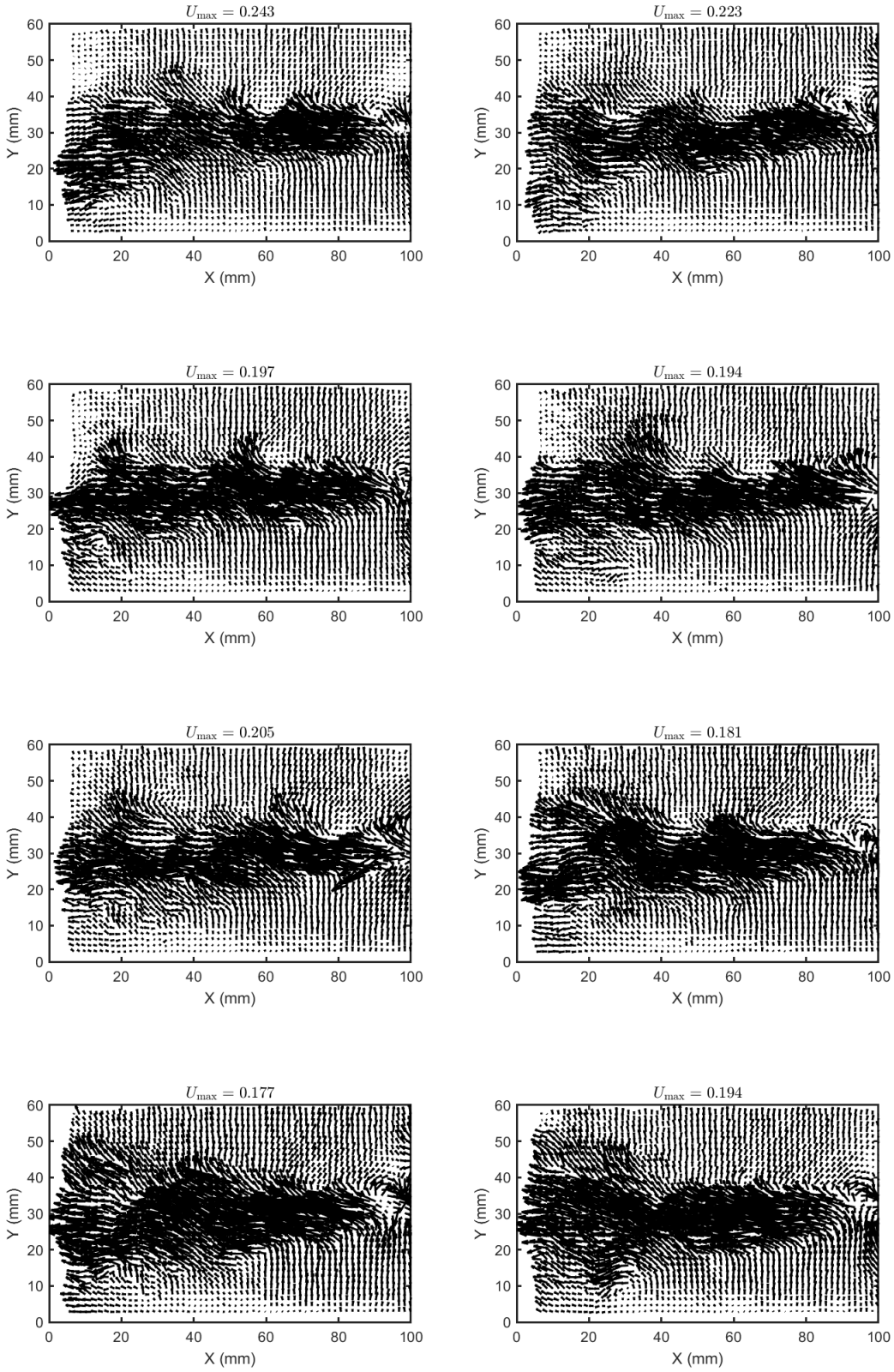

Figure G.9: Uncleaned PIV data at 190 Hz - Image 2

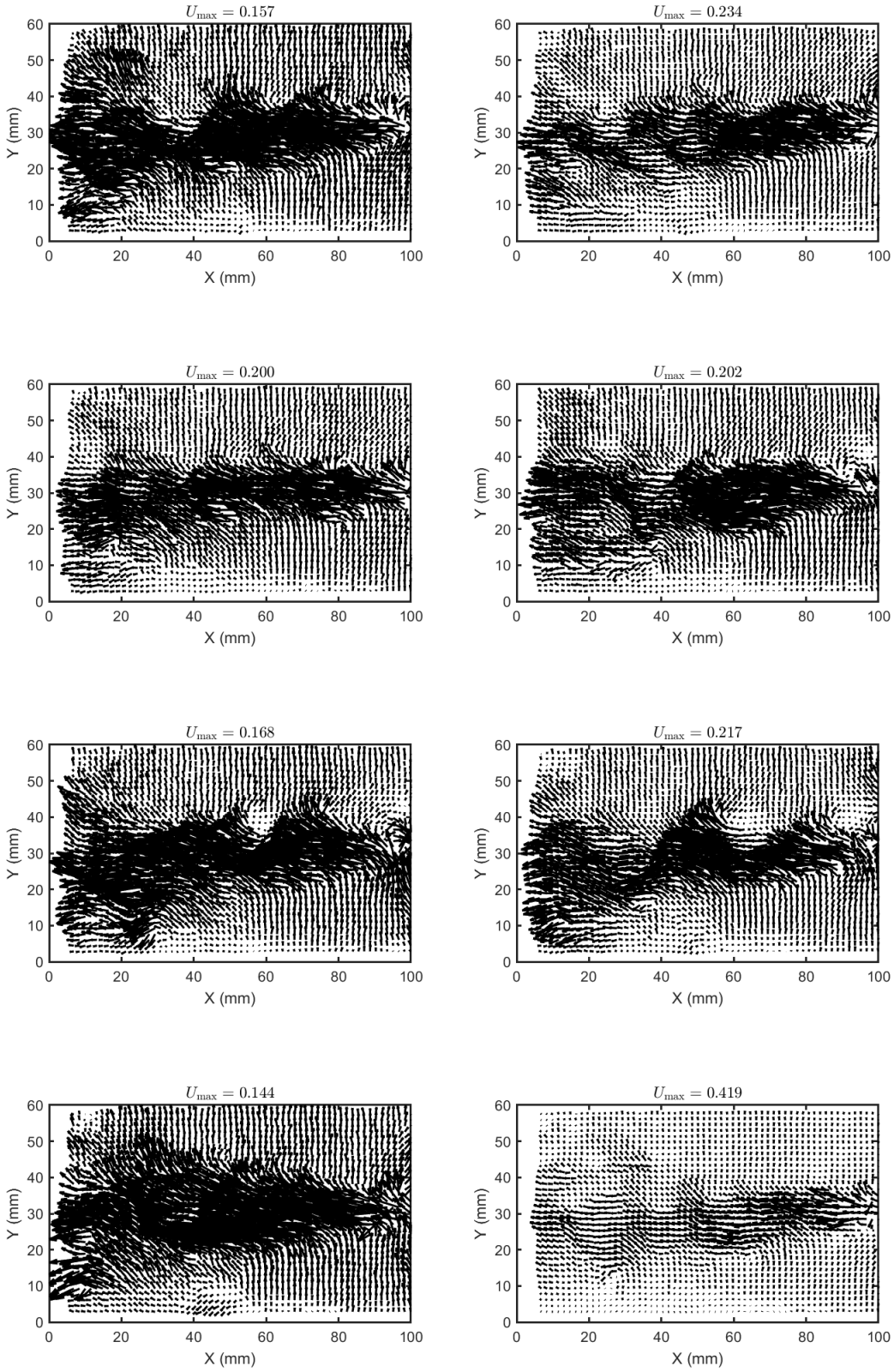

Figure G.10: Uncleaned PIV data at 190 Hz - Image 3

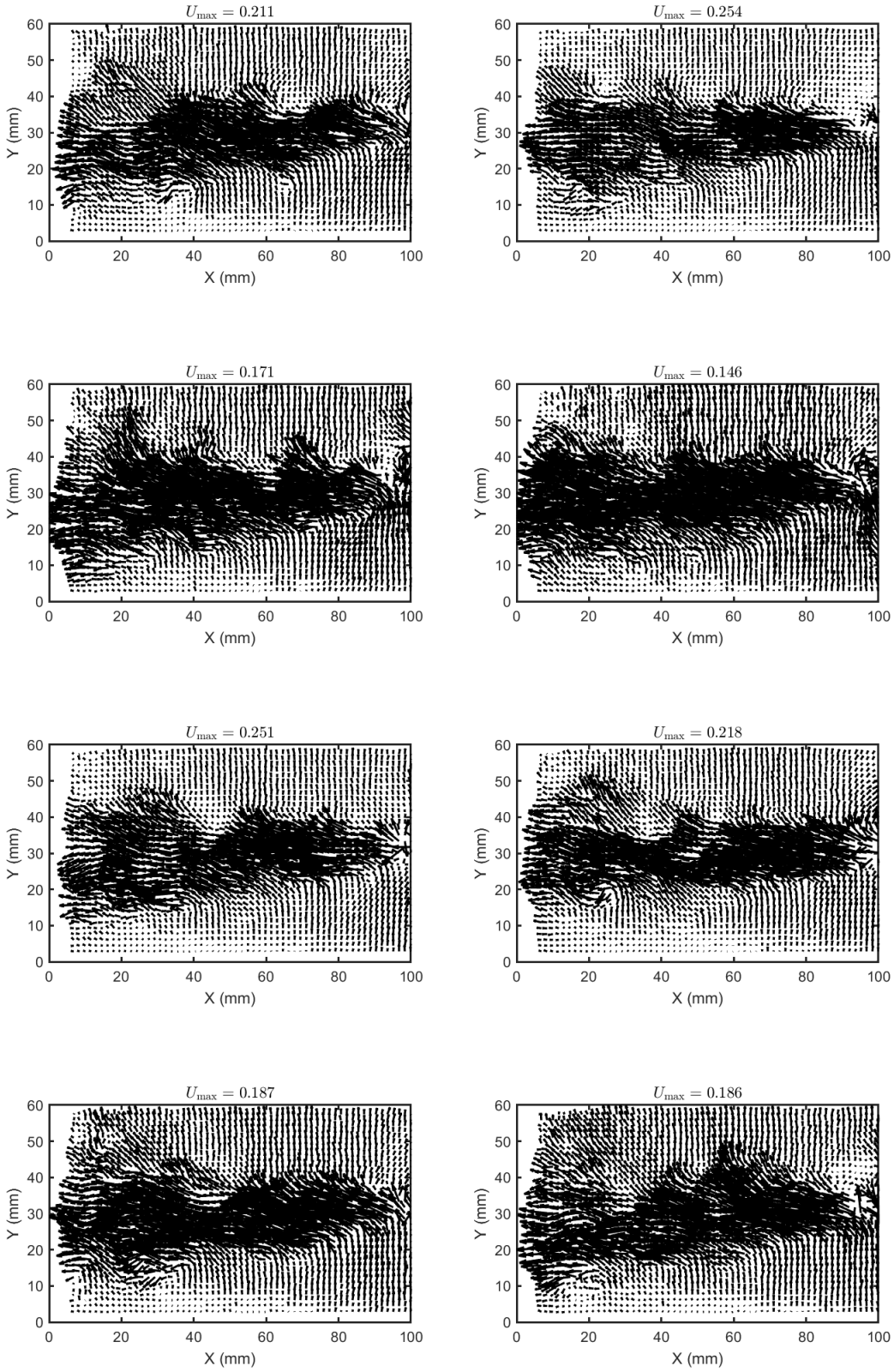

Figure G.11: Uncleaned PIV data at 190 Hz - Image 4

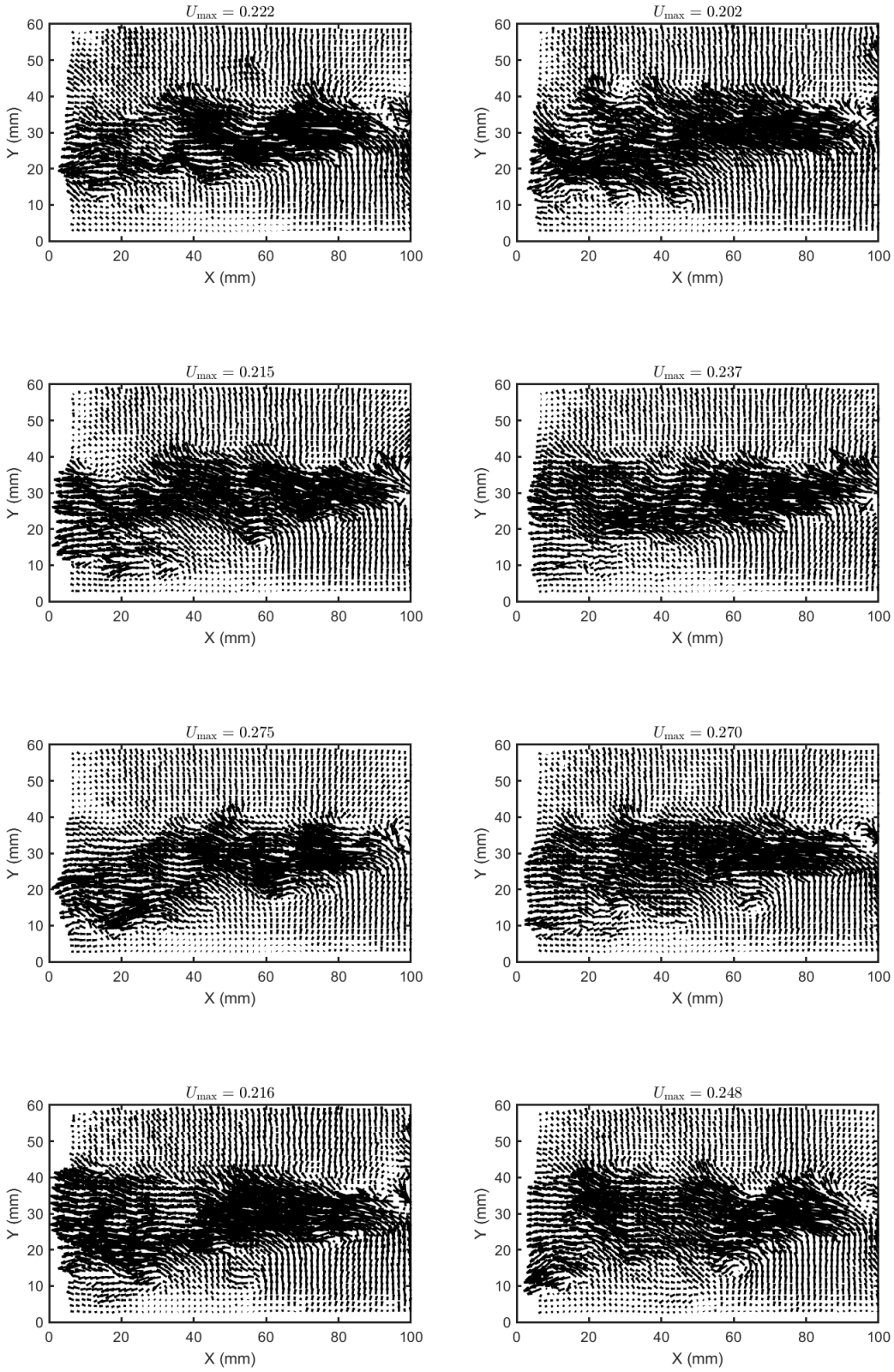

Figure G.12: Uncleaned PIV data at 190 Hz - Image 5

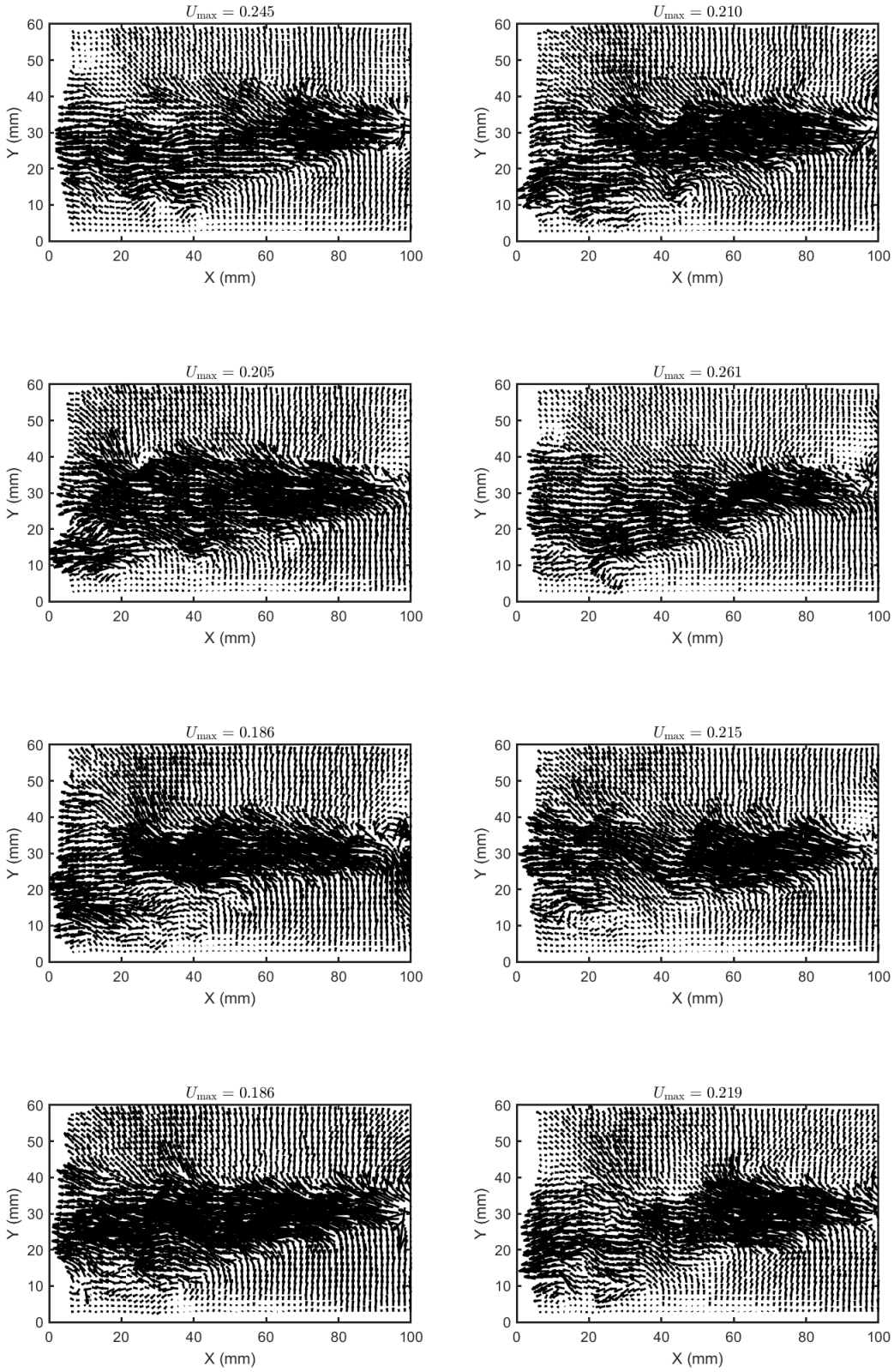

Figure G.13: Uncleaned PIV data at 190 Hz - Image 6

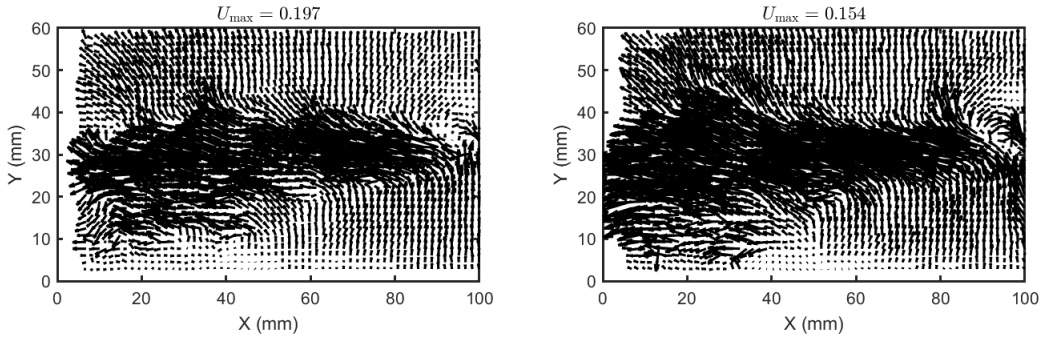

Figure G.14: Uncleaned PIV data at 190 Hz - Image 7

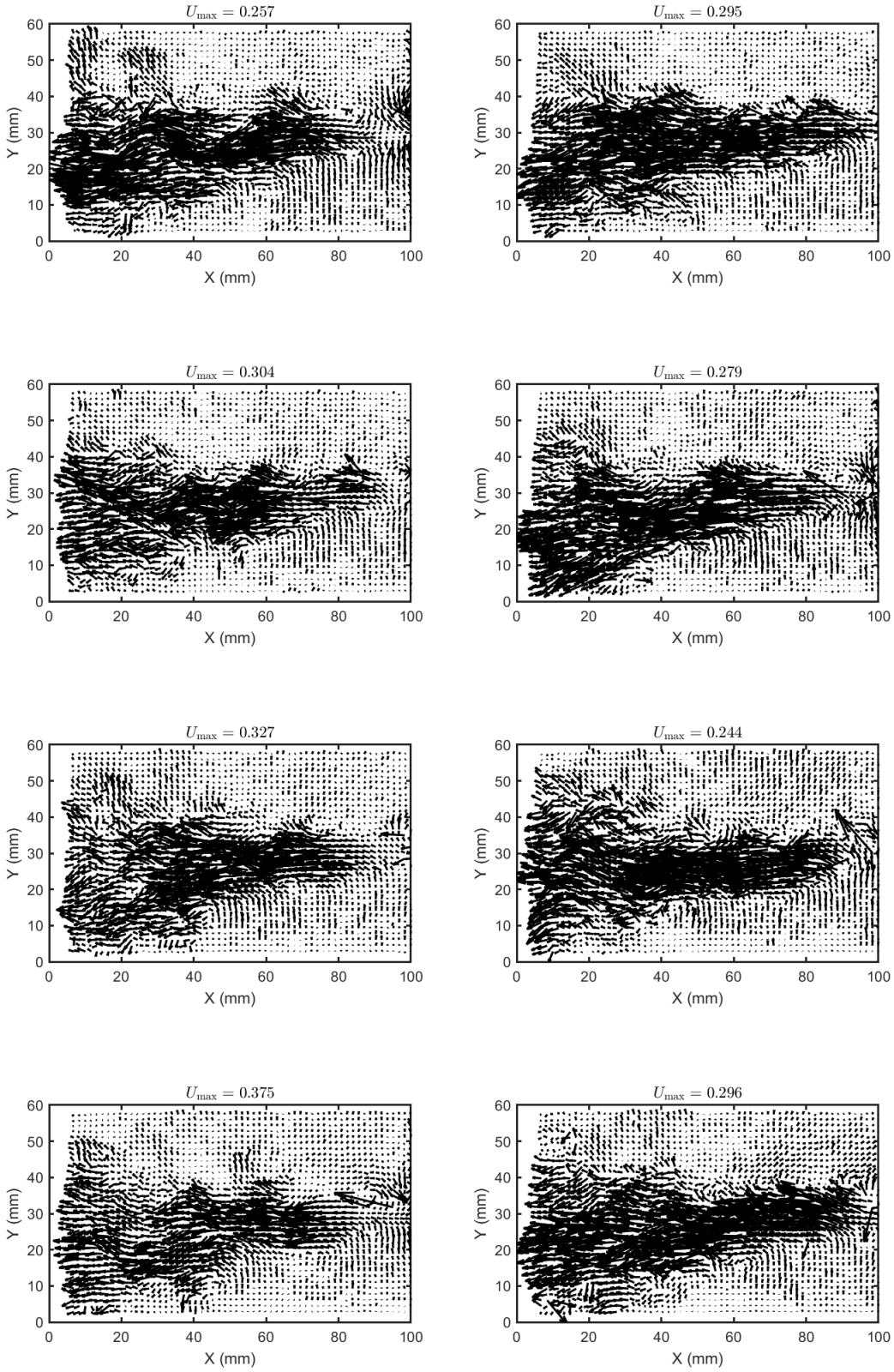

Figure G.15: Uncleaned PIV data at 200 Hz - Image 1

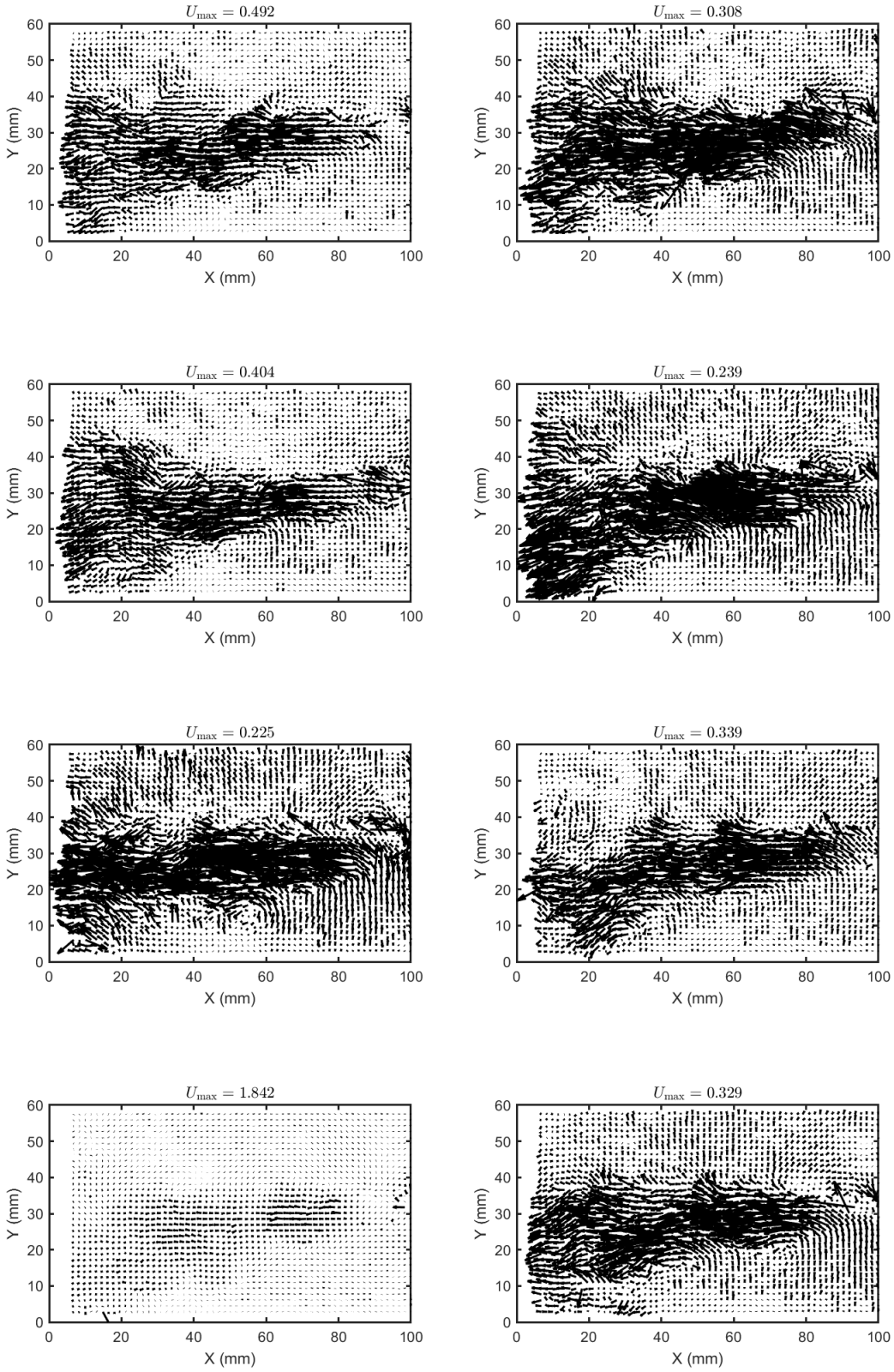

Figure G.16: Uncleaned PIV data at 200 Hz - Image 2

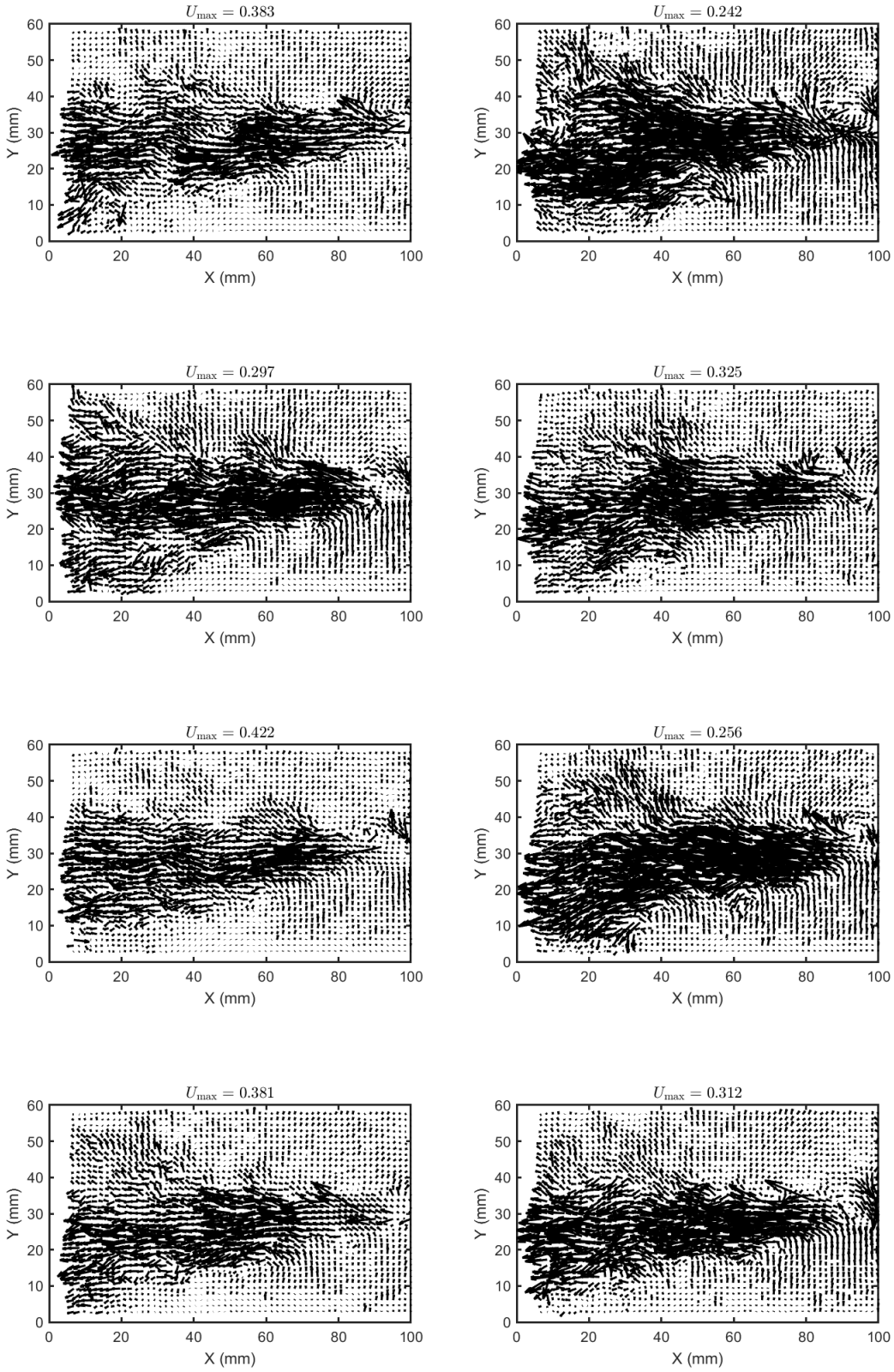

Figure G.17: Uncleaned PIV data at 200 Hz - Image 3

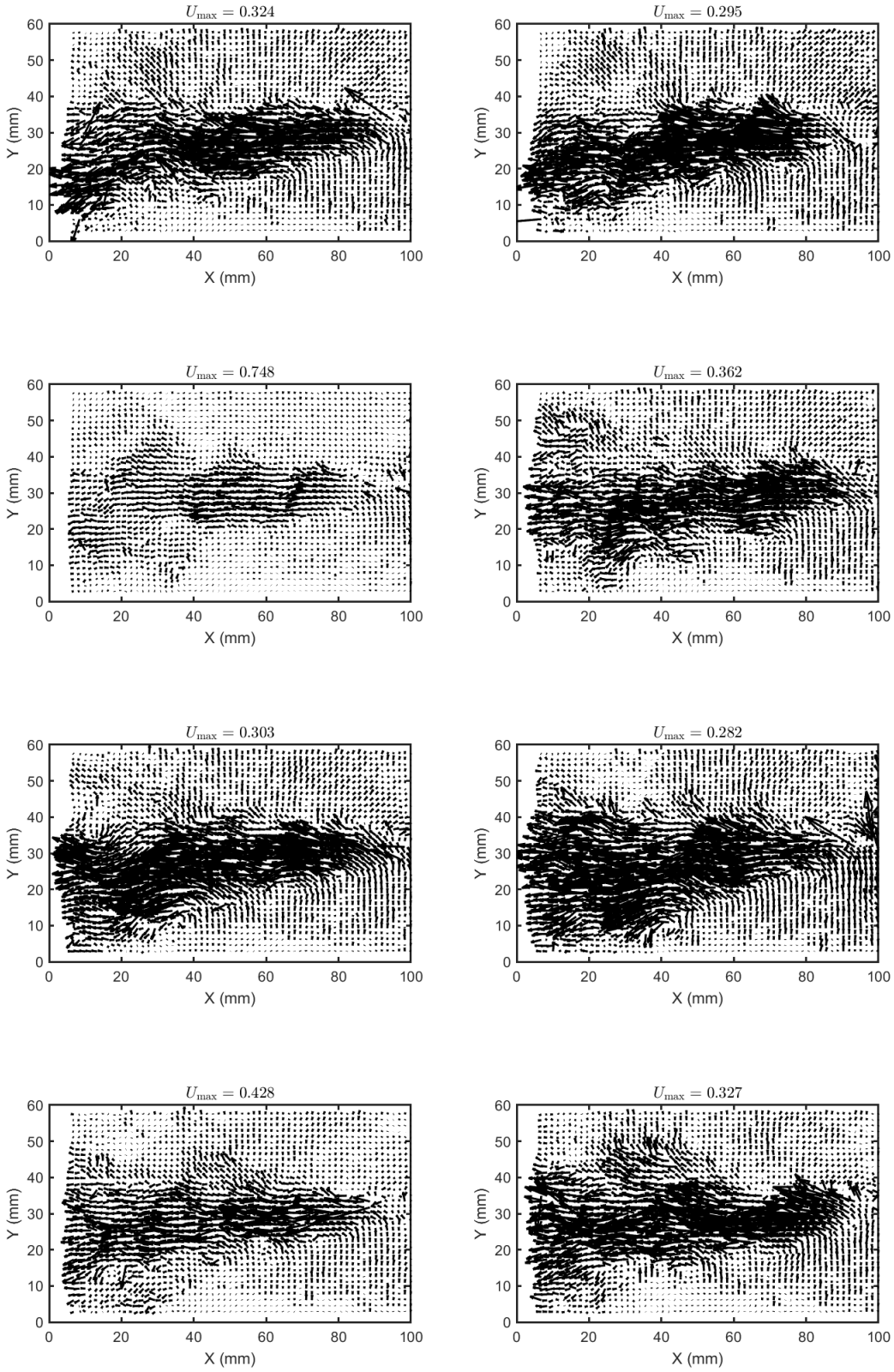

Figure G.18: Uncleaned PIV data at 200 Hz - Image 4

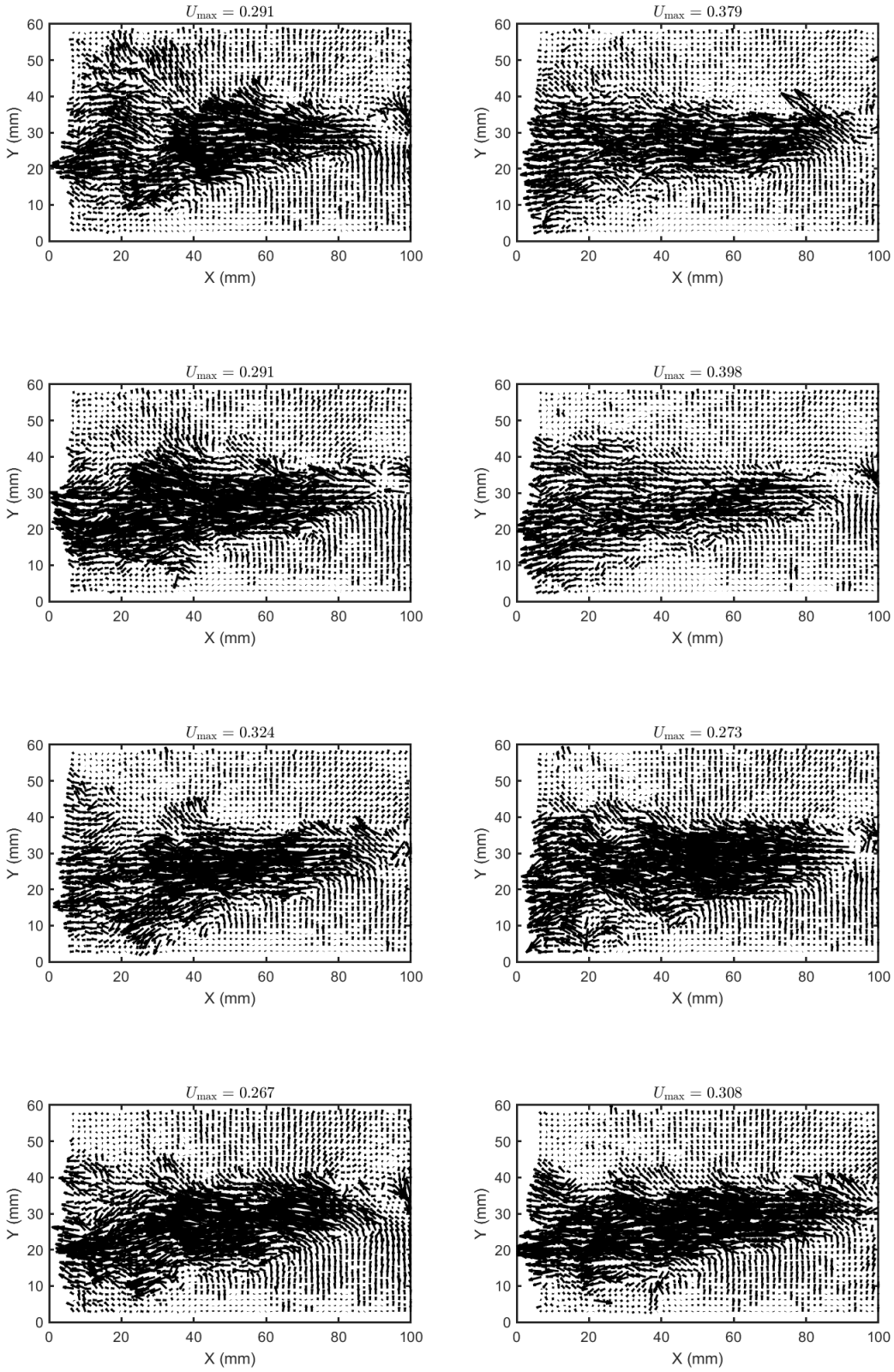

Figure G.19: Uncleaned PIV data at 200 Hz - Image 5

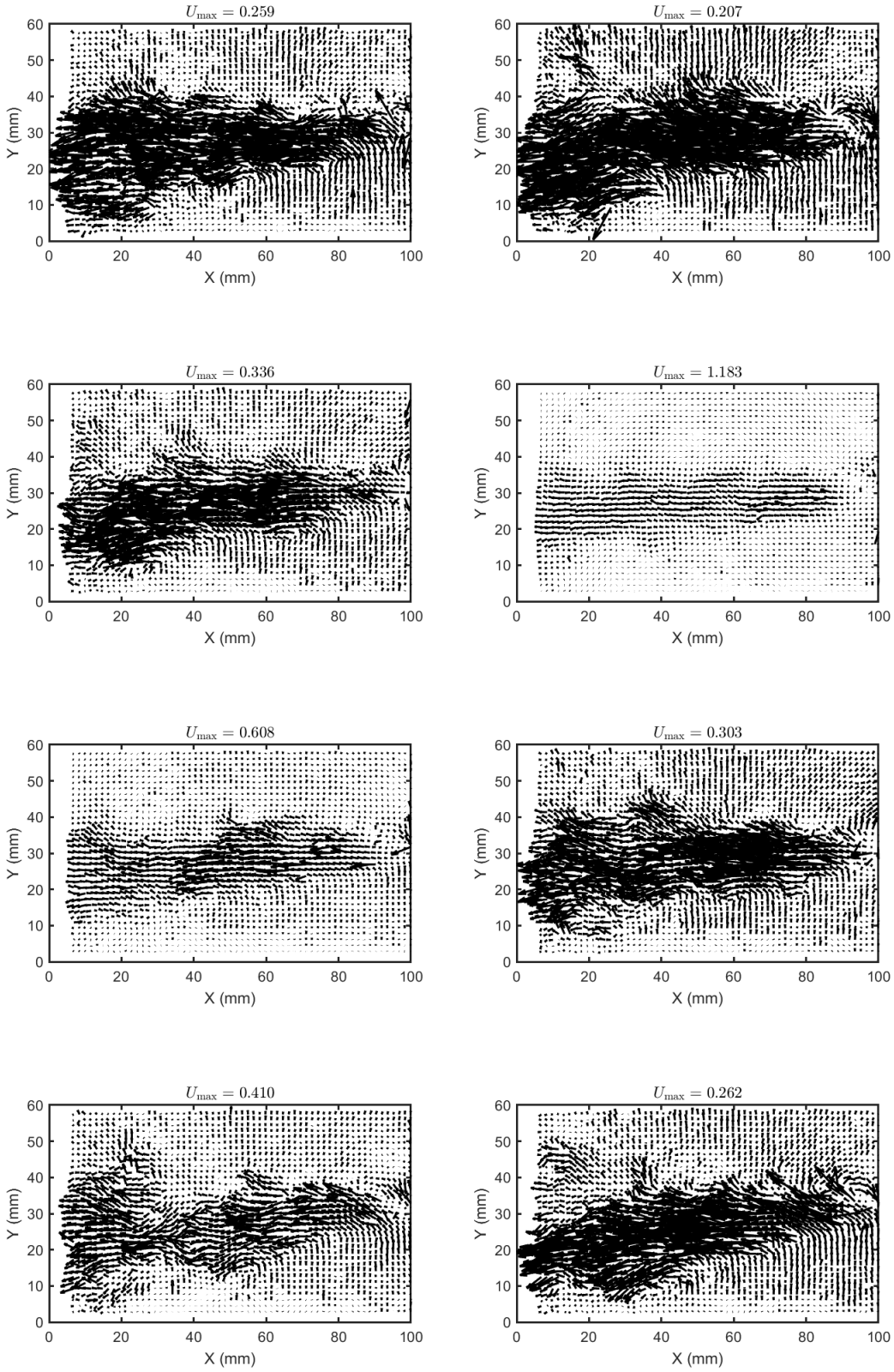

Figure G.20: Uncleaned PIV data at 200 Hz - Image 6

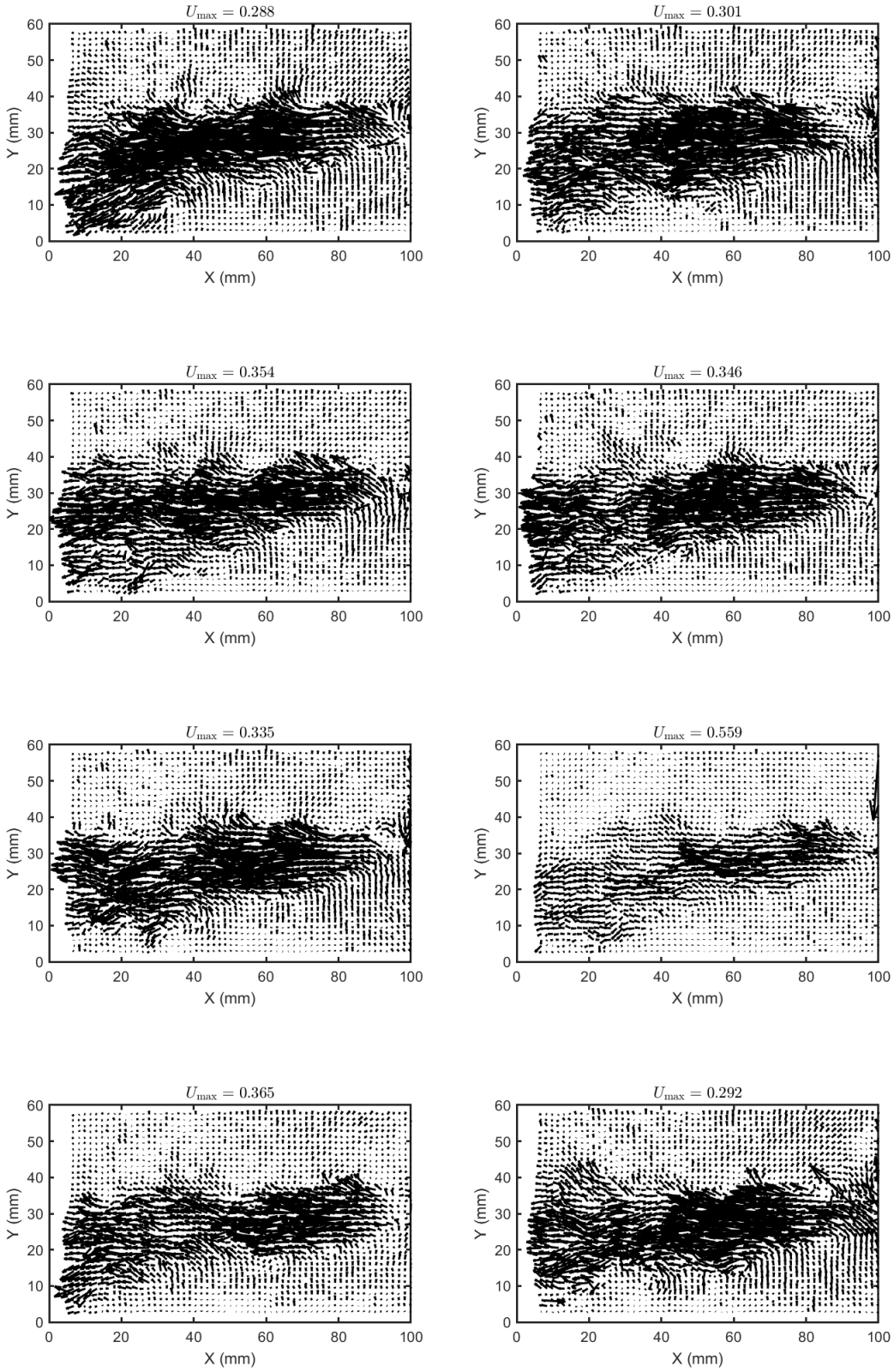

Figure G.21: Uncleaned PIV data at 200 Hz - Image 7

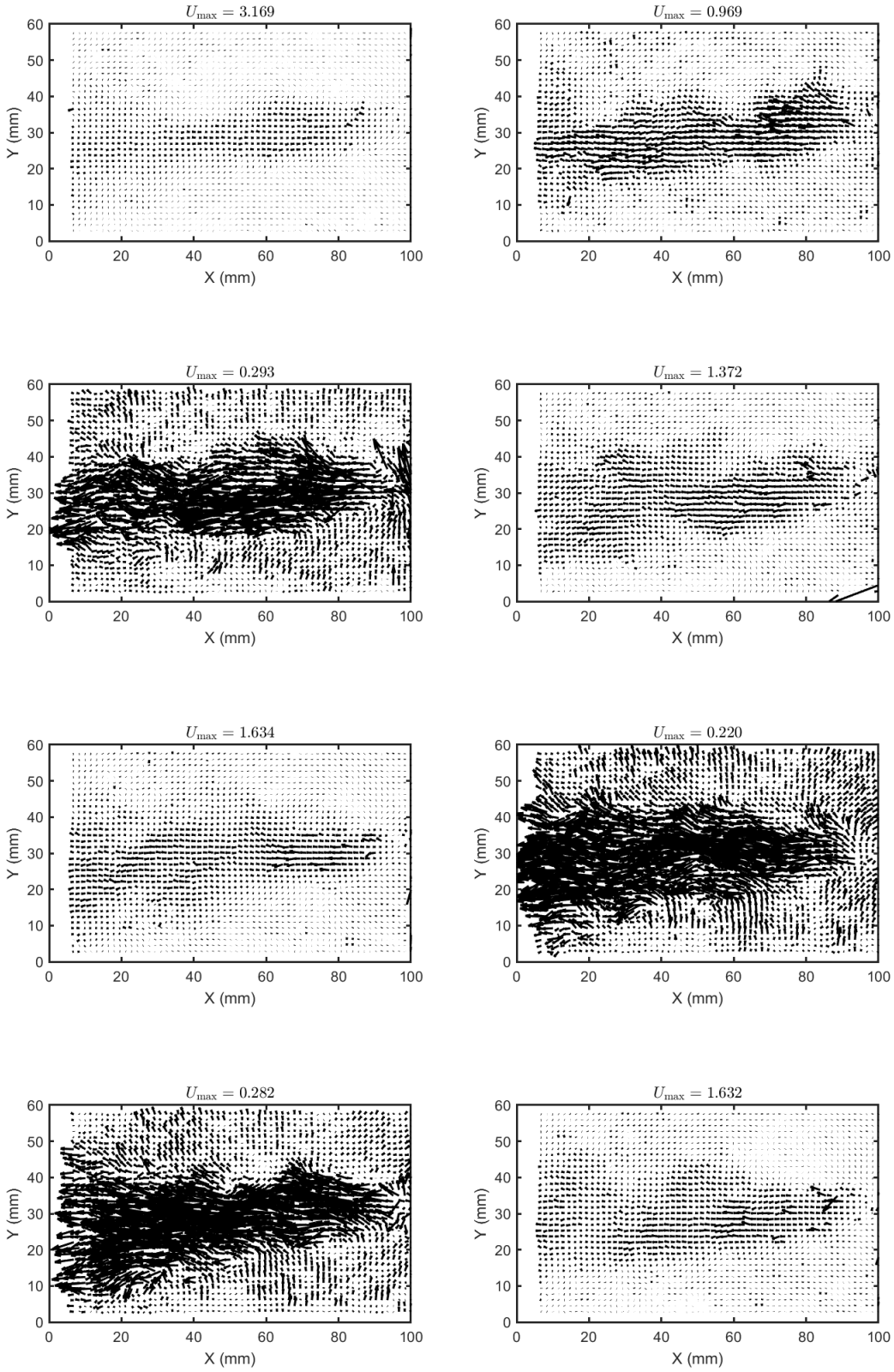

Figure G.22: Uncleaned PIV data at 210 Hz - Image 1

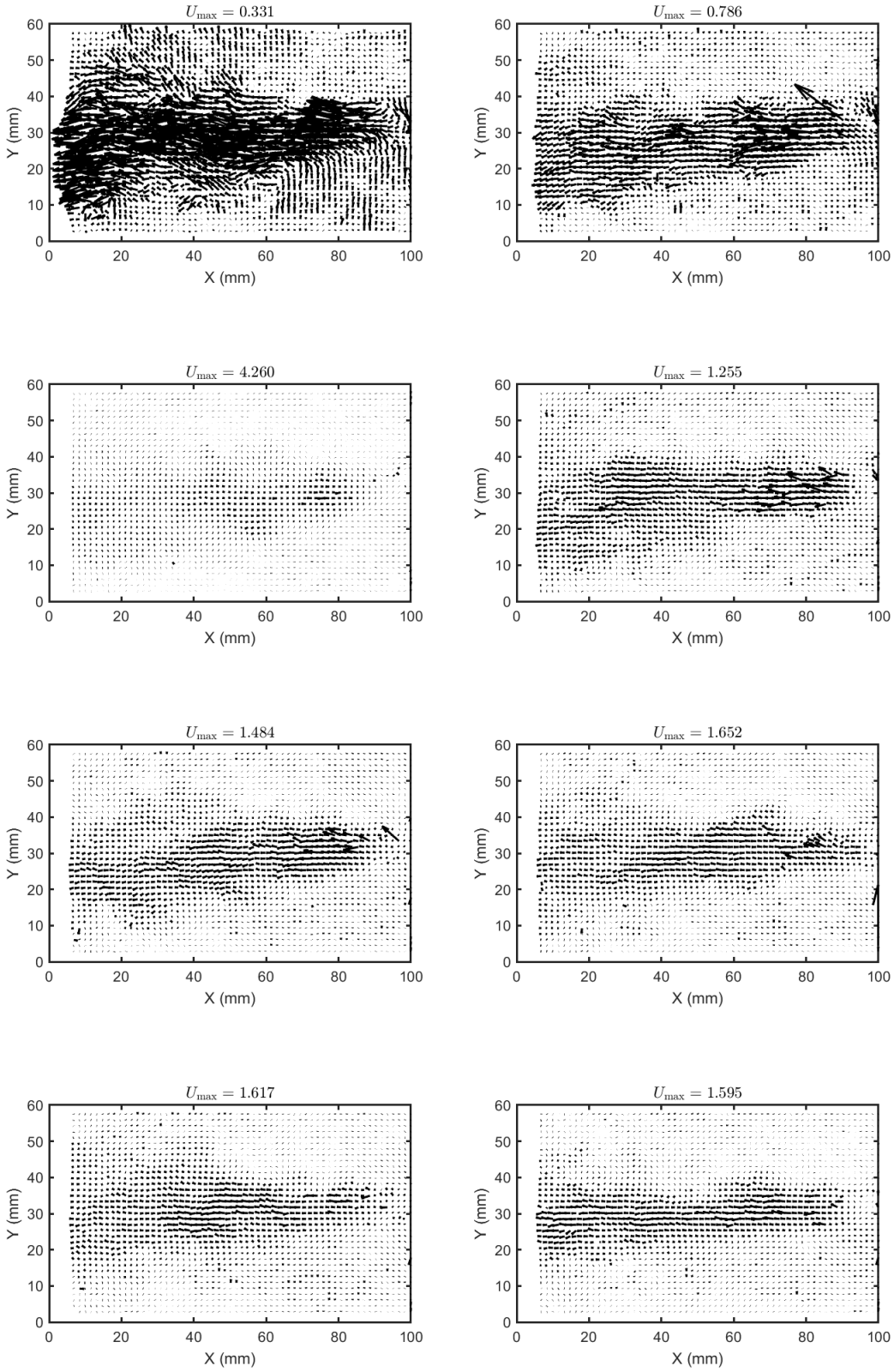

Figure G.23: Uncleaned PIV data at 210 Hz - Image 2

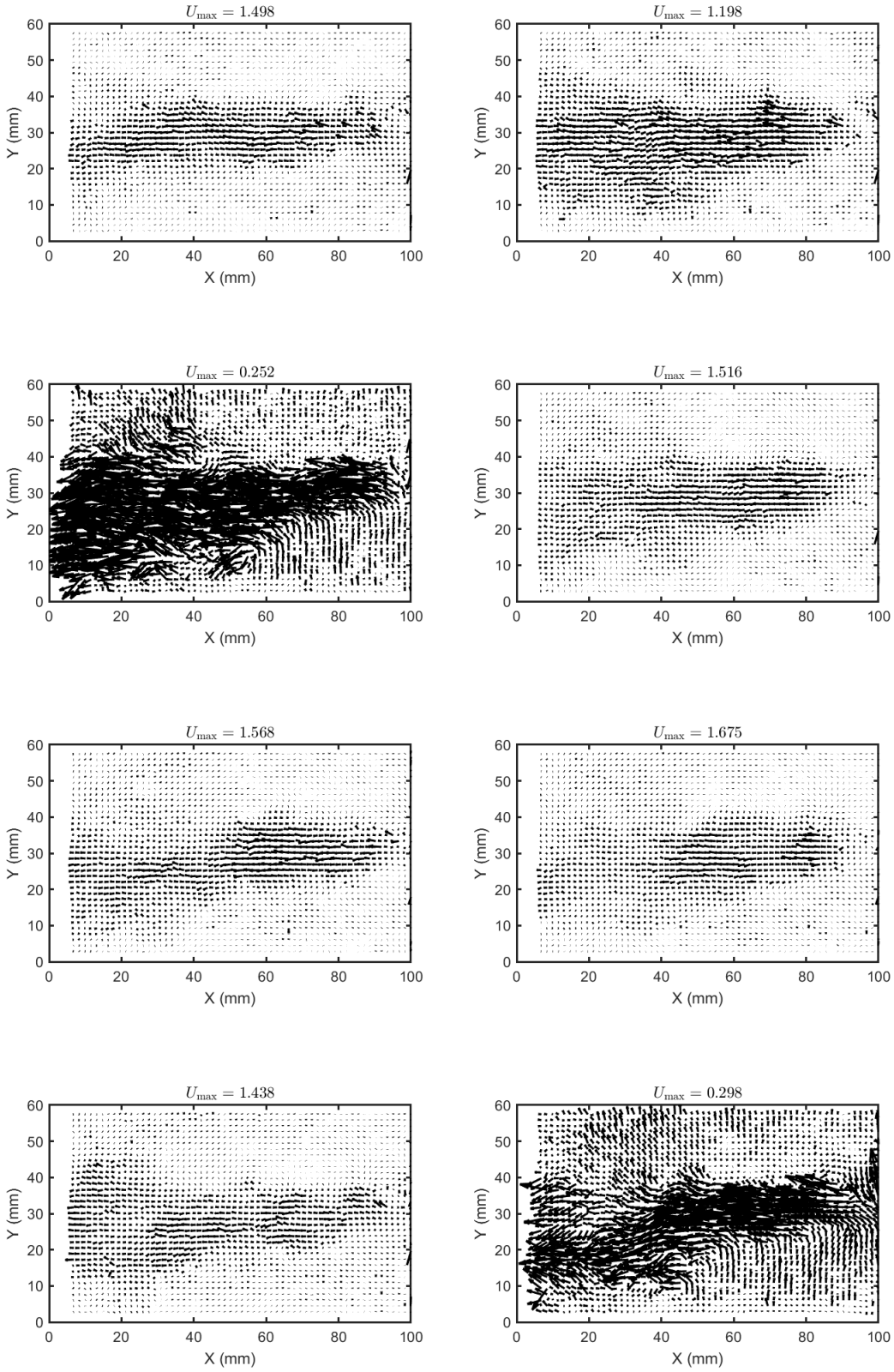

Figure G.24: Uncleaned PIV data at 210 Hz - Image 3

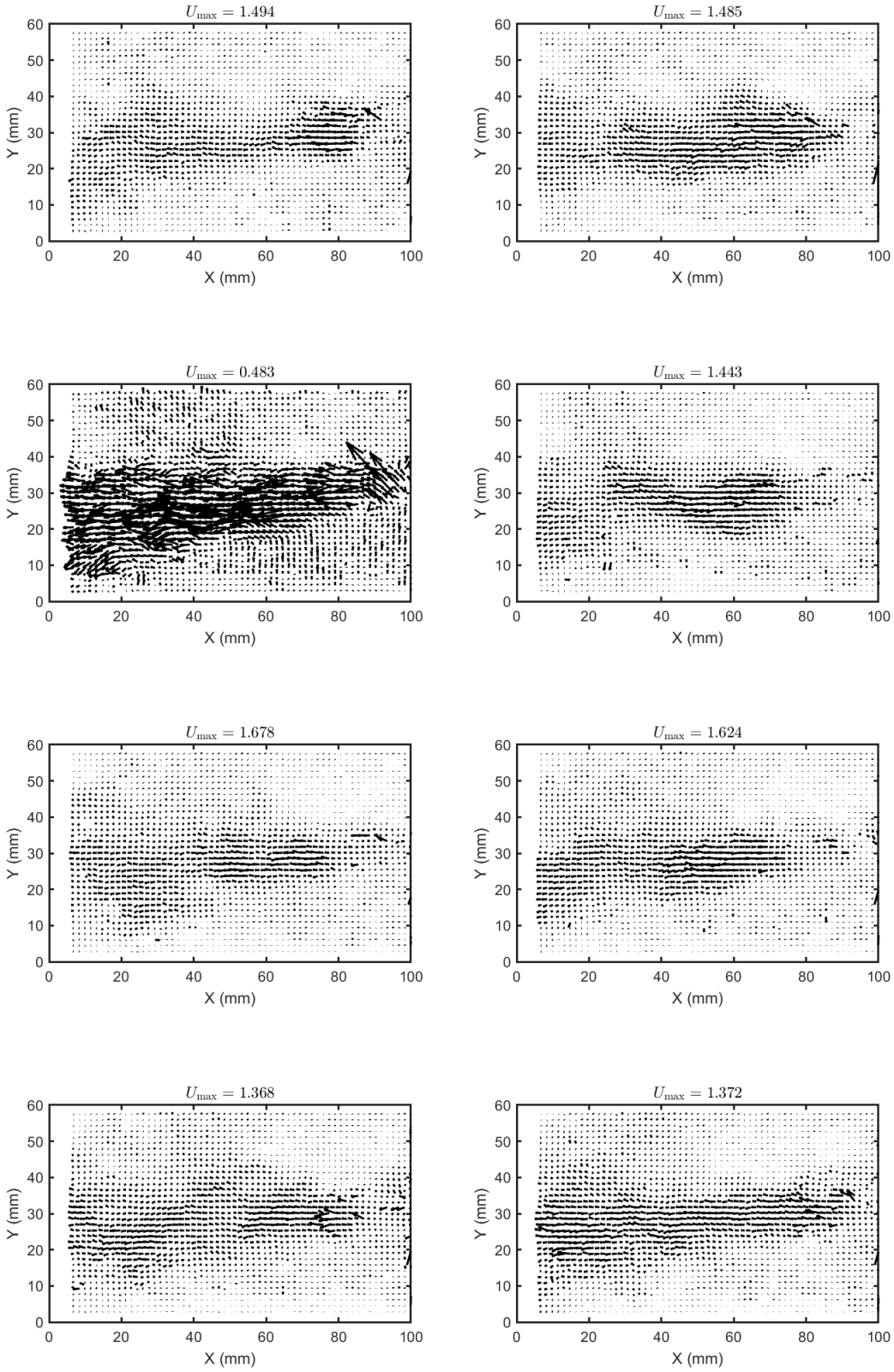

Figure G.25: Uncleaned PIV data at 210 Hz - Image 4

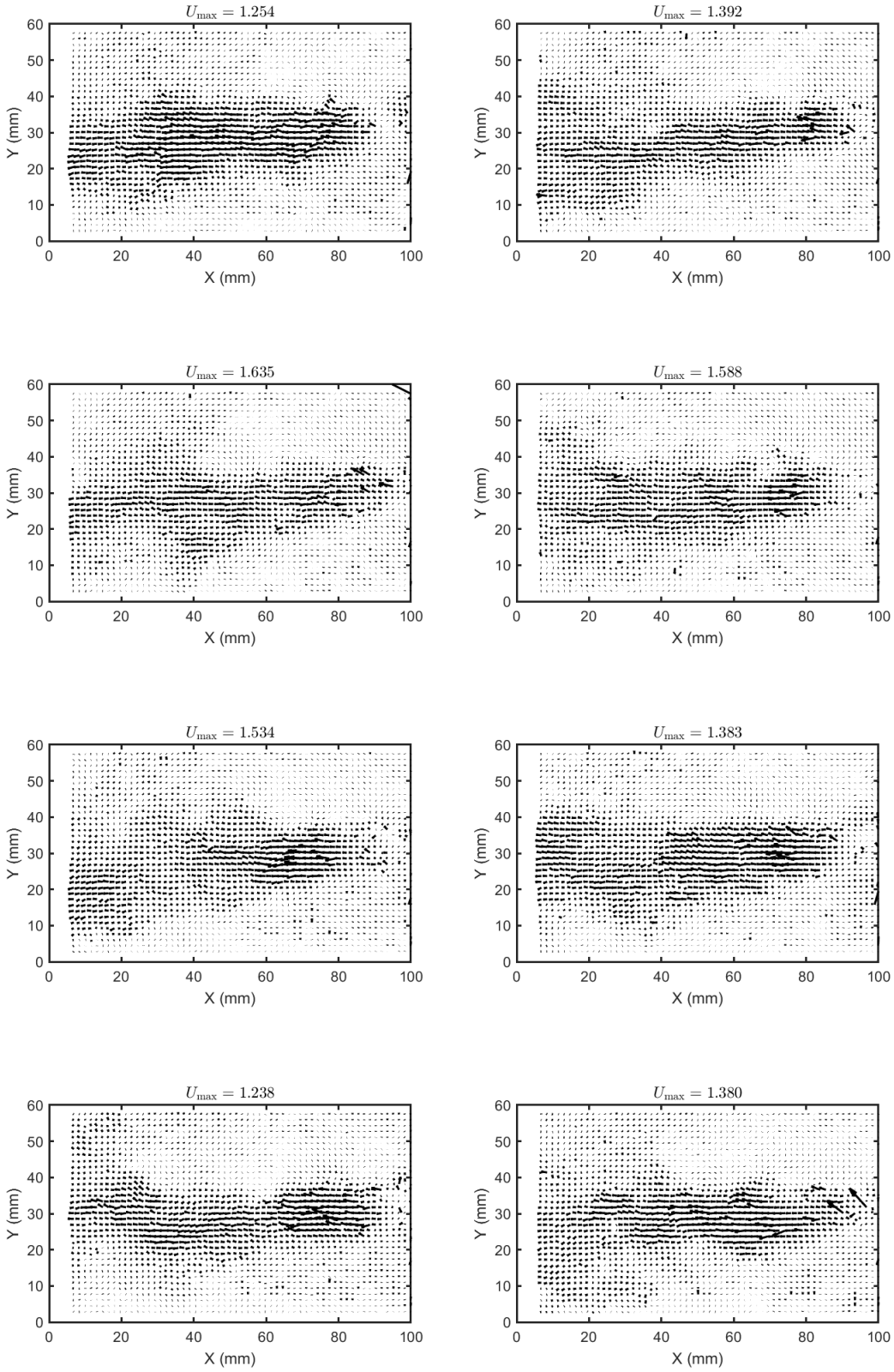

Figure G.26: Uncleaned PIV data at 210 Hz - Image 5

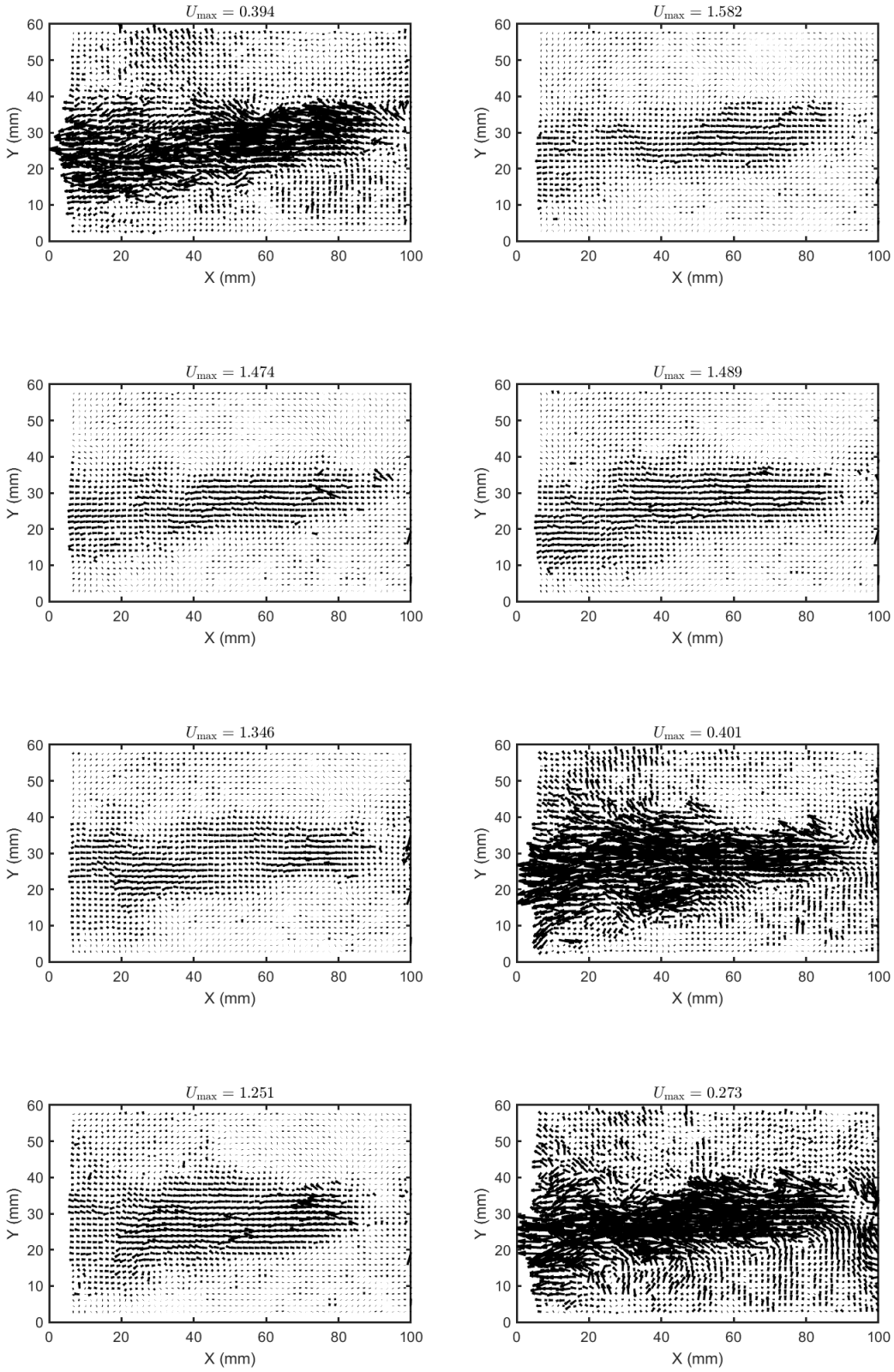

Figure G.27: Uncleaned PIV data at 210 Hz - Image 6

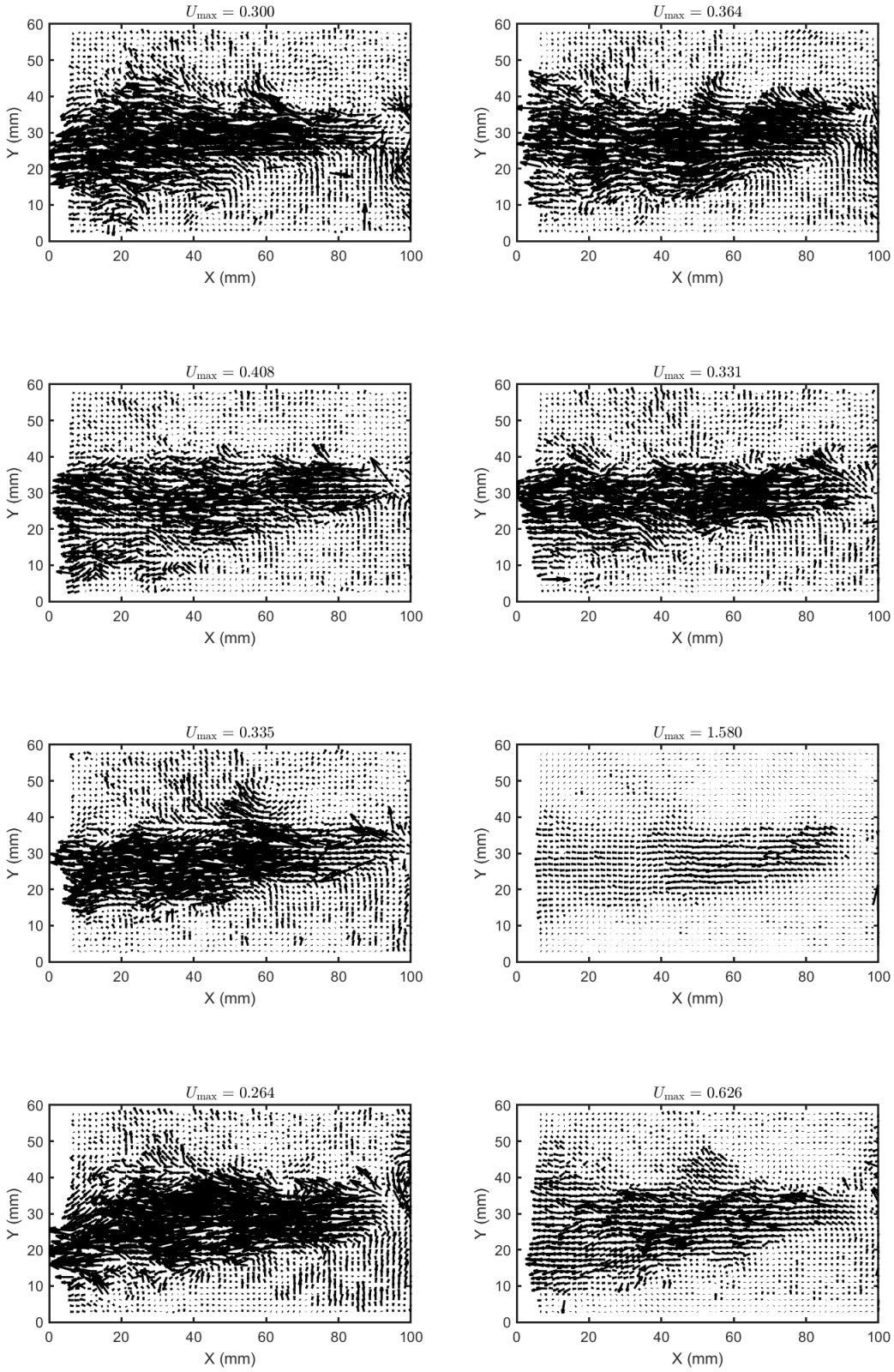

Figure G.28: Uncleaned PIV data at 210 Hz - Image 7

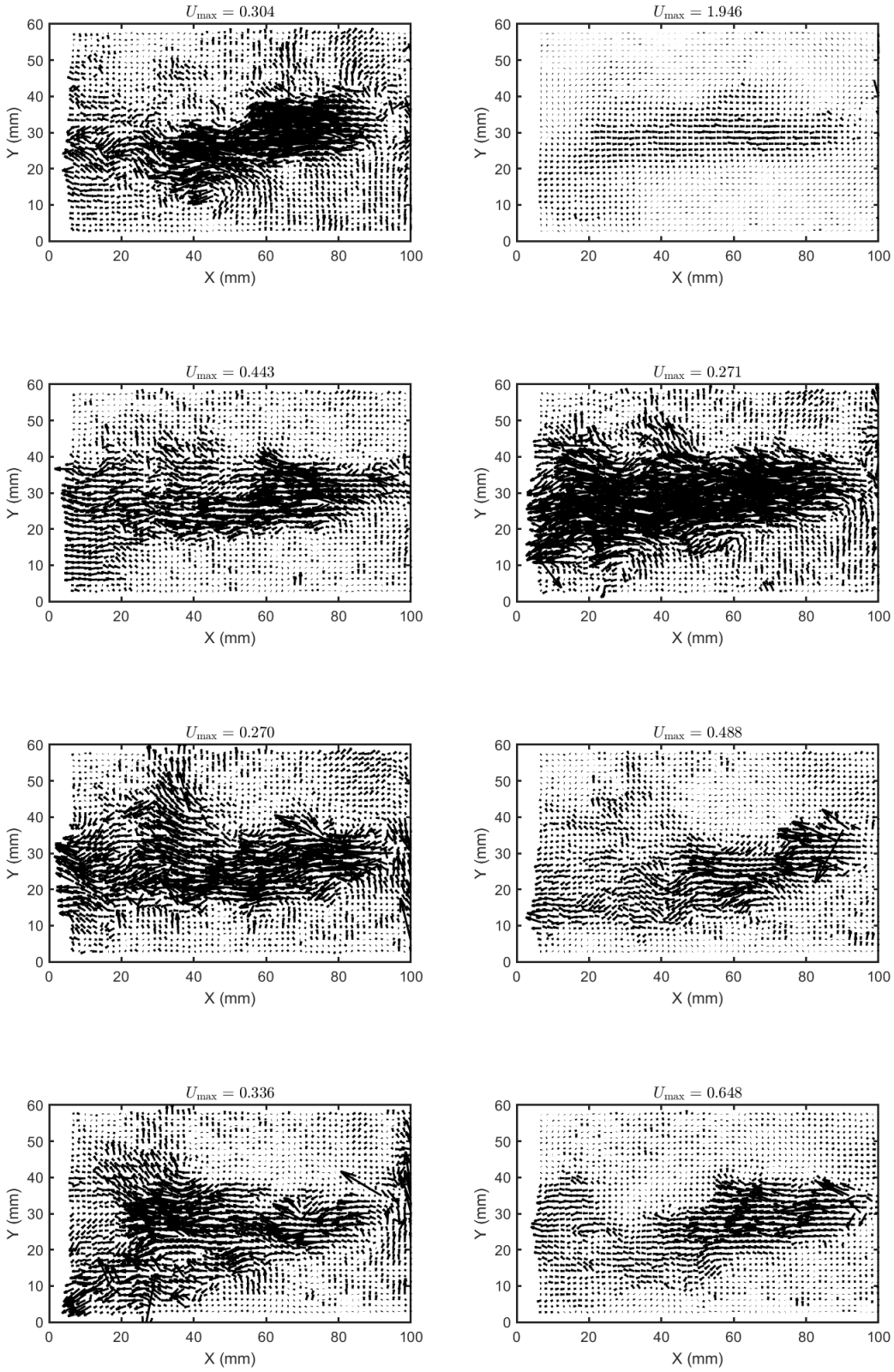

Figure G.29: Uncleaned PIV data at 220 Hz - Image 1

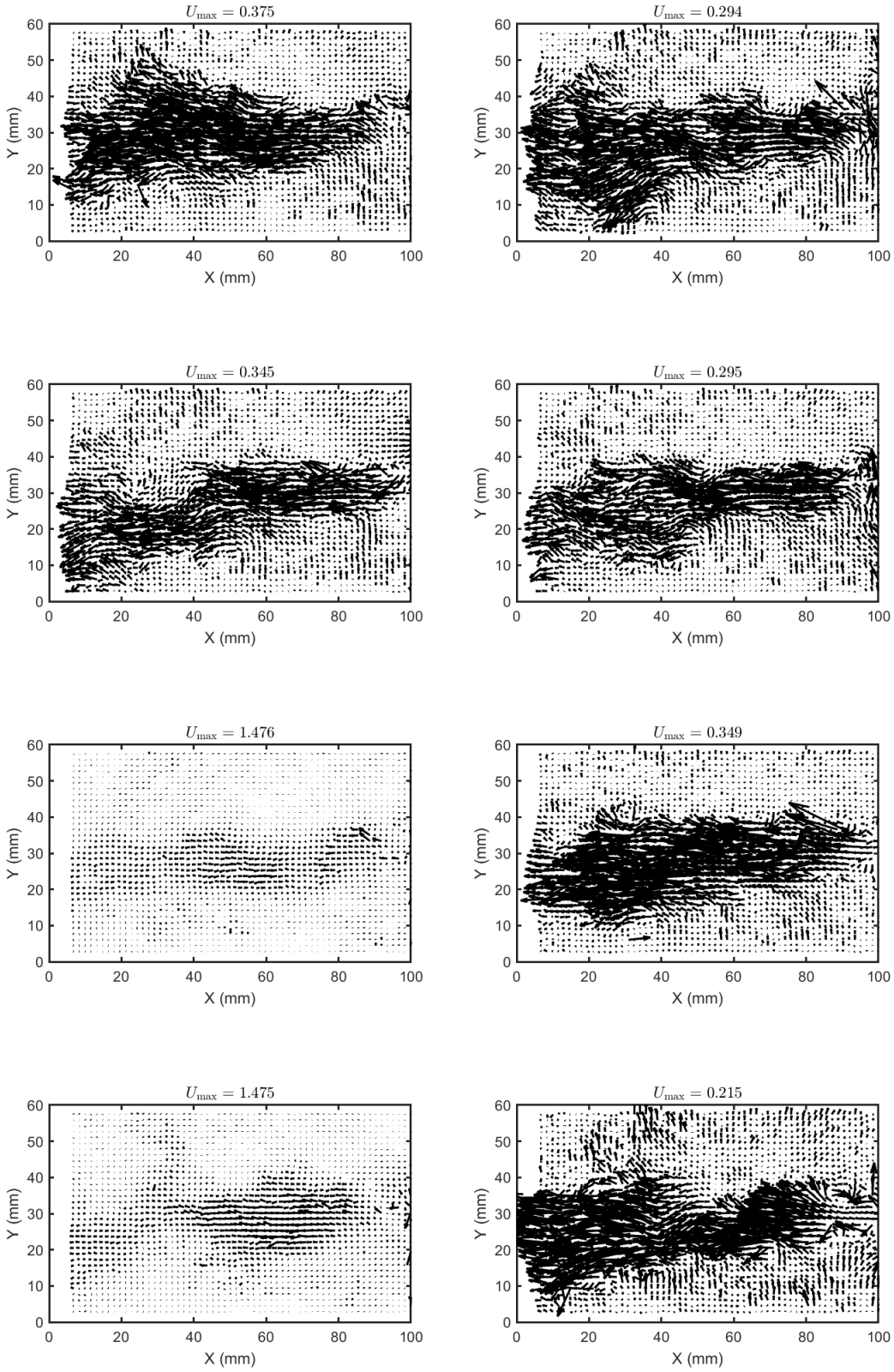

Figure G.30: Uncleaned PIV data at 220 Hz - Image 2

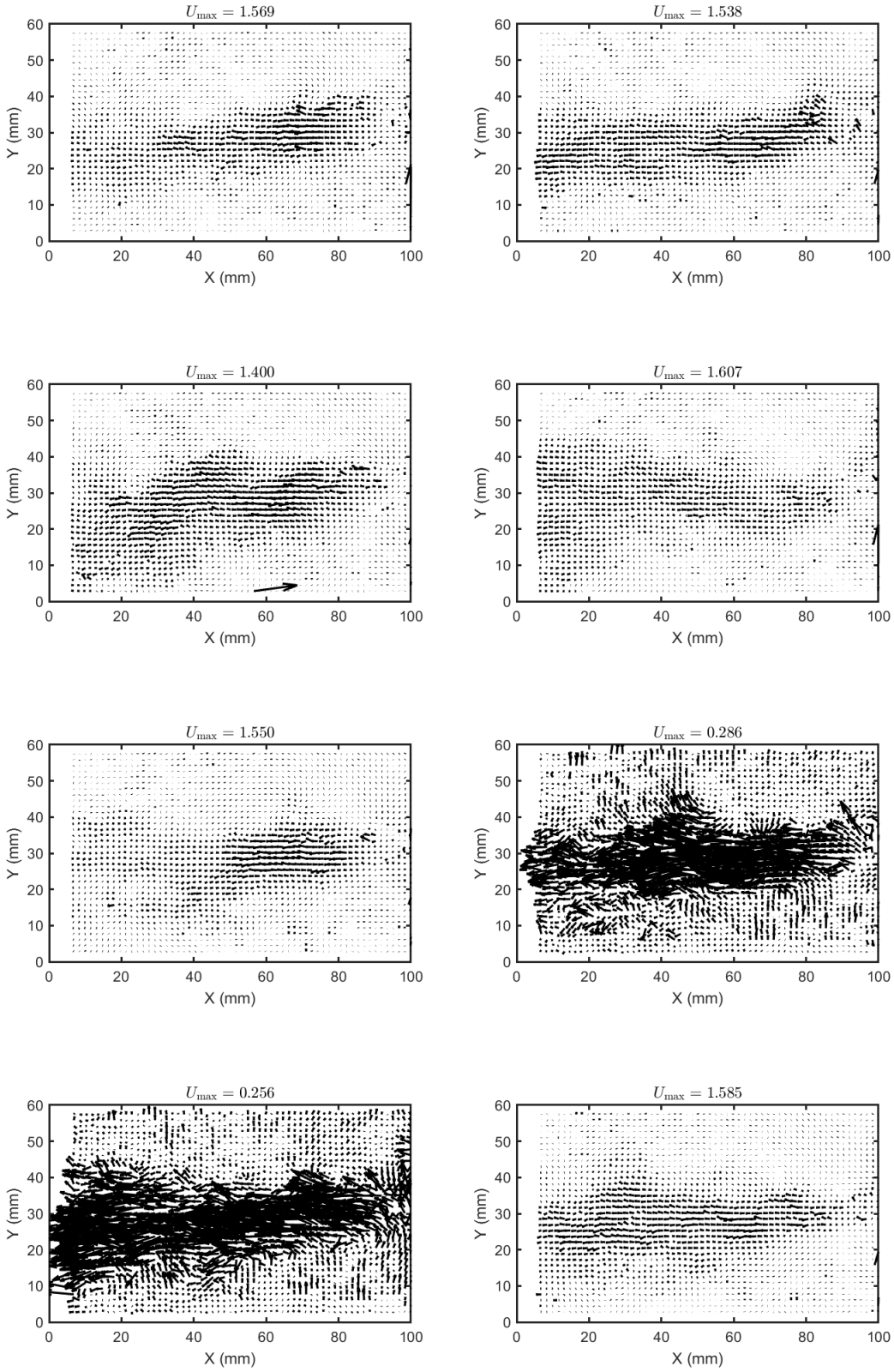

Figure G.31: Uncleaned PIV data at 220 Hz - Image 3

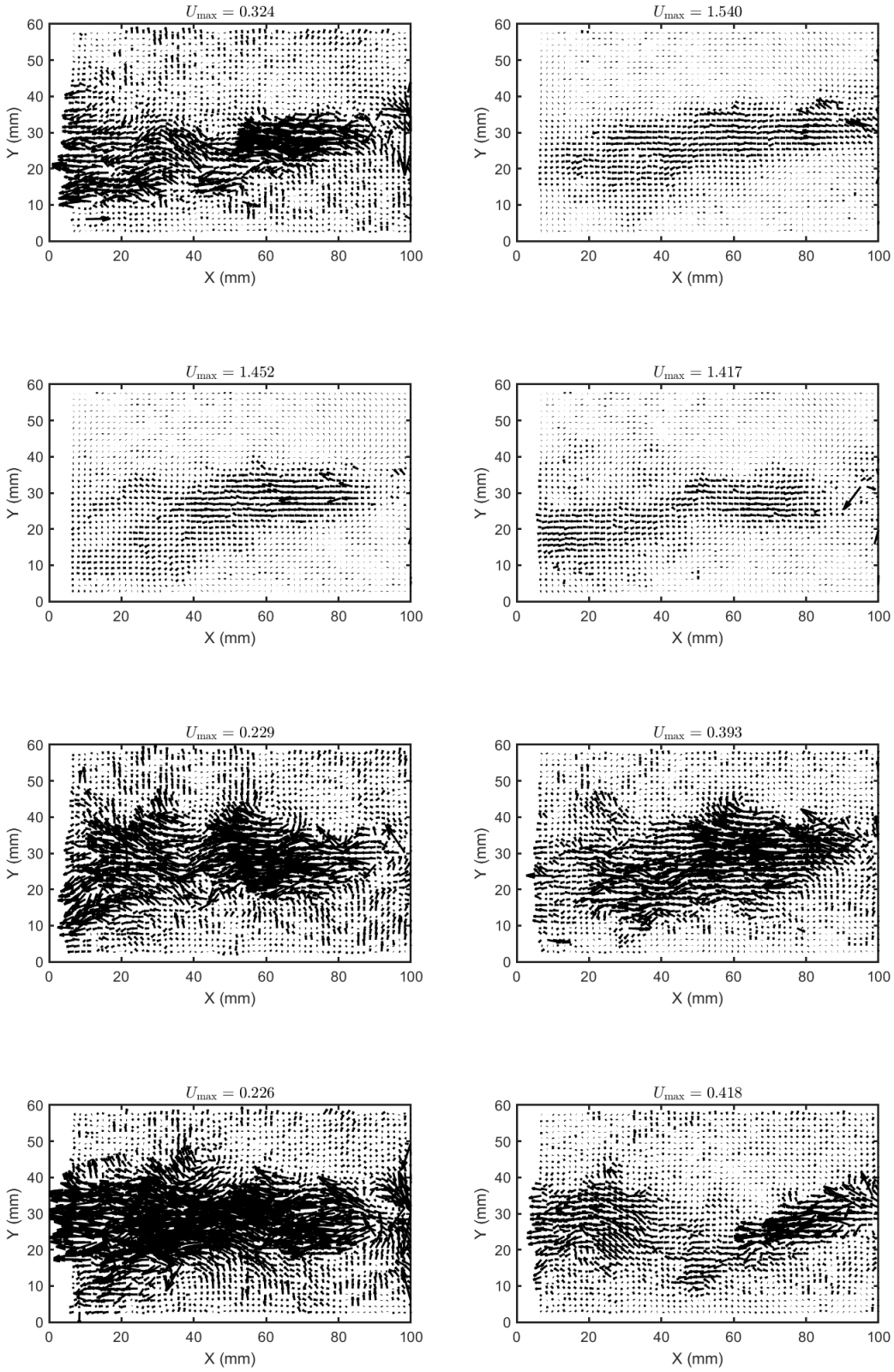

Figure G.32: Uncleaned PIV data at 220 Hz - Image 4

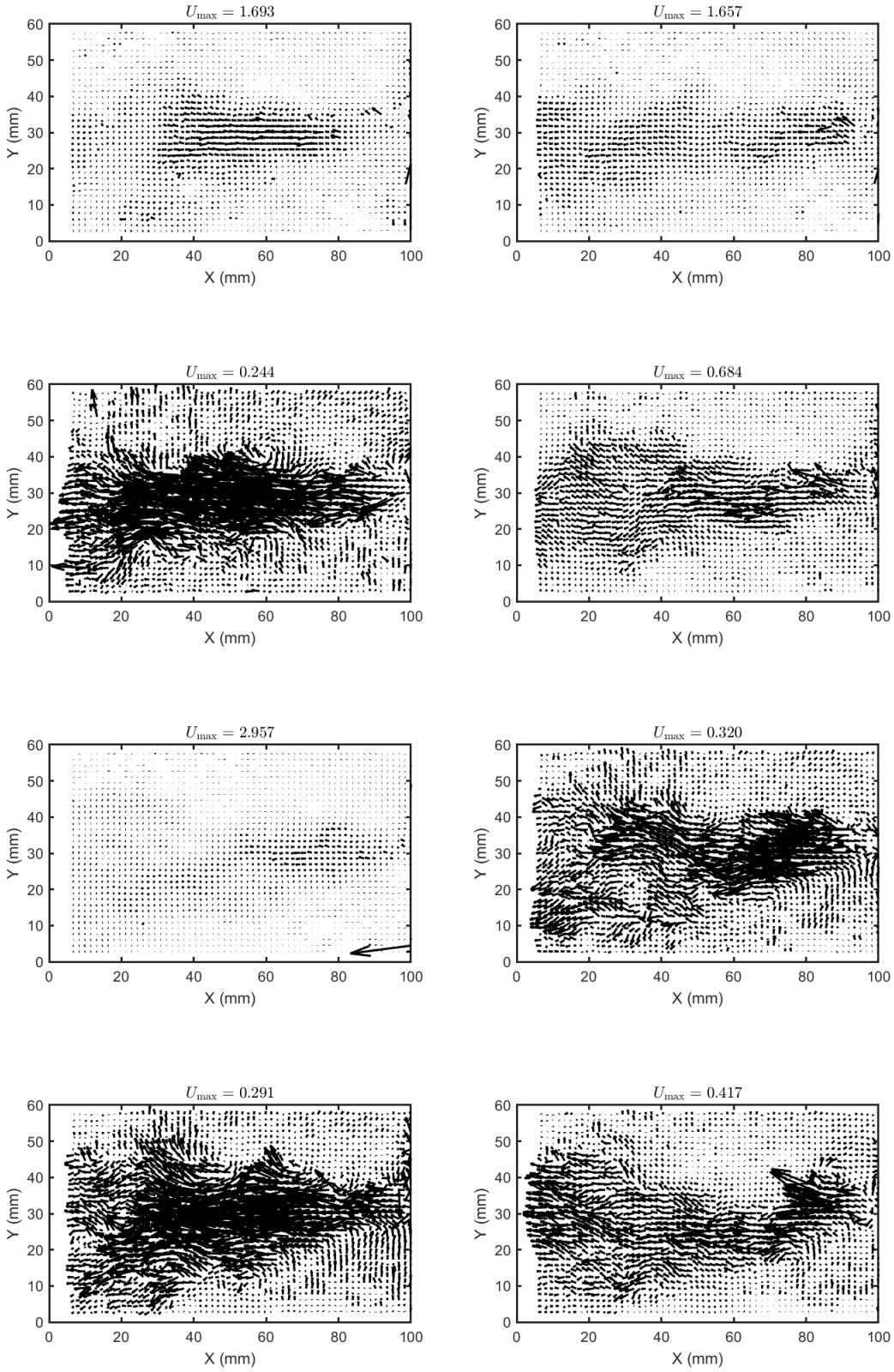

Figure G.33: Uncleaned PIV data at 220 Hz - Image 5

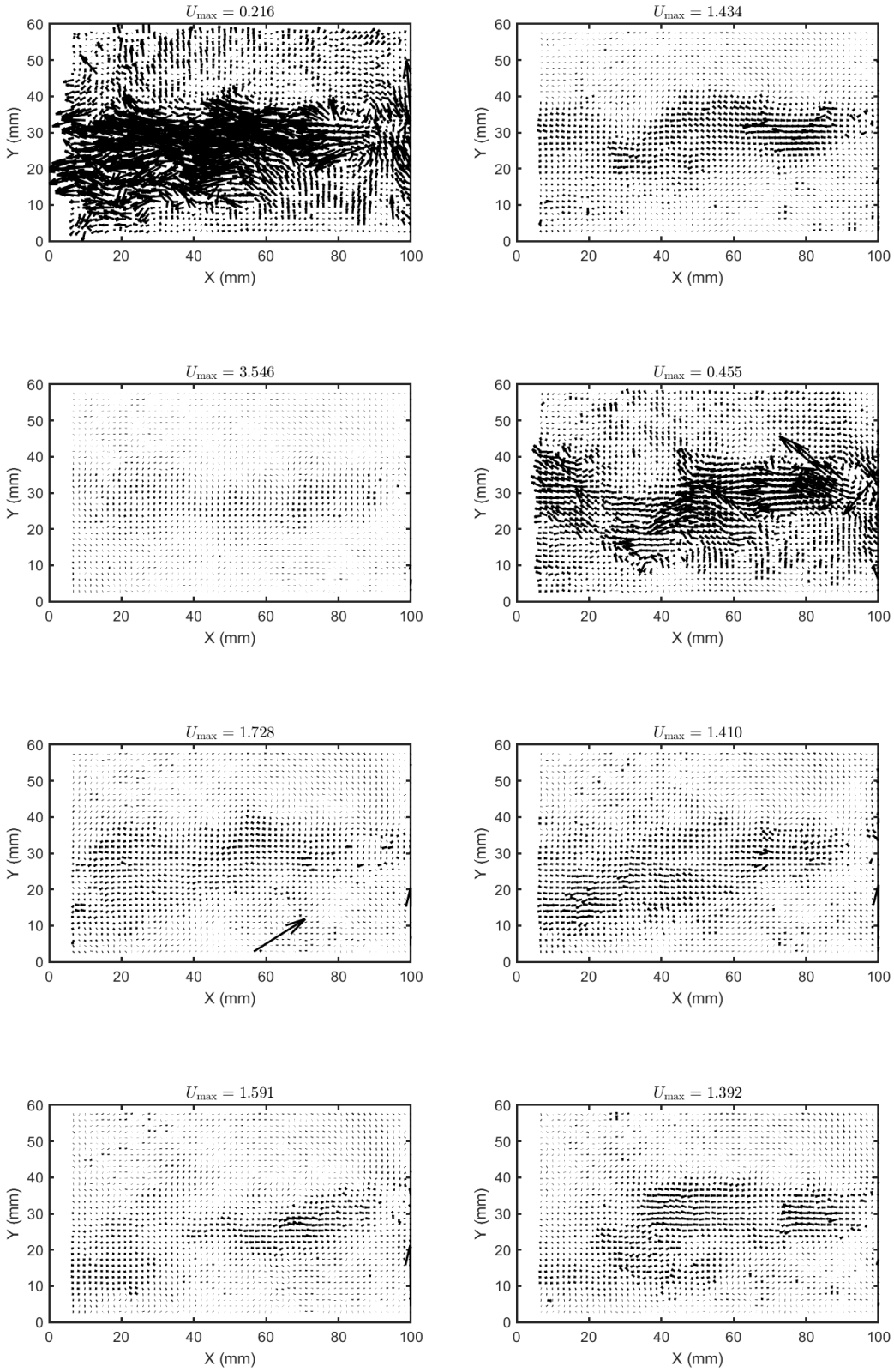

Figure G.34: Uncleaned PIV data at 220 Hz - Image 6

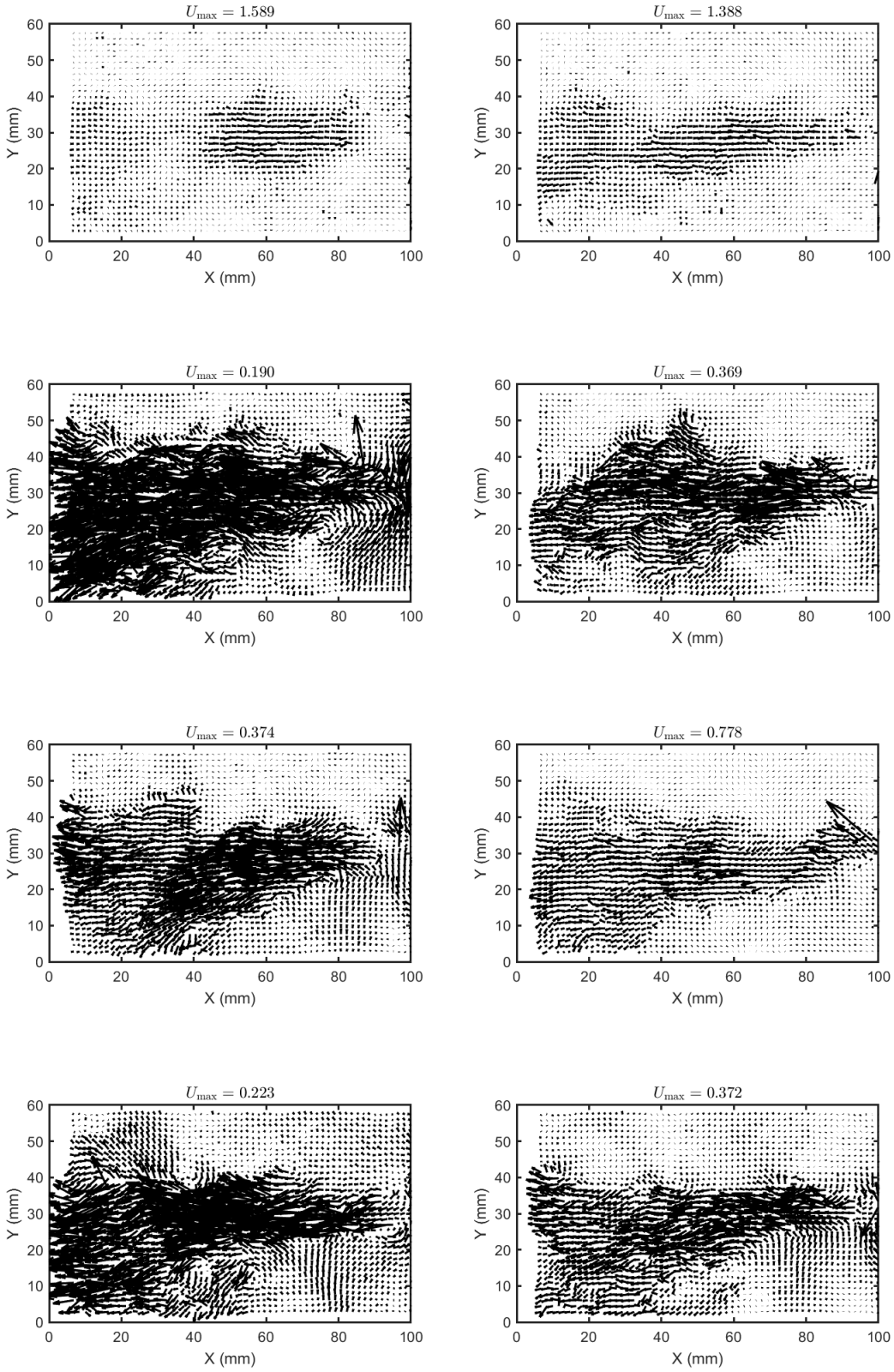

Figure G.35: Uncleaned PIV data at 220 Hz - Image 7

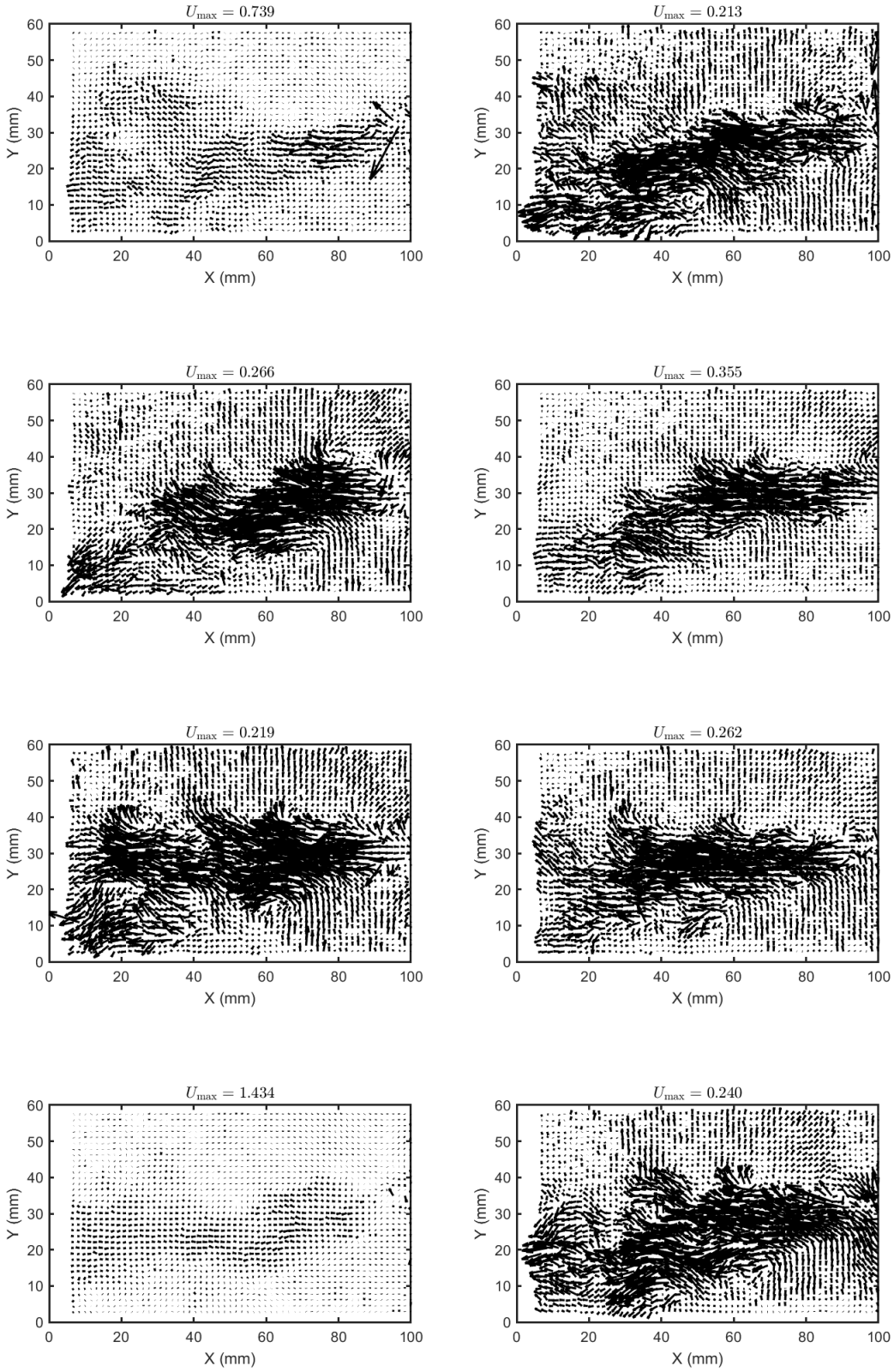

Figure G.36: Uncleaned PIV data at 230 Hz - Image 1

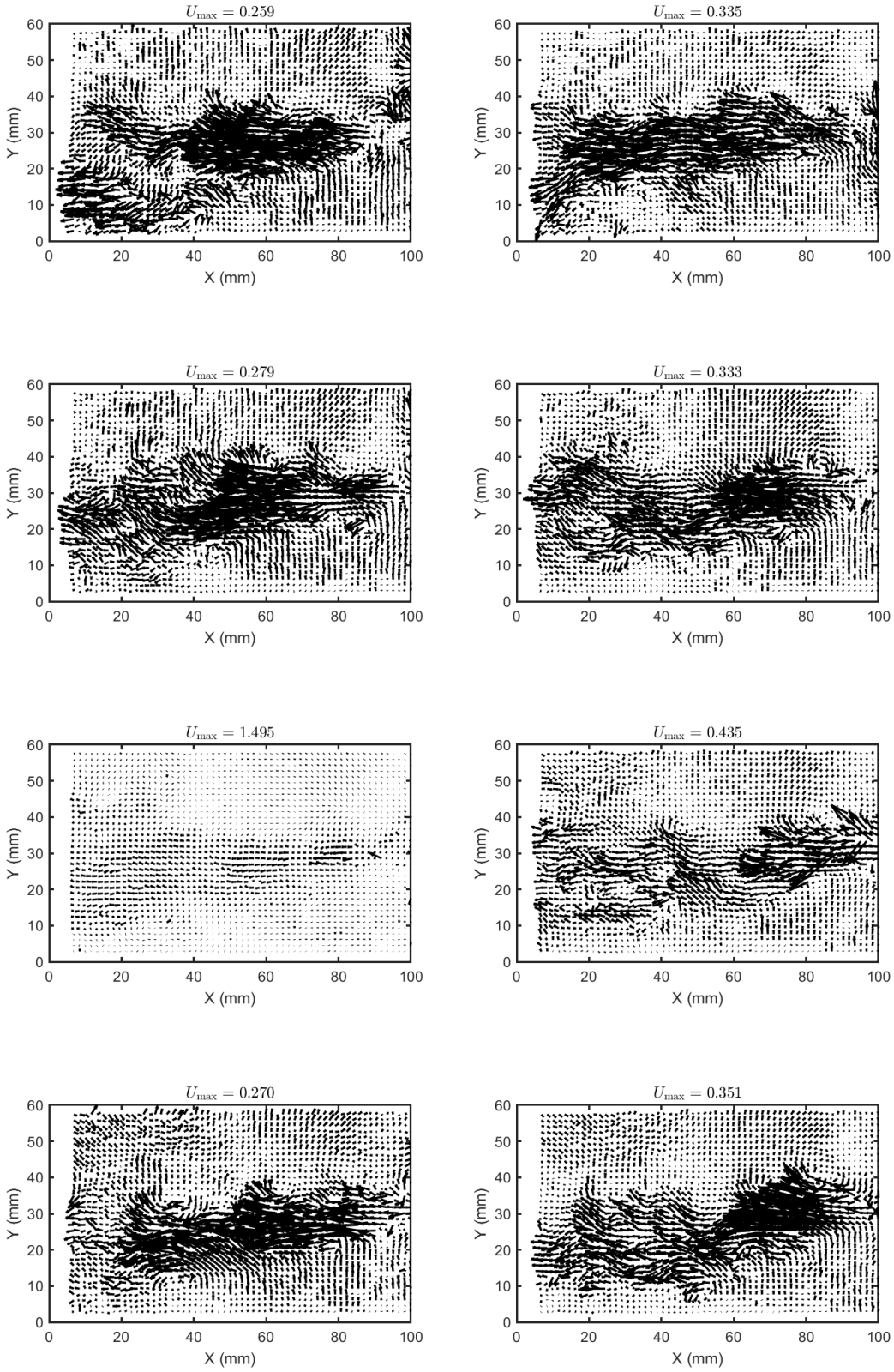

Figure G.37: Uncleaned PIV data at 230 Hz - Image 2

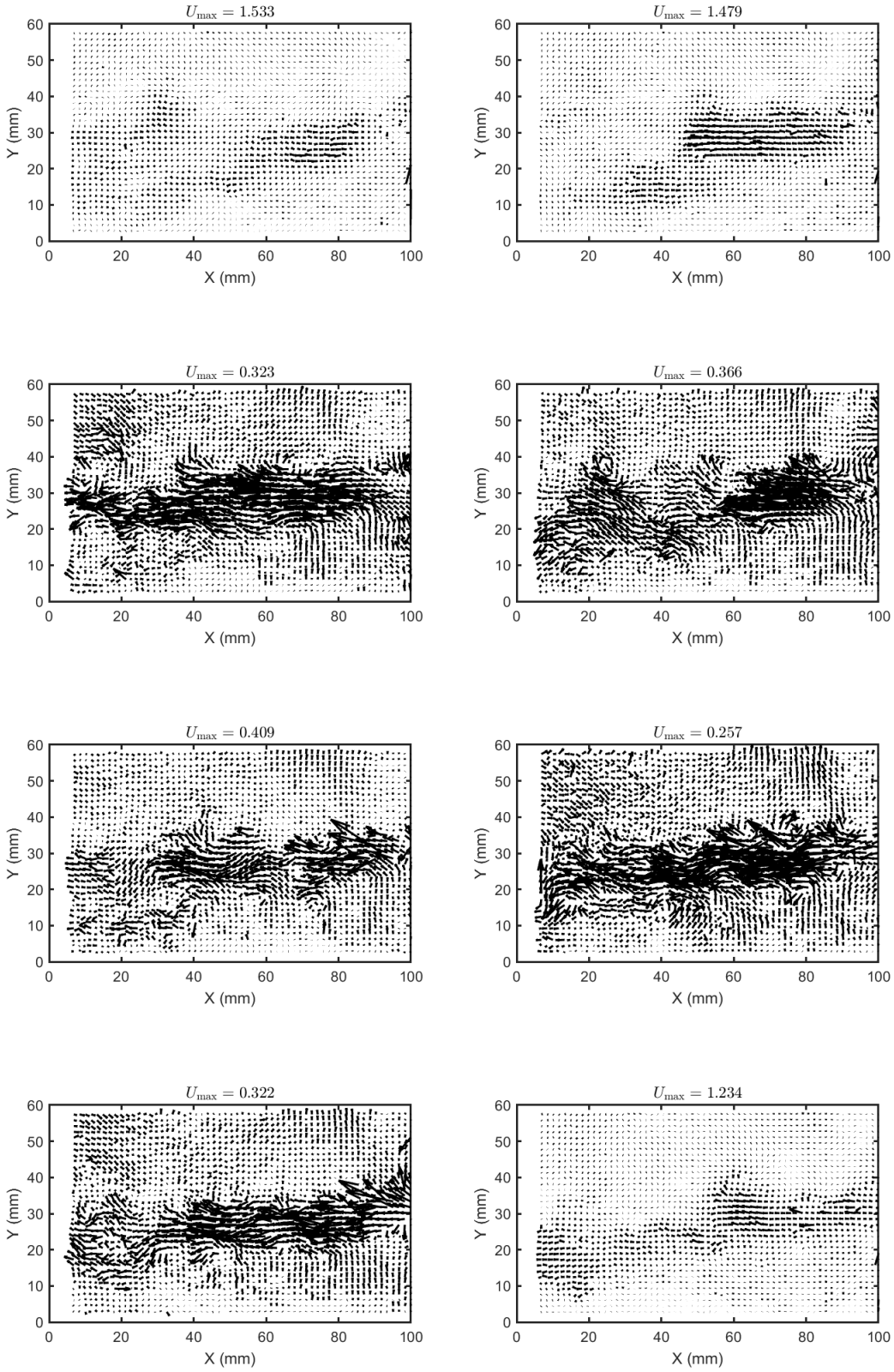

Figure G.38: Uncleaned PIV data at 230 Hz - Image 3

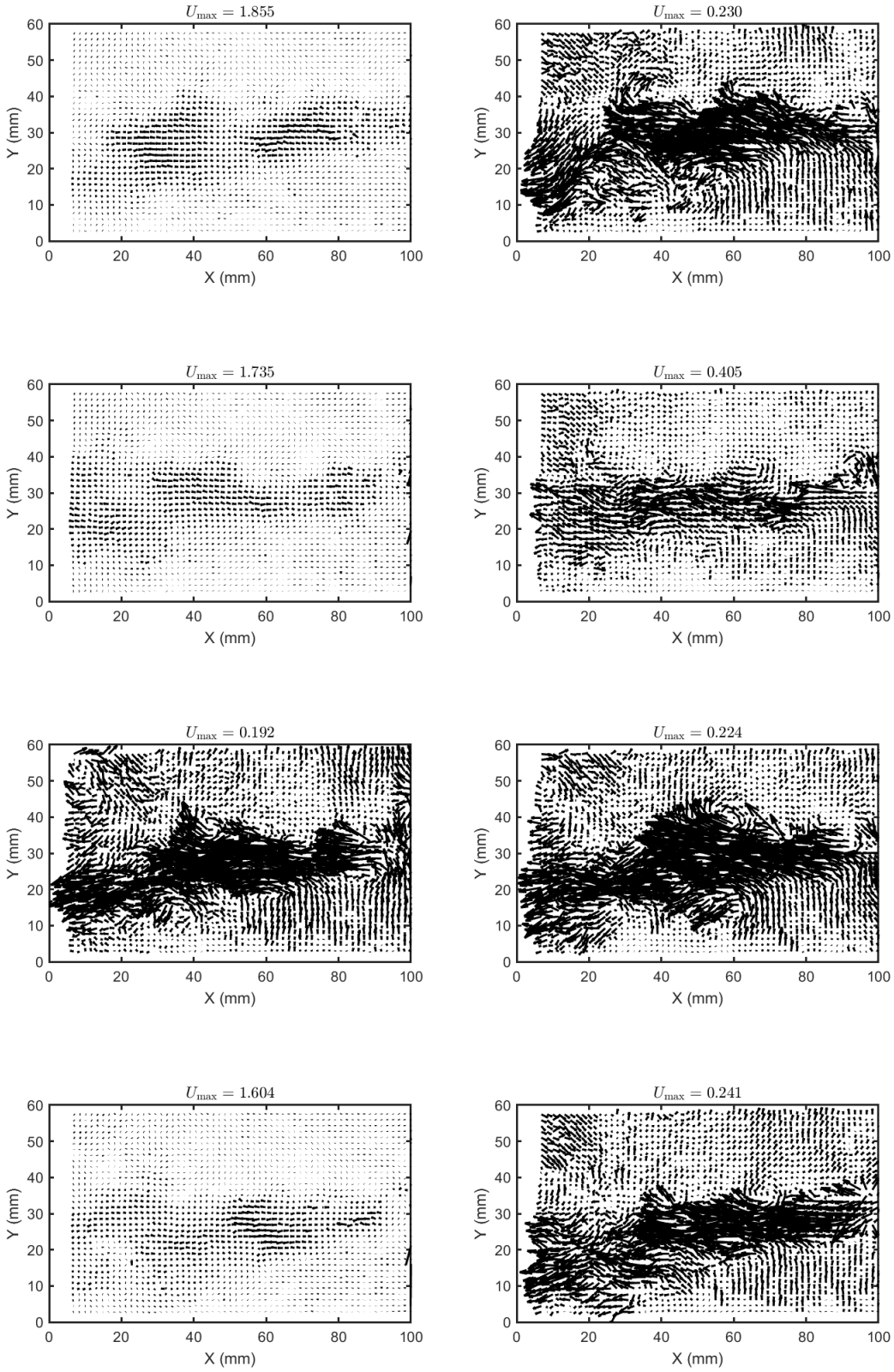

Figure G.39: Uncleaned PIV data at 230 Hz - Image 4

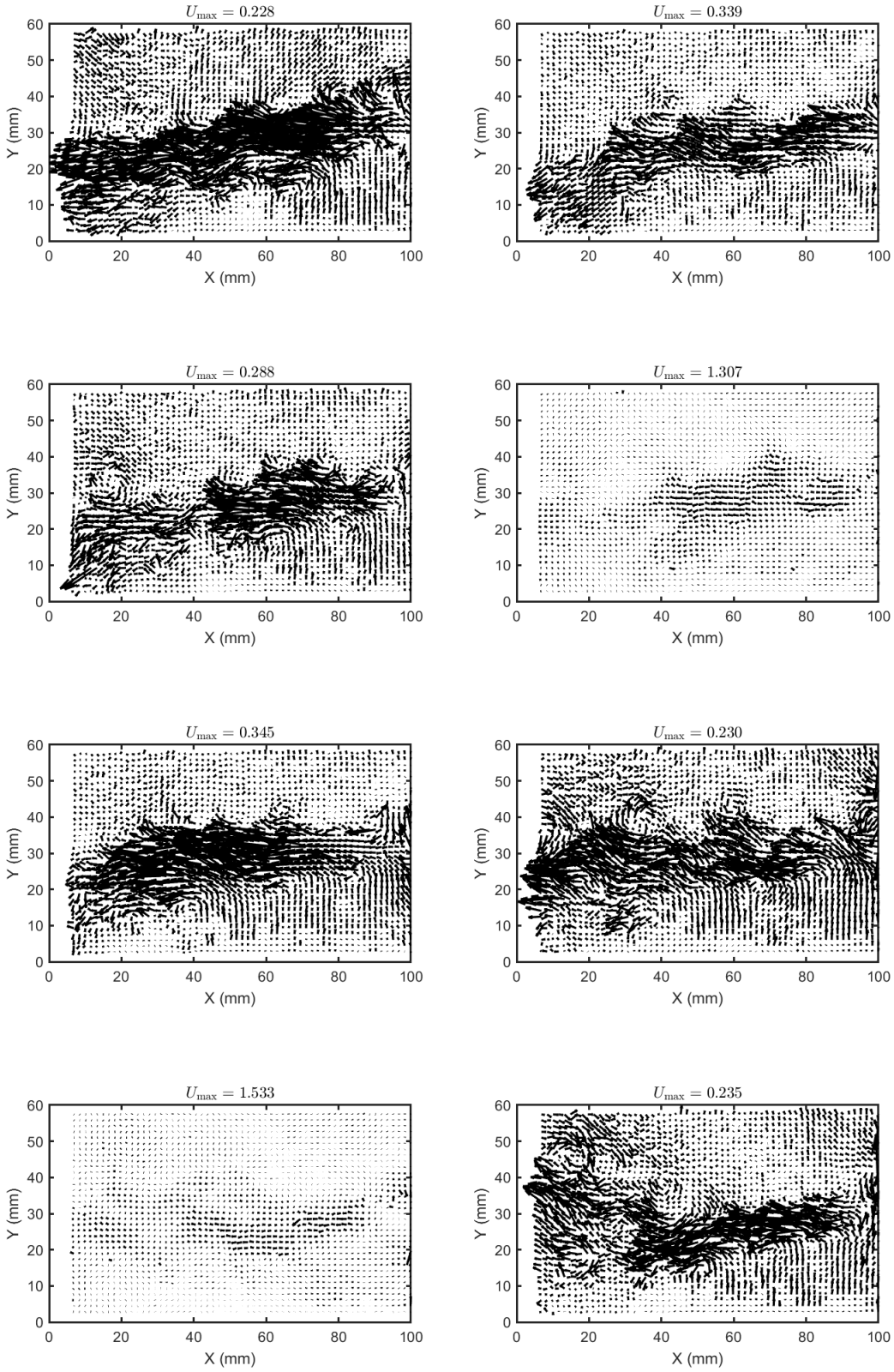

Figure G.40: Uncleaned PIV data at 230 Hz - Image 5

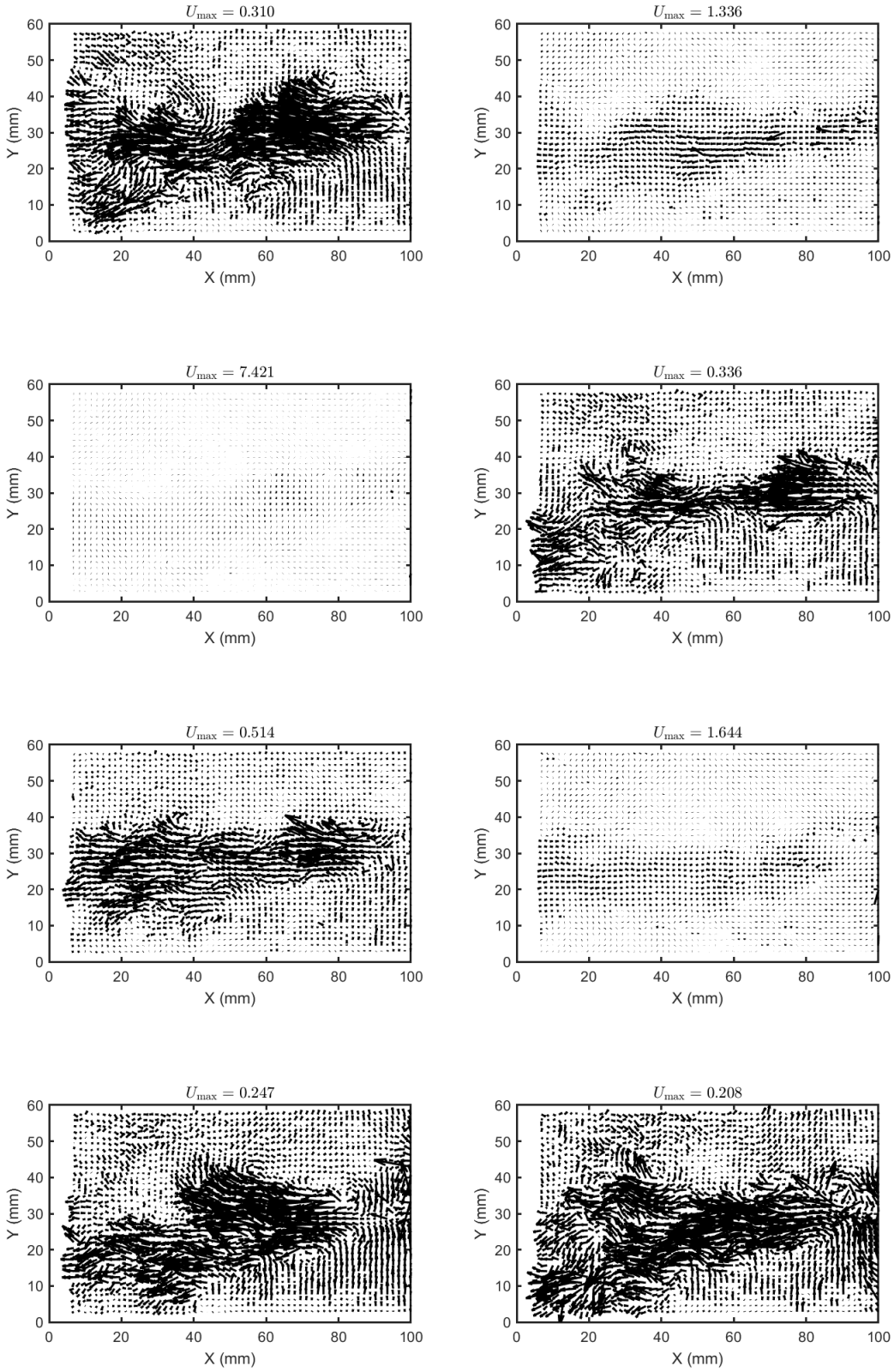

Figure G.41: Uncleaned PIV data at 230 Hz - Image 6

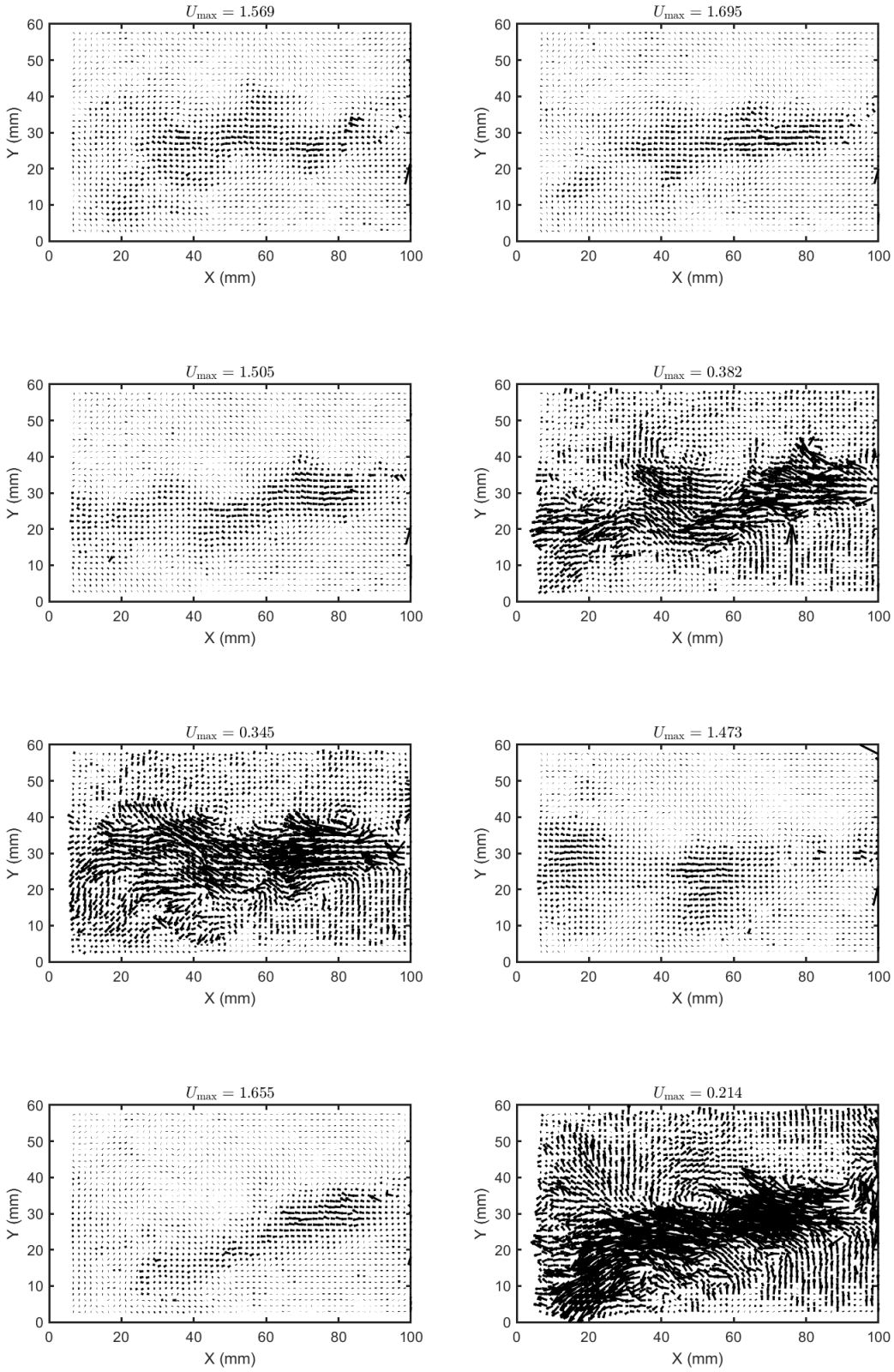

Figure G.42: Uncleaned PIV data at 230 Hz - Image 7

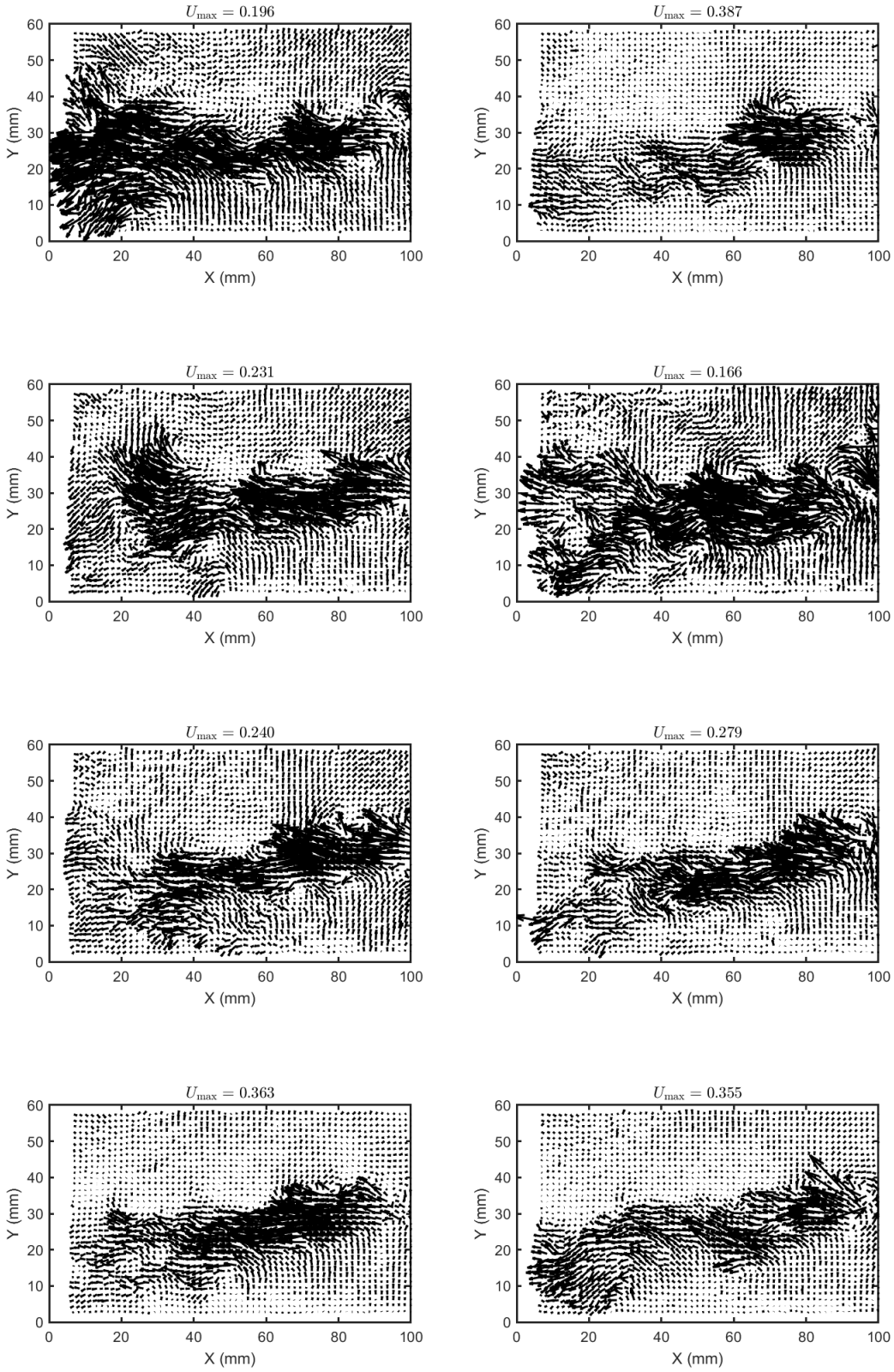

Figure G.43: Uncleaned PIV data at 240 Hz - Image 1

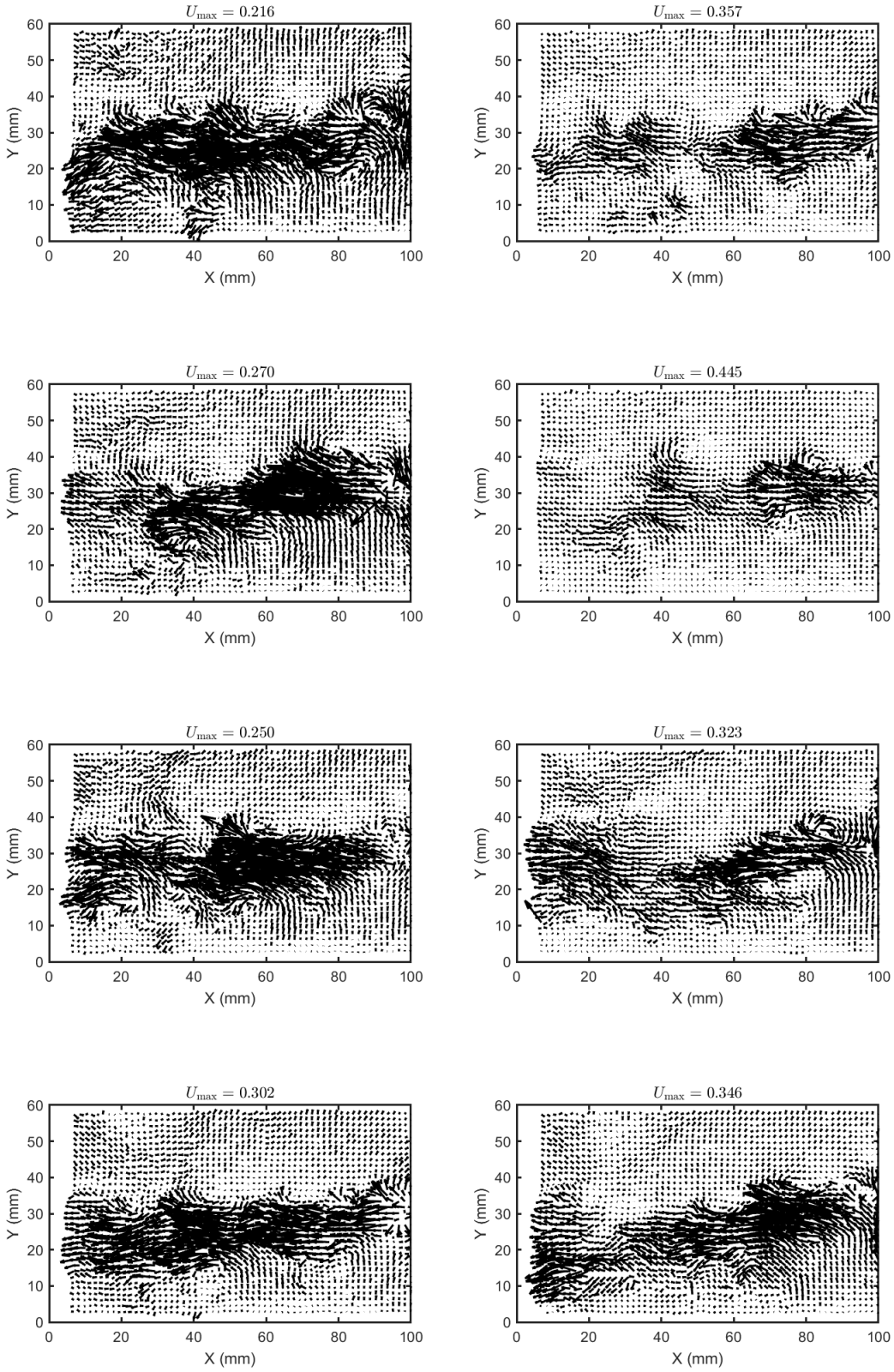

Figure G.44: Uncleaned PIV data at 240 Hz - Image 2

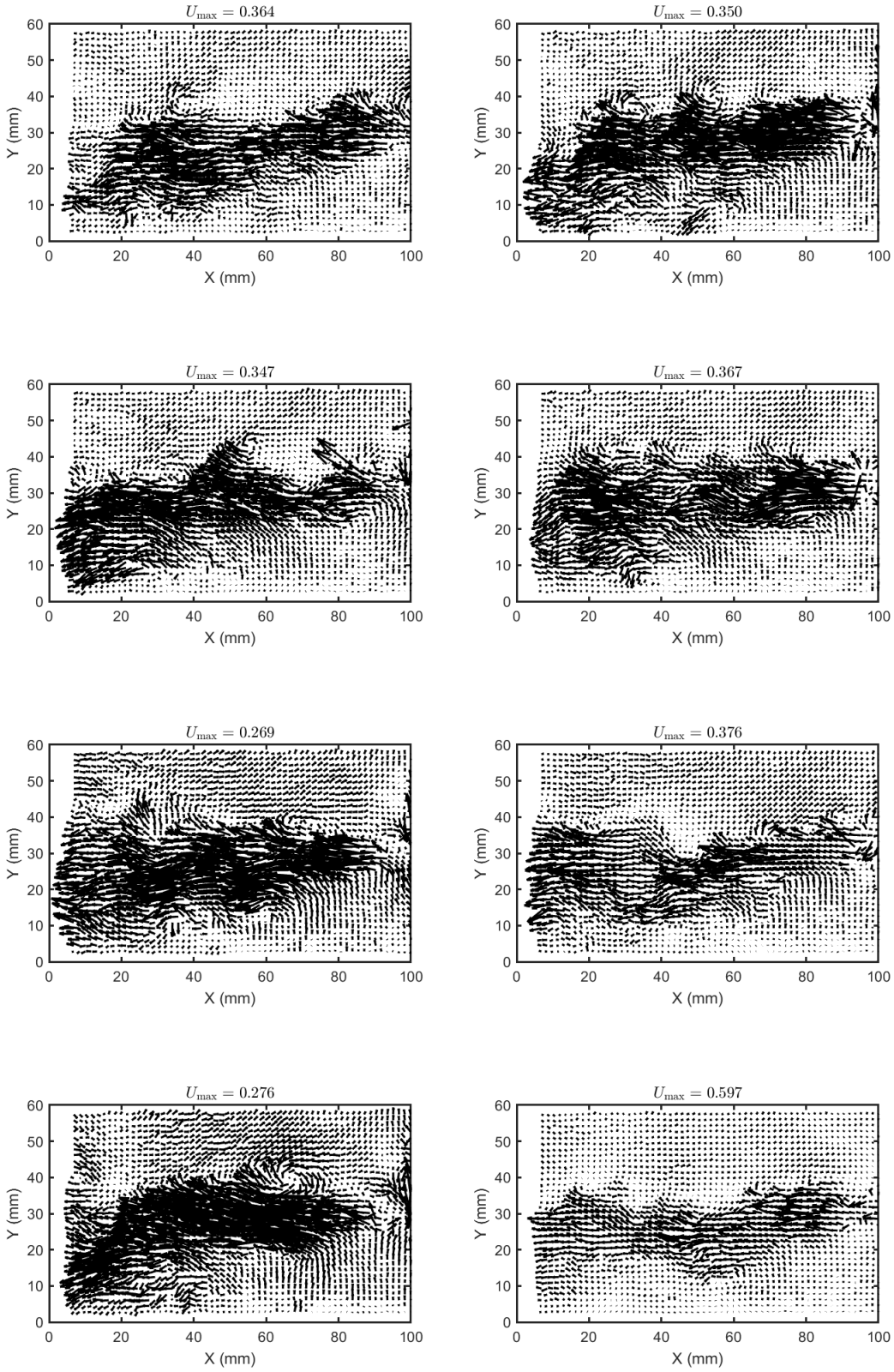

Figure G.45: Uncleaned PIV data at 240 Hz - Image 3

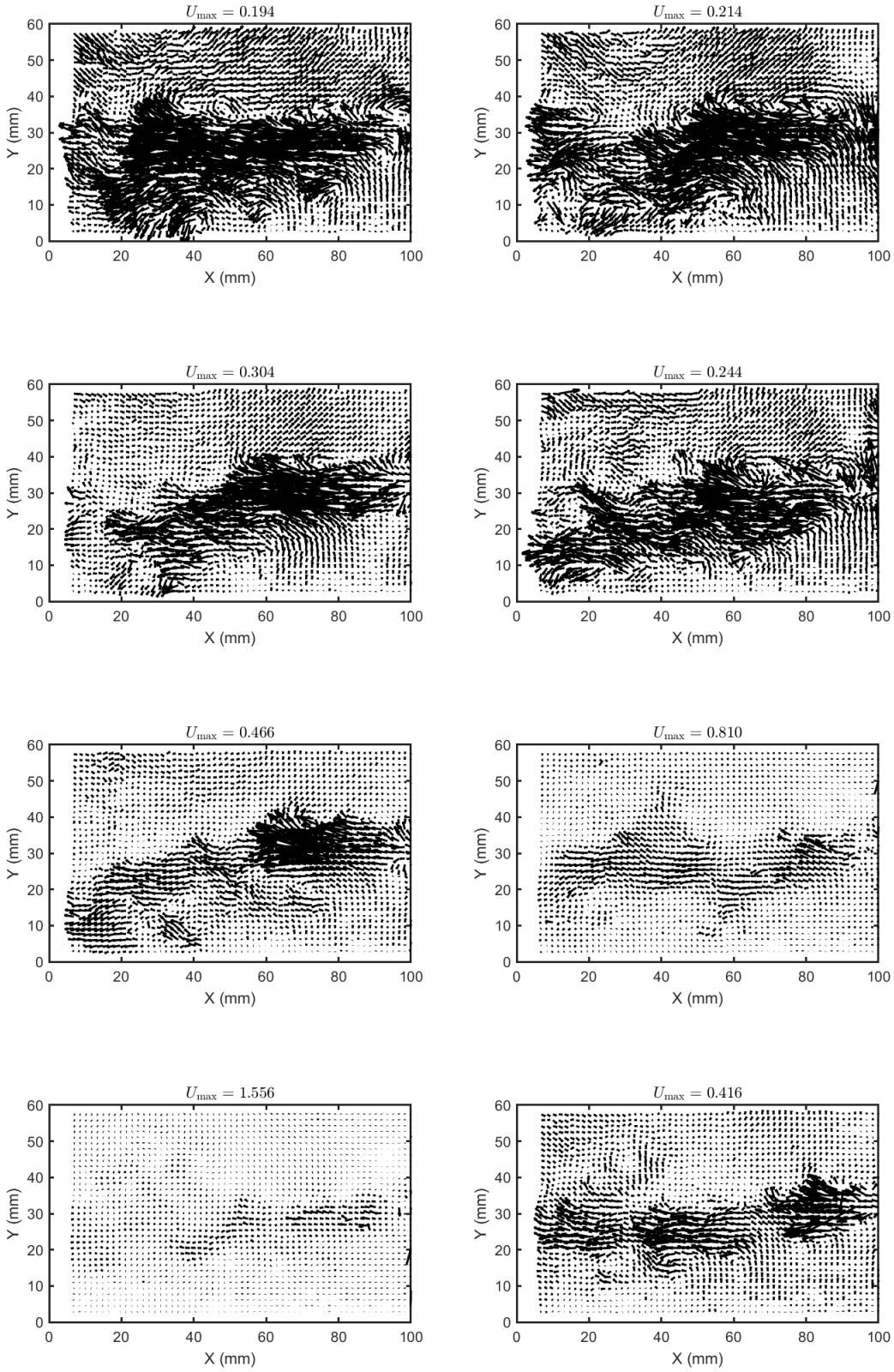

Figure G.46: Uncleaned PIV data at 240 Hz - Image 4

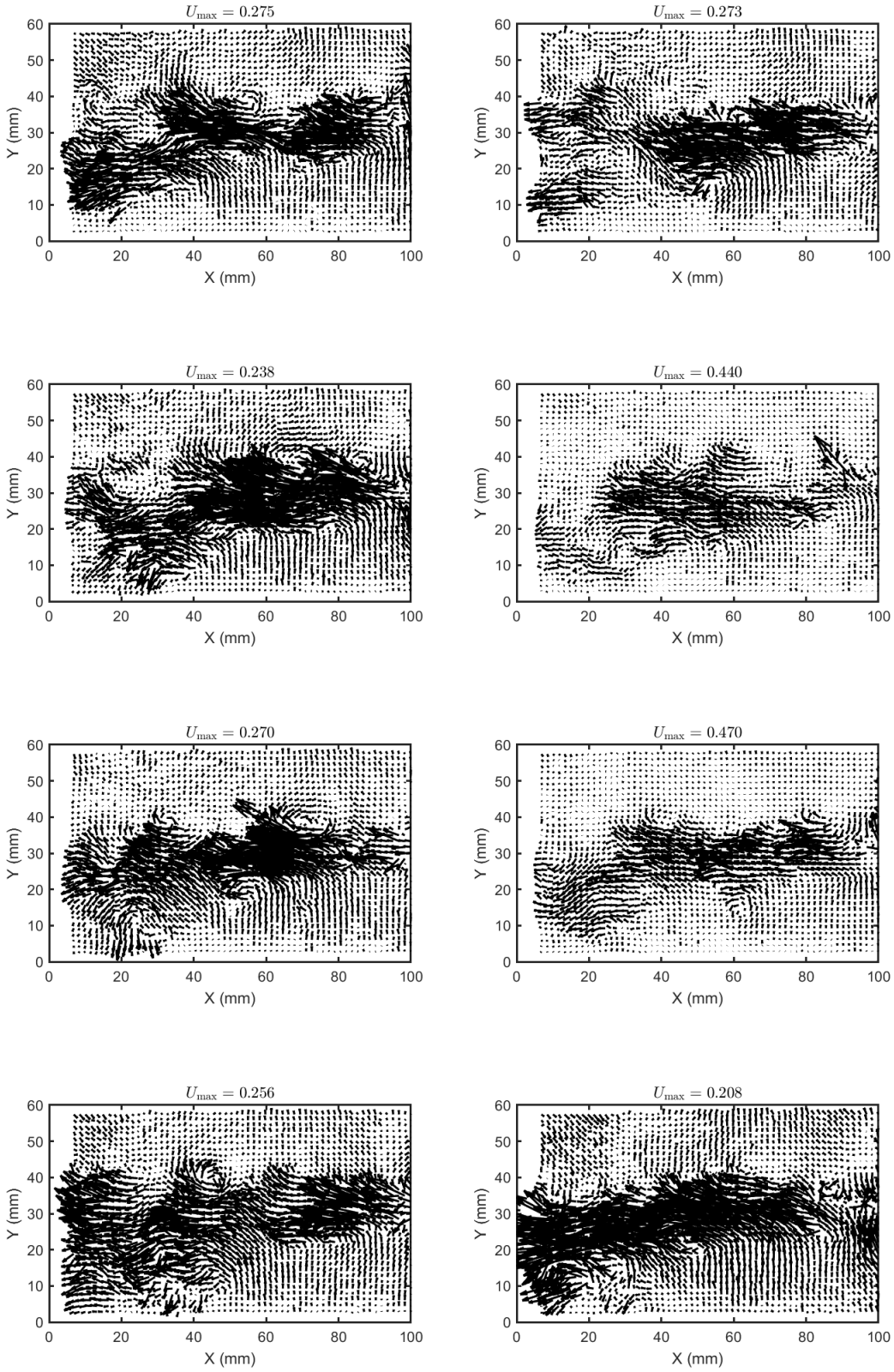

Figure G.47: Uncleaned PIV data at 240 Hz - Image 5

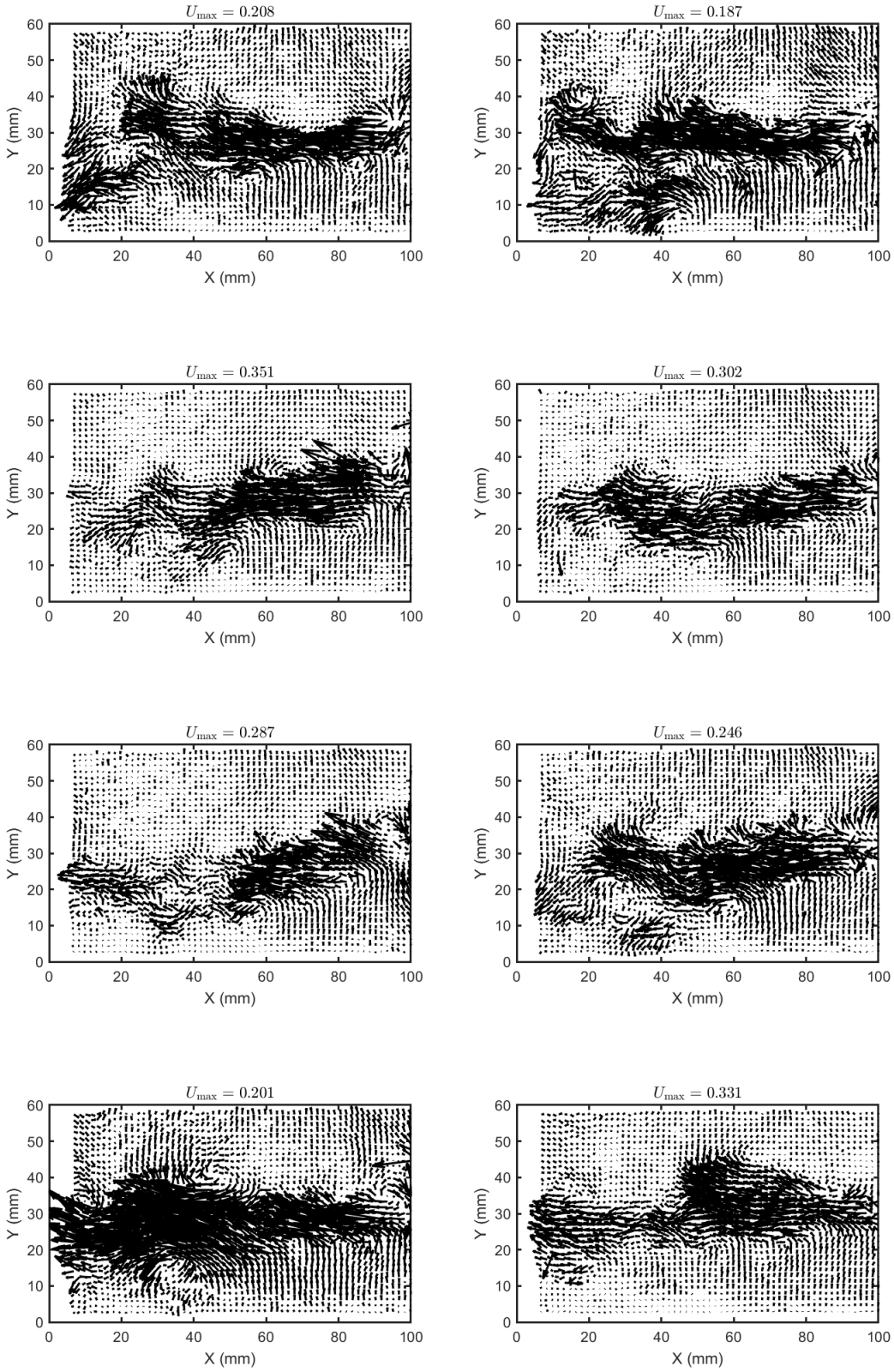

Figure G.48: Uncleaned PIV data at 240 Hz - Image 6

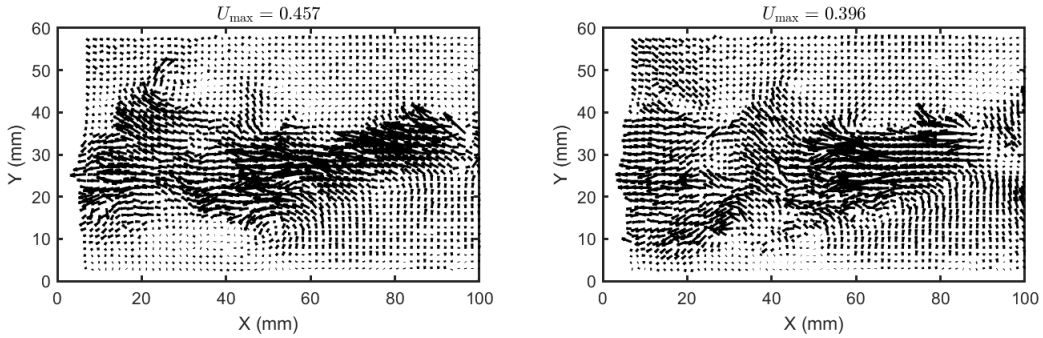

Figure G.49: Uncleaned PIV data at 240 Hz - Image 7

Appendix H

Lab view of Liquid Synthetic Jet Impingement Study

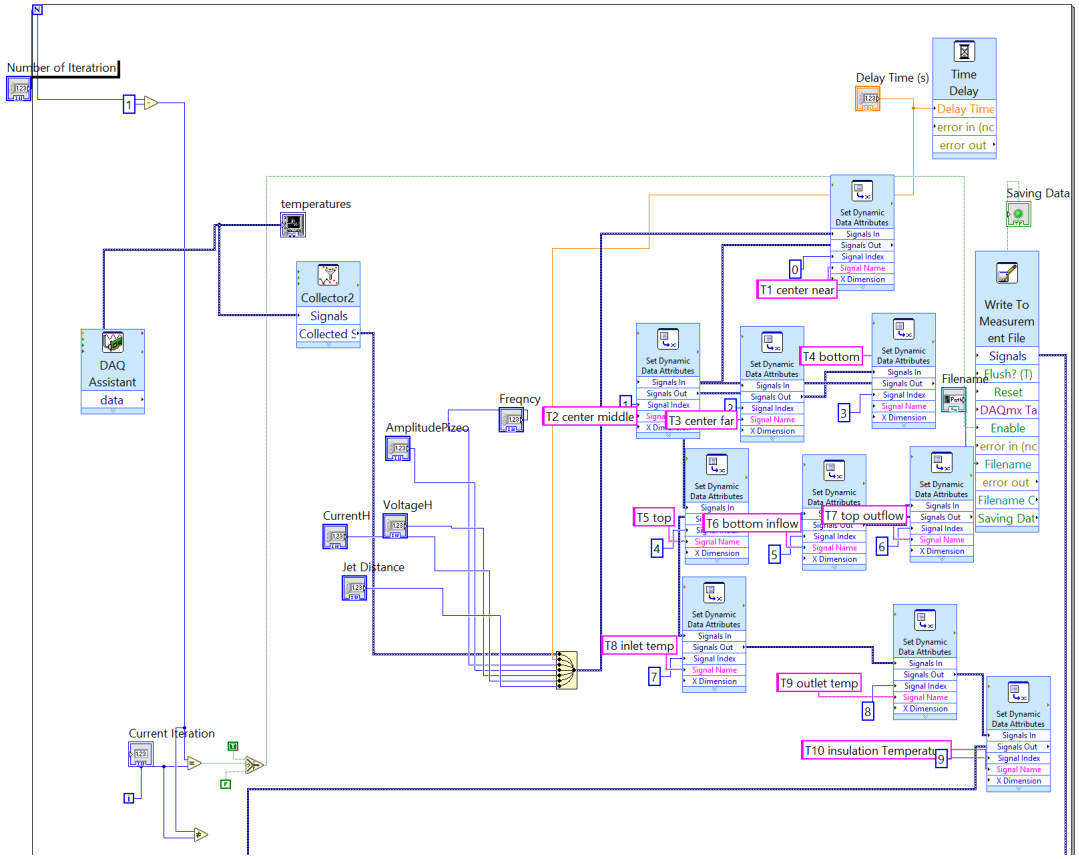

Figure H.1: Labview Page 1.

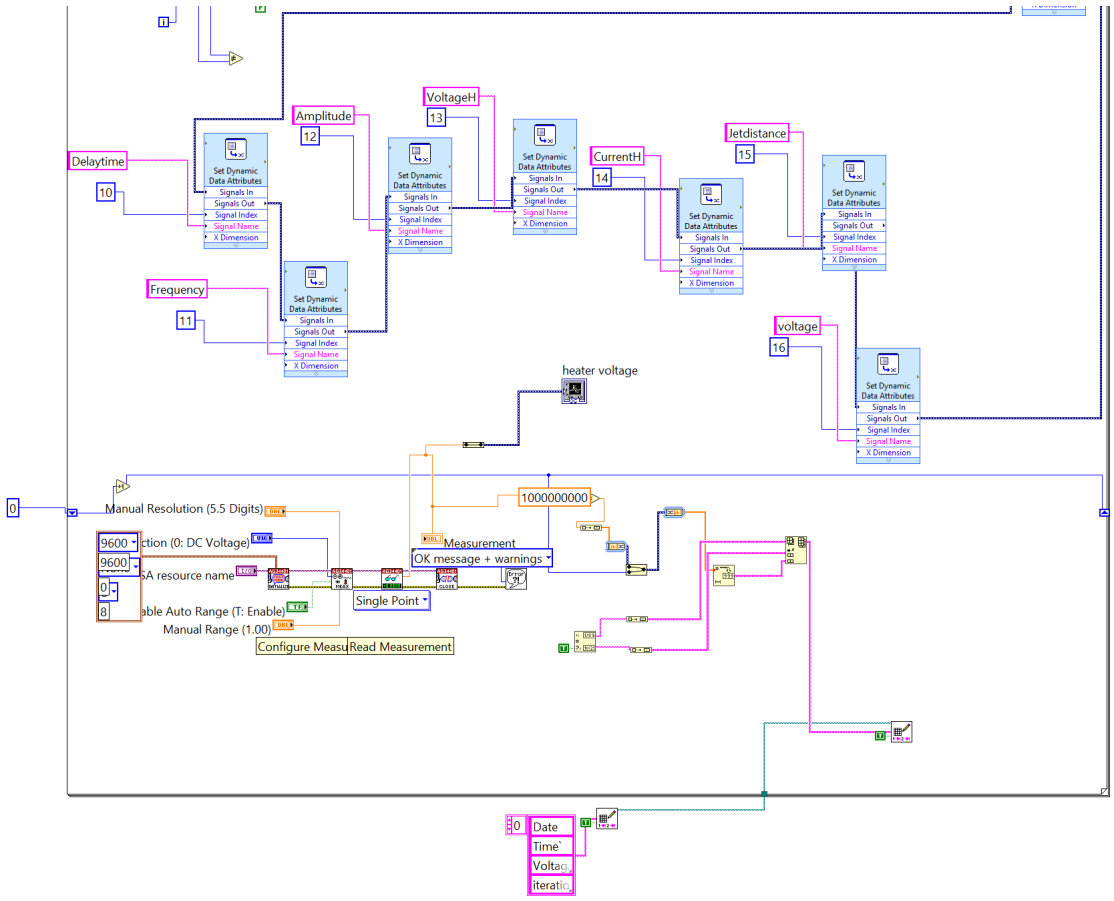

Figure H.2: Labview Page 2.

Appendix I

Deflection UDF

```
1
2  #include "udf.h"
3
4  DEFINE_GRID_MOTION(mw, domain, dt, time, dtime)
5  {
6  face_t f;
7  Thread *tf = DT_THREAD(dt);
8  int n;
9  Node *v;
10 real NV_VEC(velocity), NV_VEC(axis);
11 real NV_VEC(origin), NV_VEC(rvec);
12 real freq;
13 real amp;
14 real length;
15
16 SET_DEFORMING_THREAD_FLAG(THREAD_T0(tf));
17
18 freq = 155;
19 amp = 5.00e-005;
20 length = 17.5e-003;
21 NV_S(velocity,=,0.0);
22 NV_D(axis,=,0.0,0.0,1.0);
23 NV_D(origin,=,0.0,0.0,0.0);
24
25 begin_f_loop(f, tf)
26 {
27 f_node_loop(f, tf, n)
28 {
29 v = F_NODE(f, tf, n);
30 if(NODE_POS_NEED_UPDATE(v))
31 {
32 NODE_POS_UPDATED(v);
33 NODE_Z(v) = amp*(1-(pow((NODE_X(v)), 2)+pow((NODE_Y(v)),
      2))/(pow((length), 2)))*sin(2*M_PI*freq*time);}}}
34 end_f_loop(f,tf);}
```

Listing I.1: UDF for Fluent